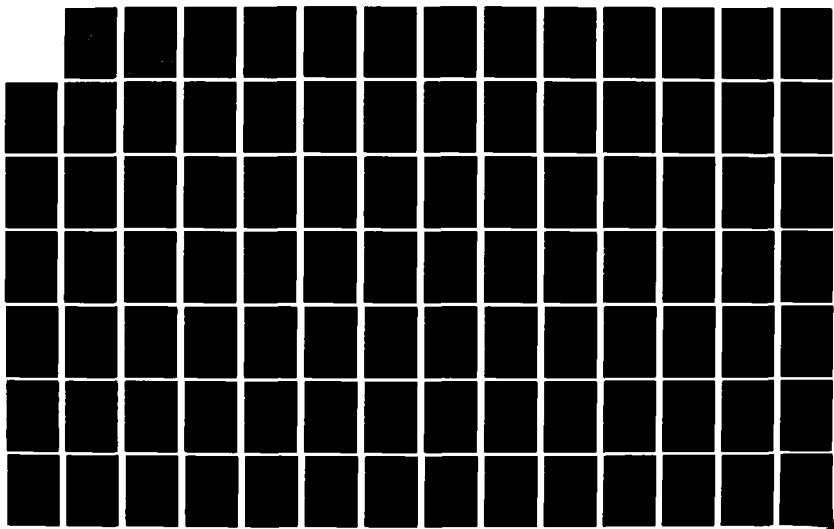
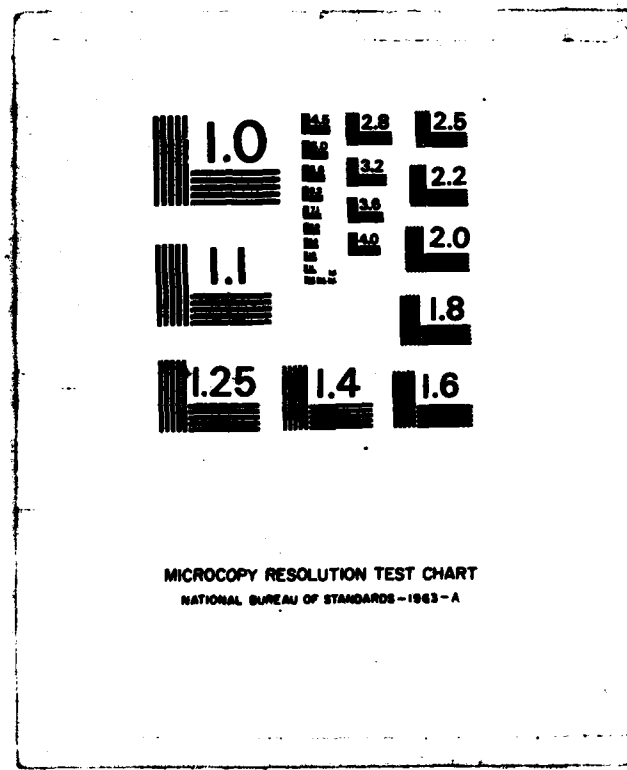


AD-A122 023 ACOUSTIC PROPAGATION AND BARRIER DIFFRACTION OVER AN 1/3
IMPEDANCE PLANE(U) PENNSYLVANIA STATE UNIV UNIVERSITY
PARK APPLIED RESEARCH LAB. M R NOBILE 13 OCT 82

UNCLASSIFIED ARL/PSU/TM-82-210 N00024-79-C-6043 F/G 12/1 NL





ADA122023

(6)

ACOUSTIC PROPAGATION AND BARRIER DIFFRACTION OVER AN
IMPEDANCE PLANE

Matthew A. Nobile

Technical Memorandum
File No. TM 82-210
October 13, 1982
Contract No. N00024-79-C-6043

Copy No. 6

The Pennsylvania State University
Intercollege Research Programs and Facilities
APPLIED RESEARCH LABORATORY
Post Office Box 30
State College, PA 16801

APPROVED FOR PUBLIC RELEASE
DISTRIBUTION UNLIMITED

DTIC FILE COPY

NAVY DEPARTMENT

NAVAL SEA SYSTEMS COMMAND

DTIC
ELECTRONIC
S
DEC 2 1982

82 12 02 013

UNCLASSIFIED

SECURITY CLASSIFICATION OF THIS PAGE (When Data Entered)

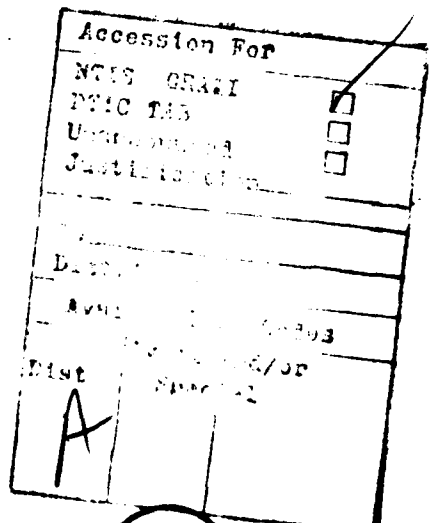
REPORT DOCUMENTATION PAGE		READ INSTRUCTIONS BEFORE COMPLETING FORM
1. REPORT NUMBER 82-210	2. GOVT ACCESSION NO. AD-A122023	3. RECIPIENT'S CATALOG NUMBER
4. TITLE (and Subtitle) ACOUSTIC PROPAGATION AND BARRIER DIFFRACTION OVER AN IMPEDANCE PLANE		5. TYPE OF REPORT & PERIOD COVERED Ph.D. Thesis, November 1982
7. AUTHOR(s) Matthew A. Nobile		6. PERFORMING ORG. REPORT NUMBER 82-210
9. PERFORMING ORGANIZATION NAME AND ADDRESS The Pennsylvania State University Applied Research Laboratory, P.O. Box 30 State College, PA 16801		8. CONTRACT OR GRANT NUMBER(s) N00024-79-C-6043
11. CONTROLLING OFFICE NAME AND ADDRESS Naval Sea Systems Command Department of the Navy Washington, DC 20362		10. PROGRAM ELEMENT, PROJECT, TASK AREA & WORK UNIT NUMBERS .
14. MONITORING AGENCY NAME & ADDRESS(if different from Controlling Office)		12. REPORT DATE October 13, 1982
		13. NUMBER OF PAGES 217 pages
		15. SECURITY CLASS. (of this report)
		15a. DECLASSIFICATION/DOWNGRADING SCHEDULE
16. DISTRIBUTION STATEMENT (of this Report) Approved for public release, distribution unlimited, per NSSC (Naval Sea Systems Command), November 12, 1982		
17. DISTRIBUTION STATEMENT (of the abstract entered in Block 20, if different from Report)		
18. SUPPLEMENTARY NOTES		
19. KEY WORDS (Continue on reverse side if necessary and identify by block number) thesis, acoustic, propagation, barrier, diffraction		
20. ABSTRACT (Continue on reverse side if necessary and identify by block number) The reflection of a spherical acoustic wave by a flat impedance plane is a deceptively simple problem. There is, in fact, no exact closed-form solution. In practice, approximate methods are employed to predict the received pressure, the most popular of which relies on the use of the classical plane wave reflection coefficient, which proves to be deficient for grazing angles of incidence. The primary objective of this study was to derive a more exact solution to the problem of point source propagation over a "locally-reacting," impedance or		

UNCLASSIFIED

SECURITY CLASSIFICATION OF THIS PAGE(When Data Entered)

"ground" plane. This objective was met with the derivation of an asymptotic series solution. One of the most important features of this solution is that higher-order terms can be calculated from preceding terms in the series by the use of recursion formulae, also derived here. Comparing data predicted from this solution with that from a numerical integration of the exact expression showed the asymptotic series to be extremely accurate, even for very low values of the parameter kR . As expected, the plane wave solution often showed major deviations from the exact integral solution.

A secondary goal was to incorporate the new propagation solution into a barrier model so that ground reflections in addition to edge diffraction could be accounted for. Only the first term in the asymptotic ground propagation solution was used for this purpose, as it was shown to be sufficiently accurate for many practical cases. Thus, an "Edge-Plus-Images" barrier diffraction model was developed in the second phase of this study. The results of preliminary sensitivity tests reported here are very encouraging, and indicate that the barrier model should afford a higher degree of accuracy than available with similar models employing the plane wave reflection coefficient.



UNCLASSIFIED

SECURITY CLASSIFICATION OF THIS PAGE(When Data Entered)

ABSTRACT

The reflection of a spherical acoustic wave by a flat impedance plane is a deceptively simple problem. There is, in fact, no exact closed-form solution. In practice, approximate methods are employed to predict the received pressure, the most popular of which relies on the use of the classical plane wave reflection coefficient, which proves to be deficient for grazing angles of incidence.

The primary objective of this study was to derive a more exact *acoustic* solution to the problem of point-source propagation over a *locally-reacting*, *impedance* or *ground* plane. This objective was met with the derivation of an asymptotic series solution. One of the most important features of this solution is that higher-order terms can be calculated from preceding terms in the series by the use of recursion formulae, also derived here. Comparing data predicted from this solution with that from a numerical integration of the exact expression showed the asymptotic series to be extremely accurate, even for very low values of the parameter kR . As expected, the plane wave solution often showed major deviations from the exact integral solution.

A secondary goal was to incorporate the new propagation solution into a barrier model so that ground reflections in addition to edge diffraction could be accounted for. Only the first term in the asymptotic ground propagation solution was used for this purpose, as it was shown to be sufficiently accurate for many practical cases. Thus, an "Edge-Plus-Images" barrier diffraction model was developed in

the second phase of this study. The results of preliminary sensitivity tests reported here are very encouraging, and indicate that the barrier model should afford a higher degree of accuracy than available with similar models employing the plane wave reflection coefficient.

TABLE OF CONTENTS

	<u>Page</u>
ABSTRACT	iii
LIST OF TABLES	vii
LIST OF FIGURES	viii
ACKNOWLEDGEMENTS	xiv

Chapter

I. INTRODUCTION	1
1.1 Background and Statement of the Problem	1
1.2 Review of Previous Investigations	6
1.2.1 Propagation Over an Impedance Plane	8
1.2.2 Diffraction Over a Barrier	11
1.2.3 The Combined Problem of Diffraction by a Barrier on a Ground Plane	15
1.3 Scope and Importance of Study	20
II. MATHEMATICAL FORMULATION AND SOLUTION TO THE PROBLEM OF POINT SOURCE PROPAGATION OVER AN IMPEDANCE PLANE	23
2.1 Overview	23
2.2 Formulation of the Problem	29
2.2.1 The Particular Solution: A Point Source in a Free Field	30
2.2.1.1 The Field from a Point Source in Cartesian Coordinates	30
2.2.1.2 The Field from a Point Source in Cylindrical Coordinates	34
2.2.2 Total Solution: Effects of the Boundary . .	38
2.2.2.1 Total Integral Solution via Elementary Wave Functions	39
2.2.2.2 Total Integral Solution via Hankel Transforms	42
2.3 Derivation of the Asymptotic Series Solution . .	43
2.3.1 Replacement of the Pole	44
2.3.2 Variable Transformation	49

<u>Chapter</u>	<u>Page</u>
2.3.2.1 Matching Transformation at the Saddle Point	50
2.3.2.2 The Transformation of the Integral	52
2.3.2.3 The Path of Integration in the t -plane	54
2.3.3 The Branch Points and Branch Cuts	59
2.3.4 The Taylor Series Expansion	61
2.3.5 The Term-by-Term Integration	66
2.3.5.1 The Formal Series Solution	72
2.3.5.2 The Q-term Form of Solution	78
2.3.5.3 The F-term Form of Solution	80
2.3.5.4 The Hankel Function Form of Solution	82
2.3.5.5 The Solution Using the First Term Only	84
2.4 The Solution for Perpendicular Incidence	85
 III. A MODEL FOR THE COMBINED PROBLEM OF POINT SOURCE PROPAGATION WITH A DIFFRACTING BARRIER	88
3.1 The Geometrical Theory of Diffraction	89
3.1.1 The GTD Solution for a Rigid Half-Plane	94
3.1.2 The GTD Solution for an Impedance Covered Half-Plane	96
3.2 The GTD Model for a Barrier on a Ground Plane	99
 IV. NUMERICAL RESULTS	108
4.1 Numerical Results for Ground Propagation Problem	108
4.1.1 Dependence on the Parameter kR	109
4.1.2 Dependence on the Reflection Angle	123
4.1.3 Received Spectra for a Practical Ground Cover	130
4.1.4 Results for Perpendicular Incidence	138
4.2 Numerical Results for the Barrier Problem	143
4.2.1 Dependence on the Parameter kR	146
4.2.2 Dependence on the Barrier Height	162
4.2.3 Dependence on the Diffraction Angle	174
4.2.4 Received Spectra for a Practical Ground Cover	180
 V. SUMMARY AND CONCLUSIONS	187
5.1 Summary	187
5.2 Conclusions	191
5.3 Suggestions for Further Research	194
 REFERENCES	195

LIST OF TABLES

<u>Table</u>	<u>Page</u>
4.1 Summary of Geometry and Impedance Conditions for the Numerical Data Plotted in Section 4.1.1.	122
4.2 Summary of Geometry and Impedance Conditions for the Numerical Data Plotted in Section 4.1.2.	129
4.3 Real and Imaginary Parts of the Impedance of Outdoor (NRC) Grass for Third-Octave Values of Frequency.	131
4.4 Real and Imaginary Parts of the Impedance of Indoor-Outdoor Carpet Material for Third-Octave Values of Frequency.	137
4.5 Summary of Geometry and Impedance Conditions for the Numerical Data Plotted in Section 4.1.3.	139
4.6 Summary of Geometry and Impedance Conditions for the Numerical Data Plotted in Section 4.2.1.	163
4.7 Summary of Geometry and Impedance Conditions for the Numerical Data Plotted in Section 4.2.2.	173
4.8 Summary of Geometry and Impedance Conditions for the Numerical Data Plotted in Section 4.2.3.	181

LIST OF FIGURES

<u>Figure</u>	<u>Page</u>
1.1 The Geometry of the Combined Propagation-Diffraction Problem. (a) perspective view. (b) side view.	2
1.2 The Geometry of the Ground Propagation Problem. (a) perspective view. (b) side view.	5
1.3 The Geometry of the Half-Plane Diffraction Problem. (a) perspective view. (b) side view.	7
1.4 Representation of Overall Problem as Superposition of Four Diffraction Paths using Source and Receiver Images.	19
2.1 Simple Reflection Problem with Images. (a) Plane Wave. (b) Spherical Wave.	24
2.2 Reflection of Elemental Segments of a Wavefront for a (a) Plane Wave or a (b) Spherical Wave.	28
2.3 The Cartesian Space Geometry. (a) Source and Receiver Coordinates. (b) Propagation Vector for a Single Elemental Plane Wave with Arbitrary Direction in the Space.	32
2.4 Geometry of Propagation Problem in Cylindrical Coordinates. Source-Receiver distance R_1 , Image-Receiver distance R_2 , Reflection Angle ψ , and Ground Admittance β	46
2.5 Complex t -plane Showing (a) Each of Two Values for the Square Root Function for Imaginary Part of the Admittance Positive or Negative; and (b) a Typical Closed Contour in the Fourth Quadrant.	57
2.6 Complex t -plane Showing Branch Cuts and Transformed Contour for Two--(a) and (b)--Representative Cases for Z_N , ψ , and β	62
2.7 Real and Imaginary Parts of the Integrand Function $U(t)$ vs. t for Z_N , ψ , and β fixed and (a) $kR_2=2.5$, (b) $kR_2=13.5$, and (c) $kR_2=33.7$	68
3.1 The Law of Edge Diffraction: Incident Ray and Diffracted Ray Subtend Equal Angles β with the Edge. Diffracted Rays form a Cone with Apex at Diffraction Point E.	90

<u>Figure</u>	<u>Page</u>
3.2 Geometry of Half-Plane Diffraction Problem in Cylindrical Coordinates. (a) side view showing Diffraction Angles ϕ_0 and ϕ . (b) top view showing Oblique Angle β	93
3.3 Angles Defining Incident and Reflection Shadow Boundaries. . .	95
3.4 Decomposition of Overall Problem into Four Half-Plane Diffraction Problems in Terms of the Geometric Theory of Diffraction. (a) The Direct Diffracted Ray. (b) The Reflected-Diffracted Ray. (c) The Diffracted-Reflected Ray. (d) The Reflected-Diffracted-Reflected Ray.	101
4.1 Calculated Data for (a) Attenuation, and (b) Reflected/Direct Ratio as a Function of kR_2 . Exact, Asymptotic Series, F-term, and Plane Wave Solutions. Small Reflection Angle, Low Impedance.	112
4.2 Calculated Data for (a) Attenuation, and (b) Reflected/Direct Ratio as a Function of kR_2 . Exact, Asymptotic Series, F-term, and Plane Wave Solutions. Small Reflection Angle, Moderately High Impedance.	116
4.3 Calculated Data for Attenuation as a Function of kR_2 . Exact, Asymptotic Series, and F-term Solutions. Grazing Incidence ($\psi=0$), Low Impedance.	117
4.4 Calculated Data for Attenuation as a Function of kR_2 . Exact, Asymptotic Series, F-term, and Plane Wave Solutions. Moderate Reflection Angle. (a) Low Impedance. (b) Moderately High Impedance.	119
4.5 Calculated Data for (a) Attenuation, and (b) Reflected/Direct Ratio as a Function of kR_2 . Exact, Asymptotic Series, F-term, and Plane Wave Solutions. Large Reflection Angle, Low Impedance.	121
4.6 Method of Varying Reflection Angle ψ while Holding Other Parameters Fixed.	124
4.7 Calculated Data for (a) Attenuation, and (b) Reflected/Direct Ratio as a Function of Reflection Angle. Exact, Asymptotic Series, F-term, and Plane Wave Solutions. Small kR_2 , Low Impedance.	125
4.8 Calculated Data for (a) Attenuation, and (b) Reflected/Direct Ratio as a Function of Reflection Angle. Exact, Asymptotic Series, F-term, and Plane Wave Solutions. Large kR_2 , Low Impedance.	126

<u>Figure</u>	<u>Page</u>
4.9 Comparison of Calculated Data for Four Values of Ground Impedance, as a Function of Reflection Angle. F-term and Plane Wave Solutions.	128
4.10 Calculated Data for (a) Attenuation, and (b) Reflected/Direct Ratio as a Function of Frequency for Propagation Over Grass. F-term and Plane Wave Solutions. Sht=0.1, Rht=0.1, Sep=50.0, Reflection Angle=0.23°.	132
4.11 Calculated Data for Attenuation as a Function of Frequency for Propagation over Grass. F-term and Plane Wave Solutions. Sep=50.0 feet. (a) Sht=1.0, Rht=1.0, and ψ = 2.3°. (b) Sht=2.0, Rht=2.0, and ψ = 4.6°.	133
4.12 Calculated Data for (a) Attenuation, and (b) Reflected/Direct Ratio as a Function of Frequency for Propagation Over Grass. F-term and Plane Wave Solutions. Sht=1.0, Rht=1.0, Sep=500.0, Reflection Angle=0.23°.	134
4.13 Calculated Data for (a) Attenuation, and (b) Reflected/Direct Ratio as a Function of Frequency for Propagation Over Carpet. F-term and Plane Wave Solutions. Sht=0.33, Rht=0.25, Sep=24.0, Reflection Angle=1.4°.	136
4.14 Calculated Data for (a) Attenuation, and (b) Reflected/Direct Ratio as a Function of kR , for Perpendicular Incidence. Exact, Two Terms in Asymptotic Series, Two Terms in Convergent Series, and Plane Wave Solutions. Low Impedance Ground.	140
4.15 Calculated Data for Attenuation for Perpendicular Incidence. Exact, Two Terms in Asymptotic Series, Two Terms in Convergent Series, and Plane Wave Solutions. (a) $Z_N = (1.0, 0.05)$. (b) $Z_N = (1.0, 0.005)$	142
4.16 Several Configurations that can be Treated by the Edge-Plus-Images Model. The geometries in (a) and (b) are mathematically equivalent. In (c) the ground need not be horizontal, and in (d) the barrier height need not be constant.	145
4.17 The Geometry of the Barrier-on-the-Ground Problem showing Parameter Definitions for Graphical Data. (a) perspective view. (b) side view. (c) top view.	147
4.18 Calculated Data for (a) Attenuation, and (b) Insertion Loss as a Function of KR. Q-term, Plane Wave, and Half-Plane Solutions. Small Source and Receiver Heights, Small Barrier Height, Low Impedance.	148

<u>Figure</u>	<u>Page</u>
4.19 Calculated Data for (a) Attenuation, and (b) Insertion Loss as a Function of KR. Q-term, Plane Wave, and Half-Plane Solutions. Small Source and Receiver Heights, Small Barrier Height, High Impedance.	152
4.20 Calculated Data for (a) Attenuation, and (b) Insertion Loss as a Function of KR. Q-term, Plane Wave, and Half-Plane Solutions. Small Source and Receiver Heights, Large Barrier Height, Low Impedance.	153
4.21 Calculated Data for (a) Attenuation, and (b) Insertion Loss as a Function of KR. Q-term, Plane Wave, and Half-Plane Solutions. Small Source and Receiver Heights, Large Barrier Height, High Impedance.	154
4.22 Calculated Data for Attenuation as a Function of KR. Q-term, Plane Wave, and Half-Plane Solutions. Large Source and Receiver Heights, Large Barrier Height, Low Impedance. . . .	156
4.23 Calculated Data for Attenuation as a Function of KR. Q-term and Plane Wave Solutions. Sht=0.25, Rht=8.0, Bht=15.0. In (a) $Z_1=(100,150)$, $Z_2=(100,150)$, and in (b) $Z_1=(100,150)$, $Z_2=(2.0,2.5)$	158
4.24 Calculated Data for Attenuation as a Function of KR. Q-term and Plane Wave Solutions. Sht=0.25, Rht=8.0, Bht=15.0. In (a) $Z_1=(2.0,2.5)$, $Z_2=(100,150)$, and in (b) $Z_1=(2.0,2.5)$, $Z_2=(2.0,2.5)$	159
4.25 Comparison of Results for Perpendicular and Oblique Incidence on the Edge as a Function of KR. Q-term, Plane Wave, and Half-Plane Solutions. Hard Ground, $\beta = 90^\circ$ and $\beta = 50^\circ$	161
4.26 Calculated Data for (a) Attenuation, and (b) Insertion Loss as a Function of Barrier Height. Q-term, Plane Wave, and Half-Plane Solutions. Small Source and Receiver Heights, Small kR, Low Impedance.	164
4.27 Calculated Data for (a) Attenuation, and (b) Insertion Loss as a Function of Barrier Height. Q-term, Plane Wave, and Half-Plane Solutions. Small Source and Receiver Heights, Small kR, High Impedance.	165
4.28 Calculated Data for (a) Attenuation, and (b) Insertion Loss as a Function of Barrier Height. Q-term, Plane Wave, and Half-Plane Solutions. Small Source and Receiver Heights, Large kR, Low Impedance.	167

<u>Figure</u>	<u>Page</u>
4.29 Calculated Data for (a) Attenuation, and (b) Insertion Loss as a Function of Barrier Height. Q-term, Plane Wave, and Half-Plane Solutions. Small Source and Receiver Heights, Large kR, High Impedance.	168
4.30 Calculated Data for Attenuation as a Function of Barrier Height. ^-term, Plane Wave, and Half-Plane Solutions. Sht=4.0, Rht=4.0, kR=50.0. In (a) $Z_N=(1.5,2.0)$ and in (b) $Z_N=(15.0,20.0)$	169
4.31 Calculated Data for (a) Attenuation, and (b) Insertion Loss as a Function of Barrier Height. Q-term, Plane Wave, and Half-Plane Solutions. Sht=0.1, Rht=8.0, kR=1000, and $Z_N=(1.3,1.2)$	171
4.32 Calculated Data for (a) Attenuation, and (b) Insertion Loss as a Function of Barrier Height. Q-term, Plane Wave, and Half-Plane Solutions. Sht=0.5, Rht=0.5, kR=400, and $Z_N=(1.5,2.0)$	172
4.33 Calculated Data for (a) Attenuation, and (b) Insertion Loss as a Function of Diffraction Angle. Q-term, Plane Wave, and Half-Plane Solutions. Sht=0.2, $R_2=12.0$, kR=5.0, Bht=5.0, and $Z_N=(1.5,2.0)$	175
4.34 Calculated Data for (a) Attenuation, and (b) Insertion Loss as a Function of Diffraction Angle. Q-term, Plane Wave, and Half-Plane Solutions. Sht=0.2, $R_2=12.0$, kR=5.0, Bht=5.0, and $Z_N=(15.0,20.0)$	176
4.35 Calculated Data for (a) Attenuation, and (b) Insertion Loss as a Function of Diffraction Angle. Q-term, Plane Wave, and Half-Plane Solutions. Sht=0.2, $R_2=12.0$, kR=100, Bht=5.0, and $Z_N=(1.5,2.0)$	177
4.36 Calculated Data for (a) Attenuation, and (b) Insertion Loss as a Function of Diffraction Angle. Q-term, Plane Wave, and Half-Plane Solutions. Sht=0.2, $R_2=12.0$, kR=100, Bht=5.0, and $Z_N=(15.0,20.0)$	178
4.37 Calculated Data for (a) Attenuation, and (b) Insertion Loss as a Function of Frequency. Q-term and Plane Wave Solutions. Sht=0.25, Rht=0.25, Bht=15.0, and $Z_N=RIGID$	182
4.38 Calculated Data for (a) Attenuation, and (b) Insertion Loss as a Function of Frequency. Q-term and Plane Wave Solutions. Sht=0.25, Rht=0.25, Bht=15.0, and $Z_N=GRASS$	184

<u>Figure</u>	<u>Page</u>
4.39 Calculated Data for (a) Attenuation, and (b) Insertion Loss as a Function of Frequency. Q-term and Plane Wave Solutions. Sht=0.25, Rht=0.25, Bht=0.5, and Z_N =GRASS	185
5.1 The Preferred Q-term Form of the Asymptotic Series Solution. Q is the Spherical Wave Reflection Coefficient..	190

Acknowledgements

I would like to thank my thesis advisor, Dr. Sabih I. Hayek, for his support and guidance and for lending his time and expertise freely and continually throughout the course of this study. I am also indebted to Dr. James M. Lawther for his active interest in the research topic. His knowledge and experience were called upon often, and his suggestions and insights were most welcome. Further appreciation is extended to Dr. Eugen J. Skudrzyk, Dr. Jiri Tichy, Dr. Alan D. Stuart, and Dr. Vernon H. Neubert for actively participating on my doctoral committee.

The Graduate Program in Acoustics and the Applied Research Laboratory deserve special acknowledgement for making available their excellent and complete facilities, which I utilized constantly throughout my graduate career.

Regarding the manuscript itself, I am very grateful to Ed McGarvey and Rebecca Nordberg, who helped prepare the illustrations and graphs, and to Janice Hall, who typed the mathematical equations.

Finally, had there not been constant inspiration and encouragement from my wife, Nancy, who, concurrently, was involved in her own demanding Ph. D. research, the completion of this dissertation would not have been possible.

This work was supported in part by the Applied Research Laboratory of The Pennsylvania State University under contract with the U. S. Naval Sea Systems Command.

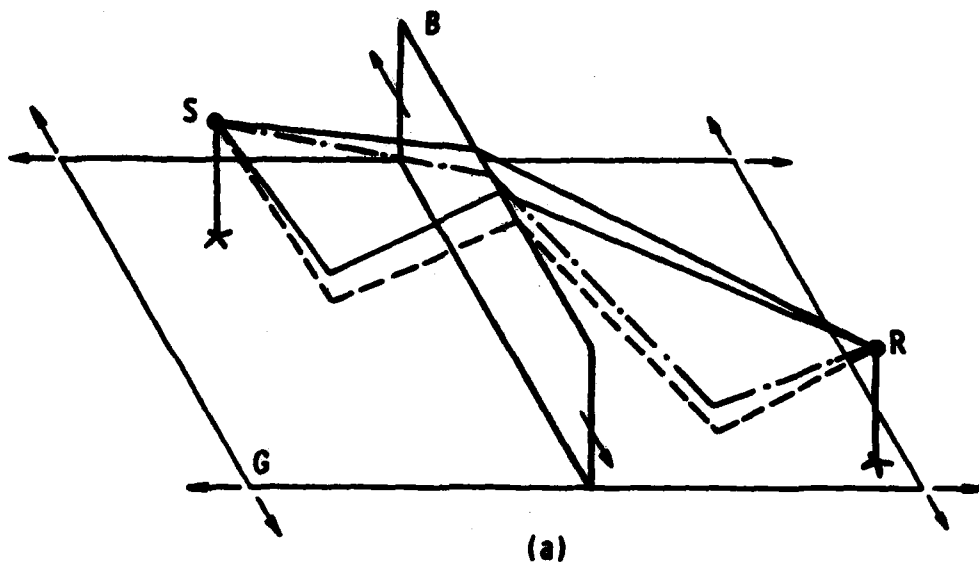
CHAPTER I

INTRODUCTION

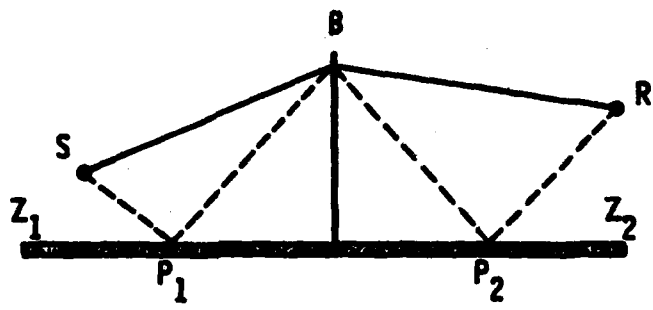
The problem of spherical wave acoustic propagation over an-
impedance plane continues to attract attention within the scientific
community, although the results of the first major theoretical studies
on the subject appeared in the literature over thirty years ago. Much
consideration is also being given to the effects on the sound field
when a diffracting barrier is located between the source and receiver.
At first glance, such strong research interest--a reliable indication
that these problems are far from "solved"--may be surprising,
especially in view of the fact that many of the underlying
mathematical concepts were well-developed over a century ago in the
field of optics, and further refined in the early 1900's in the field
of electromagnetics. However, in response to more contemporary
research needs--particularly those of underwater acoustics as well as
community and aircraft noise control--a re-evaluation of previous
results has become necessary.

1.1 Background and Statement of the Problem

Figure 1.1 (a) and (b) shows the geometry of the overall problem,
where sound propagates from the source S to the receiver R over a
diffracting plane B on, and perpendicular to, an impedance plane G.
Although delineated for clarity, the impedance plane is actually
infinite in both of its dimensions, while the diffracting plane is



(a)



(b)

Figure 1.1 The Geometry of the Combined Propagation-Diffraction Problem. (a) perspective view.
(b) side view.

infinite in one dimension and finite in the other. The infinite extents are represented by small arrows in Figure 1.1 (a). Without loss of generality, the impedance plane G can be assumed to be "horizontal" and therefore referred to as the "ground plane," while the diffracting plane B can be assumed "vertical," of finite "height," infinitely "long," and referred to as the "barrier." The term "barrier" is appropriate for the diffracting plane since it will generally be assumed in this study, as is usually the case in practice, that the receiver is in its acoustic "shadow" relative to the source.

The impedance of the ground plane may take different values on the source and receiver sides of the barrier (Z_1 and Z_2 in Figure 1.1 [b]); however, it will be assumed constant on either side. A fundamental constraint here is that the impedance of the ground plane does not depend on the angle of the incident acoustic energy, and so it may be fully described by specifying only its value at normal incidence.¹

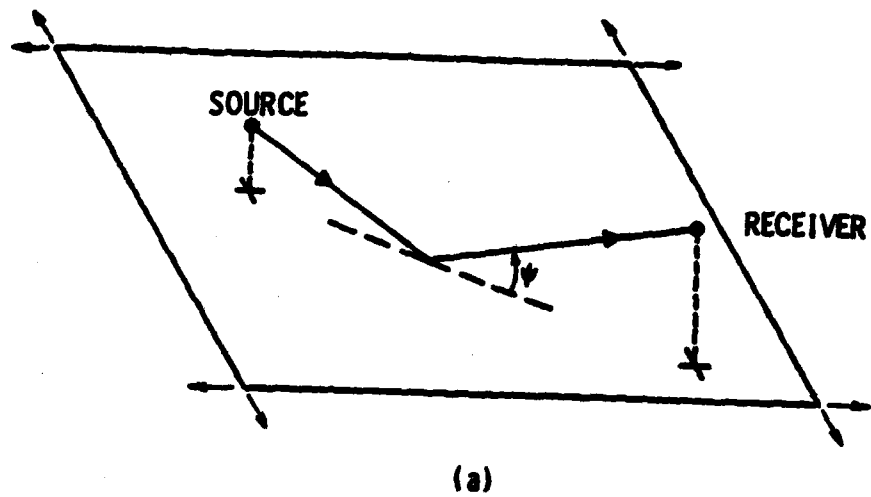
The flow of acoustic energy from the source to the receiver may be regarded as proceeding by way of four distinct paths, shown as rays with exaggerated spacing in Figure 1.1 (a). Thus, there is (i) a direct path over the barrier without ground interaction (path SBR in Figure 1.1 [b]); (ii) a reflected-direct path (SP_1BR) for energy that

¹ This is the same as saying that the surface will not support acoustic particle velocities at angles other than normal, or that the surface is "locally reacting." It is becoming common to use "impedance plane" to imply these characteristics.

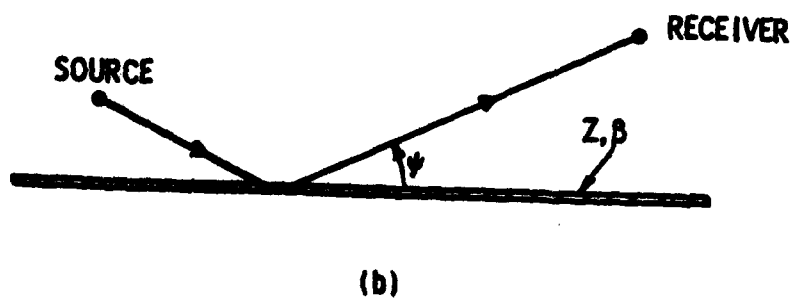
is first reflected from the ground on the source side of the barrier and then diffracted over the barrier to the receiver; (iii) a direct-reflected path (SBP_2R), where the ground reflection is on the receiver side of the barrier; and (iv) a reflected-reflected path (SP_1BP_2R) for energy first reflected from the source-side ground, then diffracted by the barrier, and finally reflected to the receiver from the receiver-side ground.

The overall problem of a barrier on a ground plane splits quite naturally into two parts: propagation over an impedance plane and diffraction by a barrier. The former is illustrated in Figure 1.2 (a) and (b). This deceptively simple problem has no closed-form solution. Complexities derive from the fact that the spherical waves from the point source are not easily matched to the planar boundary conditions dictated by the impedance plane.

It is with regard to this problem that the first major deficiencies in classical theory became apparent. Older studies assumed that the incident acoustic energy was in the form of plane waves, for which the problem is amenable to solution. However, since plane waves are a fiction of mathematics (implying a source of energy "infinitely far" away), the resulting solution becomes inaccurate when applied to more realistic source-receiver configurations. Moreover, for angles of incidence that approach grazing, the plane wave theory is not useful at all. Hence, modern researchers, working on problems where grazing incidence is the rule, have been forced to take into account the sphericity of the incident wavefronts.



(a)



(b)

Figure 1.2 The Geometry of the Ground Propagation Problem.
(a) perspective view. (b) side view.

The second part of the problem under study, the diffraction by the barrier, is illustrated in Figure 1.3 (a) and (b). The case for which the barrier extends to infinity in the two directions indicated by the small arrows (thus, a "half plane" or "semi-infinite" plane) has received considerable attention in the past. Yet it is clear that a barrier located on a ground plane as in Figure 1.1 does not fit such a case, and to use classical results without modification to describe the diffraction process here would be imprecise. The effects of the ground plane must be taken into account, and these effects become more pronounced as the barrier height decreases.

The research to be described in this thesis has retained, and expanded upon, many of the constructs of classical half-plane diffraction theory in formulating a model for the overall problem depicted in Figure 1.1; however, a scheme has been devised for fusing these constructs with the results of an original, more exact solution to the ground propagation problem of Figure 1.2. Predictions, based on this approach, to acoustic propagation problems involving a diffracting barrier located on a ground plane should result in a higher degree of accuracy than available from current models.

1.2 Review of Previous Investigations

The composite problem of acoustic propagation over a ground plane in the presence of a diffracting barrier has been addressed only recently. But, as mentioned in the preceding section, the components parts of the problem--namely, reflection at a plane interface and

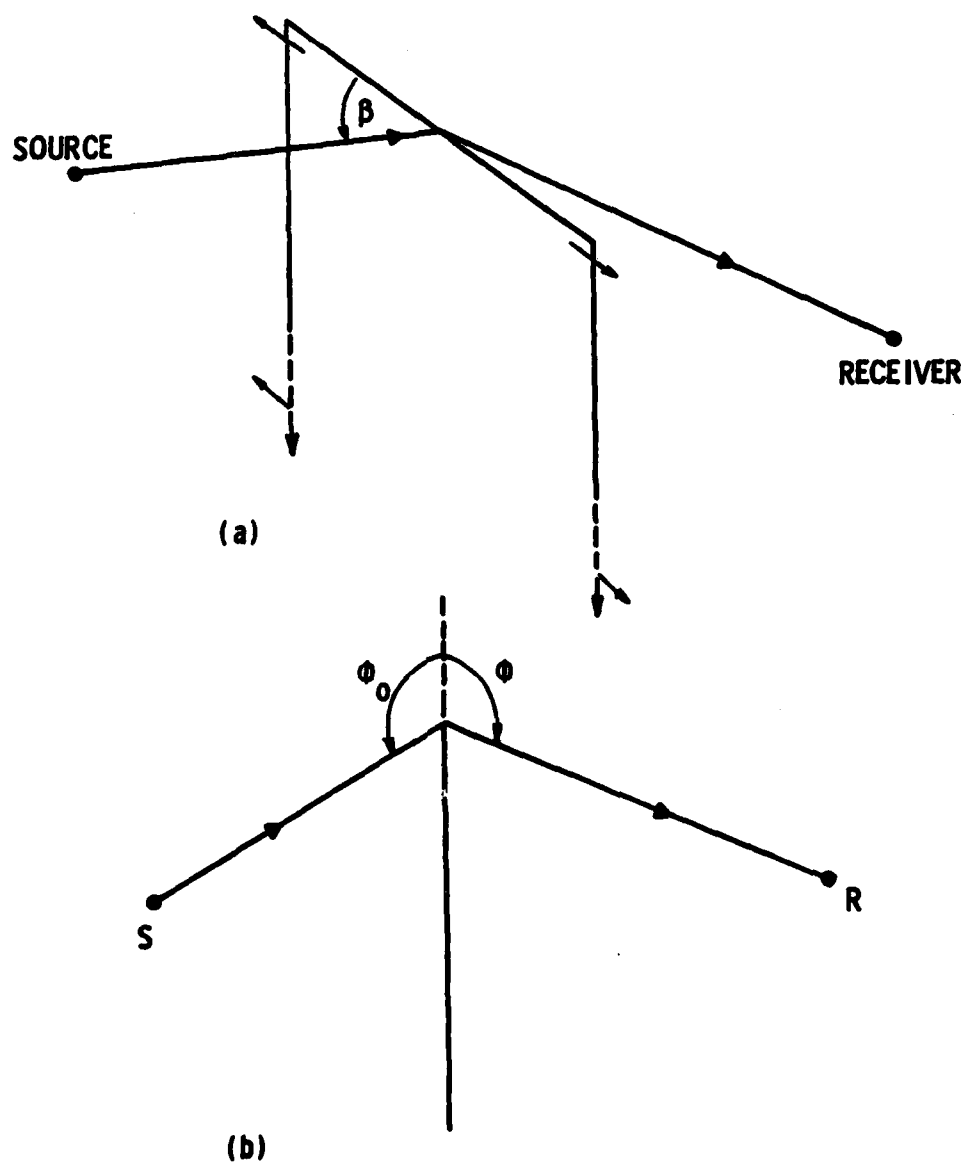


Figure 1.3 The Geometry of the Half-Plane Diffraction Problem. (a) perspective view. (b) side view.

diffraction by a half plane--are classical and have been well-studied separately.

1.2.1 The Problem of Propagation Over an Impedance Plane

The origins of the formal reflection problem were in the field of optics. Thomas Young (1773-1829) and Augustin Fresnel (1788-1827) performed the earliest work on plane waves at perpendicular incidence to an interface. In the mid-1800's, Simeon Poisson, George Green, Lord Rayleigh, and Herman Helmholtz researched the analogous acoustical reflection problem, including oblique incidence.²

Sommerfeld (1909, 1926), working in the field of electromagnetics, was the first to solve the spherical-wave reflection problem, stated as a dipole source on a finitely-conducting earth. Weyl (1919) re-formulated the problem by modelling the radiation from a point source located above the earth as a superposition of an infinite number of elementary plane waves, propagating in different (complex) directions. In the derivation, each component wave is reflected according to the classical plane wave laws.³

² A good discussion of such historical foundations may be found in Lindsay (1972).

³ Although the final forms of the Sommerfeld and Weyl solutions are very similar, the former contains, while the latter lacks, an explicit "surface wave" term. Much controversy followed on this subject (some of which continues today for the acoustical problem), the nature of which can be gleaned from Norton (1937; pp. 1193-1195, pp. 1234-1236) or Stratton (1941, pp. 573-587).

The Sommerfeld and Weyl integral formulations were not conducive to numerical calculations or physical insight until Van der Pol (1935) applied several ingenious substitutions that simplified certain integrals appearing in the derivations. Norton (1936, 1937) expanded upon these and other results from Van der Pol and Niessen (1930) and, with the aid of equations by Wise (1931), generated the most useful results up to that time. His final expressions for the field, though approximate, were in terms of the complex complementary error function, for which numerical values could be calculated. Although scattered research continued on the electromagnetic reflection problem, it is fair to say that the inquiry was essentially completed with Norton's publications.

The acoustical problem of spherical wave reflection was first attacked by Rudnick (1947), who relied heavily on the electromagnetic theories of Van der Pol and Norton. He adapted and applied these results to the problem of determining the sound field from a point source in the vicinity of a plane interface between two fluid media. In subsequent papers with Lawhead (Lawhead and Rudnick, 1951a, 1951b), Rudnick extended his solution to apply to a point source located above an impedance plane. Approximations analogous to those made by Norton also enabled Rudnick and Lawhead to reduce the integrals appearing in the Van der Pol formulation to the error function form, from which they obtained and plotted numerical results. About the same time, Ingard (1951) applied Weyl's method to the impedance plane problem and obtained results very similar to Rudnick's, although the methods of analysis were quite different.

More recent theoretical studies have expanded upon the foundations laid by Rudnick, Lawhead, and Ingard. Paul (1957) studied the two-media problem, applying the method of steepest descent as modified by Ban s and Wesley (1953), to the Sommerfeld-Rudnick theory and obtained two asymptotic solutions, one valid near the interface and the other valid in the region above the source. Wenzel (1974) analyzed the impedance plane problem via Green's functions and contour integration, and obtained integrals to which he applied asymptotic techniques for various extremes of the surface impedance. The "surface wave" was attributed much importance by Wenzel and an explicit term appeared in his solution. Chien and Soroka (1975, 1980) applied Ban s' (1966) double saddle point method of integration--the "method of subtraction of the pole"--to derive an asymptotic expression for the total field, which contained the complementary error function. Their solution is explicit through terms in $1/R^2$, where R is the distance from the source image in the plane to the receiver. Thomasson (1976, 1977) employed the method of steepest descent, along with several variable transformations, and also expressed his solution in terms of the error function. His result is very similar to the first term of Chien and Soroka's full solution. In a subsequent effort (concurrent with the present study), Thomasson (1980) generated an asymptotic expansion of his exact integral representation. He also gave recursion relations for the coefficients in this expansion to enable higher-order terms to be derived or, more

readily, calculated on a digital computer.⁴

In addition to the principal studies above, there have been many other investigations--some theoretical, but most experimental--on the subject of sound propagation above an impedance plane over the past decade. The following selected listing may serve as a guide for further information: Attenborough (1982); Attenborough, Hayek, and Lawther (1980); Briquet and Filippi (1977); Butov (1981); Chessell (1977); Delany and Bazley (1970); Donato (1976a, 1976b); Embleton, Piercy, and Olson (1976); Filippi and Habault (1978); Habault (1980); Habault and Filippi (1981); Hayek, Lawther, Kendig and Simowitz (1978); Hayek, Attenborough, and Lawther (1980); Hayek, Lawther, and Tate (1980); Lawther, Hayek, Tate, and Nobile (1980); Naghieh and Hayek (1981); Pao and Evans (1971); Rasmussen (1982); and Van Moorhem (1975).

1.2.2 The Problem of Diffraction by a Barrier

With its origins in optics and its development in electromagnetics, the study of wave diffraction around obstacles has experienced a new surge of interest in the field of acoustics, primarily among scientist working in community noise control and underwater acoustics. The body of literature on the subject of diffraction is immense, even when limited to studies of the half

⁴ Although not realized by Thomasson, it has been shown in the course of the present study that Chien and Soroka's full solution (to terms in $1/R^2$) could be extracted identically from the first few terms in Thomasson's asymptotic solution.

plane. Thus, only a general survey will be given here.

Thomas Young, in 1800, was the first to critically study the diffraction problem, but his assertions that the phenomenon was local to the diffracting edge were rejected by Fresnel in 1815. Instead, Fresnel employed Huygens' principle and the wave nature of light to develop a mathematical theory which became the foundation for more modern research in diffraction. Helmholtz, in 1859, and, independently, Kirchoff, in 1882, derived their well-known integral equation relating the field at an arbitrary point in a region to the value of the field and its derivatives on the bounding, or diffracting, surface.

Modern diffraction theory has its roots in the research of Sommerfeld (1896), whose rigorous approach using an extension of image theory yielded an exact integral expression for the diffraction of a plane wave by a rigid (or, alternatively, perfectly soft) half plane. Carslaw (1898) continued Sommerfeld's research on the half plane and derived a solution for a point source. MacDonald (1901, 1915) addressed the problem of wedge diffraction--for both a point and a line source--using the classical "separation of variables" technique and expressed his solution as an infinite series of appropriate eigenfunctions. He showed how this series could be re-written in integral form and noted, for the particular case when the wedge "collapsed" to a straight edge, that this integral solution was identical to that given previously by Carslaw. MacDonald went on to derive an asymptotic form for his exact solution in terms of Fresnel

integrals, a form which is utilized often in modern diffraction studies.

Redfearn (1940), recognizing "the practical importance of the problem of reduction of noise at a point due to an unavoidable source of sound at a second point," (p. 273) was the first to seek a simplified, engineering approach and solution to the edge diffraction problem for the acoustical case. Drawing analogies from heat conduction theory,⁵ he put Sommerfeld's solution into a form for a point source, discarded the second of two integral terms (which, in fact, represents the source image in the diffracting plane), assumed the gradient of the field is zero on the faces of the barrier (an assumption first proposed by Kirchoff), and finally, generated a solution in terms of a single geometrical parameter. Redfearn's paper seems to have attracted little attention at the time of its publication, but it was re-discovered in the early 1960's when it served as the impetus for more modern single-number prediction schemes for attenuation of community noise by barriers.

In response to the advances in radio communications in the late 1940's and early 1950's, researchers began looking for practical means of obtaining accurate numerical results for the electromagnetic diffraction problem. Thus, the Weiner-Hopf technique became popular (Heins, 1956; Rawlins, 1975; Senior, 1952) and so-called variational techniques were applied to the problem (Levine & Schwinger, 1948,

⁵ Redfearn makes reference to "Carslaw, 'Conduction of Heat'," but gives no citation.

1949). The dual-integral method, which yields two integral equations valid in separate regions of the complex plane, was also employed (Clemmow, 1966; Jones, 1952). Although applied with success, none of these methods was especially convenient.

The breakthrough that facilitated practical solutions to many common diffraction problems was due to Keller (1958, 1962) and his work on the Geometrical Theory of Diffraction (GTD). Essentially, the GTD method extends classical geometric acoustics to include not only reflected sound rays but diffracted rays as well. The mathematical description of the diffracted rays is in terms of a "diffraction coefficient" deduced from an approximation to a "canonical" diffraction solution. For example, in the treatment of a half plane Keller used the first term in the asymptotic expansion of Sommerfeld's exact plane wave solution to derive the diffraction coefficient. His resulting GTD solution, however, is not valid in the transition regions of the geometric shadow boundaries. Recognizing this shortcoming, Kouyoumjian and Pathak (1974) incorporated previous asymptotic results from Pauli (1938) and Oberhettinger (1956) into Keller's Geometrical Theory of Diffraction to generate a uniform asymptotic solution, in terms of Fresnel integrals, which remained valid in the transition regions of the shadow boundaries.

Concerning the more complex problem of the half plane with arbitrary surface impedances, Malyuzhinets (1955, 1962) and Malyuzhinets & Tuzhlin (1970) employed generalized Fourier transforms to obtain the first rigorous solution. However, this was left in

integral form, and special, cumbersome functions were needed for its evaluation. Recently, Kendig (1977) derived a more useful, closed-form solution for this problem (as well as for the cases of rigid and soft half-plane faces--see Kendig & Hayek, 1981) using function theoretic methods. Kendig's results were expressed in terms of Fresnel integrals, which are relatively simple to evaluate numerically. A comprehensive research effort by the Applied Research Laboratory of The Pennsylvania State University (Hayek, et al., 1978) consolidated Keller's Geometrical Theory of Diffraction, Kouyoumjian's and Pathak's uniform asymptotic results, and Kendig's diffraction solution, to derive very accurate, manageable expressions for the barrier problem. These expressions serve as the basis for the diffraction work of the present study (see also Hayek, 1982; Lawther & Hayek, 1978; Lawther et al., 1980; and Hayek & Nobile, 1981).

Excellent tutorial and review material on the subject of diffraction, including extensive bibliographies may be found in Pierce (1974); Skudrzyk (1971); Bouwkamp (1954); and Bowman, Senior, & Uslenghi (1969).

1.2.3 The Combined Problem of Diffraction by a Barrier on a Ground

Plane

Due to the complicated boundary geometry, there is no exact, closed-form solution to the problem of point source diffraction by a thin, planar barrier located on a flat, impedance-covered ground plane. Neither is there an exact integral form of the solution that

can be evaluated numerically. Even when both the barrier and the ground plane are perfectly rigid, an exact solution can only be formulated (Nobile & Hayek, 1981) in terms of an integral over an infinite summation of Mathieu functions, and to extract any numerical results from this can be most difficult. Lacking, then, a general solution to which mathematical approximations could be applied, the method of attack in most studies has been one of making physical assumptions about the sound field. The fact that these assumptions differ from one author to another is principally responsible for the variety of solutions offered in the current literature. Sometimes very broad and admittedly crude assumptions produce theoretical predictions that compare favorably with experiments. However, an increase in accuracy is almost always attainable using fewer, or less broad, assumptions. The price for this is much more complexity in the mathematics and often more difficulty in extracting numerical results. Although there have been many experimental studies on this topic, the theoretical work is sparse.

Redfearn (1940), mentioned above, spoke in terms of applying his results to actual barriers erected on the ground, but he proposed no method for handling the ground reflections. Fehr (1951), on the other hand, specifically addressed the ground problem, but assumed that the ground was perfectly rigid and that both source and receiver lay directly on it; consequently, his approach simply became a matter of accounting for the pressure doubling by the ground.

Maekawa (1965, 1968) was the first to conduct a comprehensive set of experiments with the expressed purpose of obtaining a large data base for comparison with existing theories. He found that his experimental points clustered rather close to Redfearn's predicted values, and by fitting a line through the points plotted against the so-called Fresnel number, Maekawa offered a general design curve for calculating the attenuation expected from a half-plane barrier. Maekawa went on to propose a simple scheme based on his empirical curve to account for the effects of (rigid) ground reflections on the receiver side of the barrier (he assumed the source was still directly on the ground). Rathe (1969) re-phrased Maekawa's results into a form that easily yields engineering predictions. Kurze and Anderson (1971) showed that the prediction schemes of Maekawa and Rathe also remain valid for oblique incidence and additionally proposed an equation that closely describes the empirical curve.

The first theoretical studies that addressed the problem of a finite-impedance ground plane and that took into account ground reflections from the source side of the barrier in addition to those from the receiver side were done by Lindblad (1970) and Jonasson (1972). Lindblad set up a numerical integration of elementary sources (Helmholtz-Huygens integral approach⁶) over the infinite plane above the barrier. The major assumptions in his approach are that all ground reflections behave in accordance with plane wave theory, and that the fields above the barrier are precisely what they would be in

⁶ For example, see Skudrzyk (1971, chap. 23).

the absence of the diffracting barrier (the so-called "Kirchoff assumption"). Jonasson assumed that the ground was locally-reacting and that the barrier was totally absorptive. The latter condition enabled him to ignore the second term in the MacDonald solution, which Jonasson employed to describe the diffraction effects. The problem was treated as a simple superposition of four separate half-plane diffraction problems (see Figure 1.4), where the "strengths" of the ground-reflected rays were derived from spherical-wave propagation theory (Ingard, 1951).

Thomasson (1978) correctly pointed out that neither Lindblad's nor Jonasson's solution is valid for small barrier heights. In the former, the plane-wave reflection theory fails for the near-grazing rays required to construct the fields above the barrier. In the latter, the inherent assumption that each ray "sees" a semi-infinite barrier becomes unsound. Thomasson offered an integral solution that is more accurate for short (and also, for the first time, finite-length) barriers. It involves the application of his own spherical wave solution (Thomasson, 1976) to the ground reflections and an integration of the total field over the face of the barrier itself⁷ the ground reflections. However, in order to obtain a solution, Thomasson was forced to invoke the so-called "Rayleigh" or "physical optics" assumptions, which differ only slightly from the Kirchoff assumptions.

⁷ A form of Babinet's Principle is needed for this; see Bouwkamp (1954, pp. 51-52).

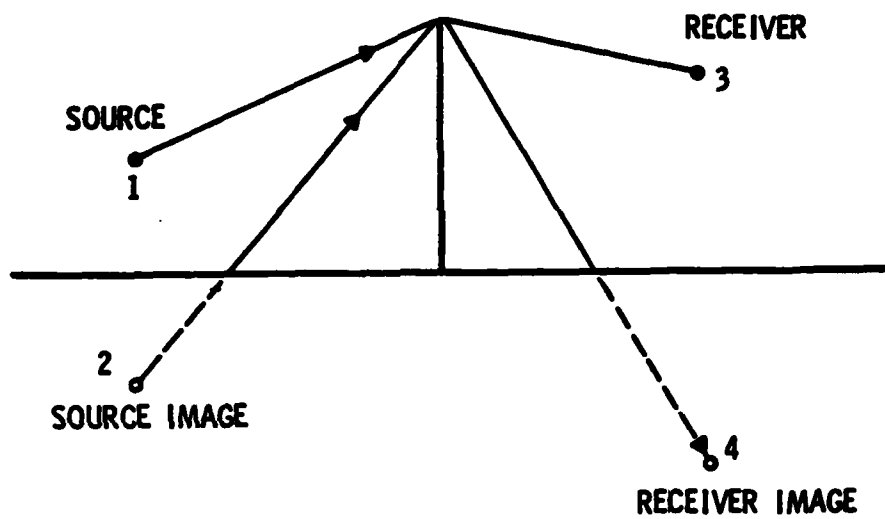


Figure 1.4 Representation of the Overall Problem as a Superposition of Four Diffraction Paths Using Source and Receiver Images.

A recent contribution by Isei (1980; see also Isei, Embleton, & Piercy, 1980) is very similar to Jonasson's treatment except that it allows for an impedance coating on the faces of the barrier.⁸ However, the impedance condition is handled heuristically by applying a plane-wave reflection coefficient to the second term in the MacDonald diffraction solution (the term ignored by Jonasson). Hayek, et al. (1978), on the other hand, used Kendig's exact diffraction solution for the impedance-covered half plane, merged this with Keller's GTD, but applied simple plane-wave theory to the ground reflections. The present study has extended the work of Hayek, et al. by incorporating into their model an original solution to the ground propagation problem.

1.3 Scope and Importance of Study

This presentation will begin with a theoretical treatment of the propagation problem--that is, a description of the field at a point (receiver) in the half space above an infinite, locally-reacting impedance plane due to a point source of energy located arbitrarily in that half space. The method of analysis is original, although an important step early in the derivation is similar to, and was inspired by, a step initially used by Van der Pol (1935) in his electromagnetic work and later adapted by Lawhead and Rudnick (1951b) to the acoustical case. This step, which involves the replacement of an

⁸ Isei apparently forgot to account for one image term in his solution, and this has been pointed out by Fujiwara (1980).

integrand pole by an equivalent integral, leads to a further integral which is intractable. Lawhead and Rudnick, following the approach of Norton (1936, 1937), made a major approximation so that the integral could be solved. The approach used in the present study avoids such an approximation. The procedure, which will be described in detail in chapter II, can be broadly outlined as follows.

First, since the major obstacle with the integral is its complicated exponential, a transformation of variables is made which changes the exponential into a more useful form. The denominator of the transformed integrand is then expanded in a Taylor series about the origin so that a term-by-term integration can be performed. Each integral in the resulting series is then solved in terms of parabolic cylinder functions, which are further expressed in terms of the complementary error function. The final formal result is thus an asymptotic series (since the assumption of "large kR "⁹ was necessary for the term-by-term integration) containing the error function plus various constants. The series is given in a general form, including recursion relations for calculating the coefficients. Thus, all of the higher-order terms in the asymptotic series can be written out explicitly and their values can be calculated readily.

The next phase in the study couples the new propagation solution with existing half-plane diffraction theory to devise a practical model for handling the combined barrier-ground plane problem. The

⁹ Here, k is the familiar propagation constant and R is the distance from the source image to the receiver.

development of this model is presented in Chapter III.

Numerical data for the ground propagation problem are generated and plotted in Chapter IV, Section 4.1. Here, the sensitivity of the results to parameters such as "kR," ground impedance, and angle of incidence is explored. For the combined barrier-ground plane problem, numerical results are presented in Section 4.2, where, in addition to the above parameters, the dependence on barrier height and diffraction angle is investigated.

Although the major scientific contribution of this research effort is the asymptotic series solution for the ground propagation problem, the model proposed in Chapter III for the combined problem is felt to be an important engineering contribution; it is more accurate than either Jonasson's or Isei's models because a more exact ground propagation theory is merged with a more exact diffraction theory. While it is true that the applicability of the proposed model to short barriers is questionable (as noted by Thomasson in regard to Jonasson's model), a numerical integration approach such as Thomasson's (1978)--which indeed might be more accurate for small barrier heights--is much more time consuming computationally, and becomes impractical when many source-receiver points must be analyzed.¹⁰

¹⁰ Most highway noise computer prediction schemes--a common application of such barrier-ground plane models--treat the flow of vehicles as a line of many incoherent point sources. As several receivers are likely to be included in any one scenario, efficient computations are essential.

CHAPTER II

MATHEMATICAL FORMULATION AND SOLUTION
TO THE PROBLEM OF
POINT SOURCE PROPAGATION OVER AN IMPEDANCE PLANE

2.1 Overview

The exact solution to the problem of plane wave reflection by an impedance plane is rudimentary and well-known.¹¹ Until recently, however, it was customary to simply take the results of the plane wave derivation and apply them to the point source (spherical wave) problem. Despite the lack of rigor, the solution so obtained was consistently confirmed by experiment, except when the sound source was very close to the reflecting plane. The heuristic derivation of this "plane-wave solution" to the point source problem can be outlined as follows.

It is well-known that when a plane wave strikes a flat, perfectly rigid surface at an angle of inclination ψ , as shown in Figure 2.1 (a), the resulting field¹² at a point (x,y) can be written as

$$\Phi(x,y) = e^{i[kx\cos\psi - ky\sin\psi]} + e^{i[kx\cos\psi + ky\sin\psi]} \quad (2.1)$$

¹¹ See, for example, Morse and Ingard ('68, p. 259).

¹² The term "field" formally refers to "velocity potential," but since harmonic waves are most likely to be considered here, it can be taken to mean "pressure" as well.

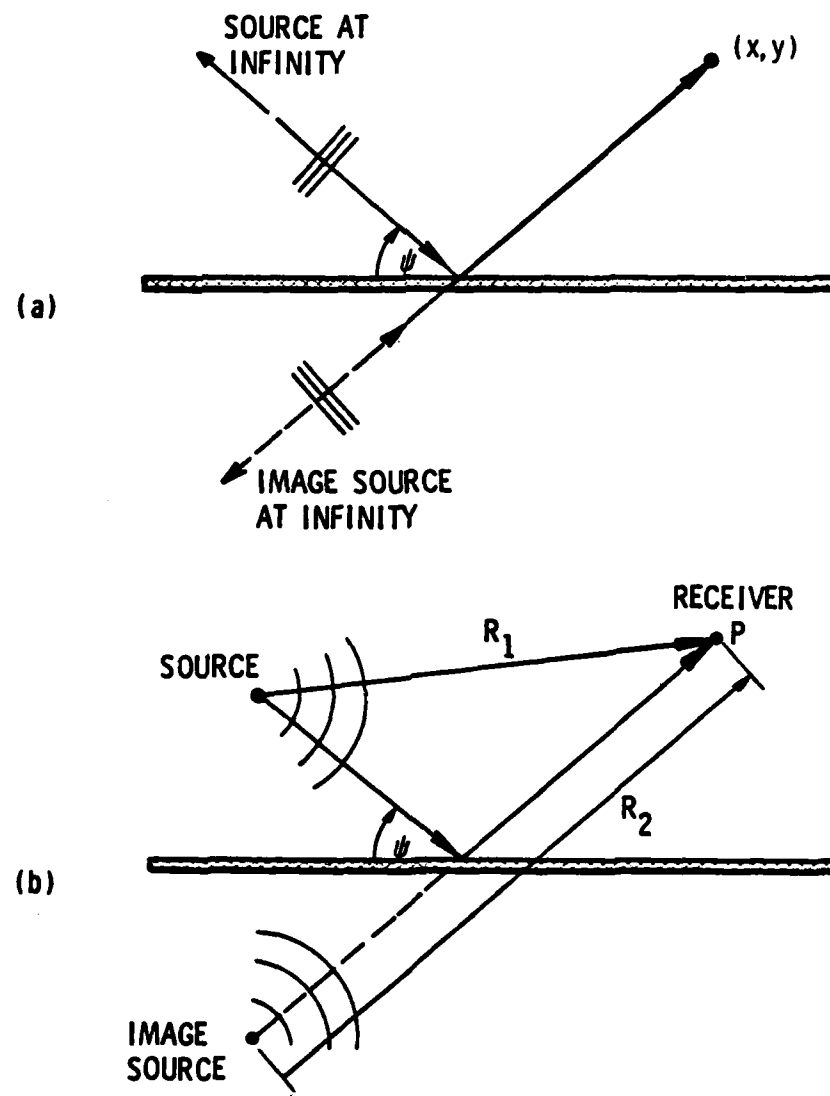


Figure 2.1 Simple Reflection Problem with Images.
(a) Plane Wave. (b) Spherical Wave

Here k is the wave number, or propagation constant, and $k = 2\pi f/c$, where f is the frequency and c is the speed of sound in the medium. A common factor $e^{-i\omega t}$, where $\omega=2\pi f$ and t is time, has been omitted from this and the following equations. The first term in Equation (2.1) is the direct contribution to the field from the source acting alone, and the second term represents the enhancement of the field due to the reflecting plane. The total field at the point (x,y) would be identically expressed if the plane were simply replaced by an "image" source, as indicated in the figure.

It is also well-known that when sound energy emanating from an ideal point source S strikes a rigid plane at an angle ψ , as shown in Figure 2.1 (b), the resulting field at the point P is given by

$$\Phi(P) = \frac{e^{ikR_1}}{R_1} + \frac{e^{ikR_2}}{R_2} , \quad (2.2)$$

where, again, the first term is the direct field from the source and the second term can be thought of as the field from an image source.

Now, if the reflecting plane were not rigid but characterized by a complex acoustic impedance Z , the plane wave solution becomes

$$\Phi(x,y) = e^{i[kx\cos\psi - kys\sin\psi]} + R_p e^{i[kx\cos\psi + kys\sin\psi]} . \quad (2.3)$$

Here R_p is the "plane wave reflection coefficient" given by

$$R_p = \frac{\sin\psi - \beta}{\sin\psi + \beta} \quad (2.4)$$

in which $\beta = \rho c/Z$ is the normalized acoustic admittance of the surface.¹³ This equation is exact for plane waves; it results from solving the full boundary value problem. The solution still retains the form of a direct term plus an image term, but now the "strength" of the image is no longer unity but R_p .

Since Equation (2.1) transforms into Equation (2.3), then Equation (2.2) should become

$$\Phi(P) = \frac{e^{ikR_1}}{R_1} + R_p \frac{e^{ikR_2}}{R_2} \quad (2.5)$$

for the spherical wave case when the rigid plane is replaced by an impedance plane. This reasoning has been employed by several researchers to support the use of Equation (2.5) to solve practical problems involving point sources. There is little mathematical basis for this equation, and it is not surprising, therefore, that when acoustic energy from a real source ceases to resemble "plane" waves--at grazing incidence, for example--the solution fails.

What is needed is a "spherical wave reflection coefficient" for the point source problem. That is, the solution should take the form

$$\Phi(P) = \frac{e^{ikR_1}}{R_1} + Q \frac{e^{ikR_2}}{R_2}, \quad (2.6)$$

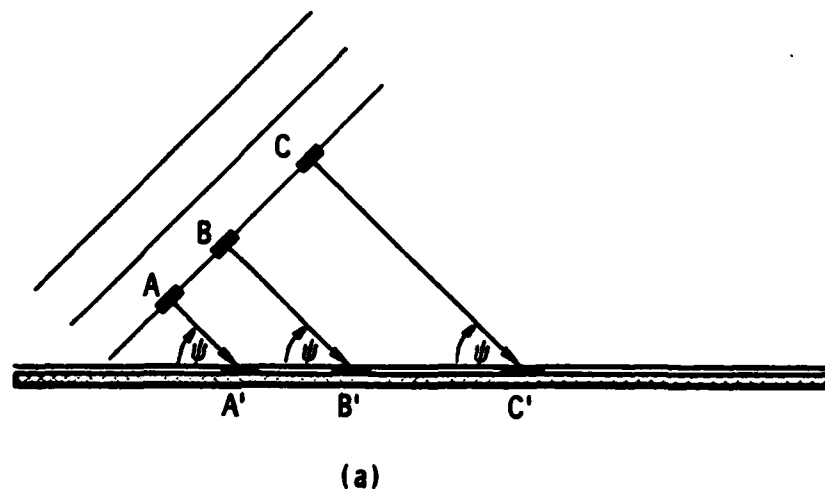
¹³ The normalization is by the characteristic impedance ρc of the medium, where ρ is the density. The normalized acoustic impedance, sometimes called the "specific acoustic impedance," is $Z_N = Z/\rho c$ and hence $\beta = 1/Z_N$.

where Q is derived analytically from the formal boundary value problem. Alternatively, a solution may be sought in the form

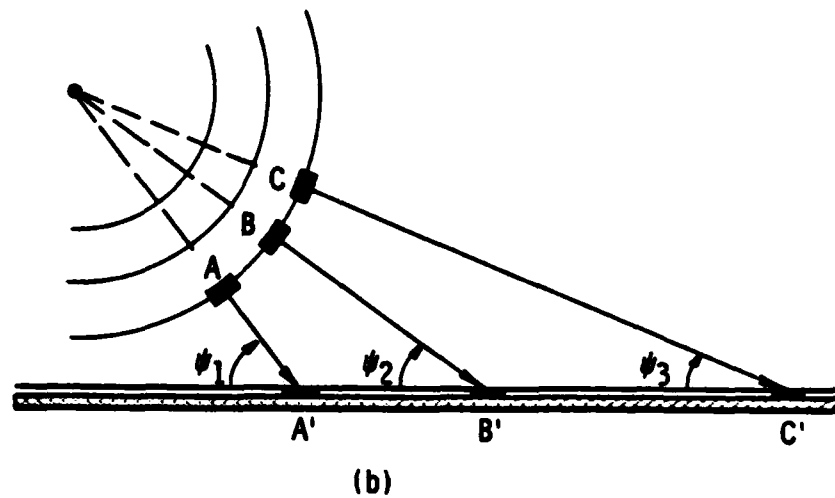
$$\Phi(P) = \frac{e^{ikR_1}}{R_1} + R_p \frac{e^{ikR_2}}{R_2} + \text{Correction term}, \quad (2.7)$$

where the correction term approaches zero in the limit when the source is very far from the boundary but becomes significant when the source is close to the impedance plane. Both of the above forms of solution will be derived in this study, but the practical selection of one form over the other will depend on the intended application.

Perhaps some physical insight about the problem can be gained before the theoretical treatment begins. Figure 2.2 (a) and (b) depicts three elemental segments along a single wavefront of either a plane wave or a spherical wave, respectively. The rays perpendicular to the two wavefronts follow the progression of the segments A, B, and C to their "striking points" along the boundary, A', B', and C'. Of course, each segment on the wavefront strikes the boundary at different times, but this is not important here. Rather, the angle of incidence with which they strike the boundary is the important factor. For the plane wave, each elemental portion of the wavefront hits the boundary at the same angle, but for the spherical wave, this is clearly not the case. With the assumption of local reactance, each ray "sees" a surface impedance proportional to its normal component of particle velocity only. This component, therefore, has the same value for each ray in Figure 2.2 (a) but different values for each ray in



(a)



(b)

Figure 2.2 Reflection of Elemental Segments of a Wavefront.
(a) Plane Wave. (b) Spherical Wave.

Figure 2.2 (b). Consequently, the phase change upon reflection is the same at the points A', B', and C' for the plane wave but varies from A' to B' to C' for the spherical wave. The plane wave is reflected as a plane wave, but the spherical wave loses its symmetry. When the ground plane is perfectly rigid (or pressure release), the angle of incidence is immaterial since the phase change is always 180 degrees. Hence, for a rigid plane (or pressure release plane) only, the spherical symmetry is preserved, and the image method is exact.

2.2 Formulation of the Problem

An idealized point source is located at a fixed but arbitrary position in the half space above a perfectly flat ground plane that extends to infinity in its two dimensions. The source radiates acoustic energy into the uniform, quiescent medium that fills the space above the plane. The resulting field at a point receiver, also located at an arbitrary position above the plane, is desired. By definition, the ground plane is "locally reacting;" that is, the value of the acoustic impedance of the surface facing the source is independent of the angle of incident energy upon the plane, and it may, therefore, be fully characterized by its value at normal incidence. Also, in this ideal case, the proximity of the ground has no effect on the radiation or "strength" of the source.

Mathematically, the problem stated above can be described by an inhomogeneous partial differential ("wave") equation subject to homogeneous, mixed boundary conditions. Allowing only single

frequency, steady-state excitations will reduce the governing differential equation to the Helmholtz equation. The general solution to such a boundary value problem comprises a particular solution to the inhomogeneous differential equation plus a separate solution, containing unknown coefficients, to the homogeneous differential equation. The total solution must satisfy the boundary conditions. For this reason, it is advantageous to express the particular and homogeneous parts of the solution in coordinates that are easily matched to the geometry of the bounding surface itself.

2.2.1 The Particular Solution: A Point Source in a Free Field

In the absence of the bounding impedance plane, the problem reduces to a point source of sound radiating into an unbounded medium. This problem is most easily described in terms of spherical coordinates, and the solution is derived in many standard textbooks. It is simply:

$$\Phi(P) = \frac{e^{ikR}}{R} , \quad (2.8)$$

where R is the distance between the point source and an arbitrary field point P. Although this uncomplicated form of solution is appealing, it can not be matched to the planar boundary conditions.

2.2.1.1 The Field from a Point Source in Cartesian Coordinates.

The boundary plane can be specified in Cartesian (x,y,z) coordinates

(for example, $z=0$), and therefore a solution to the Helmholtz equation in this system would be more useful. The inhomogeneous equation is

$$\nabla^2 \Phi(x, y, z) + k^2 \Phi(x, y, z) = -4\pi \delta(x)\delta(y)\delta(z-z_0) , \quad (2.9)$$

where the symbol ∇^2 is the Laplacian operator in rectangular coordinates,

$$\nabla^2 = \frac{\partial^2}{\partial x^2} + \frac{\partial^2}{\partial y^2} + \frac{\partial^2}{\partial z^2} \quad (2.10)$$

and the symbol δ is the Dirac delta function. The source has been arbitrarily fixed at the point $(0, 0, z_0)$ and the overall geometry is shown in Figure 2.3 (a). The solution to Equation (2.9) can most readily be obtained using Fourier transform methods, where

$$\Phi(\xi, \eta, \zeta) = \iiint_{-\infty}^{\infty} \Phi(x, y, z) e^{-i(\xi x + \eta y + \zeta z)} dx dy dz \quad (2.11)$$

is defined as the Fourier transform of $\Phi(x, y, z)$, and

$$\Phi(x, y, z) = \frac{1}{(2\pi)^3} \iiint_{-\infty}^{\infty} \Phi(\xi, \eta, \zeta) e^{i(\xi x + \eta y + \zeta z)} d\xi d\eta d\zeta \quad (2.12)$$

is then defined as the inverse Fourier transform.

Now, applying the transform to Equation (2.9) and employing the following properties of the Fourier integral and the delta function, respectively:

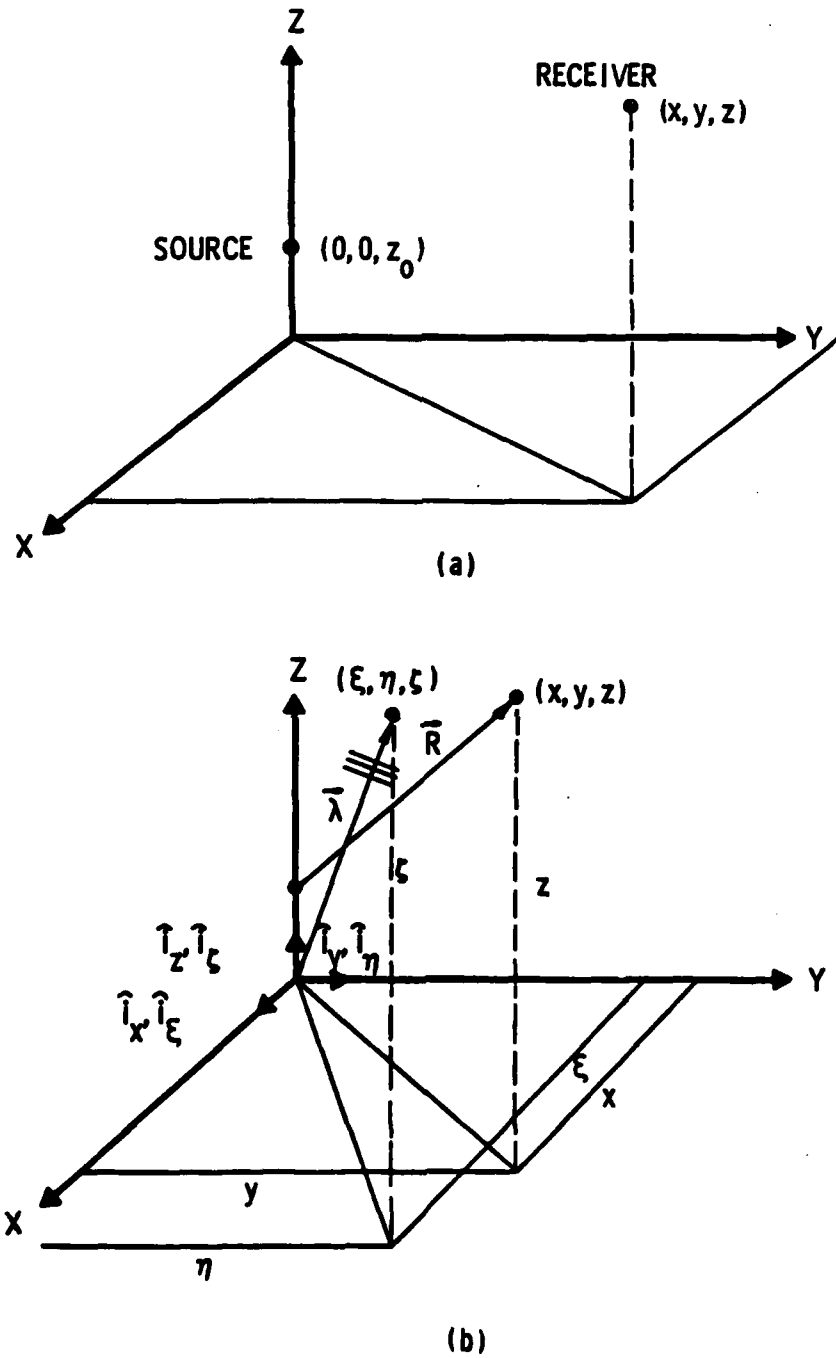


Figure 2.3 The Cartesian Space Geometry. (a) Source and Receiver Coordinates. (b) Propagation Vector for a Single Elemental Plane Wave with Arbitrary Direction in the Space.

$$\int_{-\infty}^{\infty} \left[\frac{\partial}{\partial t} f(t) \right] e^{-i\gamma t} dt = -i\gamma \bar{f}(\gamma) , \quad (2.13)$$

$$\int_{-\infty}^{\infty} \delta(t-t_0) f(t) dt = f(t_0) , \quad (2.14)$$

the field in transform space becomes

$$\Phi(\xi, \eta, \zeta) = \frac{-i\zeta z_0}{4\pi e} \frac{1}{(\xi^2 + \eta^2 + \zeta^2 - k^2)} \quad (2.15)$$

Applying the inverse transformation, Equation (2.12), to this will yield the acoustic field in the original coordinate system due to the point source at $(0,0,z_0)$. Thus,

$$\Phi(x, y, z) = \frac{1}{(2\pi)^2} \iiint_{-\infty}^{\infty} \frac{e^{i[\xi x + \eta y + \zeta(z-z_0)]}}{(\xi^2 + \eta^2 + \zeta^2 - k^2)} d\xi d\eta d\zeta . \quad (2.16)$$

The parameters ξ , η , and ζ may be thought of as components of a propagation vector, in which case the integrand in Equation (2.16) takes on the form of a plane wave. More precisely, since ξ , η , and ζ may have arbitrary and independent values, the integral describes a superposition of an infinite number of plane waves of different amplitudes propagating in different directions. Equation (2.16) can be written in a form that portrays these ideas more clearly:

$$\Phi(R) = \Phi(x, y, z) = \frac{1}{(2\pi)^2} \iiint_{-\infty}^{\infty} \frac{e^{i(\vec{\lambda} \cdot \vec{R})}}{\lambda^2 - k^2} d\xi d\eta d\zeta \quad (2.17)$$

where the propagation vector $\vec{\lambda} = \hat{\xi}\vec{i}_\xi + \hat{\eta}\vec{i}_\eta + \hat{\zeta}\vec{i}_\zeta$ has a magnitude $\lambda^2 = \xi^2 + \eta^2 + \zeta^2$, and the radius vector $\vec{R} = \hat{x}\vec{i}_x + \hat{y}\vec{i}_y + (z-z_0)\hat{z}\vec{i}_z$ has a magnitude $R^2 = x^2 + y^2 + (z-z_0)^2$. A single component plane wave with propagation vector $\vec{\lambda}$ is shown in Figure 2.3 (b) to illustrate these concepts geometrically. Finally, it should be noted that, with a few simple transformations, Equation (2.16) can be integrated (for one treatment, see Stratton, 1951, pp. 577-582) to generate the familiar point source representation of Equation (2.8).

2.2.1.2 The Field from a Point Source in Cylindrical

Coordinates. The boundary plane could be specified by a single coordinate surface in cylindrical (r, θ, z) as well as Cartesian coordinates (for example, $z=0$), and therefore a solution to the Helmholtz equation in cylindrical coordinates could be conveniently applied to the boundary conditions. The Helmholtz equation for a source located at a point $z=z_0$ along the cylindrical axis takes the form

$$\nabla^2 \Phi(r, z) + k^2 \Phi(r, z) = \frac{-2 \delta(r) \delta(z-z_0)}{r}, \quad (2.18)$$

where the Laplacian operator in cylindrical coordinates is

$$\begin{aligned} \nabla^2 &= \frac{1}{r} \frac{\partial}{\partial r} \left(r \frac{\partial}{\partial r} \right) + \frac{\partial^2}{\partial z^2} \\ &= \frac{\partial^2}{\partial r^2} + \frac{1}{r} \frac{\partial}{\partial r} + \frac{\partial^2}{\partial z^2} \end{aligned} \quad (2.19)$$

Because the source has been located directly on the z -axis of the coordinate system, there is no azimuthal angle dependence in either of the preceding equations.

The cylindrical symmetry of the problem suggests the use of Hankel transforms as a method of solution. The Hankel transform and the inverse Hankel transform are defined, respectively, as

$$\Phi^*(\lambda, z) = \int_0^\infty \Phi(r, z) r J_0(\lambda r) dr \quad (2.20)$$

and

$$\Phi(r, z) = \int_0^\infty \Phi^*(\lambda, z) \lambda J_0(\lambda r) d\lambda , \quad (2.21)$$

where J_0 is the Bessel function of order zero. Hankel transforms are discussed in detail in many texts and one important property they exhibit is

$$\int_0^\infty \left[\left(\frac{\partial^2}{\partial r^2} + \frac{1}{r} \frac{\partial}{\partial r} \right) \Phi(r, z) \right] r J_0(\lambda r) dr = -\lambda^2 \Phi^*(\lambda, z) . \quad (2.22)$$

Hence, taking the Hankel transform of Equation (2.18) results in the ordinary differential equation

$$-\lambda^2 \Phi^*(\lambda, z) + k^2 \Phi^*(\lambda, z) + \frac{d^2}{dz^2} \Phi^*(\lambda, z) = -2 \delta(z-z_0) \quad (2.23)$$

or, defining $v^2 = \lambda^2 - k^2$,

$$\frac{d^2}{dz^2} \Phi^*(\lambda, z) - v^2 \Phi^*(\lambda, z) = -2 \delta(z-z_0) . \quad (2.24)$$

Now, applying the one-dimensional Fourier transform to the axial distance z , where

$$\bar{\Phi}(\lambda, \xi) = \int_{-\infty}^{\infty} \Phi(\lambda, z) e^{-iz\xi} dz \quad (2.25)$$

and

$$\Phi(\lambda, z) = \frac{1}{2\pi} \int_{-\infty}^{\infty} \bar{\Phi}(\lambda, \xi) e^{iz\xi} d\xi \quad (2.26)$$

are defined as the Fourier transform and the inverse Fourier transform, respectively, Equation (2.24) becomes

$$-\xi^2 \bar{\Phi}^*(\lambda, \xi) - v^2 \bar{\Phi}^*(\lambda, \xi) = -2e^{-iz_0} , \quad (2.27)$$

so that the field in (Hankel- and Fourier-) transformed space becomes

$$\bar{\Phi}^*(\lambda, \xi) = \frac{2e^{-iz_0}}{(\xi^2 + v^2)} . \quad (2.28)$$

Applying the inverse Fourier transform, Equation (2.26), to this yields

$$\Phi^*(\lambda, z) = \frac{1}{\pi} \int_{-\infty}^{\infty} \frac{e^{iz\xi(z-z_0)}}{(\xi^2 + v^2)} d\xi , \quad (2.29)$$

a real integral that can be solved readily using contour integration and residue techniques. Thus,

$$\phi^*(\lambda, z) = \begin{cases} -v(z-z_0) & ; (z-z_0) > 0 \\ \frac{e}{v} & \\ +v(z-z_0) & ; (z-z_0) < 0 \\ \frac{e}{v} & \end{cases} \quad (2.30)$$

which, under the constraint $\text{Re}(v) = \text{Re}[(\lambda^2 - k^2)^{\frac{1}{2}}] > 0$, can be written¹⁴

$$\phi^*(\lambda, z) = \frac{-v|z-z_0|}{v} . \quad (2.31)$$

Finally, the inverse Hankel transform, Equation (2.21), is applied to Equation (2.31) to obtain the desired field at the point (r, z) in cylindrical coordinate space:

$$\Phi(r, z) = \frac{e^{ikR}}{R} = \int_0^\infty \frac{-v|z-z_0|}{v} \lambda J_0(\lambda r) d\lambda , \quad (2.32)$$

$$\text{where } R = \sqrt{r^2 + (z-z_0)^2} .$$

This result is the particular solution to the inhomogeneous Helmholtz equation. In other words, Equation (2.32) represents a point source radiating into a free field. From fundamental principles, it is known that functions of the form $e^{in\theta} J_n[(k^2 - h^2)^{\frac{1}{2}} r] e^{ihz}$, where h and k are propagation constants and θ is the azimuthal angle, represent elementary cylindrical waves, which are solutions to the homogeneous Helmholtz equation. The point source

¹⁴ The wavenumber k is assumed to be complex in general; that is, the medium is assumed to possess a small, but finite, amount of dissipation.

in Equation (2.32) thus represents an infinite, weighted sum of these elementary cylindrical waves propagating symmetrically about the z-axis ($n=0$). Sommerfeld (1909) was the first to derive this result, and the representation of Equation (2.32) is sometimes called the "Sommerfeld point source."

2.2.2 Total Solution: Effects of the Boundary

Each of the representations of a point source in free space—equation (2.16) in terms of plane waves and Equation (2.32) in terms of cylindrical waves—is a solution to the non-homogeneous Helmholtz equation. When a boundary such as the impedance ground plane is present, a second term must be added to the free-space solution to account for reflections. The total field can be written as $\Phi_{\text{tot}} = \Phi_i + \Phi_r$, where the components may be termed the "incident field" and the "reflected field," respectively. Because the particular solution— $\Phi_i = e^{ikR}/R$, or either of its elementary wave expansions—is unique, the reflected term Φ_r can not also be a solution to the non-homogeneous equation, but instead satisfies the homogeneous Helmholtz equation

$$\nabla^2 \Phi(r, z) + k^2 \Phi_r(r, z) = 0 . \quad (2.33)$$

As such, the solution for the reflected field Φ_r will contain arbitrary constants which can be determined by applying the boundary conditions.

2.2.2.1 Total Integral Solution via Elementary Wave Functions.

The free-space solutions developed in the previous sections also satisfy the the homogeneous Equation (2.33) at all points except at the source itself ($R=0$). The elementary plane and cylindrical waves are therefore eigenfunctions of the problem, and the reflected field can be constructed from an infinite summation (integral) of these eigenfunctions, with arbitrary weighting functions to be determined from the boundary conditions.

The expansion of the reflected field in terms of elementary plane waves was the approach used by Weyl (1919) for the electromagnetic problem and later adopted by Ingard (1951) for the acoustic case. By defining $\gamma = [\xi^2 + \eta^2 - k^2]^{1/2}$ with $\text{Re } \gamma > 0$, Equation (2.16) can be transformed into

$$\Phi(x, y, z) = \frac{1}{2\pi^2} \iint_{-\infty}^{\infty} e^{i(\xi x + \eta y)} d\xi d\eta \int_{-\infty}^{\infty} \frac{i\xi(z-z_0)}{(\xi + i\gamma)(\xi - i\gamma)} d\xi . \quad (2.34)$$

Using residue methods for the ζ -integration, this can be reduced to

$$\Phi(x, y, z) = \frac{1}{2\pi} \iint_{-\infty}^{\infty} \frac{e^{-\gamma|z-z_0|}}{\gamma} e^{i(\xi x + \eta y)} d\xi d\eta . \quad (2.35)$$

In this form, the elementary plane waves are decaying exponentially with z , and Weyl termed these "inhomogeneous" plane waves. Noting

that $\xi^2 + \eta^2 + (i\gamma)^2 = k^2$, the propagation constant k can be written as a vector with components $\vec{k} = \xi \hat{i}_x + \eta \hat{i}_y + (i\gamma) \hat{i}_z$. This suggests the transformations $i\gamma = k \cos\alpha$, $\xi = (k \sin\alpha) \cos\beta$, and $\eta = (k \sin\alpha) \sin\beta$. The resulting field at the point (x, y, z) , then, from the point source located at $z=z_0$ can be written as

$$\Phi(x, y, z) =$$

$$\frac{ik}{2\pi} \int_{\pi}^{\pi/2-i\infty} \int_0^{2\pi} e^{ik[x \sin\alpha \cos\beta + y \sin\alpha \sin\beta + |z-z_0| \cos\alpha]} \cdot \sin\alpha d\alpha d\beta . \quad (2.36)$$

The final step is to assume that the reflected field "originates" from the image point at $z = -z_0$ and thus

$$\Phi_r(x, y, z) =$$

$$\frac{ik}{2\pi} \int_{\pi}^{\pi/2-i\infty} \int_0^{2\pi} f_r(\alpha) e^{ik[x \sin\alpha \cos\beta + y \sin\alpha \sin\beta + |z+z_0| \cos\alpha]} \cdot \sin\alpha d\alpha d\beta . \quad (2.37)$$

where the unknown function $f_r(\alpha)$ must be determined from the boundary conditions. For the present case of an impedance boundary, $f_r(\alpha)$ is simply the plane wave reflection coefficient given by Equation (2.4).

The expansion of the reflected field in terms of elementary cylindrical waves was the approach used by Sommerfeld (1909) and Van der Pol (1935) for the electromagnetic problem, and later adapted by Rudnick (1947) to the acoustical case. To express the reflected field in integral form, the results of Section 2.2.1.2 are used, specifically Equation (2.32). Assuming the reflected field originates from an image point source at $z=-z_0$, the field can thus be written as

$$\Phi(r, z) = \int_0^\infty g_r(\lambda) \frac{e^{-\nu(z-z_0)}}{\nu} \lambda J_0(\lambda r) d\lambda. \quad (2.38)$$

where the unknown function $g_r(\nu)$ must be determined from the boundary conditions.

The boundary conditions for a locally reacting surface is that the ratio of the pressure p to the normal component of the velocity v_n equals the acoustic impedance of the surface. That is,

$$\left. \frac{p(r, z)}{v_n(r, z)} \right|_{z=0} = \frac{p(r, 0)}{v_n(r, 0)} \quad . \quad (2.39)$$

Since the pressure is related to the velocity potential by the fundamental equation $p = \rho \partial \Phi / \partial t$, or $p = -i\omega \rho \Phi$ for harmonic waves, and since $v_n = -\partial \Phi / \partial z$, the boundary condition can be expressed in the form

$$\frac{\partial \Phi(r, 0)}{\partial z} + ik\beta \Phi(r, 0) = 0 \quad . \quad (2.40)$$

Here $\beta = \rho c / Z$ is the normalized acoustic admittance of the surface.

When the total solution $\Phi_{tot} = \Phi_i + \Phi_r$ is substituted into Equation (2.40), the unknown function $g_r(\lambda)$ can be determined to be

$$g_r(\lambda) = \frac{\nu + ik\beta}{\nu - ik\beta} \quad . \quad (2.41)$$

Therefore, the integral form of the total solution is

$$\Phi(r, z) = \frac{e^{ikR}}{R} + \int_0^\infty \left[\frac{v + ik\beta}{v - ik\beta} \right] \frac{e^{-v(z+z_0)}}{v} \lambda J_0(\lambda r) d\lambda . \quad (2.42)$$

2.2.2.2 Total Integral Solution via Hankel Transforms. The result just obtained can be derived in a more straightforward manner using Hankel transforms. The total solution to the transformed Helmholtz equation (2.24) comprises the particular solution, Equation (2.30), plus a homogeneous solution containing two arbitrary constants to be determined from two boundary conditions. Thus, the field in transform space takes the form

$$\Phi^*(\lambda, z) = A(\lambda) e^{-vz} + B(\lambda) e^{vz} + \frac{e^{-v|z-z_0|}}{v} . \quad (2.43)$$

The first boundary condition that must be met is the Sommerfeld radiation condition specifying that the field must vanish as $z \rightarrow \infty$. Because the constraint $\text{Re}(v) > 0$ has already been imposed, the constant B must be set equal to zero. The second boundary condition is that dictated by the local reaction assumption, namely, Equation (2.40). Applying the Hankel transform, Equation (2.20) to the boundary condition yields

$$\frac{\partial \Phi^*(\lambda, 0)}{\partial z} + ik\beta \Phi^*(\lambda, 0) = 0 . \quad (2.44)$$

Substituting $\Phi^*(\lambda, z)$ from Equation (2.43) into Equation (2.44) and writing the absolute value quantity as $|z-z_0| = (z_0-z)$ for $z \rightarrow 0$ yields the desired value of the constant:

$$A(\lambda) = \left[\frac{v + ik\beta}{v - ik\beta} \right] \frac{e^{-vz_0}}{v} . \quad (2.45)$$

The solution for the field in transform space, then, becomes

$$\Phi^*(\lambda, z) = \left[\frac{v + ik\beta}{v - ik\beta} \right] \frac{e^{-v(z+z_0)}}{v} + \frac{e^{-v|z-z_0|}}{v} . \quad (2.46)$$

Finally, taking the inverse Hankel transform, Equation (2.21), of this expression, yields the integral form of the total solution. Hence,

$$\begin{aligned} \Phi(r, z) &= \int_0^\infty \frac{e^{-v|z-z_0|}}{v} \lambda J_0(\lambda r) d\lambda + \int_0^\infty \left[\frac{v + ik\beta}{v - ik\beta} \right] \frac{e^{-v(z+z_0)}}{v} \lambda J_0(\lambda r) d\lambda \\ &= \frac{e^{ikR}}{R} + \int_0^\infty \left[\frac{v + ik\beta}{v - ik\beta} \right] \frac{e^{-v(z+z_0)}}{v} \lambda J_0(\lambda r) d\lambda \end{aligned} \quad (2.47)$$

which is identical to the previous results of Equation (2.42)

2.3 Derivation of the Asymptotic Series Solution

The integral in the exact solution, Equation (2.47), appears to be intractable due to the presence of a simple pole at $v = (\lambda^2 - k^2)^{\frac{1}{2}} = +ik\beta$ and branch points at $\lambda = \pm k$. Virtually all of the researchers who have addressed the spherical wave propagation problem over the past century have been faced with this, or a very similar, integral, and all have necessarily resorted to approximation methods

for its evaluation. Those methods based on an asymptotic approach, in which a critical parameter such as "kR" is assumed to be large, have proven to be the most accurate and to provide the most useful results. In these, the real axis path of integration is continued into a contour in the complex plane that invariably must be deformed around the branch point and branch cut. It is to the resulting branch line integral that the asymptotic technique--usually the "method of steepest descents"--is applied. In addition, proper attention is paid to the simple pole, which may or may not be enclosed by the final contour depending on the specific nature of the problem.

The approach in this study is different. The pole is replaced at the outset by an integral representation, and the branch line integration is avoided through an appropriate transformation of variables. However, the "asymptotic" assumption is still necessary, but it is invoked later in the development when the integral is expanded into a Taylor series. The final form of solution will be an asymptotic series, for which the coefficients may be calculated by recursion formulae.

2.3.1 Replacement of the Pole

By re-writing $(\nu+\gamma)/(\nu-\gamma) = 1 + 2\gamma/(\nu-\gamma)$, the final solution given in Equation (2.47) for the field at the point (r,z) can be expressed as

$$\Phi(r, z) = \frac{e^{ikR_1}}{R_1} + \frac{e^{ikR_2}}{R_2} + 2\gamma \int_0^\infty \frac{e^{-v(z+z_0)}}{(v-\gamma)v} \lambda J_0(\lambda r) d\lambda \quad (2.48)$$

in which $\gamma = ik\beta$, R_1 is the distance from the source at $(0, z_0)$ to the point (r, z) , and R_2 is the distance from the image point at $(0, -z_0)$ to the point (r, z) . The geometry of the problem is illustrated in Figure 2.4.

From the fact that $1/p = \int_0^\infty e^{-pt} dt$ for $\text{Re}(p) > 0$, the pole in the integrand of Equation (2.48) can be transformed as¹⁵

$$\frac{1}{(v - \gamma)} = \int_0^\infty e^{-(v - \gamma)\eta} d\eta ; \text{Re}[v - \gamma] > 0 \quad (2.49)$$

However, it turns out that the constraint $\text{Re}(v - \gamma) > 0$ is not very convenient,¹⁶ and a better transformation would be

$$\frac{1}{i(v - \gamma)} = \int_0^\infty e^{-i(v - \gamma)\eta} d\eta ; \text{Re}[i(v - \gamma)] > 0 \quad (2.50)$$

so that

$$\frac{1}{(v - \gamma)} = i \int_0^\infty e^{-i(v - \gamma)\eta} d\eta ; \text{Re}[i(v - \gamma)] = 0 . \quad (2.51)$$

¹⁵ This step is based on a similar one first used by Van der Pol (1935) and later adopted by Lawhead and Rudnick (1951).

¹⁶ The constraint translates into $\text{Re}(v) + k\text{Im}(\beta) > 0$. Although $\text{Re}(v) > 0$, the imaginary part of β may be positive or negative, and the condition $\text{Re}(v - \gamma) > 0$ can not be guaranteed.

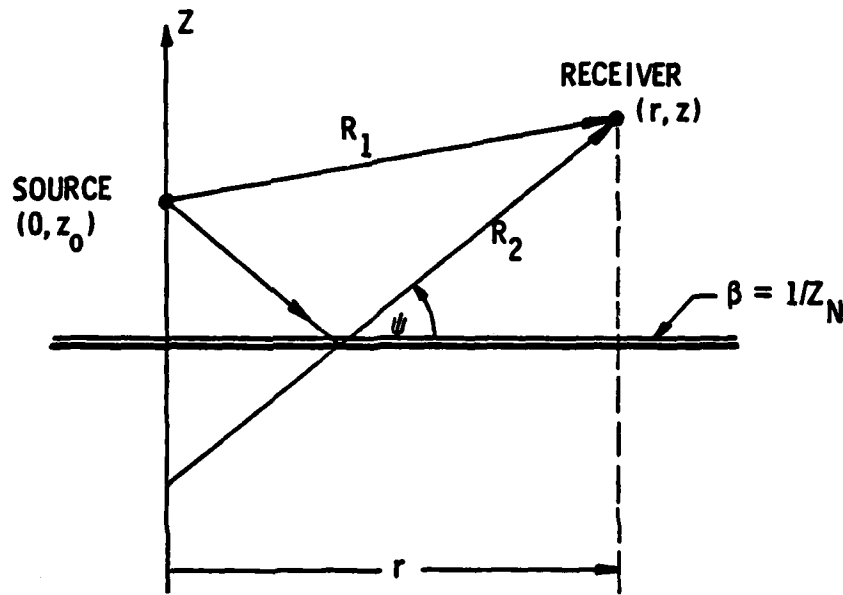


Figure 2.4 Geometry of the Propagation Problem in Cylindrical Coordinates. Source-Receiver Distance R_1 , Image-Receiver Distance R_2 , Reflection angle ψ , and Ground Admittance β .

Writing $v = v_r + iv_i$ and $\gamma = ik(\beta_r + i\beta_i) = -k\beta_i + ik\beta_r$, where the subscripts "r" and "i" indicate "real" or "imaginary" parts, respectively, then the constraint $\text{Re}[i(v-\gamma)] > 0$ translates into $(-v_i + k\beta_r) > 0$. Because the real part of the impedance $Z=R+iX$ for physical materials must be positive, then $\beta_r = R/(R^2+X^2)$ must also be positive. Thus, in order to satisfy the constraint in Equation (2.51), it is sufficient that v_i be negative. That this is indeed the case requires a closer look at the parameter v .

Assuming that the medium is not ideally lossless, the wavenumber k may be written as a complex quantity $k = k_r + ik_i$, and because e^{ikR}/R must decay for large R , the imaginary part k_i must be positive. Furthermore, if the symbol " $\sqrt{\cdot}$ " is adapted here to indicate the positive real square root (often called the "principal root"), then $v = \sqrt{\lambda^2 - k^2} = \sqrt{(\lambda^2 - k_r^2 + k_i^2)} - i(2k_r k_i)$. The real part of the quantity under the radical can be positive or negative, but the imaginary part will always be negative. Hence, the root must lie in the fourth quadrant; that is, $v_i < 0$.¹⁷

The replacement of the pole via Equation (2.51) is thus valid for general impedances (springlike or masslike), and when the result is substituted into Equation (2.48), the integral term becomes

¹⁷ This can also be shown by considering the assumed time dependence. Thus,

$$e^{v|z-z_0|} e^{-i\omega t} = e^{-v_r|z-z_0|} e^{(-v_i|z-z_0|-i\omega t)};$$

therefore, to ensure outward propagation, $v_i < 0$.

$$I_1 = 2i\gamma \int_0^\infty \left[\frac{e^{-v(h+i\eta)}}{v} \lambda J_0(\lambda r) d\lambda \right] e^{i\gamma\eta} d\eta \quad (2.52)$$

where $h=(z+z_0)$. The term in brackets resembles the Sommerfeld representation for a "point source," Equation (2.32), and therefore

$$I_1 = 2i\gamma \int_0^\infty \left[\frac{e^{ikR'}}{R'} \right] e^{i\gamma\eta} d\eta \quad (2.53)$$

where

$$R' = \sqrt{r^2 + (h+i\eta)^2} = \sqrt{r^2 + h^2 + 2ih\eta - \eta^2} \quad (2.54)$$

From Figure 2.4 it can be seen that $h/R_2 = \sin\psi$ and $r^2+h^2=R_2^2$, thus

$$R' = R_2 \left(1 + \frac{2i\eta \sin\psi}{R_2} - \frac{\eta^2}{R_2^2} \right)^{\frac{1}{2}} \quad (2.55)$$

where $\text{Re}(R') > 0$.

The integral in Equation (2.53) now takes the form

$$I_1 = 2i\gamma \int_0^\infty \frac{e^{ikR_2} \left[\left(1 + \frac{2i\eta \sin\psi}{R_2} - \frac{\eta^2}{R_2^2} \right)^{\frac{1}{2}} + i\gamma\eta \right]}{\left(1 + \frac{2i\eta \sin\psi}{R_2} - \frac{\eta^2}{R_2^2} \right)^{\frac{1}{2}}} d\eta \quad (2.56)$$

or

$$I_1 = -2k\beta \int_0^\infty \frac{e^{ikR_2[(1-\xi^2+2i\xi \sin\psi)^{\frac{1}{2}} + i\beta\xi]}}{(1-\xi^2+2i\xi \sin\psi)^{\frac{1}{2}}} d\xi \quad (2.57)$$

where the transformation $\xi=\eta/R_2$ has been applied. Although the pole has been "removed" from I_1 , the integral is still cumbersome, and a transformation of variables will now be made in order to simplify the exponential term.

2.3.2 Variable Transformation

The functional form of a single variable transformation $\xi=\xi(t)$ on a contour integral is

$$\int_{C_\xi} f(\xi) d\xi + \int_{C_t} f[\xi(t)] \frac{d\xi(t)}{dt} dt , \quad (2.58)$$

or, more specific to the case at hand,

$$\int_{C_\xi} e^{af(\xi)} F(\xi) d\xi + \int_{C_t} e^{af[\xi(t)]} F[\xi(t)] \frac{d\xi(t)}{dt} dt . \quad (2.59)$$

where C_ξ and C_t are arbitrary contours in complex ξ -space or complex t -space, respectively.

The exponential in the field solution, Equation (2.57), can be put into a simpler form by the variable transformation

$$\sqrt{1 - \xi^2 + 2i\xi \sin\psi + iB\xi} = -(t^2 + 2Bt + C) . \quad (2.60)$$

With this transformation, the original real axis path $0 \leq \xi \leq \infty$ will in general become a contour in the complex t -plane.

To determine the values of the coefficients B and C , two constraints must be placed on the transformation. The first is that the transformed contour should start at the origin; that is, $t(\xi=0)=0$. This condition immediately fixes the value $C=-1$ (again, the root on the left hand side of Equation [2.60] is taken so that the real part is positive). The second constraint on the transformation is less trivial. Of course, if the transformation were matched at any other point $t(\xi_0)=t_0$, the unknown coefficient B could be determined. However, the most judicious choice for this matching point is the so-called "saddle point" of the original integrand.

2.3.2.1 Matching Transformation at the Saddle Point. The point at which the derivative $f'(\xi)=0$ is called the "saddle point" and is a fundamentally important quantity in the asymptotic technique of "saddle point integration," also called the "method of steepest descent." At the saddle point, the integrand takes its maximum value and falls off rapidly to either side in the directions of "steepest descent." The power of this method lies in the fact that if the integration is performed along the path of steepest descent, most of the contribution to the integral comes from the immediate vicinity of the saddle point.

The saddle point ξ_0 of the integrand in Equation (2.57) satisfies

$$\frac{d}{d\xi} [i(1 - \xi^2 + 2i\xi \sin\psi)^{\frac{1}{2}} + i\beta\xi] = 0 , \quad (2.61)$$

and the saddle point t_0 for Equation (2.57) satisfies

$$\frac{d}{dt} i[-t^2 - 2Bt + 1] = 0 , \quad (2.62)$$

where the parameter a in Equation (2.59) has been set equal to kR_2 .

Therefore, solving the previous two equations, the saddle points are found to be

$$\xi_0 = i \sin\psi + \frac{i\beta \cos\psi}{\sqrt{1 - \beta^2}} \quad (2.63)$$

$$t_0 = -B$$

When these values are substituted back into the transformation, Equation (2.60), the coefficient B can be determined. Thus,

$$B^2 = -1 - \beta \sin\psi + \sqrt{1 - \beta^2} \cos\psi \quad (2.64)$$

or,

$$B = \pm i(1 + \beta \sin\psi - \sqrt{1 - \beta^2} \cos\psi)^{\frac{1}{2}} . \quad (2.65)$$

Note that at this point in the derivation there is nothing to govern the selection of the root in Equation (2.65).

2.3.2.2 The Transformation of the Integral. The transformation of the exponential factor is complete; that is,

$$e^{ikR_2[(1-\xi^2 + 2i\xi \sin\psi)^{\frac{1}{2}} + i\beta\xi]} = e^{-ikR_2[t^2 + 2Bt - 1]} \quad (2.66)$$

With reference to Equation (2.59), the next step in the transformation involves the function $F(\xi)$, which is defined here as

$$F(\xi) = \frac{1}{\sqrt{1 - \xi^2 + 2i\xi \sin\psi}} \quad (2.67)$$

In order to find $F[\xi(t)]$ where

$$F[\xi(t)] = \frac{1}{\sqrt{1 - \xi^2(t) + 2i\xi(t) \sin\psi}} \quad (2.68)$$

the quantity ξ must be expressed as a function of t . In a straightforward manner, Equation (2.60) can be solved for $\xi(t)$ as

$$\xi(t) = \frac{i}{(1 - \beta^2)} \{ \beta(-t^2 - 2Bt + 1) + \sin\psi \} \quad (2.69)$$

$$\pm [(-t^2 - 2Bt + 1 + \sin\psi)^2 - \sqrt{1 - \beta^2} \cos\psi]^{\frac{1}{2}}$$

The quantity in the square bracket can be factored so that

$$\xi(t) = \frac{i}{(1 - \beta^2)} \left\{ \beta(-t^2 + 2Bt + 1) + \sin\psi \right. \quad (2.70)$$

$$\left. - (t + B) \left[\frac{\beta + \sin\psi}{B} \right] \sqrt{1 - \frac{t^2}{H} - \frac{2Bt}{H}} \right\}$$

where

$$H = 1 + \beta \sin\psi + \sqrt{1 - \beta^2} \cos\psi \quad (2.71)$$

and where the sign of the root in Equation (2.69) had been selected to make $\xi(t=0)=0$, as required. As a check on the transformation in Equation (2.70), it is easy to confirm that $\xi(t_0)=\xi_0$. Now when $\xi(t)$ from Equation (2.70) is substituted into Equation (2.68), the integrand function $F[\xi(t)]$ can be determined. Hence,

$$F[\xi(t)] = \frac{(1 - \beta^2)}{[\alpha(t) + \beta \sin\psi] - \beta(t + B) \left[\frac{\beta + \sin\psi}{B} \right] \sqrt{\gamma(t)}} \quad (2.72)$$

in which the following shorthand notations have been introduced:

$$\alpha(t) = -t^2 - 2Bt + 1 \quad (2.73)$$

$$\gamma(t) = -\frac{t^2}{H} - \frac{2Bt}{H} + 1$$

The final step in the transformation of the integral is to derive an expression for $d\xi(t)/dt$. This is effected by differentiating the expression for $\xi(t)$ in Equation (2.70), and therefore

$$\frac{d\xi(t)}{dt} = \frac{i}{(1 - \beta^2)} \left\{ \frac{-\beta(t+B) \left[\frac{\beta + \sin\psi}{B} \right] \sqrt{\gamma(t)} + [\alpha(t) + \beta \sin\psi]}{\left[\frac{\beta + \sin\psi}{B} \right] \sqrt{\gamma(t)}} \right\} \quad (2.74)$$

The product $F[\xi(t)]d\xi(t)/dt$, then, results in the relatively simple expression

$$F[\xi(t)] \frac{d\xi(t)}{dt} = \frac{2iB}{(\beta + \sin\psi) \sqrt{1 - \frac{t^2}{H} - \frac{2Bt}{H}}} . \quad (2.75)$$

With the transformation thus complete, the original integral of Equation (2.57) can be written

$$I_1 \xrightarrow{\xi \rightarrow t} I_2 = \frac{-4ik\beta Be^{ikR_2}}{(\beta + \sin\psi)} \int_{C_t} \frac{e^{-ikR_2[t^2 + 2Bt]}}{\sqrt{1 - \frac{t^2}{H} - \frac{2Bt}{H}}} dt , \quad (2.76)$$

with H defined in Equation (2.71) and B in Equation (2.65). The integral is taken over the path C_t , the transformed contour in the t -plane. The root in the expression for B will be fixed by the choice of this integration path.

2.3.2.3 The Path of Integration in the t -plane. As the value of ξ goes from 0 to $+\infty$ along the real axis, the transformed variable t

will trace out a path in the complex t -plane. The transformation, Equation (2.60), can be readily solved for $t(\xi)$, which will describe this path; thus,

$$t(\xi) = -B \pm [B^2 - V(\xi)]^{1/2} \quad (2.77)$$

where

$$V(\xi) = -1 + \sqrt{1 - \xi^2 + 2i\sin\psi\xi} + i\beta\xi . \quad (2.78)$$

The constraint $t(\xi=0) = 0$, or

$$t(0) = -B \pm [B^2]^{1/2} \quad (2.79)$$

dictates the selection of the root in Equation (2.77).

The parameter $B = \pm i(1 + \beta\sin\psi - \sqrt{1-\beta^2}\cos\psi)^{1/2}$ can be neglected in comparison with $V(\xi)$ for $\xi \rightarrow R$, where R is some large, positive constant. Thus, from Equation (2.77),

$$\begin{aligned} t(\xi = R) &= \underset{R \rightarrow \infty}{\pm} [1 - \sqrt{1 - R^2 + 2iR\sin\psi} - i\beta R]^{1/2} \\ &= \pm [-\sqrt{-R^2} - i(\beta_r + i\beta_i) R]^{1/2} \\ &= \pm [\beta_i R - i(R + \beta_r R)]^{1/2} \end{aligned} \quad (2.80)$$

The imaginary part of the quantity inside the brackets is always negative, but the real part can be negative or positive. Thus, if

$\beta_i < 0$, the quantity in brackets is confined to the third quadrant, and the two roots will lie in the seventh and third octants. If $\beta_i > 0$, the bracketed term is in the fourth quadrant, and therefore the two roots will lie in the eighth and fourth octants. These relationships are illustrated in Figure 2.5 (a).

The octants that have been identified represent potential closure regions for the integration contour in the complex t -plane. That is, the original path along the real axis will connect via a circular arc of large radius to the point $t(R)$ expressed in Equation (2.80).

Referring to Figure 2.5 (a), it is apparent that the most convenient choice for closure is the eighth octant for $\beta_i > 0$ and the seventh octant for $\beta_i < 0$. In either case, the final closed contour will enclose a region entirely within the fourth quadrant, as shown in Figure 2.5 (b). Assuming (for the moment) that no poles or branch points lie within the enclosed region, the following relations hold from fundamental principles:

$$\int_{C_1} + \int_{C_R} - \int_{C_t} = 0 \quad (2.81)$$

where C_1 is a path along the real axis; C_R is a circular arc of arbitrarily large radius R ; and C_t is the actual transformed contour (from the original real ξ -axis). So long as the integral over C_R vanishes, the original real-axis integration in terms of ξ , Equation (2.57), can again be expressed as a real-axis integration in terms of t . That is,

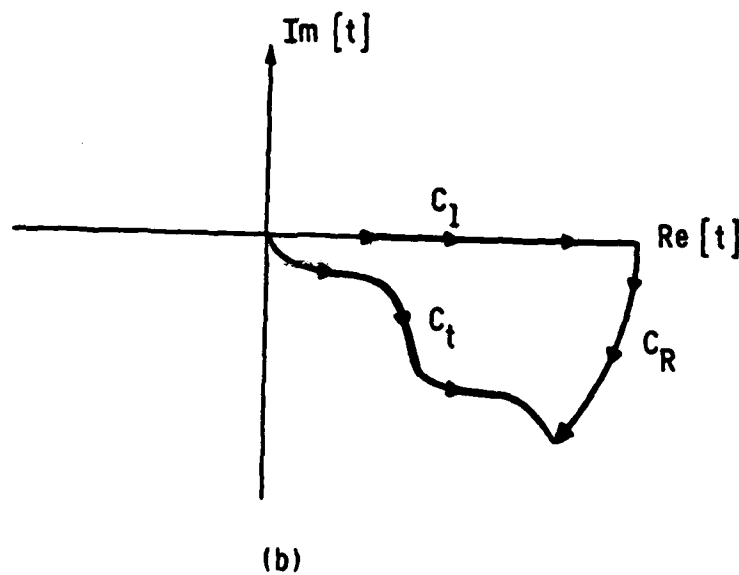
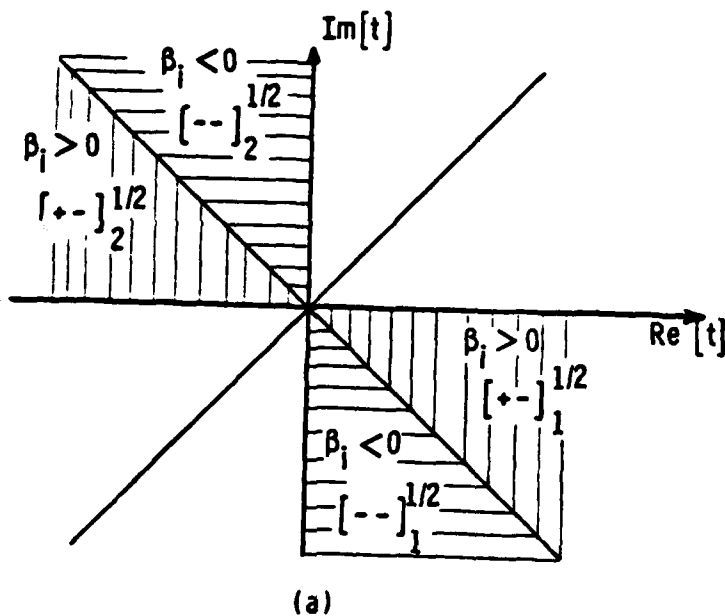


Figure 2.5 Complex t -plane Showing (a) Each of Two Values for the Square Root Function for Imaginary Part of the Admittance Positive or Negative; and (b) a Typical Closed Contour in the Fourth Quadrant.

$$\int_{\xi=0}^{\xi=\infty} d\xi = \int_{C_t} dt = \int_{C_1} dt = \int_{t=0}^{t=\infty} dt . \quad (2.82)$$

As this is the desired result, the final step in the transformation is to ensure that the integral over C_R vanishes as R gets large.

The exponent in Equation (2.76) can be written in terms of its real and imaginary parts for $t=t_r+it_i$ and $B=B_r+iB_i$ as¹⁸

$$-ikR_2(t^2 + 2Bt) = -ikR_2[(t_r + it_i)^2 + 2(B_r + iB_i)(t_r + it_i)] , \quad (2.83)$$

where the real part

$$\text{Re}[-ikR_2(t^2 + 2Bt)] = 2kR_2 t_r t_i + 2kR_2 B_r t_i + 2kR_2 B_i t_r \quad (2.84)$$

must be less than zero. First, for path C_R "starting" on the real axis, $t_i=0$, so that $\text{Re}[-ikR_2(t^2 + 2Bt)] = 2kR_2 B_i t_r$. Hence, to ensure convergence here, B_i must be negative. Furthermore, for all other points along C_R off the real axis, the first term on the right hand side of Equation (2.84) is sufficiently large to ensure that the exponent is negative regardless of the sign of B_r . Consequently, the proper root for B is now fixed, and Equation (2.65) may be re-written to enforce the constraint $B_i < 0$ as

¹⁸ The wavenumber k , which had been assumed complex for physical purposes, can here be assumed real for mathematical purposes. In the alternative, the small positive imaginary part k_i could be made arbitrarily small so that $k = k_r + ik_i \rightarrow k_r$ in the limit.

$$B = -i \sqrt{1 + \beta \sin \psi} - \sqrt{1 - \beta^2} \cos \psi ; \quad \operatorname{Re} \sqrt{} > 0 \quad (2.85)$$

and the transformed path, Equation (2.77) can be specified as

$$t(\xi) = -B - \sqrt{B^2 - V(\xi)} ; \quad \operatorname{Im} \sqrt{} > 0 \quad (2.86)$$

where the symbol $\sqrt{}$ indicates that the root is to be taken to yield a positive imaginary part.

2.3.3 The Branch Points and Branch Cuts

The simple pole that was present in the original integral (see Equation [2.48]) does not appear in the transformed integral of Equation (2.76); however, due to the multivalued nature of the denominator, a branch point is still present. It can be shown that the presence of a branch cut arising from this point will not affect the integration directly since the contour can be closed without crossing any portion of the cut. But, as will be pointed out later, the branch point is also a singularity of the integrand and, as such, will limit the radius of convergence of the Taylor series expansion of the denominator.

The branch points are simply the roots of the equation

$$-\frac{t^2}{H} - \frac{2Bt}{H} + 1 = 0 \quad (2.87)$$

where, again,

$$H = 1 + \beta \sin \psi + \sqrt{1 - \beta^2} \cos \psi \quad (2.88)$$

Therefore, the branch points are

$$t_1 = -B \pm \sqrt{2A} ; \quad \operatorname{Re} \sqrt{\cdot} > 0 \quad (2.89)$$

$$\text{where } A = \sqrt{1 - \beta^2} \cos \psi .$$

The branch cuts associated with these points have already been chosen, implicitly. That is, the specification that the root in the integral of Equation (2.76) be taken to yield a positive real part has essentially defined lines in the t -plane, across which the value of the root changes in sign. The equation describing these branch lines can be derived in a relatively straightforward manner.

In the complex z -plane, the negative real axis acts as the branch cut for the constraint $\operatorname{Re}(z)^{1/2} > 0$; that is, the equation describing the branch line is $z_{\text{line}} = -p$, for $p \geq 0$. In direct analogy, the constraint

$$\operatorname{Re}\left[-\frac{t^2}{H} - \frac{2Bt}{H} + 1\right]^{1/2} > 0 \quad (2.90)$$

translates into the defining equation for the branch line

$$\left.-\frac{t^2}{H} - \frac{2Bt}{H} + 1\right|_{\text{line}} = -p ; \quad p \geq 0 . \quad (2.91)$$

Solving this for t , gives the equation for the branch line in the t -plane. Thus,

$$t_{\text{line}} = -B \pm \sqrt{2A + pH} ; \quad p \geq 0 . \quad (2.92)$$

It can be shown that the branch lines described by this equation usually lie wholly within the first, second, or third quadrants of the t -plane, and consequently do not interfere with the closed integration contour. For the rather unrealistic case for which $\beta_1 > 0$, $|\beta| \gg 1$, and $\sin\psi \neq 0$, one of the branch points can fall in the fourth quadrant; however, the corresponding cut extends downward, and the closed contour can be perturbed-- if necessary--to avoid crossing it.

The transformed path, Equation (2.86), along with the branch cuts, Equation (2.92), are plotted in Figure 2.6 (a) and (b) for two representative combinations of admittance β and grazing angle ψ . The contours are presented here only to add insight into the problem, as the final integration need only be performed over the positive real axis.

2.3.4 The Taylor Series Expansion

The integral in Equation (2.76) can be re-written now as a real integral. Thus, disregarding the constant multiplier,

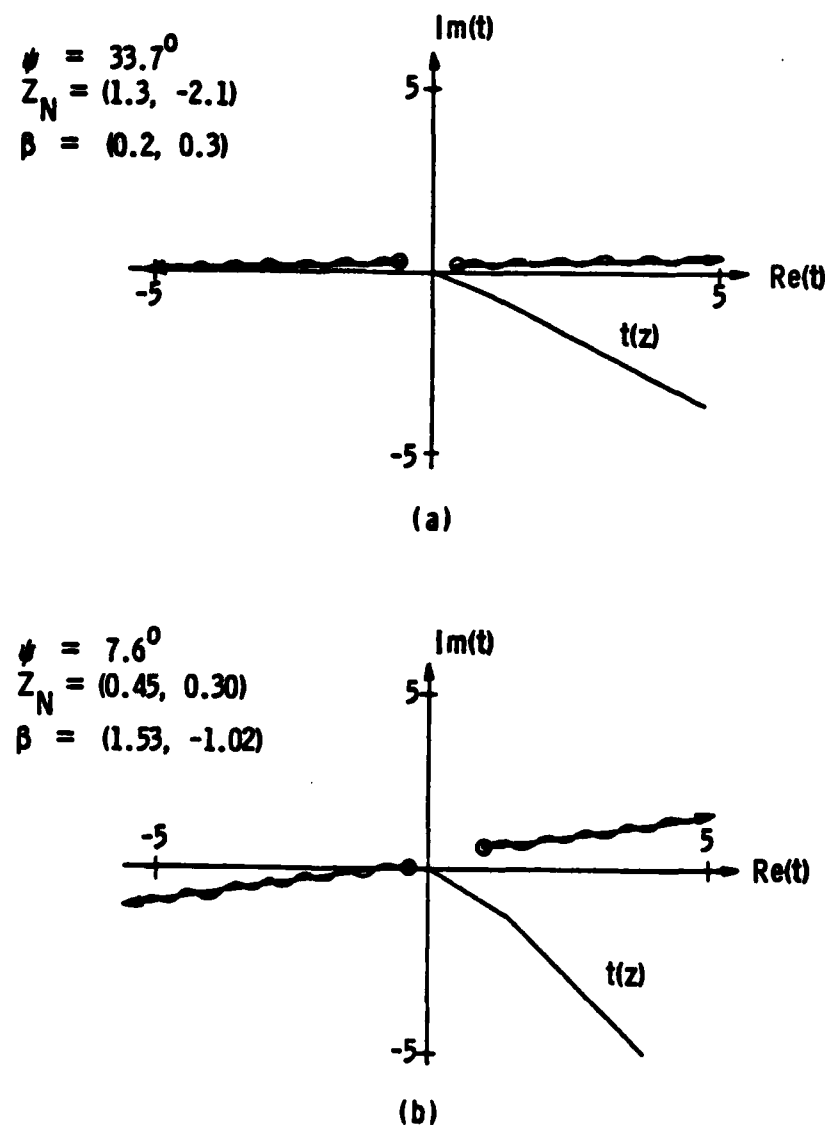


Figure 2.6 Complex t -plane Showing Branch Cuts and the Transformed Contour for two--(a) and (b)--Representative Cases for Z_N , ψ , and β .

$$I_3 = \int_0^{\infty} \frac{e^{-ikR_2[t^2 + 2Bt]}}{\sqrt{1 - \frac{t^2}{H} - \frac{2Bt}{H}}} dt \quad (2.93)$$

The square root function in the integrand is still the obstacle preventing the evaluation of this integral, so the radical will be removed by expanding it into a Taylor series about the origin. It is possible to avoid computing the derivatives normally required by Taylor's formula by noting that the given function is already in the standard form $(1+u)^{-\frac{1}{2}}$ where $u = (t^2/H + 2Bt/H)$. From the well-known result

$$(1+u)^{-\frac{1}{2}} = 1 - \frac{1}{2}u + \frac{3}{8}u^2 - \frac{5}{16}u^3 + \frac{35}{128}u^4 \dots \quad (2.94)$$

the expansion for the integral factor can be translated to be

$$\begin{aligned} \frac{1}{\sqrt{1 - \frac{t^2}{H} - \frac{2Bt}{H}}} &= + \left[\frac{B}{H} \right] t + \left[\frac{3B^2}{2H^2} + \frac{1}{2H} \right] t^2 \\ &\quad + \left[\frac{5B^3}{2H^3} + \frac{3B^2}{2H^2} \right] t^3 + \left[\frac{3}{8H^2} + \frac{15B^2}{4H^3} + \frac{35B^4}{8H^4} \right] t^4 + \dots \\ &= \sum_{n=0}^{\infty} T_n t^n . \end{aligned} \quad (2.95)$$

A general form for the Taylor coefficients T_n can also be obtained as follows:

$$T_n = \frac{1}{(2B)^n} \sum_{k=0}^{[n-2k] \geq 0} \binom{n-k}{k} a_{n-k} \left(\frac{4G}{H}\right)^{n-k} \quad (2.96)$$

where the quantity $\binom{n-k}{n}$ is the binomial coefficient; the parameter G is given by

$$G = -B^2 = 1 + \beta \sin\psi - \sqrt{1 - \beta^2} \cos\psi ; \quad (2.97)$$

and a_{n-k} is expressed by the following recursion relation:

$$\begin{aligned} a_0 &= 1 \\ a_m &= \frac{(1/2 - m)}{m} a_{m-1} . \end{aligned} \quad (2.98)$$

The notation on the summation symbol in Equation (2.96) indicates that k increases in integer steps until the expression $(n-2k) \geq 0$ is no longer satisfied (for example, if $n=6$ or $n=7$, then $k=0,1,2,3$). For reference, the values of the binomial coefficient and a_m required for an expansion through t^6 are given as follows:

$$\begin{aligned}
 & \begin{aligned} a_0 &= 1 \\ a_1 &= -1/2 \\ a_2 &= 3/8 \\ a_3 &= -5/16 \\ a_4 &= 35/128 \\ a_5 &= -63/256 \\ a_6 &= 231/1034 \end{aligned} & \begin{aligned} \binom{m}{0} &= 1 \\ \binom{m}{1} &= \binom{m}{m-1} = m \\ \binom{m}{m} &= 1 \\ \binom{4}{2} &= 6 \\ \binom{5}{2} &= 10 \\ \binom{5}{3} &= 10 \\ \binom{6}{2} &= 15 \\ \binom{6}{3} &= 20 \\ \binom{6}{4} &= 15 \end{aligned} & (2.99)
 \end{aligned}$$

As with any Taylor series, the expansion in Equation (2.95) is absolutely and uniformly convergent within any circular region in the complex plane about the expansion point ($t=0$ in this case) that does not contain a singularity. The circle of convergence for Equation (2.95) is thus limited by one of the branch points t_1 or t_2 defined in Equation (2.89). Precisely, if $|t_a|$ represents the smaller of the magnitudes $|t_1|$ and $|t_2|$, then the radius of convergence for the Taylor series will be $|t_a|$. Of course, for values of t such that $|t| > |t_a|$, the function on the left hand side of Equation (2.95) can no longer be equated to the series on the right, because the latter may diverge.

2.3.5 The Term-by-Term Integration

The integral I_3 in Equation (2.93) can now be re-written as a sum of two convergent integrals

$$\begin{aligned}
 I_3 &= I'_3 + I''_3 \\
 &= \int_0^{|ta|} e^{-ikR_2(t^2 + 2Bt)} \left[\sum_{n=0}^{\infty} T_n t^n \right] dt + \int_{|ta|}^{\infty} \frac{e^{-ikR_2(t^2 + 2Bt)}}{\sqrt{1 - \frac{t^2}{H} - \frac{2Bt}{H}}} dt . \tag{2.100}
 \end{aligned}$$

It should be emphasized, here, that no mathematical approximations have been made thus far in the derivation and so the exact expression for the field, Equation (2.47), can be written

$$\Phi(r, z) = \frac{e^{ikR_1}}{R_1} + \frac{e^{ikR_2}}{R_2} - \frac{4ikR\beta Be}{(\beta + \sin\psi)} I_3 , \tag{2.101}$$

with I_3 given above.

To insure accuracy in the approximations to be made, the relative magnitudes of the two integral terms in Equation (2.100) should be investigated. If the second integral can be neglected, then a term-by-term integration on the first integral would accurately represent the field. It is sufficient to examine first the behavior of the integrand

$$U(t) = \frac{e^{-ikR_2(t^2 + 2Bt)}}{\sqrt{1 - \frac{t^2}{H} - \frac{2Bt}{H}}} . \quad (2.102)$$

Plotted in Figure 2.7 (a), (b), and (c) are the real and imaginary parts of the function $U(t)$ versus t for three values of the parameter kR_2 . Here, β and ψ are fixed at the representative values $\beta=(0.055, -0.062)$ and $\psi=3.8^\circ$. The value of $|t_a|$ for this β and ψ is marked by a vertical bar on the t -axis and indicates the limit for t beyond which the Taylor series diverges. It is apparent from Figure 2.7 that as kR_2 increases a greater and greater contribution to the integral comes from the region in which the Taylor series converges. In other words, for large kR_2 , the integral from $t=0$ to $t=\infty$ in Equation (2.93) can be replaced by just the first integral in Equation (2.100). The condition "large kR_2 " can often be taken in a relaxed sense. In the particular case shown in Figure 2.7 (b), for instance, the relatively modest value of $kR_2=13.5$ shows a very minor contribution for $t \gtrsim |t_a|$.

There is one final step to be taken before the integral in Equation (2.93) can be expressed in a form suitable for term-by-term integration. This involves replacing the denominator in the second integral of Equation (2.100) by the Taylor series expansion, and thus writing

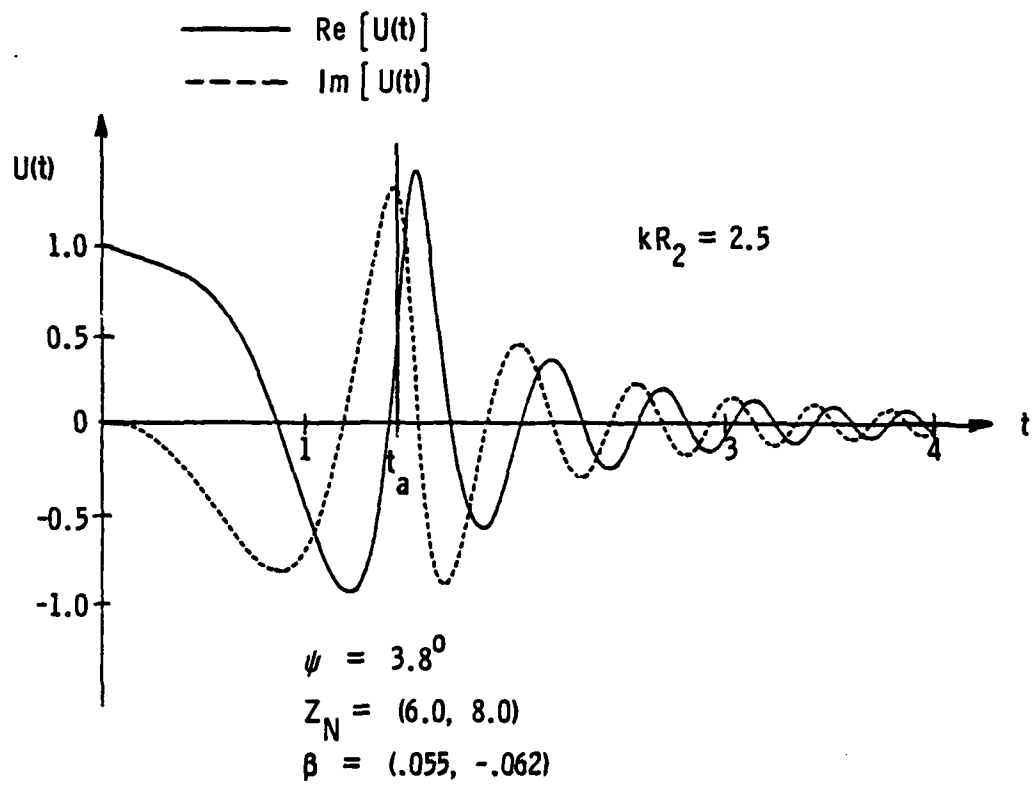


Figure 2.7 Real and Imaginary Parts of Integrand Function $U(t)$ vs. t for Z_N , ψ , and β , Fixed. (a) $kR_2 = 2.5$

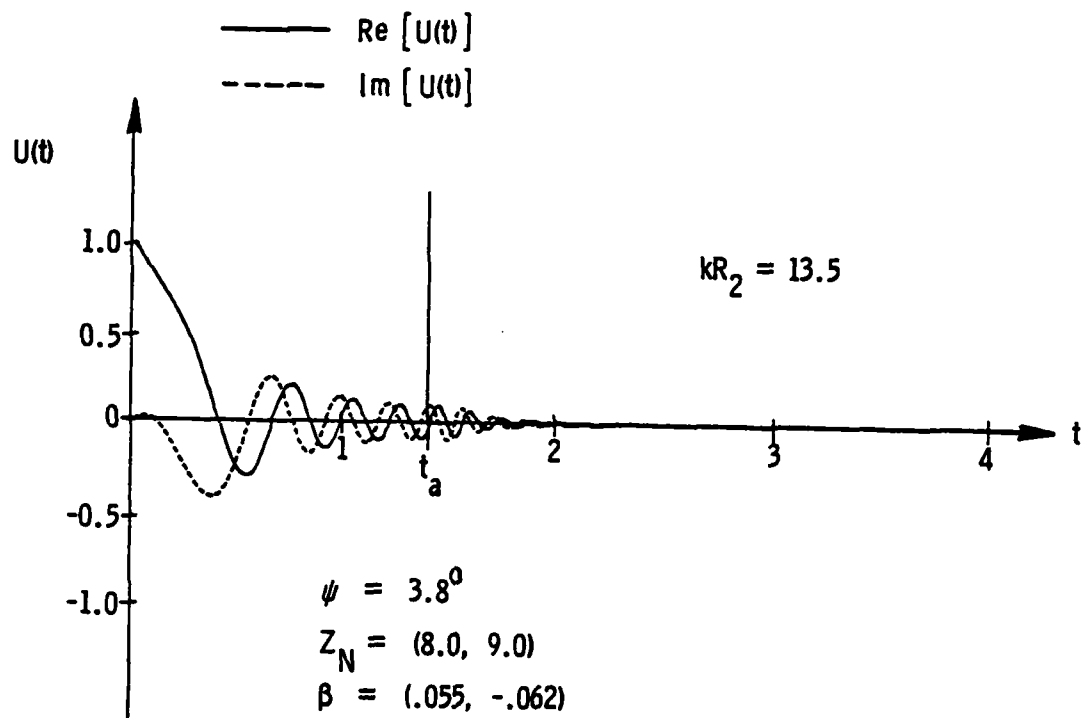


Figure 2.7 Real and Imaginary Parts of Integrand Function $U(t)$ vs. t for Z_N , ψ , and β Fixed. (b) $kR_2 = 13.5$.

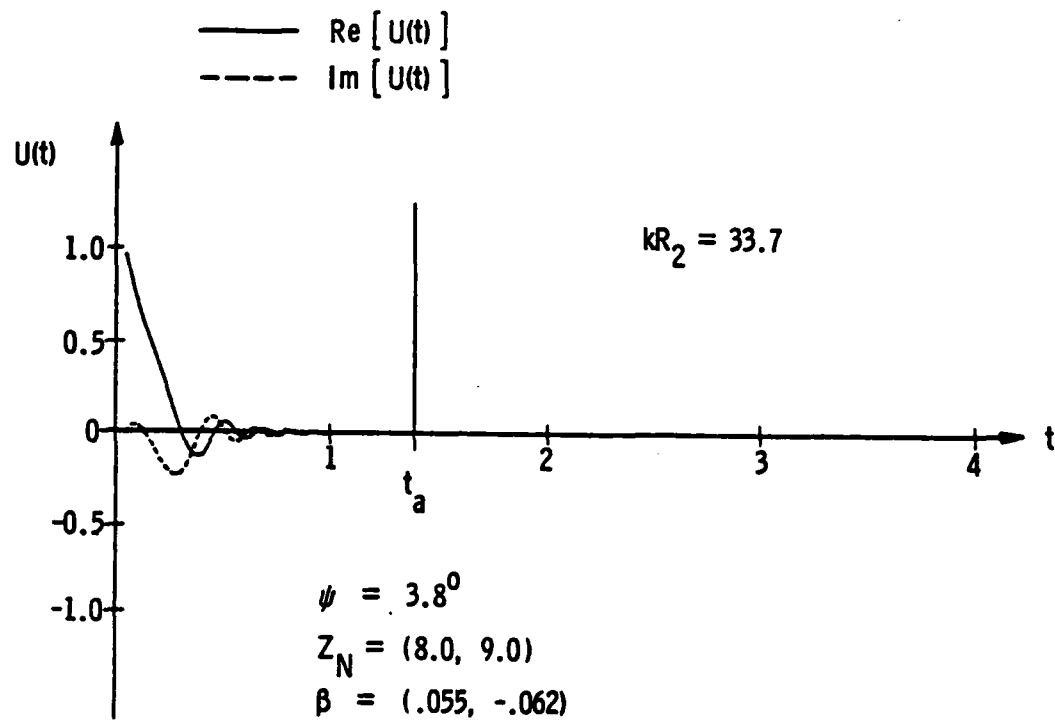


Figure 2.7 Real and Imaginary Parts of Integrand Function $U(t)$ vs. t for Z_N , ψ , and β Fixed. (c) $kR_2 = 33.7$.

$$I_4 = \int_0^{|ta|} e^{-ikR_2(t^2 + 2Bt)} \left[\sum T_n t^n \right] dt \\ + \int_{|ta|}^{\infty} e^{-ikR_2(t^2 + 2Bt)} \left[\sum T_n t^n \right] dt , \quad (2.103)$$

or

$$I_4 = \sum_{n=0}^{\infty} T_n \int_0^{\infty} t^n e^{-ikR_2(t^2 + 2Bt)} dt . \quad (2.104)$$

Clearly, from the discussion in the previous section, the second integral in Equation (2.103) does not equal the second integral in Equation (2.100) and so $I_4 \neq I_3$. However, a relationship does exist between the two integrals, namely that I_4 given by Equation (2.104) is an asymptotic expansion (sometimes called a "semi-convergent" expansion) of the integral I_3 . An asymptotic expansion converges up to a point, and then diverges. That I_4 represents an asymptotic expansion of I_3 is proven in principle in several classical mathematics texts¹⁹ and may be explained heuristically here as follows.

The second series of integrals on the right hand side of Equation (2.103) clearly diverges since it involves the Taylor series outside of its circle of convergence, but the first series converges. The

¹⁹ The necessary tools are Watson's lemma and some theorems on Laplace transforms. See, for example, Copson, 1935, p. 218.

rates of convergence and divergence are controlled by the parameter kR_2 in the exponent: the larger kR_2 , the more rapid the convergence of the first series, and the slower the divergence of the second. However, for any fixed value of kR_2 , the sum of the two integral series behaves asymptotically since it will always converge up to a certain number of terms, at which point the second series "takes over" and causes it to diverge. Moreover, recalling the conclusions drawn from Figure 2.7 (a), (b), and (c), the series up to the onset of divergence is an accurate representation of the exact integral for "large kR_2 ."

The conclusion to be drawn from this section is that

$$I_3 = \int_0^{\infty} \frac{e^{-ikR_2(t^2 + 2Bt)}}{\sqrt{1 - \frac{t^2}{H} - \frac{2Bt}{H}}} dt \sim \sum_{n=0}^{\infty} T_n \int_0^{\infty} t^n e^{-ikR_2(t^2 + 2Bt)} dt . \quad (2.105)$$

where the symbol " \sim " translates "has the asymptotic expansion" or "is asymptotically equal to." Each integral in the series is tractable, and, as a result, it will be possible to express the total field solution as an asymptotic series of closed-form terms.

2.3.5.1 The Formal Series Solution. The general integral in the series Equation (2.105) can be solved in terms of parabolic cylinder functions. The functional form is (Gradshteyn & Ryzhik, 1965, Integral #3.462[1]):

$$\int_0^\infty t^n e^{-at^2-bt} dt = \frac{1}{(2a)^{(n+1)/2}} \Gamma(n+1) e^{b^2/8a} D_{-(n+1)}(b/\sqrt{2a}) \quad (2.106)$$

where $\Gamma(m)$ is the gamma function--for integer arguments $\Gamma(m+1)=m!$ --and $D_{-p}(z)$ is the parabolic cylinder function. Several fundamental relationships involving the functions $D_{-p}(z)$ will be useful for later development (see Gradshteyn & Ryzhik, 1965, pp. 1064-1068). First,

$$D_{-1}(z) = \sqrt{\frac{\pi}{2}} e^{z^2/4} \operatorname{erfc}(z/\sqrt{2}) \quad (2.107)$$

and²⁰

$$D_{-2}(z) = z \sqrt{\frac{\pi}{2}} e^{z^2/4} \operatorname{erfc}(z/\sqrt{2}) - e^{-z^2/4}, \quad (2.108)$$

where $\operatorname{erfc}(z)$ is the complex complementary error function defined as

$$\operatorname{erfc}(z) = \frac{2}{\sqrt{\pi}} \int_z^\infty e^{-\tau^2} d\tau. \quad (2.109)$$

In addition, parabolic cylinder functions obey the following recursion relationships:

²⁰ There is a sign error in the expression for $D_{-p}(z)$ found in the text by Gradshteyn and Ryzhik. The expression given here is the corrected form.

$$D_{p+1}(z) - zD_p(z) + pD_{p-1}(z) = 0$$

$$\frac{d}{dz} D_p(z) + \frac{1}{2} zD_p(z) - pD_{p-1}(z) = 0 \quad (2.110)$$

$$\frac{d}{dz} D_p(z) - \frac{1}{2} zD_p(z) + D_{p+1}(z) = 0$$

for which the following equality (Abramowitz & Stegun, 1964, Section 7.2.8) might prove helpful:

$$\frac{d}{dz} \operatorname{erfc}(z) = -\frac{2}{\sqrt{\pi}} e^{-z^2}. \quad (2.111)$$

Using the recursion relations, it is relatively easy to derive the following explicit terms

$$D_{-3}(z) = \sqrt{\frac{\pi}{2}} e^{z^2/2} \operatorname{erfc}(z/\sqrt{2}) \left[\frac{z^2}{2} + \frac{1}{2} \right] + e^{-z^2/4} \left[-\frac{z}{2} \right] \quad (2.112)$$

$$D_{-4}(z) = \sqrt{\frac{\pi}{2}} e^{z^2/4} \operatorname{erfc}(z/\sqrt{2}) \left[-\frac{z^3}{2} - \frac{z}{2} \right] + e^{-z^2/4} \left[\frac{z^2}{6} + \frac{1}{3} \right] \quad (2.113)$$

$$D_{-5}(z) = \sqrt{\frac{\pi}{2}} e^{z^2/4} \operatorname{erfc}(z/\sqrt{2}) \left[\frac{z^4}{24} + \frac{z^2}{4} + \frac{1}{8} \right] + e^{-z^2/4} \left[-\frac{z^3}{24} - \frac{5z}{24} \right], \quad (2.114)$$

or, in general,

$$D_{-(n+1)}(z) = \sqrt{\frac{\pi}{2}} e^{-z^2/4} \operatorname{erfc}(z/\sqrt{2}) Q_{-(n+1)}(z) + e^{-z^2/4} P_{-(n+1)}(z) , \quad (2.115)$$

where

$$\begin{aligned} Q_{-1}(z) &= 1 & P_{-1}(z) &= 0 \\ Q_{-2}(z) &= -z & P_{-2}(z) &= 1 \\ Q_{-(n+1)}(z) &= -\frac{z}{n} Q_{-n}(z) + \frac{1}{n} Q_{-(n-1)}(z) \\ P_{-(n+1)}(z) &= -\frac{z}{n} P_{-n}(z) + \frac{1}{n} P_{-(n-1)}(z) . \end{aligned} \quad (2.116)$$

Now, translating "z" in the above to "b/ 2a" and substituting Equation (2.115) back into Equation (2.106) yields a recursion relation for the integral itself. That is,

$$\int_0^\infty t^n e^{-at^2-bt} dt = \frac{1}{2} \sqrt{\frac{\pi}{a}} e^{b^2/4a} \operatorname{erfc}(b/2\sqrt{a}) \bar{E}_n + \bar{K}_n \quad (2.117)$$

where

$$\bar{E}_m = \frac{1}{(2a)^{m/2}} \Gamma(m+1) Q_{-(m+1)}(b/2\sqrt{a}) \quad (2.118)$$

and

$$\bar{K}_m = \frac{1}{(2a)^{(m+1)/2}} \Gamma(m+1) P_{-(m+1)}(b/2\sqrt{a}) . \quad (2.119)$$

Noting that $\Gamma(m+1) = (m+1)\Gamma(m)$, the coefficients \bar{E}_m and \bar{K}_m can be expressed more concisely as

$$\bar{E}_m = -\frac{b}{2a} \bar{E}_{m-1} + \frac{m}{2a} \bar{E}_{m-2} \quad (2.120)$$

and

$$\bar{K}_m = -\frac{b}{2a} \bar{K}_{m-1} + \frac{m}{2a} \bar{K}_{m-2} \quad (2.121)$$

where

$$\begin{aligned} \bar{E}_0 &= 1 & \bar{K}_0 &= 0 \\ \bar{E}_1 &= -\frac{b}{2a} & \bar{K}_1 &= \frac{1}{2a} \end{aligned} \quad (2.122)$$

The general integral at the beginning of this section has thus been solved in terms of the complementary error function and two general coefficients, for which recursion relations are provided. The specific integral of interest here--Equation (2.105)--can now be expressed from the above results by translating "a" to " ikR_2 " and "b" to " $2ikR_2B$." Thus, the asymptotic expansion of the integral I_3 in Equations (2.93) and (2.105) can be written in the final form

$$I_3 \sim \sum_{n=0}^{\infty} T_n [e_0 E_n + K_n] \quad (2.123)$$

where

$$E_m = -BE_{m-1} + \frac{(m-1)}{2ikR_2} E_{m-2} \quad (2.124)$$

$$K_m = -BK_{m-1} + \frac{(m-1)}{2ikR_2} K_{m-2}$$

and $E_0 = 1 \quad K_0 = 0$
 $E_1 = -B \quad K_1 = 1/2ikR_2 .$

In addition, the parameter e_0 has been introduced as

$$e_0 = \frac{1}{2} \sqrt{\frac{\pi}{ikR_2}} e^{-\lambda^2} \operatorname{erfc}(-i\lambda) \quad (2.125)$$

where

$$\lambda^2 = ikR_2 [1 + \beta \sin\psi - (1 - \beta^2)^{\frac{1}{2}} \cos\psi] \quad (2.126)$$

and

$$\lambda = \sqrt{ikR_2} \sqrt{1 + \beta \sin\psi - (1 - \beta^2)^{\frac{1}{2}} \cos\psi} . \quad (2.127)$$

All complex square roots in the above equations--including $(1 - \beta^2)^{\frac{1}{2}}$ --are to be taken to yield a positive real part. It must be stressed that the definition for λ in Equation (2.127) has been derived from the argument of the parabolic cylinder function, and the roots must be taken separately as indicated. This is important because, in general, $\sqrt{ipf(z)} \neq \sqrt{ip} \sqrt{f(z)}$, when p is a positive constant and positive real roots are taken.

The full solution for the field at the point (r, z) can now be written as

$$\Phi(r, z) \sim \frac{e^{ikR_1}}{R_1} + \frac{e^{ikR_2}}{R_2} - \frac{4ik\beta Be}{(\beta + \sin\psi)} \sum_{n=0}^{\infty} T_n [e_o E_n + K_n] . \quad (2.128)$$

2.3.5.2 The Q-term Form of Solution. As mentioned in section 2.1, it is often desirable to express the total field as a simple sum of a direct component from the source plus a reflected component that appears to originate from an "image" source at $(r, -z_0)$. Hence, a solution of the form

$$\Phi(r, z) = \frac{e^{ikR_1}}{R_1} + Q \frac{e^{ikR_2}}{R_2} \quad (2.129)$$

will be sought in this section.

The last term in Equation (2.128) can be re-written as

$$T_3 = \frac{\beta}{(\beta + \sin\psi)} \frac{e^{ikR_2}}{R_2} \sum_{n=0}^{\infty} [-2ikBR_2 e_o T_n E_n - 2ikBR_2 T_n K_n] . \quad (2.130)$$

Furthermore, it is convenient to re-express the product $T_n E_n$ as

$$T_n E_n = \left[\sum_{n=0}^{(n-2k) \geq 0} \binom{n-k}{k} a_{n-k} \left(\frac{4G}{H}\right)^{n-k} \right] \left[\frac{E_n}{(2B)^n} \right] = T_n^* E_n^* \quad (2.131)$$

where

$$T_n^* = \sum_{k=0}^{n-2k \geq 0} \binom{n-k}{k} a_{n-k} \left(\frac{4G}{H}\right)^{n-k} \quad (2.132)$$

and the factor $E_n^* = E_n / (2B)^n$. New recursion relationships can be derived for the starred coefficients, so that

$$\begin{aligned} E_0^* &= 1 & E_1^* &= \frac{E_1}{2B} = -\frac{1}{2} \\ E_m^* &= -\frac{1}{2} E_{m-1}^* - \frac{(m-1)}{8ikR_2G} E_{m-2}^* , \end{aligned} \quad (2.133)$$

where the fact that $B^2 = -G$ has been used.

Similarly the term $(-2ikBR_2)T_n K_n$ can be re-expressed as the simple product $T_n^* K_n^*$ where

$$\begin{aligned} K_0^* &= 0 & K_1^* &= -\frac{1}{2} \\ K_m^* &= -\frac{1}{2} K_{m-1}^* - \frac{(m-1)}{8ikR_2G} K_{m-2}^* . \end{aligned} \quad (2.134)$$

When Equation (2.130) is substituted back into Equation (2.128), the total field may be expressed in the form of Equation (2.129), with the "spherical wave reflection coefficient" Q given by

$$Q = 1 + \frac{2\beta}{(\beta + \sin\psi)} \sum_{n=0}^{\infty} T_n^* [e_1 E_n^* + K_n^*] . \quad (2.135)$$

Here, the parameter e_1 has been introduced where

$$\begin{aligned} e_1 &= -2ikBR_2 e_0 = -kR_2 \sqrt{\frac{\pi}{ikR_2}} e^{-\lambda^2} \operatorname{erfc}(-i\lambda) \\ &= i\sqrt{\pi} \lambda e^{-\lambda^2} \operatorname{erfc}(-i\lambda) , \end{aligned} \quad (2.136)$$

and λ is defined by Equation (2.127).

2.3.5.3 The F-term Form of Solution. The asymptotic series solution developed in section 2.3.5.1 can also be put into a form that provides a more direct comparison to the classical plane wave solution. As such, the solution would comprise a direct component from the source, a "plane-wave reflected" component, plus a correction term that accounts for the sphericity of the wavefronts (see Equation [2.7]). Historically, several approximate solutions in both electromagnetics and acoustics have been expressed in such a form, and these contain the so-called "F-term" or "attenuation factor." The solutions are expressed as

$$\Phi(r, z) = \frac{e^{ikR_1}}{R_1} + R_p \frac{e^{ikR_2}}{R_2} + (1 - R_p) F \frac{e^{ikR_2}}{R_2}, \quad (2.137)$$

where R_p is the plane wave reflection coefficient,

$$R_p = \frac{\sin\psi - \beta}{\sin\psi + \beta}. \quad (2.138)$$

This form of solution is easily derived from the Q-term form given in the previous section. Thus,

$$\frac{2\beta}{(\beta + \sin\psi)} = \frac{\sin\psi + \beta - \sin\psi + \beta}{(\beta + \sin\psi)} = 1 - R_p \quad (2.139)$$

and, therefore

$$\begin{aligned} Q &= R_p + (1 - R_p) F \\ &= 1 + (1 - R_p) \sum_{n=0}^{\infty} T_n^* [e_1 E_n^* + K_n^*] \end{aligned}$$

Solving this for F gives the final result

$$F = 1 + \sum_{n=0}^{\infty} T_n^* [e_1 E_n^* + K_n^*]$$

where T_n^* is given by

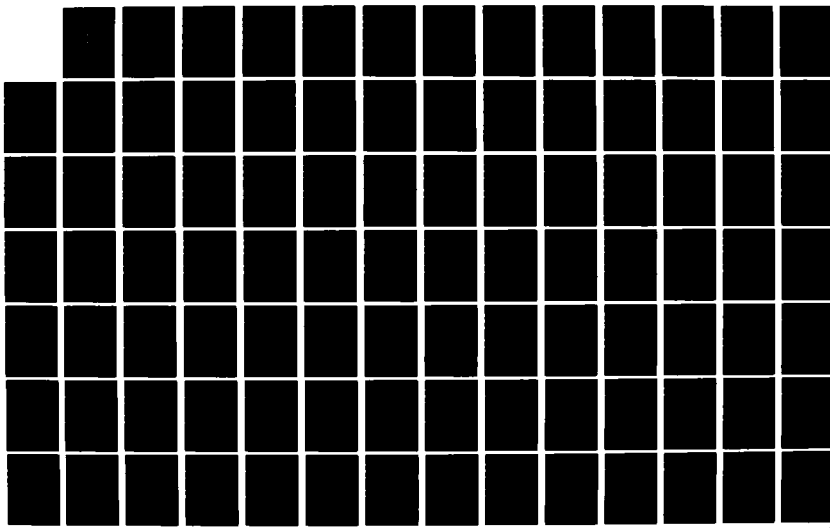
Equation 2.139.

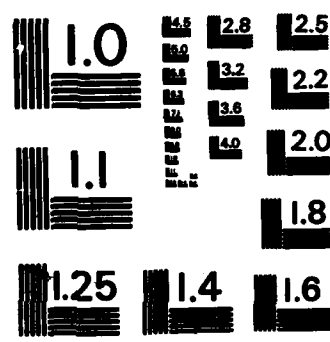
Equation 2.140.

AD-A122 023 ACOUSTIC PROPAGATION AND BARRIER DIFFRACTION OVER AN
IMPEDANCE PLANE(U) PENNSYLVANIA STATE UNIV UNIVERSITY
PARK APPLIED RESEARCH LAB. M A NOBILE 13 OCT 82
UNCLASSIFIED ARL/PSU/TM-82-210 N00024-79-C-6843 2/3

F/G 12/1.

NL





MICROCOPY RESOLUTION TEST CHART
NATIONAL BUREAU OF STANDARDS - 1963 - A

2.3.5.4 The Hankel Function Form of Solution. The results of at least one recent study (Chien & Soroka, 1975), which applied asymptotic techniques to the point source propagation problem, were expressed directly in terms of the zero-order Hankel function. The same function has also appeared in component terms (most often, the "surface wave" term) in other solutions offered in the literature. In view of this, the asymptotic series solution will be expressed in an alternate form that is also in terms of the Hankel function. It is offered here mainly to facilitate comparisons with other solutions, as the series forms presented so far in this study are the preferred forms of solution. (The series solutions, in conjunction with the recursion formulae, translate readily into computer programs for providing numerical data.)

The first few product terms $T_n^* E_n^*$ from the Q-term solution, Equation (2.135), can be written out explicitly to generate the following series:

$$\begin{aligned}
 \sum_{\text{Partial}} T_n^* E_n^* &= \left[1 + \frac{1}{2} \left(\frac{G}{H} \right) + \frac{3}{8} \left(\frac{G}{H} \right)^2 + \frac{5}{16} \left(\frac{G}{H} \right)^3 + \dots \right]_a \\
 &\quad + \frac{1}{4ikR_2 H} \left[1 + \frac{3}{2} \left(\frac{G}{H} \right) + \frac{15}{8} \left(\frac{G}{H} \right)^2 + \frac{35}{16} \left(\frac{G}{H} \right)^3 + \dots \right]_b \quad (2.142) \\
 &\quad + \frac{9}{32(ikR_2 H)^2} \left[1 + \frac{5}{2} \left(\frac{G}{H} \right) + \frac{35}{8} \left(\frac{G}{H} \right)^2 + \frac{105}{16} \left(\frac{G}{H} \right)^3 + \dots \right]_c \\
 &\quad + \dots +
 \end{aligned}$$

where the parameters H and G are repeated here as

$$\begin{aligned} H &= 1 + \beta \sin \psi + (1 - \beta^2)^{\frac{1}{2}} \cos \psi \\ G &= 1 + \beta \sin \psi - (1 - \beta^2)^{\frac{1}{2}} \cos \psi \end{aligned} \quad (2.143)$$

Each of the series in the brackets subscripted a, b, and c can be recognized to be simple expansions of the form $(1+x)^\alpha$ such that

$$\begin{aligned} \left[\quad \right]_a &= \left(1 - \frac{G}{H} \right)^{-1/2} \\ \left[\quad \right]_b &= \left(1 - \frac{G}{H} \right)^{-3/2} \\ \left[\quad \right]_c &= \left(1 - \frac{G}{H} \right)^{-5/2} . \end{aligned} \quad (2.144)$$

Using the fact that $[1-(G/H)] = [(F-G)/H] = 2A/H$, where $A=(1-\beta^2)^{\frac{1}{2}}\cos\psi$, the partial series in Equation (2.142) can be re-written as

$$\begin{aligned} \sum_{\text{Partial}} T_n^* E_n^* &= \left(\frac{F}{2A} \right)^{\frac{1}{2}} \left[1 + \frac{1}{4ikR_2 F} \left(\frac{F}{2A} \right) + \frac{9}{32(ikR_2)F^2} \left(\frac{F}{2A} \right)^2 + \dots \right] \\ &= \left(\frac{F}{2A} \right)^{\frac{1}{2}} \left[1 + \frac{1}{8ikR_2 A} + \frac{9}{128(ikR_2 A)^2} + \dots \right] \end{aligned} \quad (2.145)$$

Comparing this to the asymptotic expansion of the Hankel function

$H_0^{(1)}(z)$ (see, for example, Abramowitz & Stegun, 1964, Section 9.2.8)

$$H_o^{(1)}(z) = \sqrt{\frac{2}{\pi z}} e^{iz} \left[1 + \frac{1}{8iz} + \frac{9}{128(iz)^2} + \dots \right] \quad (2.146)$$

enables Equation (2.145) to be re-phrased as

$$\sum_{n=0}^{\infty} T_n^* E_n^* = \left(\frac{F}{2A}\right)^{\frac{1}{2}} \left[\frac{\pi i k R_2 A}{2}\right]^{\frac{1}{2}} e^{-ikR_2 A} H_o^{(1)}(kR_2 A) . \quad (2.147)$$

With the added fact that $HG=(\beta+\sin\psi)^2$, the total solution given by Equations (2.129) and (2.135) can be expressed in the final form

$$\begin{aligned} \Phi(r, z) &= \frac{e^{ikR_1}}{R_1} + \frac{e^{ikR_2}}{R_2} \\ &- k\beta\pi e^{-ikR_2^2 \beta \sin\psi} \operatorname{erfc}(-i\lambda) H_o^{(1)}[kR_2(1 - \beta^2)^{\frac{1}{2}} \cos\psi] \\ &+ \frac{2\beta}{(\beta + \sin\psi)} \frac{e^{ikR_2}}{R_2} \sum_{n=0}^{\infty} T_n^* X_n^* . \end{aligned} \quad (2.148)$$

2.3.5.5 The Solution Using the First Term Only. For many cases of practical interest, the parameter kR_2 is large²¹ and the asymptotic solution is rapidly convergent in the initial terms. Thus, using only

²¹ As examples: At 1000 Hz., for source and receiver on the ground and separated by 100 feet, the value of kR_2 is 559. At 200 Hz., for source and receiver 4 feet above the ground and separated by 20 feet, the value of kR_2 is 22.

the first ($n=0$) term in Equation (2.135) often provides sufficient accuracy. In such instances, the total solution can be written as

$$\Phi(r, z) = \frac{e^{ikR_1}}{R_1} + \frac{e^{ikR_2}}{R_2} [R_p + (1 - R_p)] F_1 \quad (2.149)$$

where

$$F_1 = 1 + i\sqrt{\pi} \lambda e^{-\lambda^2} \operatorname{erfc}(-i\lambda) \quad (2.150)$$

and, again,

$$\lambda = \sqrt{ikR_2} \sqrt{1 + \beta \sin\psi - \sqrt{1 - \beta^2} \cos\psi} \quad (2.151)$$

$\operatorname{Re} \sqrt{\quad} > 0$.

2.4 The Solution for Perpendicular Incidence

Although the asymptotic series solution is valid for $\psi=90^\circ$ (receiver directly above or below the source), an exact solution can be obtained for this special case in a straightforward way. Thus, when $\sin\psi = 1$ is substituted into the original transformed integral, Equation (2.67), and it is noted that $(1 - \xi^2 + 2i\xi) = (1 + i\xi)^2$, the integral can be re-written as

$$\begin{aligned}
 I_1 &= -2k\beta \int_0^\infty \frac{e^{-ikR_2[1+i(1+\beta)\xi]}}{(1+i\xi)} d\xi \\
 &= 2ik\beta e^{-ikR_2} \int_0^\infty \frac{e^{-kR_2(1+\beta)\xi}}{(\xi-i)} d\xi . \tag{2.152}
 \end{aligned}$$

Using the relation (Gradshteyn & Ryzhik, 1965, Integral #3.352[4])

$$\int_0^\infty \frac{e^{-\mu x}}{x+\beta} dx = -e^{\beta\mu} Ei(-\mu\beta) \quad [|\arg\beta|<\pi ; \operatorname{Re}\mu>0] \tag{2.153}$$

where Ei is the exponential integral defined by

$$Ei(w) = \int_{-\infty}^w \frac{e^x}{x} dx , \tag{2.154}$$

the integral I_1 in Equation (2.152) becomes

$$I_1 = -2ik\beta e^{-ikR_2} Ei[ikR_2(1+\beta)] . \tag{2.155}$$

Furthermore, $Ei(w)$ has the convergent series expansion (Abramowitz & Stegun, 1964, Section 5.1.10)

$$Ei(-w) = \gamma + \ln w + \sum_{n=1}^{\infty} \frac{(-1)^n w^n}{n! n} , \tag{2.156}$$

where γ is the Euler constant, $\gamma=0.57721\ 56649\dots$. The exponential integral also has the asymptotic expansion for large argument (Abramowitz & Stegun, 1964, Section 5.1.51)

$$\begin{aligned} Ei(-w) &\sim -\frac{e^{-w}}{w} \left\{ 1 - \frac{1}{w} + \frac{1 \cdot 2}{w^2} - \frac{1 \cdot 2 \cdot 3}{w^3} + \dots \right\} \\ &\sim -\frac{e^{-w}}{w} \sum_{k=0}^{\infty} \frac{(-1)^k k!}{w^k}; \quad |\arg w| < \frac{3\pi}{2} . \end{aligned} \quad (2.157)$$

In summary, the total field at the receiver point for perpendicular incidence ($r=0$) is

$$\Phi(z) = \frac{e^{ikR_1}}{R_1} + \frac{e^{ikR_2}}{R_2} - 2ik\beta e^{-ikR_2} \beta Ei[ikR_2(1+\beta)], \quad (2.158)$$

in which R_2 may be replaced by $R_2 = h = z + z_0$.

When kR_2 is very large, the first term in the asymptotic series, Equation (2.157), may be used so that the total field becomes

$$\begin{aligned} \Phi(z) &= \frac{e^{ikR_1}}{R_1} + \frac{e^{ikR_2}}{R_2} - \frac{2\beta e^{ikR_2}}{R_2(1+\beta)} \\ &= \frac{e^{ikR_1}}{R_1} + \left(\frac{1-\beta}{1+\beta} \right) \frac{e^{ikR_2}}{R_2} . \end{aligned} \quad (2.159)$$

thus reducing to the "plane wave" solution (Equations [2.4] and [2.5] with $\sin \psi = 1$).

CHAPTER III

A MODEL FOR THE COMBINED PROBLEM OF POINT SOURCE PROPAGATION WITH A DIFFRACTING BARRIER

When a barrier located on an impedance plane obstructs the line of sight from a point source to a point receiver, acoustic energy reaches the receiver by diffraction over the edge of the barrier. The "canonical" problem of point source diffraction by an ideal half plane is relatively well understood; however, the attempts to apply its solution directly to the problem here have met with little success. This is due to the fact that when a barrier is located on the ground, the incident field at its edge is not a simple monopole field. Instead, it is a complex field resulting from the propagation over the impedance plane. Furthermore, the ground plane interactions on the receiver side of the barrier must be accounted for when predicting the total field behind the barrier.

In this chapter, an "Edge-Plus-Images" model will be described that merges the propagation results of the preceding chapter with half-plane diffraction theory. The mathematical model is readily programmable on a digital computer, and thus practical, engineering calculations can be obtained with little trouble. Although the following discussion is in terms of a vertical barrier on a ground plane, the results are general and may be applied to any thin, planar protrusion from a flat, impedance-covered surface.

3.1 The Geometrical Theory of Diffraction

The use of Keller's Geometrical Theory of Diffraction (GTD) in solving practical problems has met with universal success, and it will serve here as the foundation in building the diffraction model for a barrier on a ground plane. The derivation of the GTD formulation will not be given here since this information is available in many texts as well as in Keller's original papers on the subject (see the references cited in Chapter 1). The predictions of the theory have been tested and confirmed many times in both the fields of electromagnetics and acoustics. Agreement with exact analytical solutions, when available, has been excellent; correlation with experiments, in the absence of mathematical solutions, has also been encouraging. Furthermore, although it is in principle a high-frequency method, the GTD often performs with a high degree of accuracy down to wavelengths comparable to the size of the scattering object.

Essentially, the GTD supplements the approach of classical geometrical acoustics by including "diffracted rays," which, as opposed to "specularly reflected rays," can penetrate into the "shadow zone." And just as the law of conservation of energy flux in a "bundle of rays" (Fermat's principle) leads to Snell's law for specular reflection (angle of incidence = angle of reflection), similar arguments applied to the diffracted rays lead to the "law of edge diffraction." With reference to Figure 3.1, Fermat's principle prescribes that the total path length for the edge-diffracted ray S-E-P should be a minimum (out of all possible paths connecting the

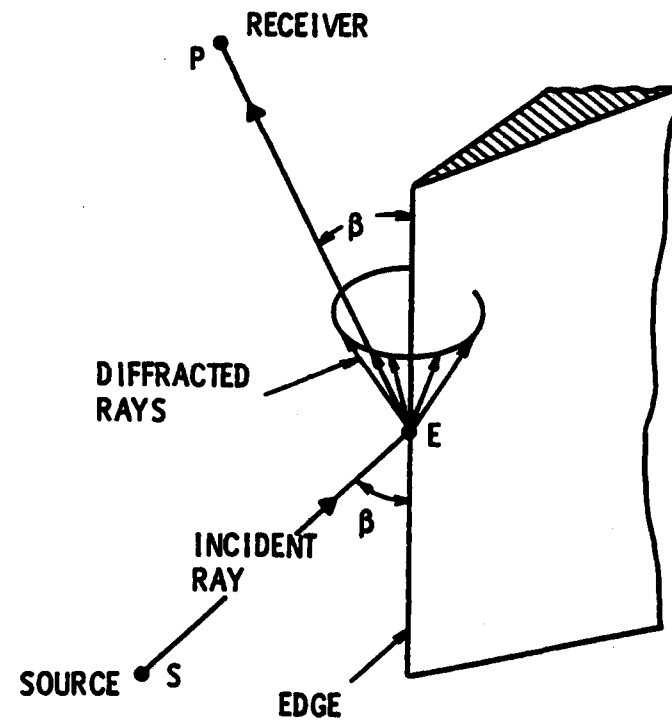


Figure 3.1 The Law of Edge Diffraction: Incident Ray and Diffracted Ray Subtend Equal Angles β with the Edge. Diffracted Rays form a Cone with Apex at Diffraction Point E.

points). Hence, the law of edge diffraction can be stated as: when an incident ray strikes an edge at an angle β , the set of diffracted rays will comprise all those rays that also make an angle β (in the "forward" direction) with the edge.²² The resulting "cone" of diffracted rays is illustrated in the figure. If the edge is straight (as it is in the present barrier problem), the point E will be unique, and only a single diffracted ray will reach the receiver.²³

Generally, the edge-diffracted field is described in the GTD formulation by several factors: (a) a reference field at some point along the ray, (b) a geometrical spreading factor depending on the radii of curvature of the edge and of the incident and diffracted ray bundles, and (c) a phase factor accounting for the propagation of energy over the entire length of the ray path. The reference field is usually given at the point E on the edge and is expressed in terms of a "diffraction coefficient," which describes the ratio of the diffracted energy to the incident energy. It can be shown that for a spherical wave incident upon a straight edge, the diffracted field at the receiver point P can be expressed in GTD terms as:

²² The notation " β " for this angle has been adopted here in order to be consistent with the customary usage in the literature. Hopefully, the context will prevent any confusion with the admittance " β ."

²³ If the edge were not straight as shown, but curved, the angle β would be measured from the line tangent to the edge at the point E. Thus, the possibility for several rays reaching the receiver from different points along the edge would exist.

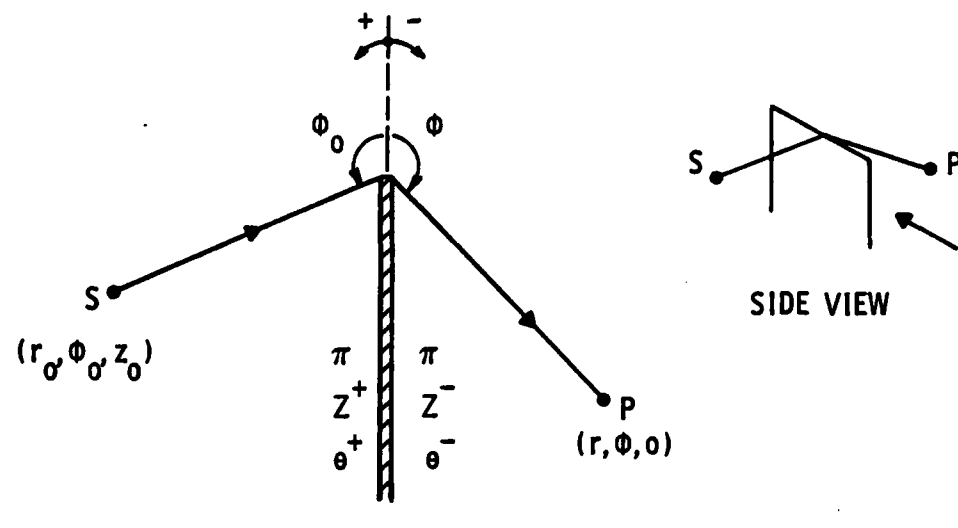
$$\Phi_{\text{diff}}(P) = \Phi_{\text{inc}}(E) D_e(\phi_o, \phi, \beta) \sqrt{\frac{R_1}{R_2(R_1 + R_2)}} e^{ikR_2}, \quad (3.1)$$

where the angles and distances are defined as in Figure 3.2. Here, $\Phi_{\text{inc}}(E)$ is the incident field at the point E on the edge. For a simple point source, therefore,

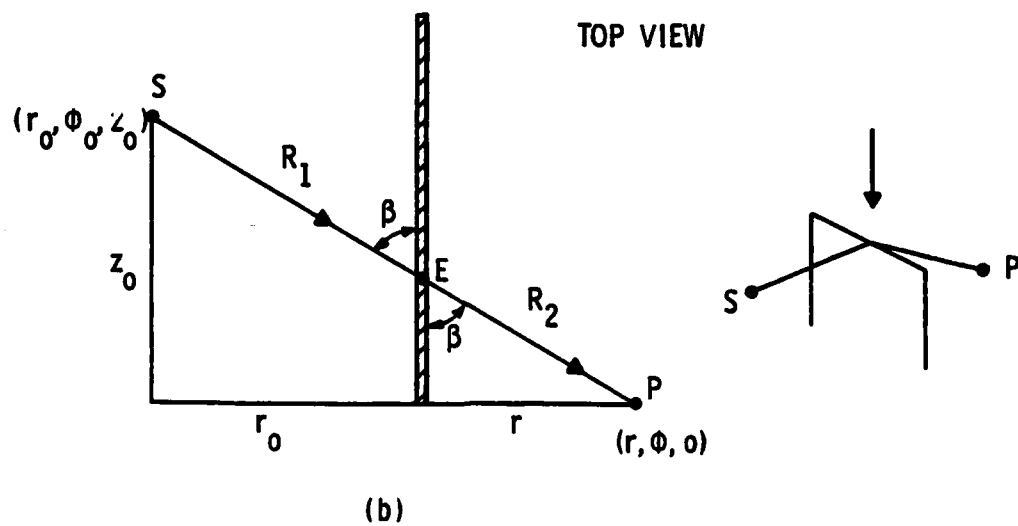
$$\Phi_{\text{inc}}(E) = \frac{e^{ikR_1}}{R_1}. \quad (3.2)$$

The factor D_e is the diffraction coefficient for a straight edge; the square root quantity is the geometrical spreading factor; and the last term accounts for the phase along the ray from the edge to the receiver.

Probably the strongest advantage of the GTD formulation is that all the relevant properties of the diffracting obstacle are contained in the diffraction coefficient itself. If a wedge were being considered instead of a straight edge, the diffracted field would have the same form as Equation (3.1) only the diffraction coefficient would be derived from wedge-diffraction theory. For objects with complex geometries, the diffraction coefficient would be taken from the canonical problem (half-plane, wedge, sphere, cylinder, etc.) that most closely describes the local shape of the object at the diffraction point.



(a)



(b)

Figure 3.2 Geometry of the Half-Plane Problem in Cylindrical Coordinates. (a) Side View Showing Diffraction Angles ϕ_0 and ϕ . (b) Top View Showing Oblique Angle β .

3.1.1 The GTD Solution for a Rigid Half-Plane

In Keller's original work on the Geometrical Theory of Diffraction applied to the rigid or pressure release half-plane problem, he deduced the diffraction coefficient from the first term in the expansion of Sommerfeld's exact solution. Thus,

$$D_e(\phi_0, \phi, \beta) = \frac{e^{-i\pi/4}}{2\sqrt{2\pi k} \sin\beta} \left[\frac{1}{\cos\left(\frac{\phi_0 + \phi}{2}\right)} \mp \frac{1}{\cos\left(\frac{\phi_0 - \phi}{2}\right)} \right] \quad (3.3)$$

-, rigid

+, pressure release

The diffraction coefficient has singularities at $\phi = -\pi + \phi_0$ and at $\phi = \pi - \phi_0$, which correspond to the physical shadow boundaries as shown in Figure 3.3. Furthermore, when $\sin\beta \rightarrow 0$, the solution becomes invalid. This latter condition corresponds to z_0 in Figure 3.3 being very large relative to r_0 and r .

Many researchers have modified the Sommerfeld coefficient or derived independent expressions in terms of Fresnel integrals, which remain valid in the transition regions of the shadow boundaries. The more exact diffraction coefficient for a rigid half-plane can be written (Hayek, in Varadan & Varadan, 1982) as

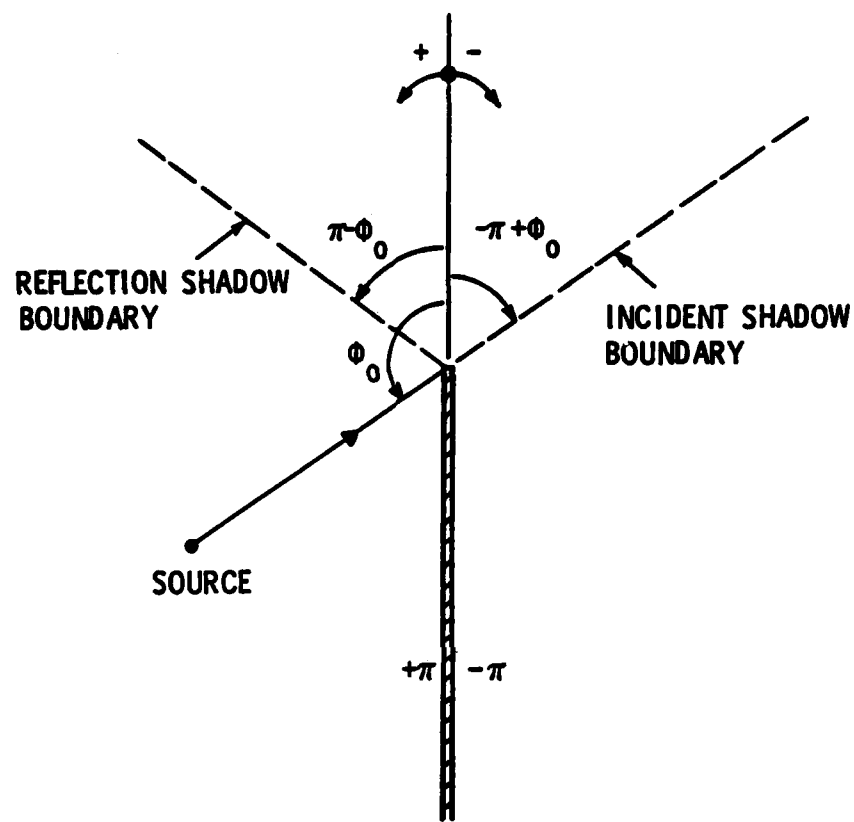


Figure 3.3 Angles Defining Incident and Reflection Shadow Boundaries.

$$\begin{aligned}
 D(\phi, \phi_0, \beta) = & \frac{\operatorname{sgn}(A) \sqrt{kL} e^{-iA^2}}{\sqrt{2k} 2 \sin\beta} [1 - \sqrt{2} e^{-i\pi/4} F^*(|A|)] \\
 & + \frac{\operatorname{sgn}(B) \sqrt{kL} e^{-iB^2}}{\sqrt{2k} 2 \sin\beta} [1 - \sqrt{2} e^{-i\pi/4} F^*(|B|)] ,
 \end{aligned} \tag{3.4}$$

where $\operatorname{sgn}(x)$ means the sign of the argument x , and

$$\begin{aligned}
 A &= \sqrt{kL} \cos \left(\frac{\phi + \phi_0}{2} \right) , \\
 B &= \sqrt{kL} \cos \left(\frac{\phi - \phi_0}{2} \right) , \\
 L &= \frac{2R_1 R_2}{R_1 + R_2} \sin^2 \beta ,
 \end{aligned} \tag{3.5}$$

and $F^*(x) = C(x) + i S(x)$,

$$\text{where } C(x) = \sqrt{\frac{2}{\pi}} \int_0^x \cos t^2 dt , \quad S(x) = \sqrt{\frac{2}{\pi}} \int_0^x \sin t^2 dt$$

are the Fresnel cosine and sine integrals, respectively.

3.1.2 The GTD Solution for an Impedance Covered Half-Plane

Recently, an exact integral solution has been derived (Kendig, 1977) for the diffraction by a half-plane with locally-reacting impedance surfaces. The advantage of this solution over a similar contribution by Malyuzhinets (1955, 1962) is that Kendig's exact

integrand is in closed form, thus allowing asymptotic techniques to be applied to the integral for its evaluation. The resulting solution has been adapted to the GTD formulation (Hayek, et al., 1978) and the diffraction coefficient can be written:

$$D_e(\phi, \phi_0, \beta) = \frac{\text{sgn } (A) \Phi_1(\phi) \sqrt{kL} e^{-ikA}}{\sin \beta} [1 - \sqrt{2} e^{-i\pi/4} F^*(|A|)] \\ - \frac{\text{sgn } (B) \Phi_2(\phi) \sqrt{kL} e^{-ikB}}{\sin \beta} [1 - \sqrt{2} e^{-i\pi/4} F^*(|B|)] \quad (3.6)$$

in which the parameters are defined by Equation (3.5). In addition, the special functions Φ_1 and Φ_2 contain the impedance information and can be expressed as

$$\Phi_{1,2} = \frac{1}{4} \left[(\Gamma_1 + \Gamma_2) \sin \frac{\phi \pm \phi_0}{2} \pm (\Gamma_1 - \Gamma_2) \right], \quad (3.7)$$

in which

$$\Gamma_{1,2} = \frac{[\sin\theta \mp \sin\theta^{\pm}]}{\left[\sin\theta^{\pm} + 2 \cos \frac{\phi}{2} \cos \frac{\phi_0}{2}\right]} \cdot \frac{\left\{ \sin\theta^{\mp} + 2 \cos \frac{\phi}{2} \left[\cos \left(\frac{\phi + \phi_0 \mp \pi}{4} \right) \pm \sin \left(\frac{\phi - \phi_0 \mp \pi}{4} \right) \right] \right\}}{\left\{ \sin\theta^{\pm} + 2 \cos \frac{\phi}{2} \left| \cos \left(\frac{\phi + \phi_0 \mp \pi}{4} \right) \pm \sin \left(\frac{\phi - \phi_0 \mp \pi}{4} \right) \right| \right\}} \quad (3.8)$$

The impedance of the half-plane surfaces has been expressed in terms of the so-called "Brewster" angles θ^+ , for the face at $\phi = +\pi$, and θ^- , for the face at $\phi = -\pi$, where

$$\sin\theta^{\pm} = \frac{\rho c}{Z^{\pm} \sin\beta} \quad (3.9)$$

Because the field at the receiver is affected more by the impedance on the insonified (source-facing) surface of the half-plane than by that on the "dark" surface, an expression for the case when $\theta^- = 0$ (rigid) and θ^+ arbitrary might be useful for practical cases. Thus, for the impedance-rigid half-plane, the special functions become:

$$\phi'_{1,2} = \pm \frac{1}{2} \left[\Gamma'_1 \sin^2 \left(\frac{\phi \mp \pi \mp \phi_0}{4} \right) - \Gamma'_2 \cos^2 \left(\frac{\phi \mp \pi \mp \phi_0}{4} \right) \right], \quad (3.10)$$

where

$$\Gamma_1' = \frac{(\sin\phi - \sin\theta^+) \cos\phi/4}{\left[\sin\theta^+ + 4 \cos \frac{\phi}{2} \cos \frac{\phi}{4} \cos \left(\frac{\phi_0 + \pi}{4}\right)\right] \sin \frac{\phi_0 + \pi}{4}}, \quad (3.11)$$

and

$$\Gamma_2' = \frac{\left[\sin\theta^+ + 4 \cos \frac{\phi}{2} \cos \frac{\phi}{4} \cos \left(\phi_0 - \frac{\pi}{4}\right)\right] \sin \frac{\phi}{4}}{\left[\sin\theta^+ + 2 \cos \frac{\phi}{2} \cos \frac{\phi_0}{2}\right] \sin \frac{\phi_0 + \pi}{4}} \quad (3.12)$$

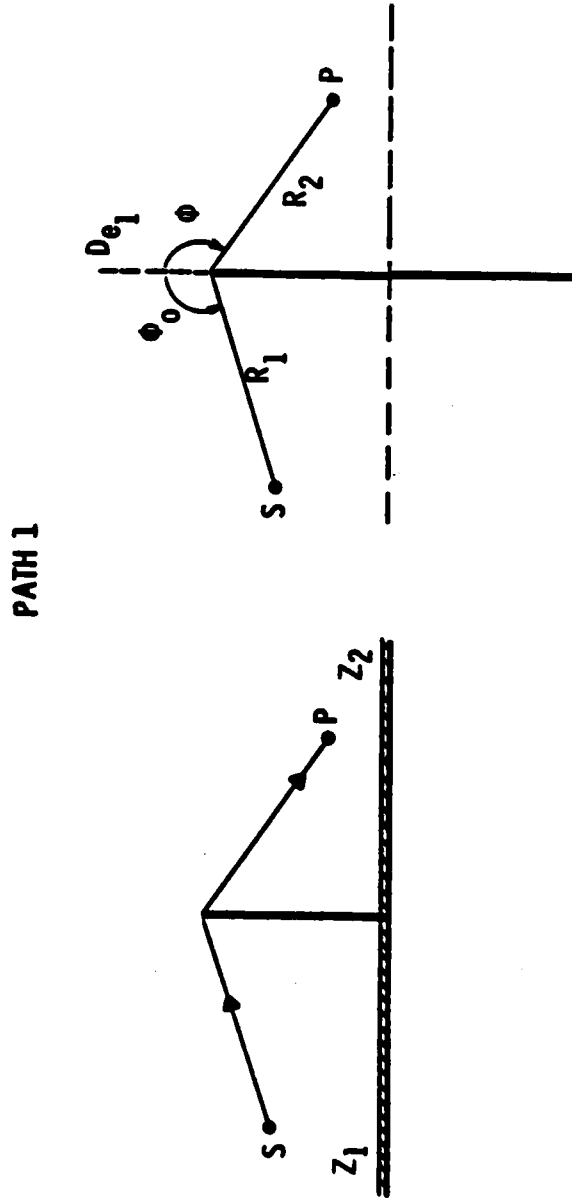
3.2 The GTD Model for the Barrier on a Ground Plane

Having defined the edge-diffraction coefficients to be employed in the Geometrical Theory of Diffraction formulation, it is now a simple matter of incorporating the ground effects into the model. Just as the diffraction effects were lumped into the coefficient $D(\phi_0, \phi, \beta)$ in Equation (3.1), the incident field at the barrier edge is totally contained in the term $\Phi_{inc}(E)$. When a locally-reacting ground plane is present beneath the source, $\Phi_{inc}(E)$ is no longer a simple monopole field but instead represents the total field that exists at the edge point E. This field is derived from the ground propagation solution described in Chapter 2 and will be modelled as a superposition of two ray paths--the direct path and the ground-reflected "image" path. Similarly, the energy spreading from the point E on the edge to the receiver does so via direct and ground-reflected paths. The ground reflections are handled by simple geometrical acoustics; however, the "spherical wave reflection coefficient" is used.

The construction of the "Edge-Plus-Images" model can best be explained with the help of illustrations. Figure 3.4 shows schematically how the propagation from source to receiver can be modelled as a superposition of four distinct half-plane diffracted ray paths. In Figure 3.4 (a), the "direct" ray from source--to edge--to receiver does not interact with the ground and so is represented by the standard GTD half-plane equation. The diffraction coefficient can be either that from Equation (3.6) for an impedance-covered barrier or that from Equation (3.4) for a rigid barrier. In the equations in Figure 3.4, the geometrical spreading factor $A(R_a, R_b)$ is simply (see Equation [3.1])

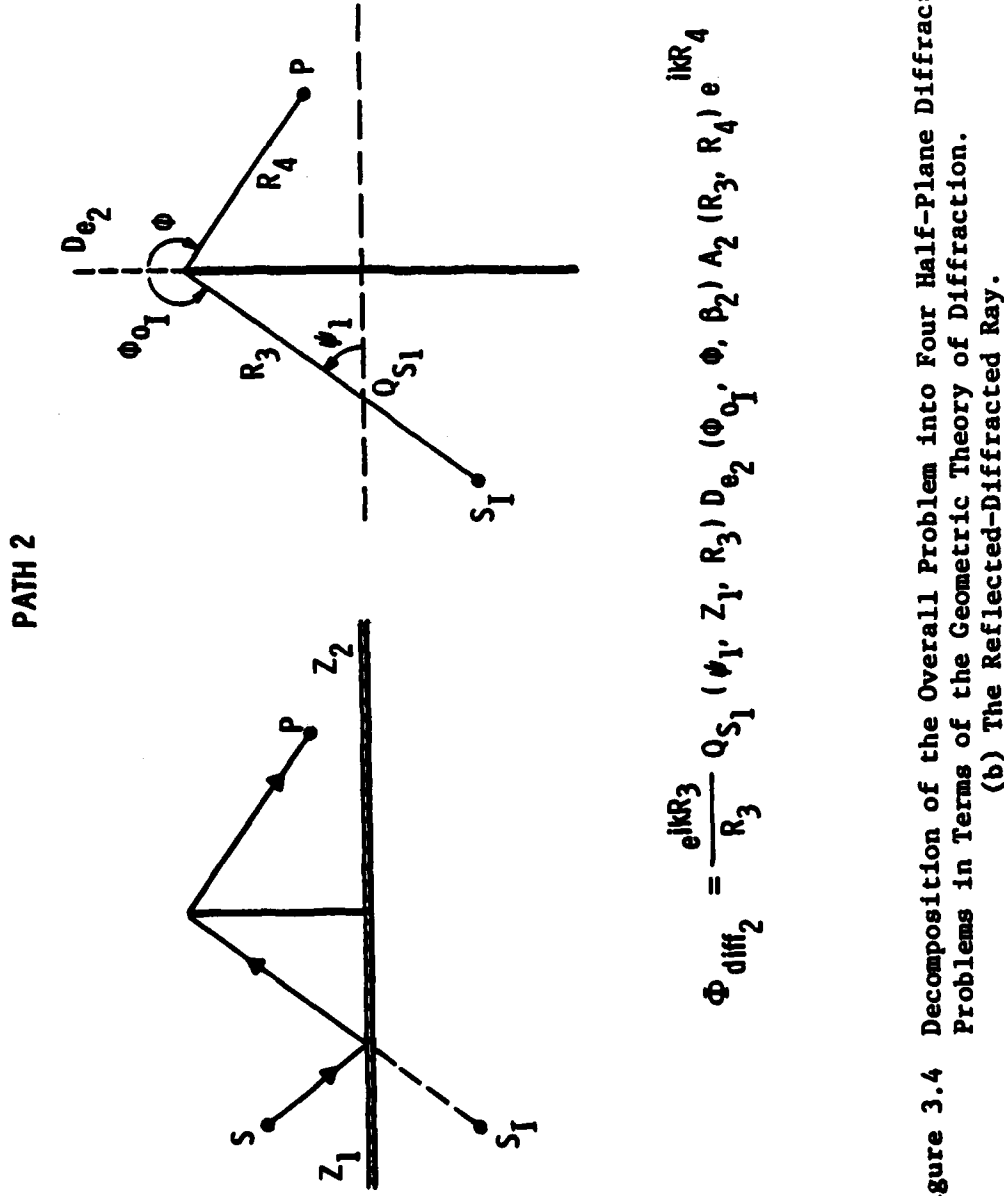
$$A(R_a, R_b) = \sqrt{\frac{R_a}{R_a(R_a + R_b)}} . \quad (3.13)$$

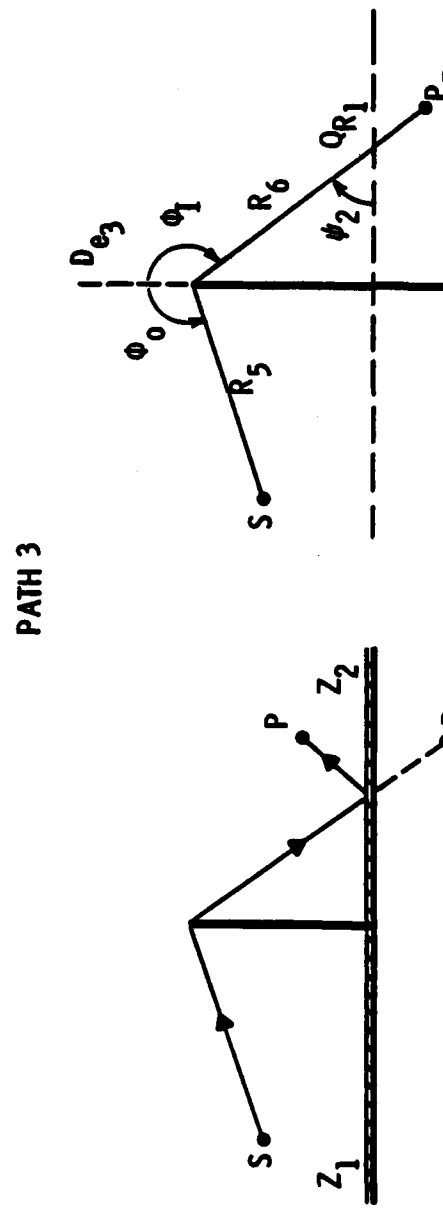
In Figure 3.4 (b), the source-ground-edge-receiver ray is still modelled as a half-plane diffraction problem, but the incident ray is assumed to originate from the source "image" in the ground S_1 and is correspondingly modified by the spherical wave reflection coefficient $Q_{S_1}(\psi_1, Z_1, R_3)$. In the most general sense, this reflection coefficient is as given by Equation (2.140), but in almost all practical situations, the first term in the expansion provides sufficient accuracy. Therefore, the model has been implemented here using F_1 , as defined by Equations (2.149) and (2.150), for the ground reflections. As indicated, the factor Q_{S_1} depends on the reflection angle ψ_1 , the ground impedance on the source side Z_1 , and the image-to-edge distance



$$\Phi_{\text{diff}_1} = \frac{e^{ikR_1}}{R_1} D_{e_1}(\phi_0, \phi, \beta_1) A_1(R_1, R_2) e^{ikR_2}$$

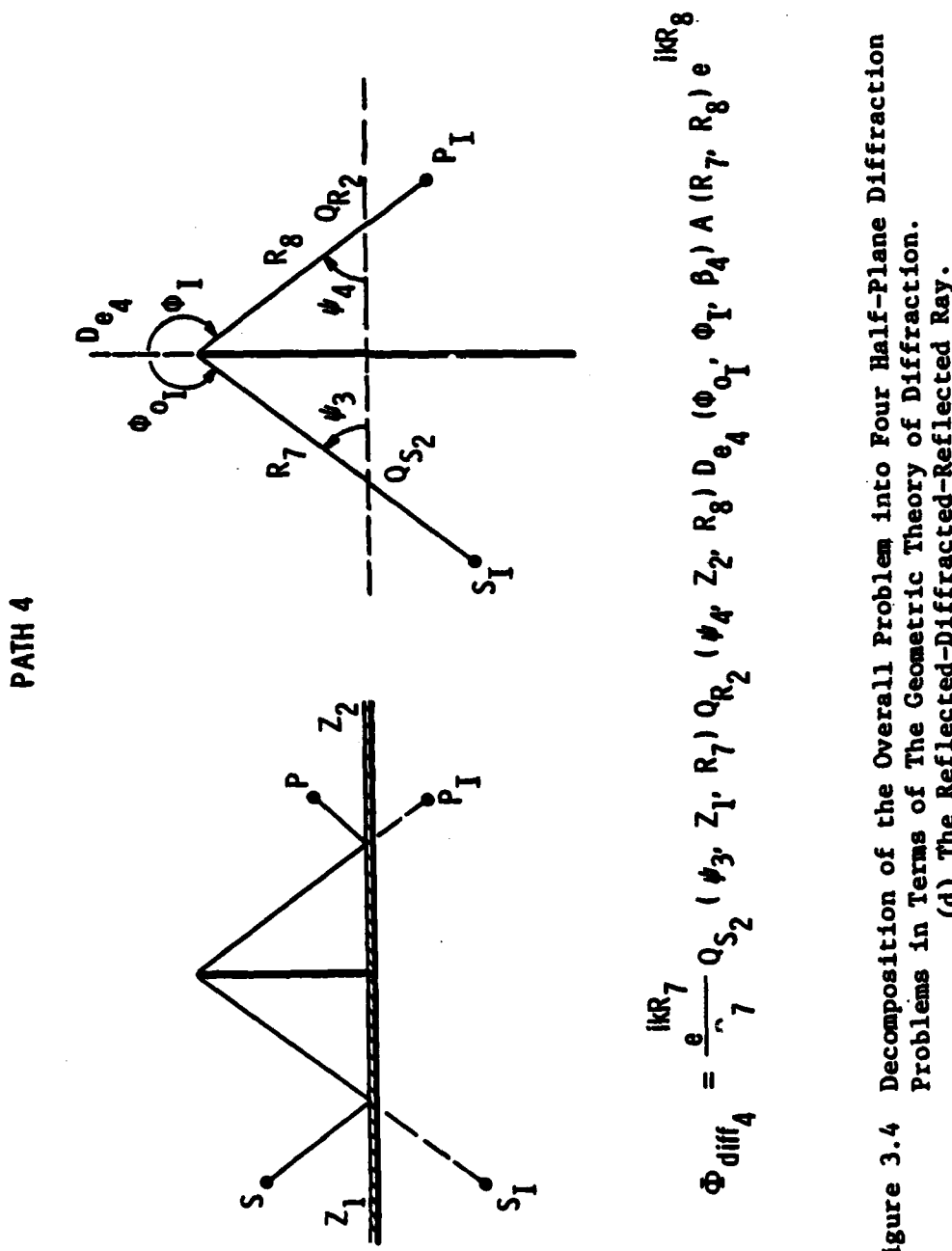
Figure 3.4 Decomposition of Overall Problem into Four Half-Plane Diffraction Problems in Terms of the Geometric Theory of Diffraction.
 (a) The Direct Diffracted Ray





$$\Phi_{\text{diff}_3} = \frac{iR_5}{R_5} q_{R_1} (\psi_2, R_6) D_{e_3} (\phi_0, \phi_1, \beta_3) A_3 (R_5, R_6) e^{\frac{iR_6}{R_5}}$$

Figure 3.4 Decomposition of the Overall Diffraction Problem into Four Half-Plane Problems in Terms of The Geometric Theory of Diffraction.
(c) The Diffracted-Direct Ray.



R_3 . It is interesting to note that the edge-to-receiver distance R_4 for this path differs, in general, from the analogous distance R_2 for path 1. This is a consequence of the law of edge diffraction. Since the incident ray is coming from the source image and not the source itself, it makes a different angle with the edge and defines a different "point E" along the edge. Therefore, the exit ray to the receiver (making an equal angle with the edge) must correspondingly change in length. The diffraction coefficients reflect this fact also, and thus the notation for the D_e 's has subscripts on the angle β .

Similar reasoning applies to path 3, the source-edge-ground-receiver ray, where $Q_{R_1}(\psi_2, z_2, R_6)$ depends on the properties of the ground on the receiver side of the barrier. To model the final source-ground-edge-ground-receiver path, two reflection coefficients Q_{S_2} and Q_{R_2} are required, as indicated. Note that since a different angle β is again defined by this ray path, the ground reflection angles ψ_3 and ψ_4 are generally not equal to ψ_1 and ψ_2 , respectively. The total diffracted field at the receiver is

$$\Phi_{\text{diff tot}} = \Phi_{\text{diff}_1} + \Phi_{\text{diff}_2} + \Phi_{\text{diff}_3} + \Phi_{\text{diff}_4} . \quad (3.14)$$

If the receiver were located outside of the acoustic shadow cast by the barrier--note: each ray path shown in Figure 3.4 defines its own shadow boundaries--then the appropriate non-diffracted geometrical fields must be added to the above solution to obtain the total field at the receiver. That is, with reference to Figure 3.3,

$$\begin{aligned}\Phi_{\text{tot}} &= \Phi_{\text{diff}}_{\text{tot}} & -\pi \leq \phi \leq -\pi + \phi_0 \\ \Phi_{\text{tot}} &= \Phi_{\text{inc}} + \Phi_{\text{diff}}_{\text{tot}} & -\pi + \phi_0 \leq \phi \leq \pi - \phi_0 \\ \Phi_{\text{tot}} &= \Phi_{\text{inc}} + \Phi_{\text{ref}} + \Phi_{\text{diff}}_{\text{tot}} & \pi - \phi_0 \leq \phi \leq \pi\end{aligned}\quad (3.15)$$

where Φ_{inc} is the direct field from source to receiver, and Φ_{ref} is the barrier-reflected field.

Several limiting cases, which simplify the model equations in Figure 3.4, may be of practical interest. Thus,

- (a) When the source ground is rigid, $Q_{S_1} = Q_{S_2} = 1.0$
- (b) When the receiver ground is rigid, $Q_{R_1} = Q_{R_2} = 1.0$
- (c) When the source is on the ground, $Q_{S_1} = Q_{S_2}$;
 $R_1 = R_3 = R_7$; $R_2 = R_4$; $R_6 = R_8$;
 $\phi_0 = \phi_{0_1}$; $\beta_1 = \beta_2$ and $\beta_3 = \beta_4$; $Q_{S_1} = Q_{S_2}$;
 $A_1 = A_2$ and $A_3 = A_4$; therefore, $D_{e_1} = D_{e_2}$
and $D_{e_3} = D_{e_4}$.
- (d) When the receiver is on the ground, $Q_{R_1} = Q_{R_2}$;
 $R_2 = R_6 = R_8$; $R_1 = R_5$ and $R_3 = R_7$;
 $\phi = \phi_I$; $\beta_1 = \beta_3$ and $\beta_2 = \beta_4$;
 $A_1 = A_3$ and $A_2 = A_4$; therefore, $D_{e_1} = D_{e_3}$
and $D_{e_2} = D_{e_4}$.

(e) When the source and receiver are both on the ground,

$$\Phi_{\text{diff}}_2 = Q_S \Phi_{\text{diff}}_1 \quad \Phi_{\text{diff}}_3 = Q_R \Phi_{\text{diff}}_1$$

$$\text{and } \Phi_{\text{diff}}_4 = Q_S Q_R \Phi_{\text{diff}}_1 .$$

(f) When the source and receiver are both on a rigid ground,

$$\Phi_{\text{diff}}_{\text{tot}} = 4\Phi_{\text{diff}}_1 .$$

CHAPTER IV

NUMERICAL RESULTS

The mathematical solution for the spherical wave propagation problem, as well as the model developed for barrier diffraction, are functions of several geometrical and physical parameters. To determine how the sound field at the receiver predicted by the spherical wave theory differs from that predicted from the classical plane wave theory, numerical results for several representative source-receiver geometries will be presented in this chapter. For propagation in the absence of a barrier, the dependence on the parameter kR , the reflection angle ψ , and the ground impedance Z_N , will be investigated. When a diffracting barrier is present, the dependence of the field on barrier height and diffraction angle will also be studied.

In practice, it may be important to know when a problem demands the use of the more exact spherical wave theory, since the gain in accuracy could be significant. Conversely, the plane wave solution is extremely simple, and its accuracy may be sufficient enough to make its use economically advisable. This is particularly true for problems in which a continuous, physically-extended source of sound is being modelled as a sequence of point sources (such as the flow of highway traffic), and for which the field calculations, therefore, must be performed many times.

4.1 Numerical Results for the Ground Propagation Problem

This section presents graphical data predicted from the ground propagation theories given in Chapter 2. The ground plane is assumed to be locally-reacting with its impedance specified by real and imaginary parts (since the time convention $e^{-i\omega t}$ has been adopted here, a positive imaginary part X of the impedance $Z_N = R + iX$ corresponds to a "springlike" reactance). Data from the spherical wave theory derived in this study is presented in two forms, representing two levels of complexity. First, the full asymptotic series solution is used as the most accurate description of the field; second, only the first term in this series is employed, as an approximation. Preliminary tests have shown that both of these forms are so close to the exact solution for many practical impedance and geometrical conditions that graphs of the data would essentially show one curve. For this reason, the values of the parameters chosen for many of the following plots are deliberately "atypical" so that differences in the data may be seen and studied.

4.1.1 Dependence on the Parameter kR_2

As noted in the derivation in Chapter 2, the asymptotic series solution for the point-to-point ground propagation problem approaches the exact (integral) solution as the parameter kR_2 increases in value. For $kR_2 \gg 1$ the series--in Equation (2.130), for instance--is extremely convergent and accurate in the first few terms, well below

the point where the terms begin to diverge. As kR_2 gets smaller, more terms are necessary for accuracy, yet, correspondingly, the onset of divergence occurs sooner. Finally, when kR_2 is very small, divergence is immediate, and increasing the number of terms only degrades the accuracy of the solution.

For very large kR_2 , the curvature of the wavefronts becomes locally "plane" in the vicinity of the ground reflection point, and the asymptotic solution should approach the desired plane wave solution. That this is indeed the case is confirmed by the numerical data.

The graphs in this section, as well as most of the others in this chapter, compare four descriptions of the sound field at the receiver. The numerical data were calculated on a digital computer (IBM Model 3033 Processor) from (i) a fine-point numerical integration²⁴ of the exact integral expression in Equations (2.93) and (2.101), (ii) an "optimal" number of terms in the formal asymptotic series solution given by Equation (2.128), (iii) the first term in the latter series as represented by Equations (2.149) - (2.151), and (iv) the plane-wave reflection coefficient form of the solution, Equations (2.4) and (2.5). For calculations using the asymptotic series, a truncation of the series was made at the point where the terms just begin to diverge--although always including a minimum of two or a maximum of fifteen terms. The solution using only the first term in the series

²⁴ The numerical integration was performed using a standard five-point Newton-Cotes quadrature technique taking a finer and finer mesh of points until the desired degree of convergence was obtained.

is referred to as the "F-term solution" in the following discussion.

To facilitate comparisons of the data within each graph, the curves in this chapter have been drawn as straight line segments joining discrete, calculated points. Strictly speaking, then, the values on a line segment between two calculated points do not represent valid data, and the apparent "jaggedness" of the curves in some regions is not indicative of the true shape of the data. The number of calculated data points may vary from one plot to the next, but they are always equally-spaced along the axis, and their actual locations can usually be deduced, if necessary.

The data for the case where both the source height (Sht) and the receiver height (Rht) are 1.0 feet above the impedance plane, and where the separation (Sep) is 38 feet (corresponding to a reflection angle of $\psi=3^{\circ}$), are plotted in Figure 4.1 (a) and (b). The normalized ground impedance has been assigned the relatively low value $Z_N = (0.3, 0.5)$. The vertical axis for Figure 4.1 (a) is in terms of the attenuation, defined as

$$\text{Attenuation} = -20 \log_{10} \left| \frac{\phi_{\text{tot}}}{\phi_{\text{dir}}} \right| \quad \text{dB ,} \quad (4.1)$$

where ϕ_{tot} is the total (direct plus reflected) field at the receiver, and ϕ_{dir} is the direct field only (e^{ikR_1/R_1}). The latter is the "free" field that would have existed at the receiver in the absence of the ground. The same quantity defined by Equation (4.1) is sometimes referred to as the "excess attenuation relative to spherical

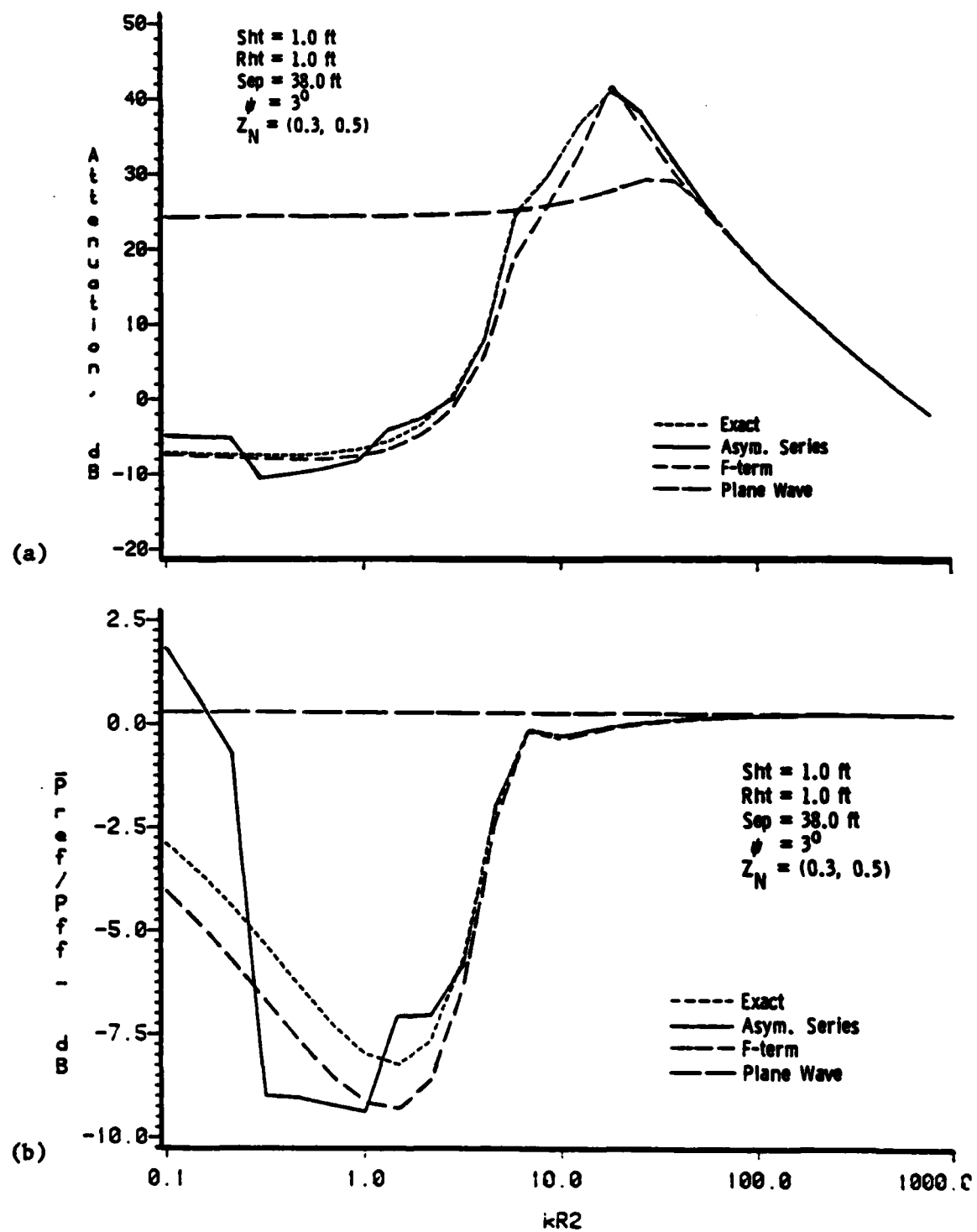


Figure 4.1 Calculated Data for (a) Attenuation, and (b) Reflected/Direct Ratio as a Function of kR_2 . Exact, Asymptotic Series, F-term, and Plane Wave Solutions. Small Reflection Angle, Low Impedance.

spreading." Finally, it should be noted that a negative value of attenuation means that the received field has been enhanced relative to free field level.

Figure 4.1 (b) presents the same data in terms of the magnitude of the ratio of reflected to direct energy. In practice, this form of presentation may be more useful for pulsed or transient experiments in which the direct and reflected waves can be measured separately. For reference, the reflected term Φ_{ref} for each curve is given as follows (with quantities defined in Chapter 2):

1) Exact Integral:

$$\Phi_{ref_1} = \frac{e^{ikR_2}}{R_2} - \frac{4ik\beta Be^{ikR_2}}{(\beta + \sin\psi)} \int_0^{\infty} \frac{e^{-ikR_2[t^2+2Bt]}}{\sqrt{1 - \frac{t^2}{F} - \frac{2Bt}{F}}} dt . \quad (4.2)$$

2) Asymptotic Series:

$$\Phi_{ref_2} = \frac{e^{ikR_2}}{R_2} - \frac{4ik\beta Be^{ikR_2}}{(\beta + \sin\psi)} \sum_{n=0}^{\infty} T_n [e_0 E_n + K_n] . \quad (4.3)$$

3) First Term Only:

$$\Phi_{ref_3} = \frac{e^{ikR_2}}{R_2} [R_p + (1 - R_p) F_1] \quad (4.4)$$

$$F_1 = 1 + i\sqrt{\pi} \lambda e^{-\lambda^2} \operatorname{erfc}(-i\lambda)$$

$$4) \text{Plane Wave: } \Phi_{ref_4} = R_p \frac{e^{ikR_2}}{R_2} ; \quad R_p = \frac{(\sin\psi - \beta)}{(\sin\psi + \beta)} \quad (4.5)$$

As expected, and as is readily apparent from either Figure 4.1 (a) or (b), the plane wave solution (long-dashed line) is not very accurate for this near-grazing incidence geometry. On the other hand,

the asymptotic series solution (solid line) agrees well with the exact integral (short-dashed line) for $kR_2 \geq 3$, a surprisingly low value for kR_2 . Below this value, the series is divergent, and the predictions become erratic. The medium-dashed line shows that using only the first term in the full solution--the F-term solution--gives very good agreement, differing by a few dB for medium values of kR_2 . It is remarkable, though, that the F-term solution yields very good predictions down to $kR_2 = 0.1$, corresponding, for the distances considered here, to a frequency of 0.03 Hz.

All four solutions eventually agree when kR_2 is sufficiently large. Physical intuition predicts this--the wavefronts "look" like plane waves--but it can also be deduced from the governing equations. For example, with reference to Equation (4.4), as kR_2 gets large, λ also gets large, and F_1 can be shown to have the asymptotic expansion (see, in part, Abramowitz & Stegun, 1964, section 7.1.23):

$$F_1 \sim 2i\sqrt{\pi} \lambda e^{-\lambda^2} H[-\text{Im}(\lambda)] - \frac{1}{2\lambda^2} - \frac{1 \cdot 3}{4\lambda^4} - \frac{1 \cdot 3 \cdot 5}{8\lambda^6} - \dots \quad (4.6)$$

where the Heaviside operator

$$H[z] = \begin{cases} 1 ; & \text{Im}(z) > 0 \\ 0 ; & \text{Otherwise} \end{cases} \quad (4.7)$$

is necessary to account for the fact that $\text{erfc}(-z) = 2 - \text{erfc}(z)$.

Thus, F_1 becomes negligible as kR_2 gets large, and Equation (4.4) reverts to the plane wave solution.

The attenuation plotted in Figure 4.2 (a) and the ratio of the fields in Figure 4.2 (b) are for the same source-receiver geometry as in the previous case, but for a higher ground impedance, $Z_N = (2.0, 3.0)$. Two observations can immediately be made when Figure 4.1 and Figure 4.2 are compared. First, the exact, the full asymptotic series, and the first-term-only solutions are in very close agreement, even for values of kR_2 down to 0.1. In fact, for $kR_2 \geq 4$, the predictions are essentially identical. Second, the "overall" level of attenuation is lower for the higher impedance ground. This trend is also not surprising, and in the limit of a rigid ground, both the classical theory and the present spherical wave theory predict a "gain" of -6 dB.

Some further, less obvious, conclusions can be drawn from the results of Figures 4.1 and 4.2. The peak of maximum attenuation (centered at about $kR_2=20$ for $Z_N=[0.3,0.5]$ and at about $kR_2=150$ for $Z_N=[2.0,3.0]$) is not a result of propagation path length interference, but rather is strictly an "impedance effect." For a fixed geometry, this maximum will move to higher and higher frequencies as the impedance increases and will eventually disappear or "merge" with the first true path length interference peak in the limit when the ground becomes rigid.

Figure 4.3 illustrates the numerical results for the case where source and receiver are both directly on the ground ($\psi = 0^\circ$) and separated by 57 feet. The impedance is the same as in Figure 4.1, $Z_N = (0.3, 0.5)$. The plane wave curve is not shown here, since the

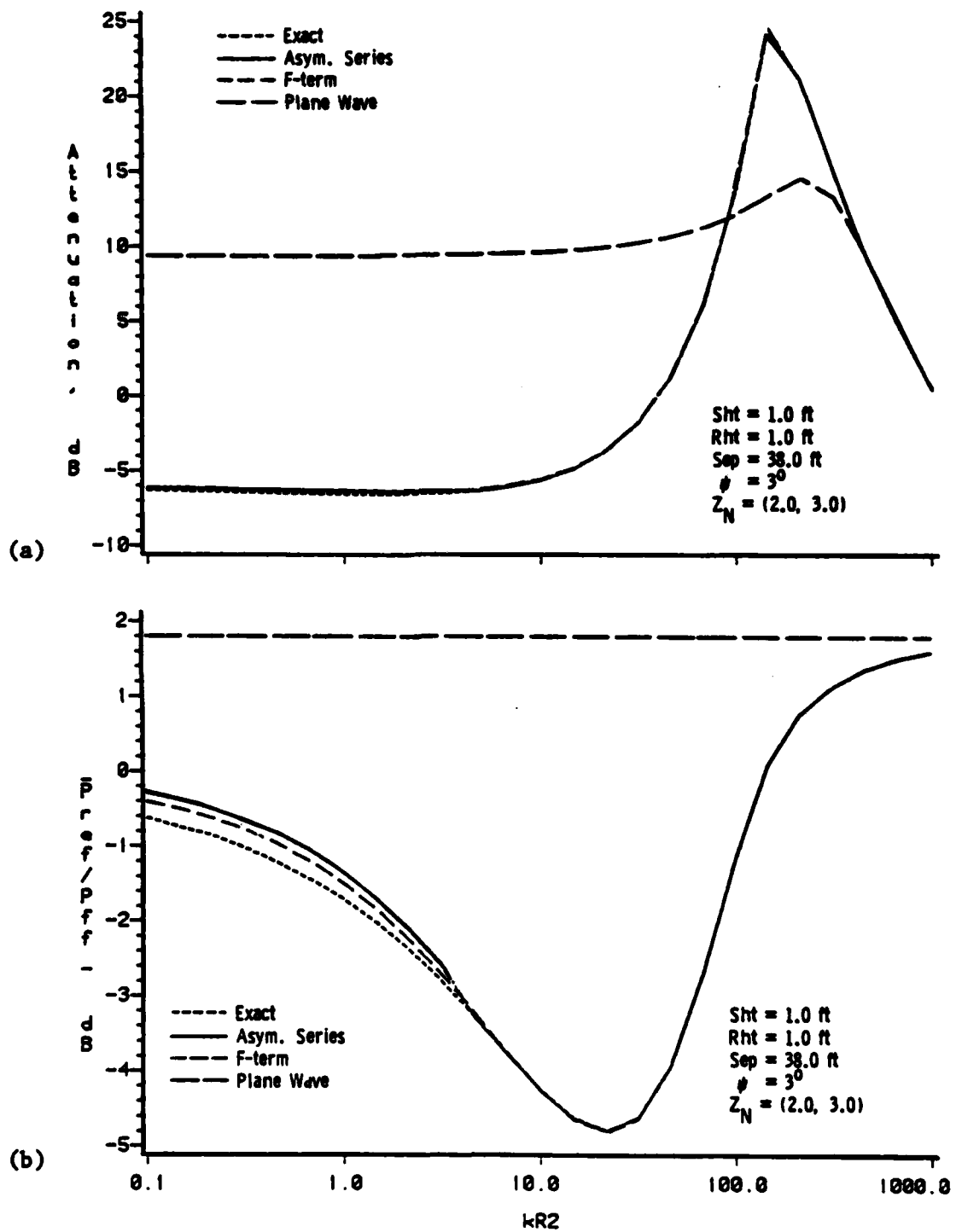


Figure 4.2 Calculated Data for (a) Attenuation, and (b) Reflected/Direct Ratio as a Function of kR_2 . Exact, Asymptotic Series, F-term, and Plane Wave Solutions. Small Reflection Angle, Moderately High Impedance.

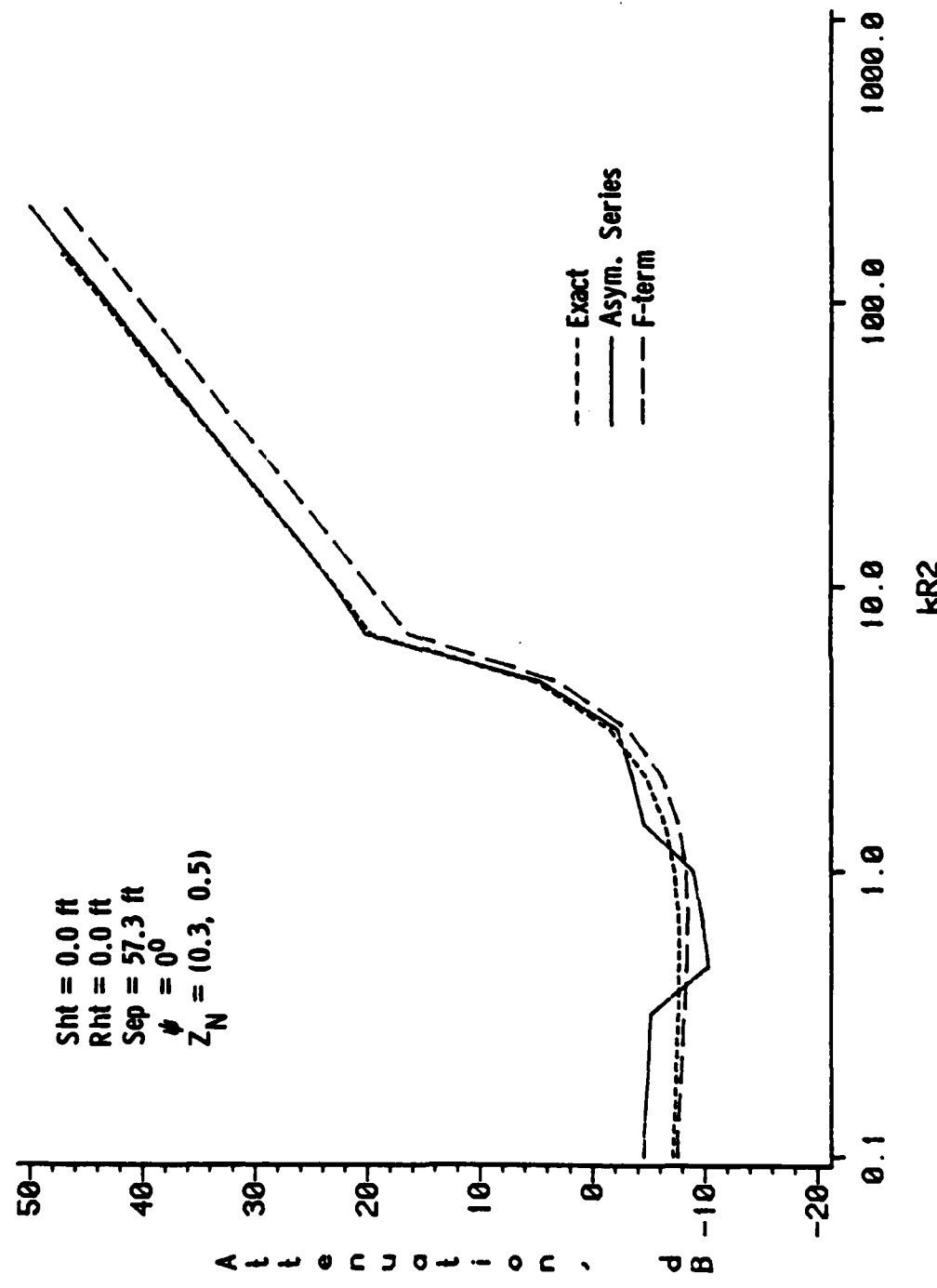


Figure 4.3 Calculated Data for Attenuation as a Function of kR^2 : Exact, Asymptotic Series, and F-term Solutions. Grazing Incidence ($\psi=0$), Low Impedance.

predicted attenuation would be infinite for all values of kR_2 ($R_p = -1$, $R_1=R_2$). The asymptotic solution again gives extreme accuracy for $kR_2 \geq 4$, while the F-term solution differs by only a few dB over most of the range.

An interesting fact can be observed in either Figure 4.1 (a) or in Figure 4.3. That is, for very low kR_2 , the exact solution (as well as the F-term solution) predicts a gain of the order -7 dB. Thus, the field at the receiver is actually higher than that which would exist if the ground were perfectly reflective. This is again a direct effect of the finite ground impedance and has been referred to in various ways in the literature, among them the "surface wave effect," a "ducting of energy," a "focalization" phenomenon, and a "surface layer effect." Whatever the terminology, this phenomenon--the gain could be higher than 7 db--is a testament to the fact that the reflected wave is not spherically symmetric, but that instead energy is "re-radiated" along the entire boundary. This re-radiation is with different phases from different points along the surface and could result in constructive interference at certain field points.

Some conclusions about the effect of increasing the reflection angle can be drawn from the next pair of plots in Figure 4.4 (a) and (b). Here, the source and receiver have been raised to five feet above the ground ($\psi=10^\circ$), and the impedance is $Z_N=(0.3, 0.5)$ in the former and $Z_N=(2.0, 3.0)$ in the latter. The counterpart cases are those in Figures 4.1 (a) and 4.2 (a). Comparing Figure 4.1 (a) to Figure 4.4 (a) and Figure 4.2 (a) to Figure 4.4 (b) shows that the

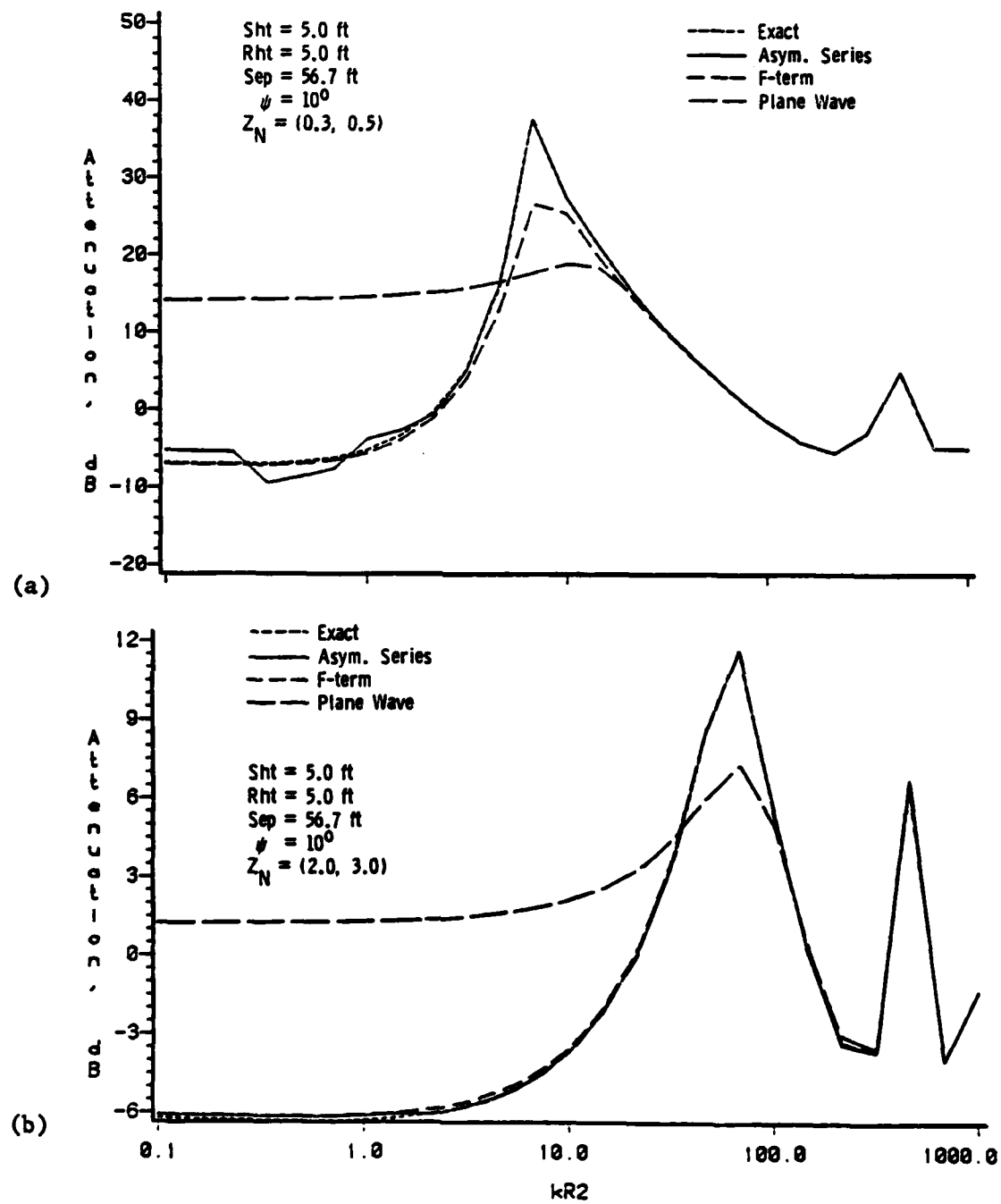


Figure 4.4 Calculated D_a for Attenuation as a Function of kR_2 .
Exact, Asymptotic Series, F-term, and Plane Wave
Solutions. Moderate Reflection Angle. (a) Low Impedance.
(b) Moderately High Impedance.

peak of maximum attenuation shifts to lower values of kR_2 as ψ increases. Inherent in this trend is the fact that the range of kR_2 for which the plane wave solution becomes valid begins at a lower value when the source and receiver are situated at a higher elevation above the ground. Furthermore, for each impedance case, the overall attenuation decreases as ψ gets larger, due to the fact that the ground appears "harder" at larger reflection angles. It might be interesting to note that the second peak in both Figure 4.4 (a) and (b) (at $kR_2 \approx 500$) is, in fact, due to path length differences and hence does not shift significantly as ψ goes from 3° to 10° ($R_1 = R_2$). Conversely, the impedance peak shifts by more than an order of magnitude.

To complete this section, numerical results for a case of a very large angle of reflection and a very low impedance are presented in Figure 4.5 (a) and (b). The source height is 10 feet; the receiver height is 20 feet; the separation is 30 feet ($\psi=45^\circ$); and the ground impedance is $Z_N=(0.4, 0.3)$. Here, the impedance-effect attenuation peak has shifted to a very low value of kR_2 , and path length interference prevails for $kR_2 > 10$. The plane wave solution yields predictions as accurate as the F-term predictions for all kR_2 greater than about 5.

Table 4.1 summarizes the geometry and impedance conditions for the cases plotted in this section.

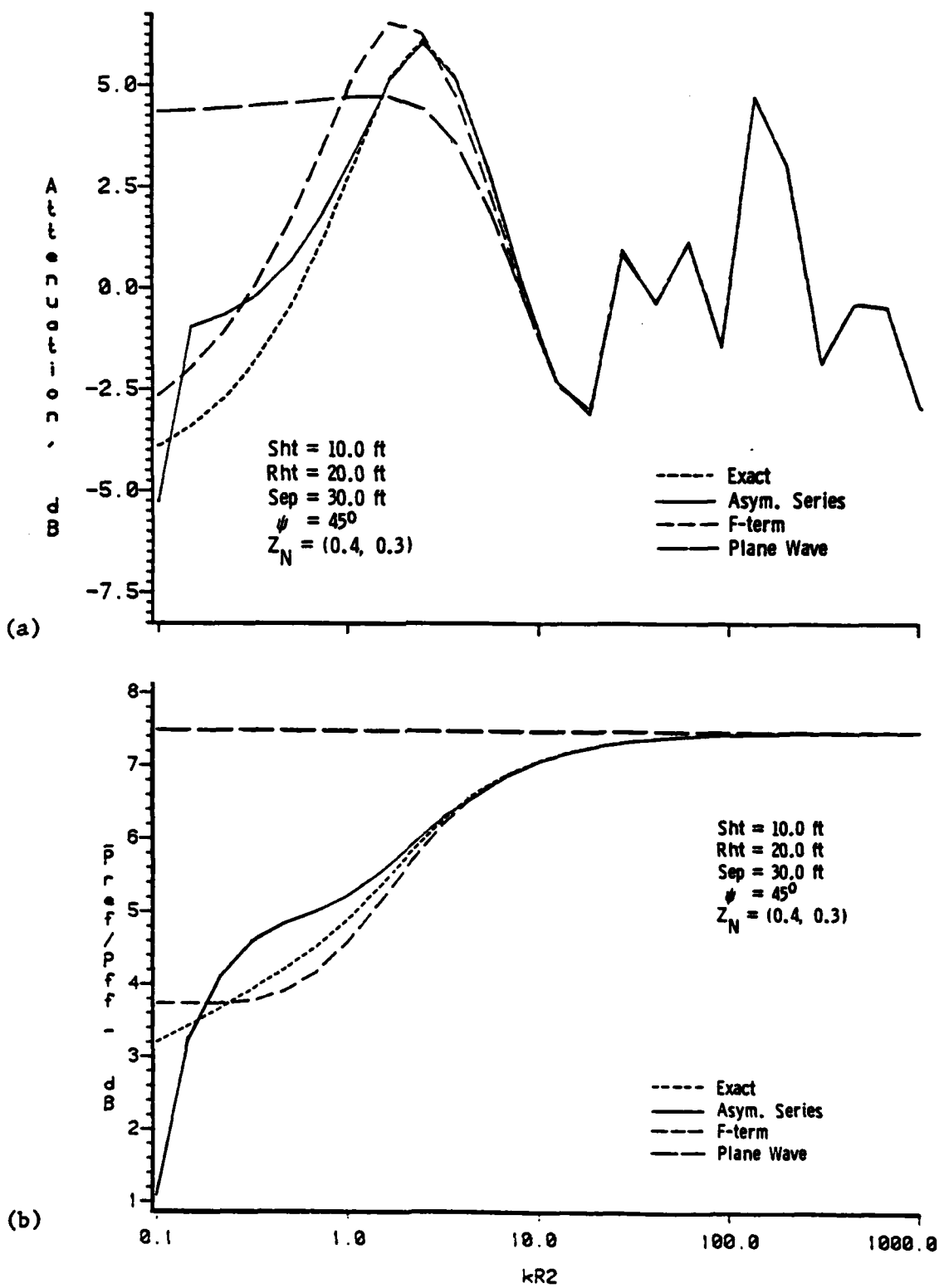


Figure 4.5 Calculated Data for (a) Attenuation and (b) Reflected/Direct Ratio as a Function of kR_2 . Exact, Asymptotic Series, F-term, and Plane Wave Solutions. Large Reflection Angle, Low Impedance.

Table 4.1

Summary of Geometry and Impedance Conditions
for the Numerical Data Plotted in Section 4.1.1.

<u>Source Height (ft.)</u>	<u>Receiver Height (ft.)</u>	<u>Separation (ft.)</u>	<u>ψ</u>	<u>Z_N</u>	<u>Figure</u>
1.0	1.0	38.0	3°	(0.3, 0.5)	4.1 (a), 4.1 (b)
1.0	1.0	38.0	3°	(2.0, 3.0)	4.2 (a), 4.2 (b)
0.0	0.0	57.3	0°	(0.3, 0.5)	4.3
5.0	5.0	56.7	10°	(0.3, 0.5)	4.4 (a)
5.0	5.0	56.7	10°	(2.0, 3.0)	4.4 (b)
10.0	20.0	30.0	45°	(0.4, 0.3)	4.5 (a), 4.5 (b)

4.1.2 Dependence on Reflection Angle

To investigate the dependence of reflection angle ψ on the received acoustic field, it is necessary to hold the parameter kR_2 constant. Thus, the approach illustrated in Figure 4.6 was used for generating the numerical data plotted in this section. The source image-to-receiver distance R_2 , the source height, and the frequency are held constant as the receiver point revolves around the image. In this way, ψ varies from its initial position with the receiver on the ground to its final value of 90° . Of course, R_1 also will vary with the angle , but all of the parameters in the reflected field terms will remain constant.

The results plotted in Figure 4.7 and Figure 4.8 compare two values of the parameter kR_2 for a low value of ground impedance Here, the source height is fixed slightly above the ground at 0.1 feet; R_2 is 12 feet; $Z_N = (1.2, 1.8)$; and $kR_2 = 6.7$ (frequency = 100 Hz.) in Figure 4.7 and $kR_2 = 33.5$ (frequency = 500 Hz.) in Figure 4.8.

The asymptotic series solution is indistinguishable from the exact integral solution for all values of ψ , and only very slight differences can be detected with the F-term form of solution. On the contrary, the plane wave solution is totally inaccurate for small grazing angles yet improves as ψ increases. For the low value of $kR_2 = 6.7$, this improvement is not significant until ψ is greater than 30° , whereas for the modestly-high value of $kR_2 = 33.5$, the plane wave solution is highly accurate for values above $\psi=5^\circ$

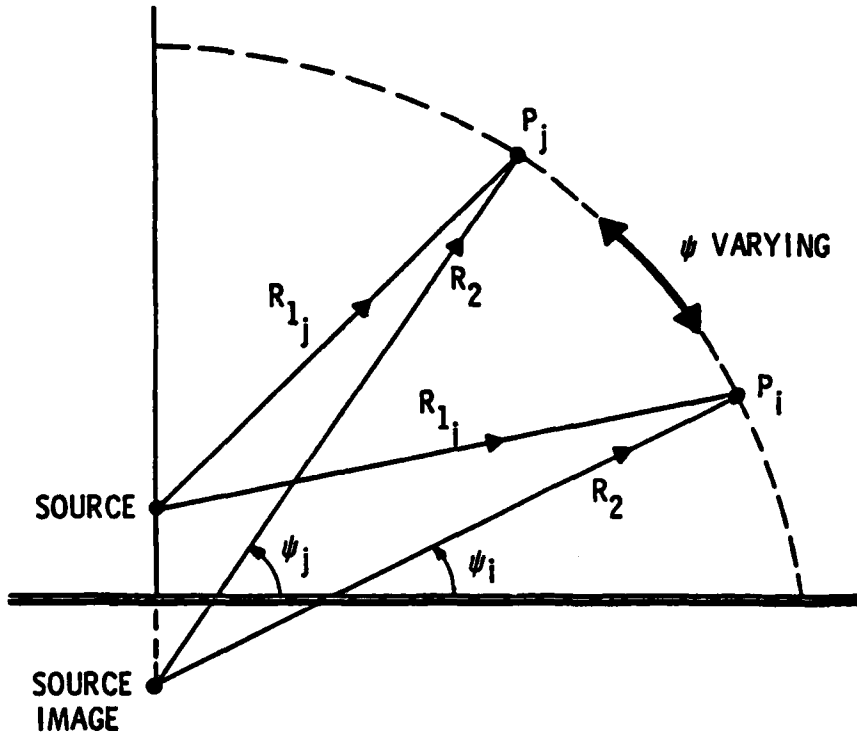


Figure 4.6 Method of Varying Reflection Angle ψ while Holding Other Parameters Fixed.

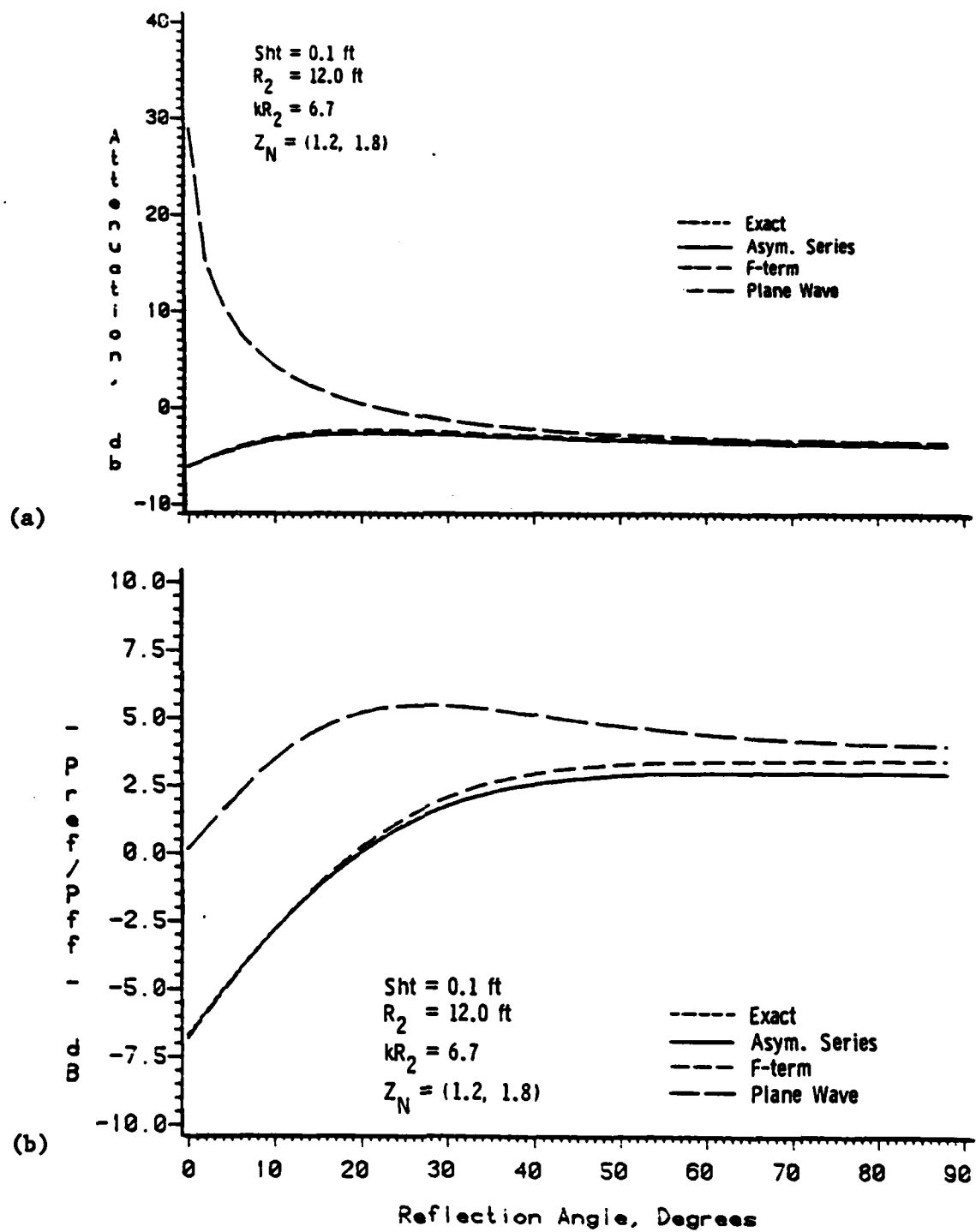


Figure 4.7 Calculated Data for (a) Attenuation and (b) Reflected/Direct Ratio as a Function of Reflection Angle. Exact, Asymptotic Series, F-term, and Plane Wave Solutions. Small kR_2 , Low Impedance.

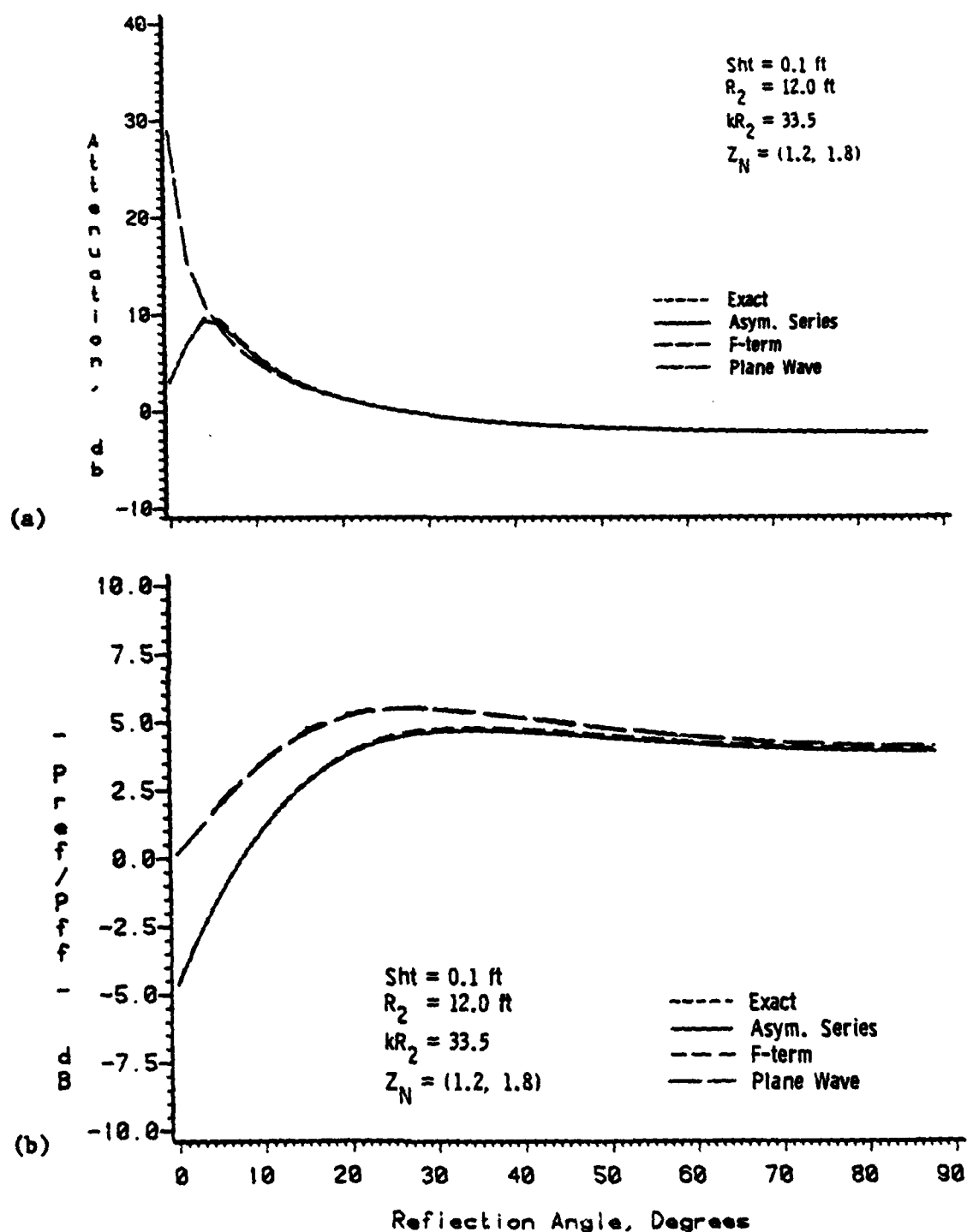


Figure 4.8 Calculated Data for (a) Attenuation and (b) Reflected/Direct Ratio as a Function of Reflection Angle. Exact, Asymptotic Series, F-term, and Plane Wave Solutions.
Large kR_2 , Low Impedance.

The response curves of attenuation vs. reflection angle will be different for different ground impedances. In Figure 4.9 are plotted four sets of curves corresponding to four values of impedance that differ by factors of ten from each other. The plane wave solution is compared to the F-term solution only, since the latter has been consistently close to the exact and asymptotic solutions. The value of kR_2 has been fixed deliberately low to force differences in the solutions so that the trends in the data could be observed. Here, the source height is at 1.0 feet; R_2 is fixed at 12 feet; $kR_2 = 3.35$ (frequency = 50 Hz.); and the four values of impedance are as shown on the graph. As expected, the bottom two sets of curves show that as the impedance increases from $Z_N = (1.0, 0.5)$ to $Z_N = (10.0, 5.0)$, the two solutions fall closer into accord. However, the top two sets of curves show the opposite trend. For the extremely low impedance $Z_N = (0.01, 0.005)$, the solutions are identical, yet as the impedance increases tenfold to $Z_N = (0.1, 0.05)$, the predictions begin to differ. This is an interesting result, but it should not be surprising. The plane wave theory, based on the image method, is exact for either infinitely rigid or pressure release surfaces. Therefore, as $Z \rightarrow 0$, the plane wave solution becomes more accurate, and it should agree with the spherical wave F-term solution.

The geometry and impedance conditions for the cases plotted in this section are summarized in Table 4.2.

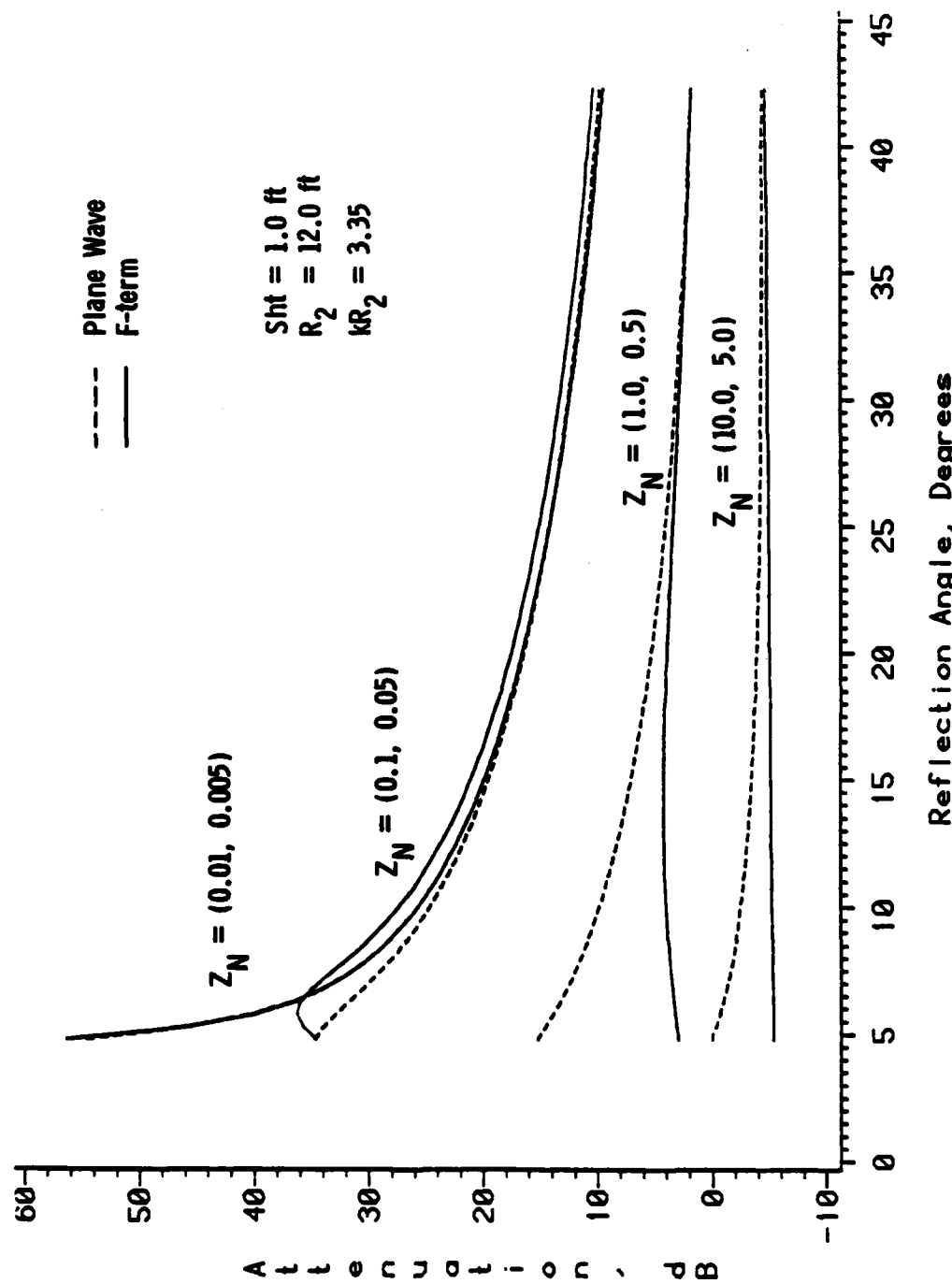


Figure 4.9 Comparison of Calculated Data for Four Values of Ground Impedance, as a Function of Reflection Angle. F-term and Plane Wave Solutions.

Table 4.2

**Summary of Geometry and Impedance Conditions
for the Numerical Data Plotted in Section 4.1.2.**

<u>Source Height (ft.)</u>	<u>R₂</u>	<u>kR₂</u>	<u>Frequency</u>	<u>Z_N</u>	<u>Figure</u>
0.1	12.0	6.7	100 Hz.	(1.2, 1.8)	4.7 (a), 4.7 (b)
0.1	12.0	33.5	500 Hz.	(1.2, 1.8)	4.8 (a), 4.8 (b)
1.0	12.0	3.35	50 Hz.	(0.01, 0.005)	4.9
1.0	12.0	3.35	50 Hz.	(0.1, 0.05)	4.9
1.0	12.0	3.35	50 Hz.	(1.0, 0.5)	4.9
1.0	12.0	3.35	50 Hz.	(10.0, 5.0)	4.9

4.1.3 Received Spectra Over a Practical Ground Cover

In several of the previous graphs, the value of ground impedance was held constant as kR_2 or frequency varied. While this may be necessary for studying the sensitivity of various parameters, the impedance of actual surfaces is rarely frequency-independent. The problem in practice is more often: given a ground surface between a source and a receiver characterized by its impedance measured at several discrete frequencies, predict the attenuation at the receiver. A common ground cover is outdoor grass, and one particular type--the so-called NRC²⁵ grass--has the third-octave values of impedance shown in Table 4.3. Using the values of frequency and impedance given in the table, plots of attenuation versus frequency have been generated and are plotted in Figures 4.10 - 4.12. The first two of these graphs shows the effect of symmetrically raising both source and receiver, while keeping the horizontal separation constant. Thus, with a separation of 50 feet, the source and receiver move from 0.1 feet above the ground ($\psi=0.23^\circ$) in Figure 4.10, to 1.0 feet ($\psi=2.3^\circ$) in Figure 4.11 (a), and to 2.0 feet ($\psi=4.5^\circ$) in Figure 4.11 (b). Although the impedance is not constant here, the trend of the attenuation maximum moving to lower frequencies and the overall attenuation decreasing with increasing ψ noted in section 4.1.2 is still apparent. Again, the plane wave solution becomes more accurate

²⁵ The impedance of this outdoor surface was measured by several methods at the National Research Council in Ottawa (Embleton, et al., 1975); hence the abbreviation in the name.

Table 4.3

Real and Imaginary Parts of the Impedance
of Outdoor (NRC) Grass for Third-Octave Values of Frequency.

<u>Frequency</u>	<u>Real</u>	<u>Imaginary</u>
63	20.0	28.0
80	18.0	26.0
100	18.0	24.0
125	16.0	22.0
163	14.0	19.0
200	13.0	17.0
250	12.0	14.0
315	9.9	12.0
400	9.0	10.0
500	8.0	8.0
630	6.0	6.0
800	5.0	5.0
1000	4.0	4.0
1250	3.0	3.0
1630	2.5	2.5
2000	2.0	2.0
2500	2.0	2.0
3150	2.0	2.0
4000	2.0	2.0
5000	2.0	2.0
6300	2.0	2.0
8000	2.0	2.0
10000	2.0	2.0

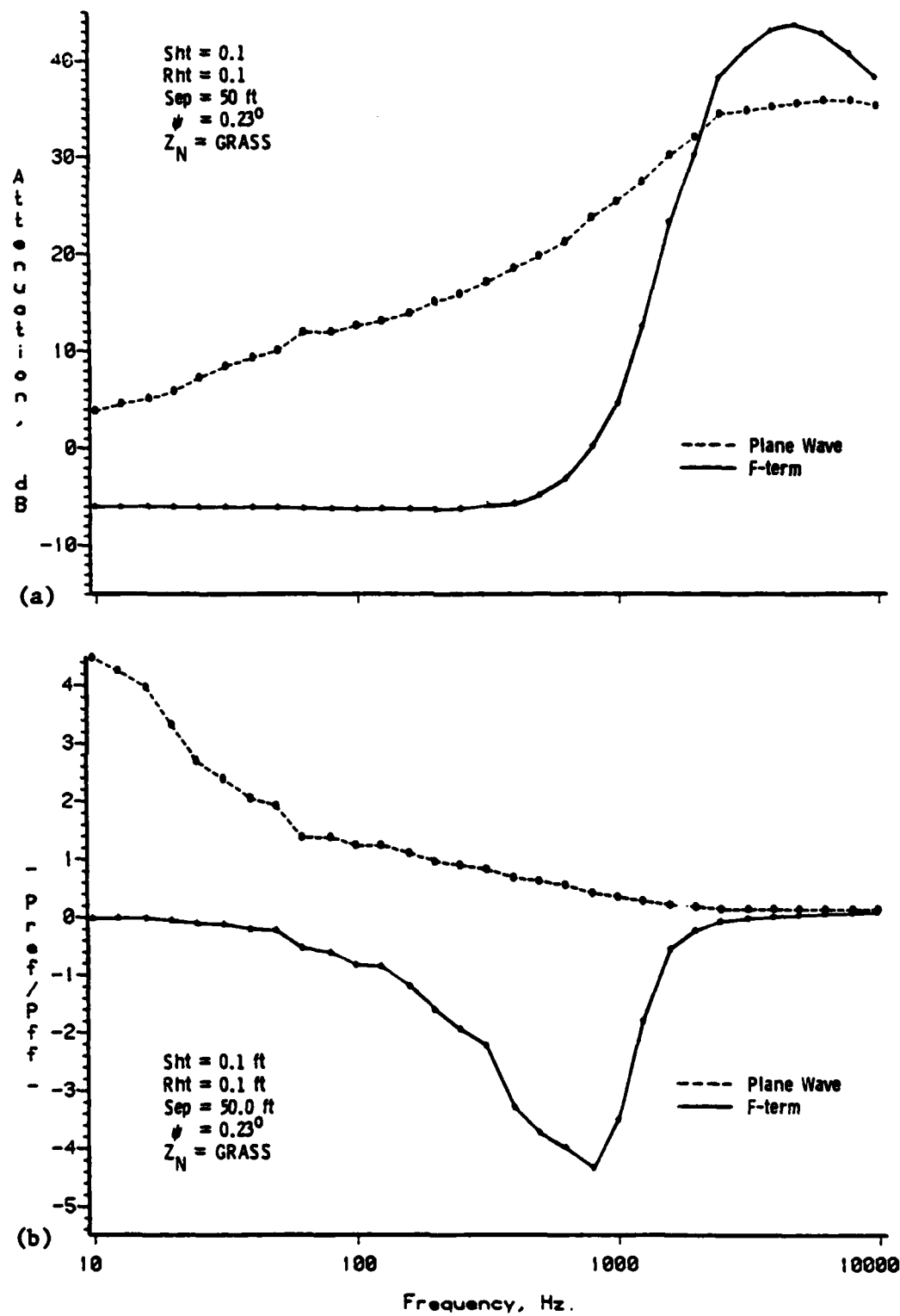


Figure 4.10 Calculated Data for (a) Attenuation and (b) Reflected/Direct Ratio as a Function of Frequency for Propagation Over Grass. F-term and Plane Wave Solutions.
Sht=0.1, Rht=0.1, Sep=50.0, Reflection Angle=0.23°.

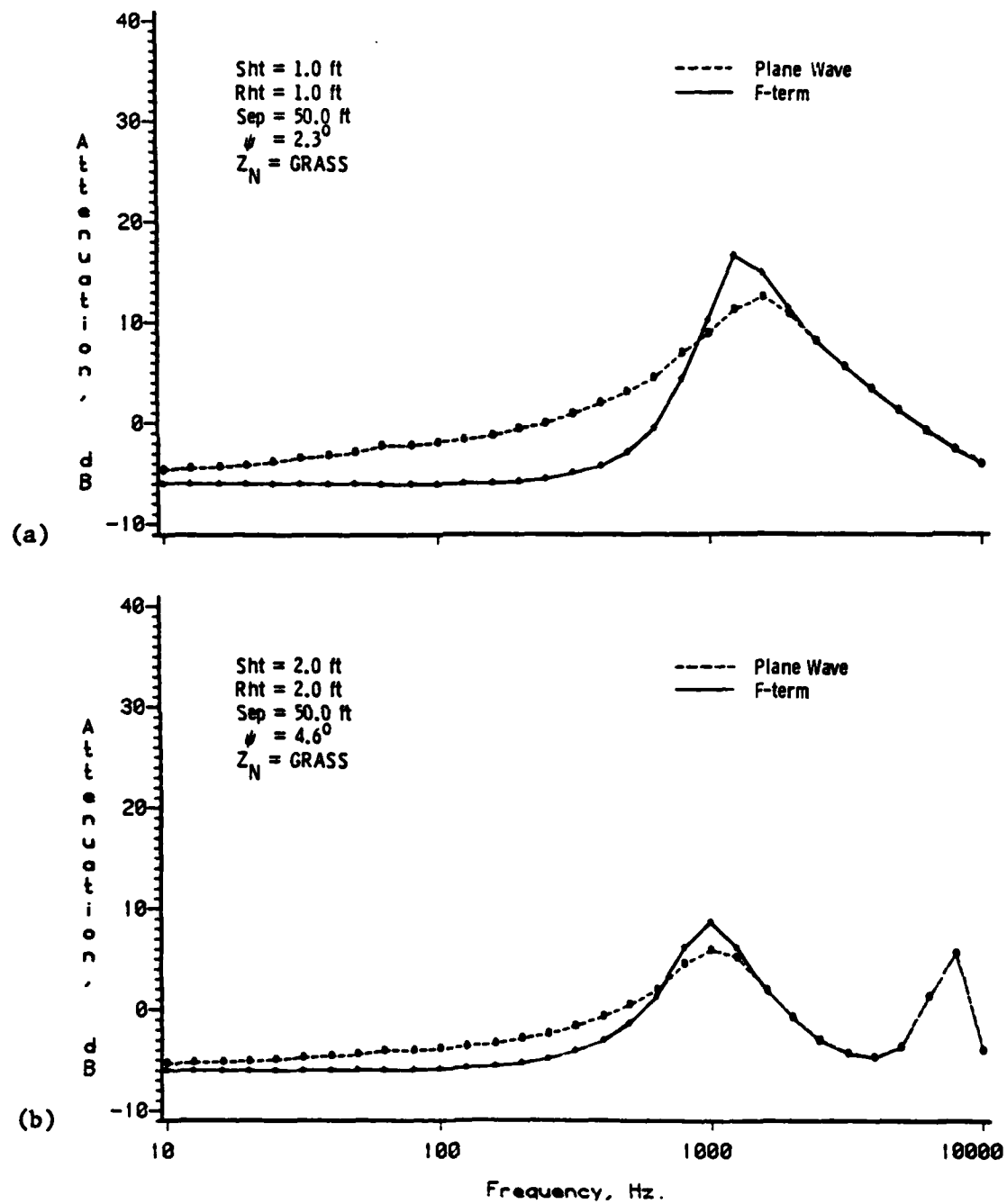


Figure 4.11 Calculated Data for Attenuation as a Function of Frequency for Propagation over Grass. F-term and Plane Wave Solutions.
 (a) Sep=50.0, Sht=1.0, Rht=1.0, and ψ = 2.3°.
 (b) Sep=50.0, Sht=2.0, Rht=2.0, and ψ = 4.6°.

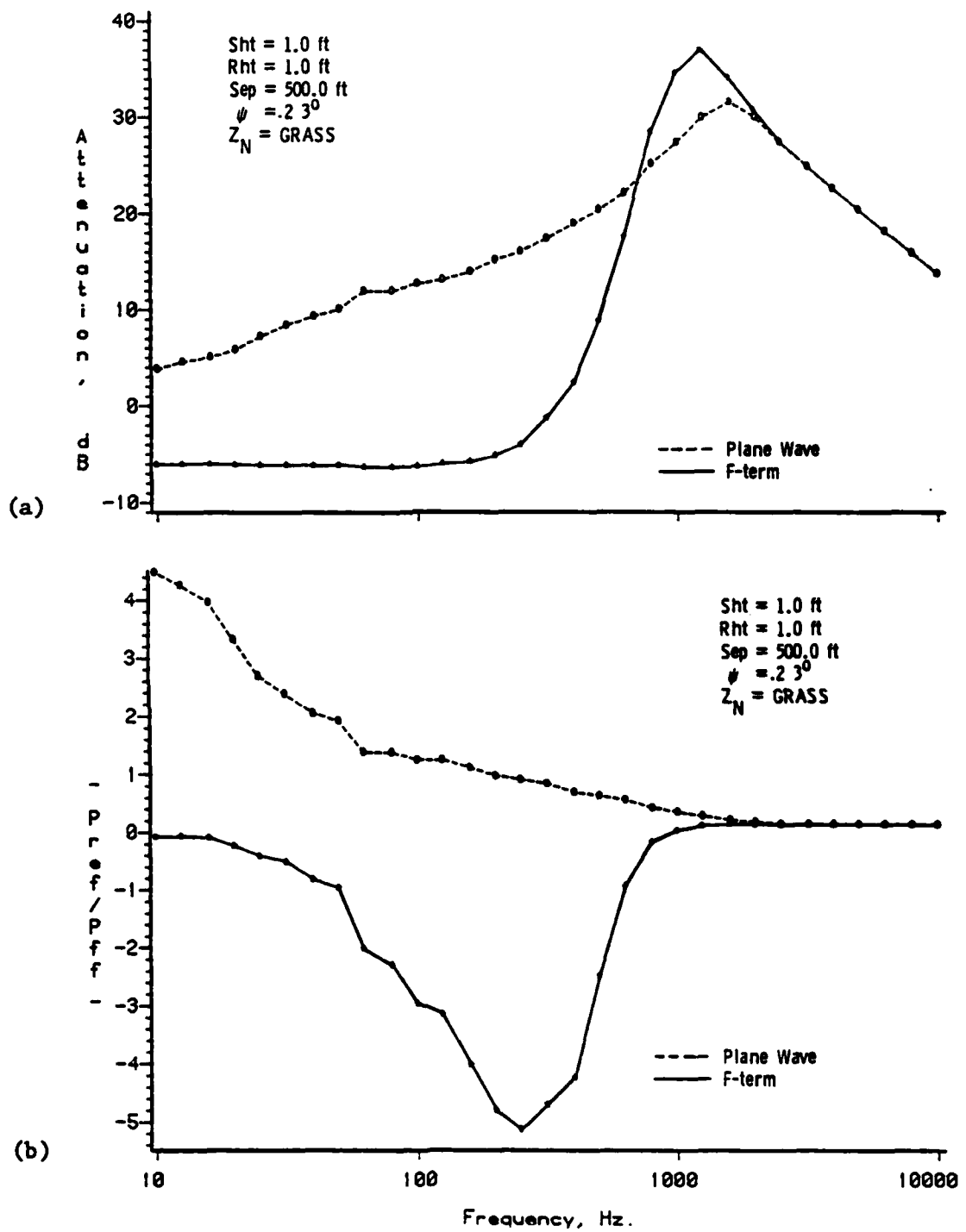


Figure 4.12 Calculated Data for (a) Attenuation and (b) Reflected/Direct Ratio as a Function of Frequency for Propagation over Grass. F-term and Plane Wave Solutions.
Sht=1.0, Rht=1.0, Sep=500.0, Reflection Angle= 0.23° .

for larger angles of reflection. Of practical interest is the fact that the grass-covered ground appears rigid (attenuation = -6 dB) for frequencies below about 800 Hz. The low-frequency noise of automobiles and trucks is not well-attenuated over grassland.

The data in Figure 4.12 are for source and receiver both 1.0 feet above the ground and separated by 500 feet. In this case, then, the reflection angle is the same as for the case plotted in Figure 4.10, namely $\psi = 0.23^\circ$, but the distance R_2 is larger. With reference to Figure 4.10 (b) and 4.12 (b), it can be seen that the reflected field for the plane wave has not changed at all since R_p is independent of R_2 ; however, the spherical-wave reflected field is quite different in Figure 4.12 than in Figure 4.10 because the F-term itself depends explicitly on R_2 (see Equation 4.4).

To conclude this section, data for near-grazing propagation over a ground surface comprising an indoor-outdoor carpet material is presented in Figure 4.13. The impedance values for the material are given in Table 4.4. This particular carpet has found use in reduced-scale model experiments (Lawther, et al., 1980), and hence the frequencies in both Table 4.4 and in Figure 4.13 are higher than those presented thus far. The interesting feature in the plotted data is that the "gain" is well in excess of -6 dB for several values of frequency. This is most clearly shown in Figure 4.13 (b) where the magnitude of the reflected field, given by Equation 4.4, can be more than 3 times as great as the direct field.

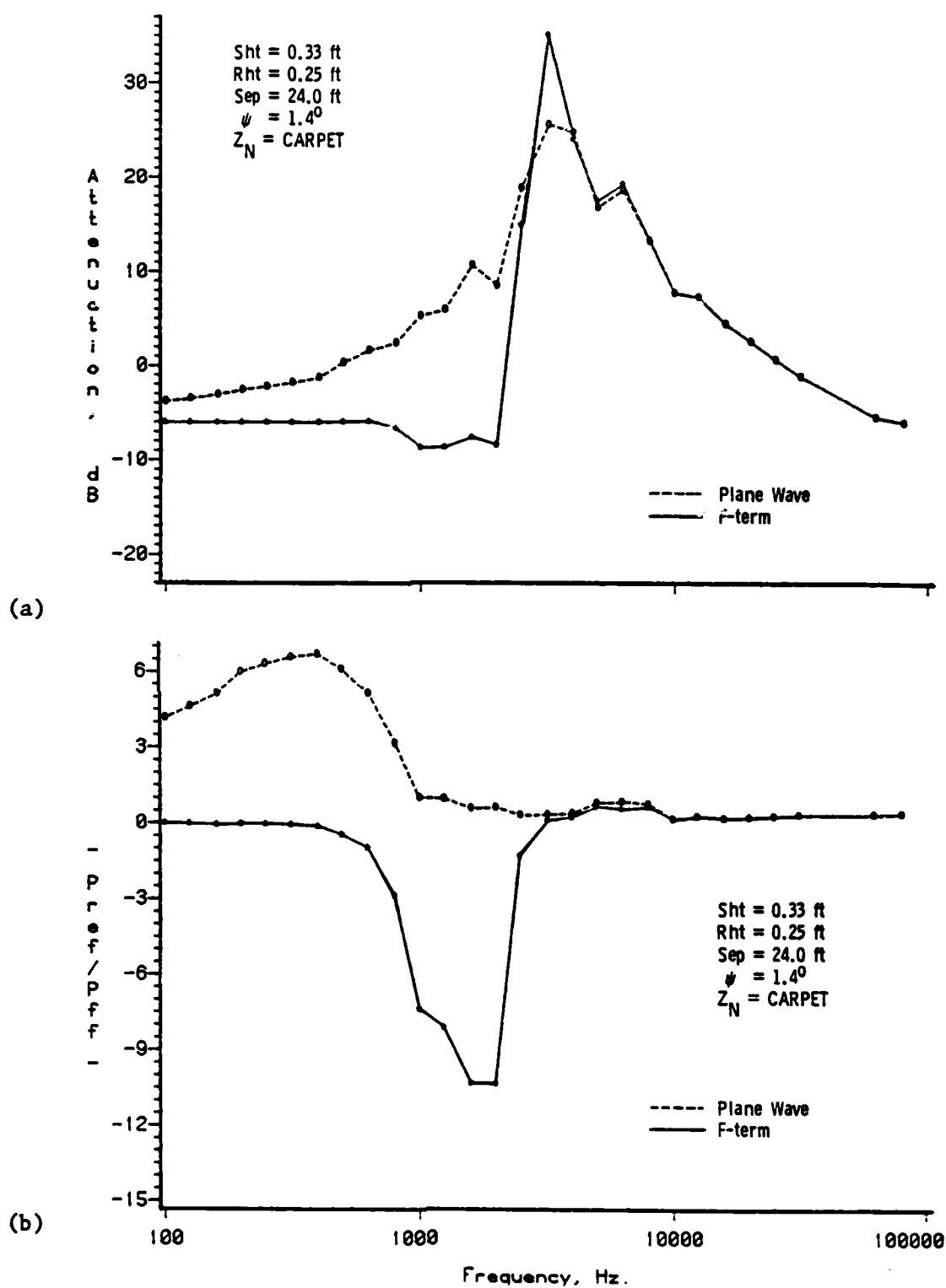


Figure 4.13 Calculated Data for (a) Attenuation and (b) Reflected/Direct Ratio as a Function of Frequency for Propagation over Carpet. F-term and Plane Wave Solutions. Sh_t=0.33, R_{ht}=0.25, Sep=24.0, ψ =1.4°.

Table 4.4

**Real and Imaginary Parts of the Impedance
of Indoor-Outdoor Carpet Material
for Third-Octave Values of Frequency.**

<u>Frequency</u>	<u>Real</u>	<u>Imaginary</u>
500	20.00	25.00
630	15.00	20.00
800	9.00	18.55
1000	2.53	13.02
1250	2.44	12.13
1630	1.41	7.41
2000	1.52	9.63
2500	0.74	4.26
3150	0.80	3.29
4000	0.91	2.38
5000	1.90	1.52
6300	1.99	3.47
8000	1.77	2.04
10000	0.34	-0.59
12500	0.63	0.89
16300	0.40	0.12
20000	0.51	0.11
25000	0.63	-0.12
31500	0.74	-0.23
62500	0.80	-0.40
80000	0.90	-0.23

The geometry and impedance conditions for the plots given in this section are summarized in Table 4.5

4.1.4 Results for Perpendicular Incidence

The exact solution to the problem of point source reflection by an impedance plane for perpendicular incidence is given in Section 2.4 in terms of the exponential integral. For small arguments the exponential integral could be expressed in a convergent series expansion, and for large arguments, it can be written in terms of its asymptotic expansion. As has been shown, the first term in the asymptotic series will generate the plane wave solution given by Equation (2.159).

Plotted in Figure 4.14 are the magnitudes of the ratios, in dB, of (a) the total field at the receiver to the free field and (b) the reflected field at the receiver to the free field for a source 3.0 feet, and a receiver 1.0 feet, above the ground plane, respectively. The impedance of the ground is $Z_N = (1.4, 1.3)$. The short-dashed curve represents the exact solution to the perpendicular incidence problem, obtained by numerically integrating Equation (2.152). The medium-dashed line is the calculated solution using the first two terms in the convergent series expansion of the exponential integral, Equation (2.156), and the long-dashed line is the solution using the first two terms in the asymptotic series, Equation (2.157). Finally, the solid line curve is the plane wave solution.

Table 4.5

**Summary of Geometry and Impedance Conditions
for the Numerical Data Plotted in Section 4.1.3.**

<u>Source Height (ft.)</u>	<u>Receiver Height (ft.)</u>	<u>Separation (ft.)</u>	<u>Ψ</u>	<u>Z_N</u>	<u>Figure</u>
0.1	0.1	50.0	0.23°	GRASS	4.10 (a), 4.10 (b)
1.0	1.0	50.0	2.3°	GRASS	4.11 (a)
2.0	2.0	50.0	4.6°	GRASS	4.11 (b)
1.0	1.0	500.0	0.23°	GRASS	4.12 (a), 4.12 (b)
0.33	0.25	24.0	1.4°	CARPET	4.13 (a), 4.13 (b)

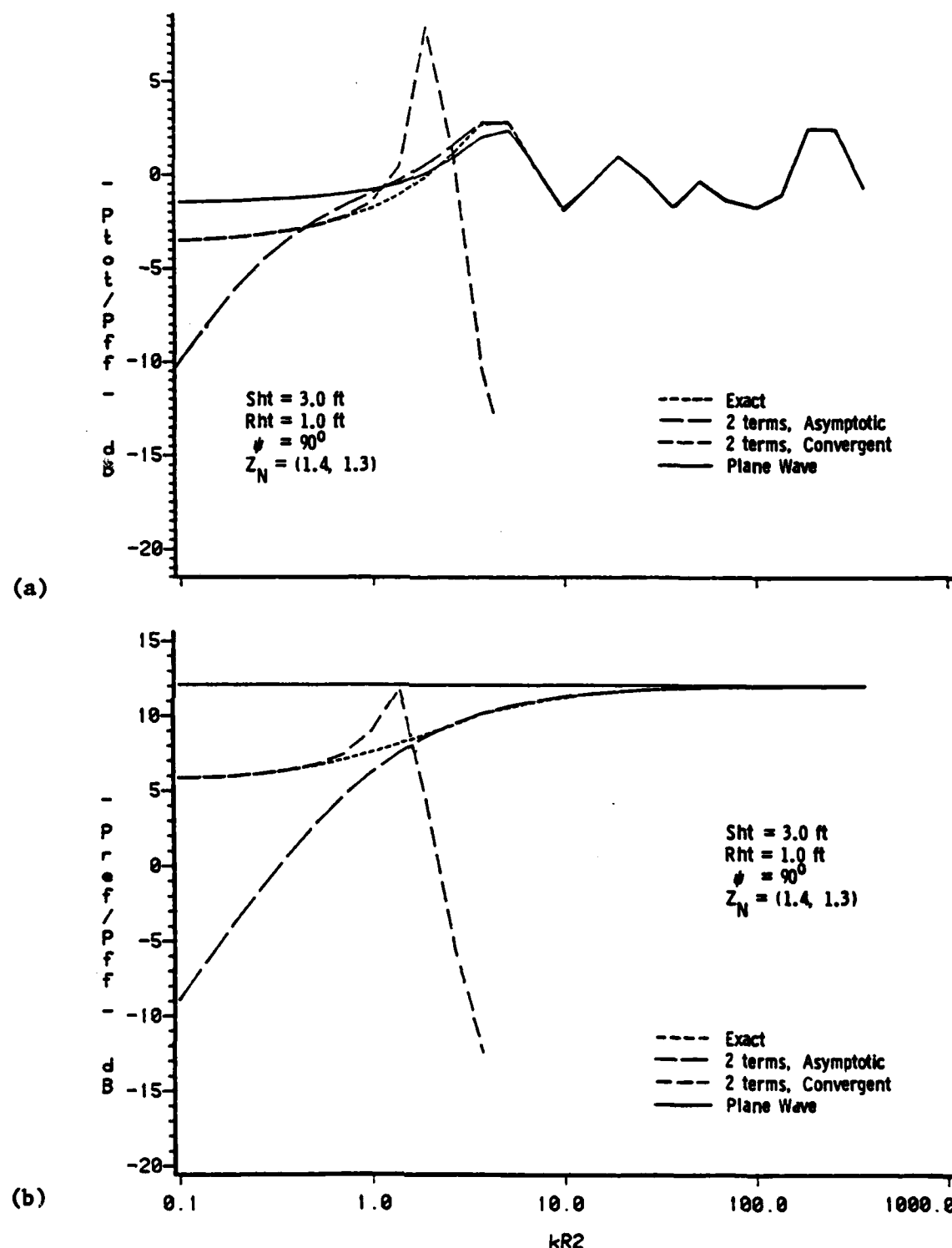


Figure 4.14 Calculated Data for (a) Attenuation and (b) Reflected/Direct Ratio as a Function of kR^2 , for Perpendicular Incidence. Exact, Two Terms in Asymptotic Series, Two Terms in Convergent Series, and Plane Wave Solutions. Low Z_N .

It can be seen that the predictions using the first two terms in the convergent series is very accurate for $kR_2 < 1$ but veers erratically for values above that. When the first two terms in the asymptotic series are used, on the other hand, excellent agreement with the exact solution is obtained for $kR_2 \geq 3$, whereas the plane wave solution (referring to Figure 4.14 [b]) requires $kR_2 \geq 50$, or so. It should be emphasized that these results are for a relatively low value of impedance, and that for most practical impedance surfaces (in acoustical studies in air) the plane wave solution will be much more in accord with the exact solution.

Whether the value of kR_2 is small or large, there is one ground impedance region for which the plane wave solution, if used, should be applied with caution. That is where the value of admittance $\beta \rightarrow 1$. From Equation (2.159), it can be seen that the reflected field vanishes for $\beta=1$, and the attenuation becomes zero. Physically, this is simply the ideal "matched" condition where $Z_N=1$ (unnormalized impedance = ρc), and no energy is reflected. The spherical wave theory, however, does predict some reflected energy for this case. Figure 4.15 (a) and (b). show the familiar "standing wave pattern" that is obtained when the source is held fixed at some distant point above the plane (here, 100 feet) and the receiver is moved away from the surface. Experiments based on this standing wave pattern (using a pressure microphone or hydrophone) are often conducted to calculate the value of surface impedance. The ground impedance in Figure 4.15 (a) is $Z_N = (1.0, 0.05)$ and in Figure 4.15 (b) is $Z_N = (1.0, 0.005)$.

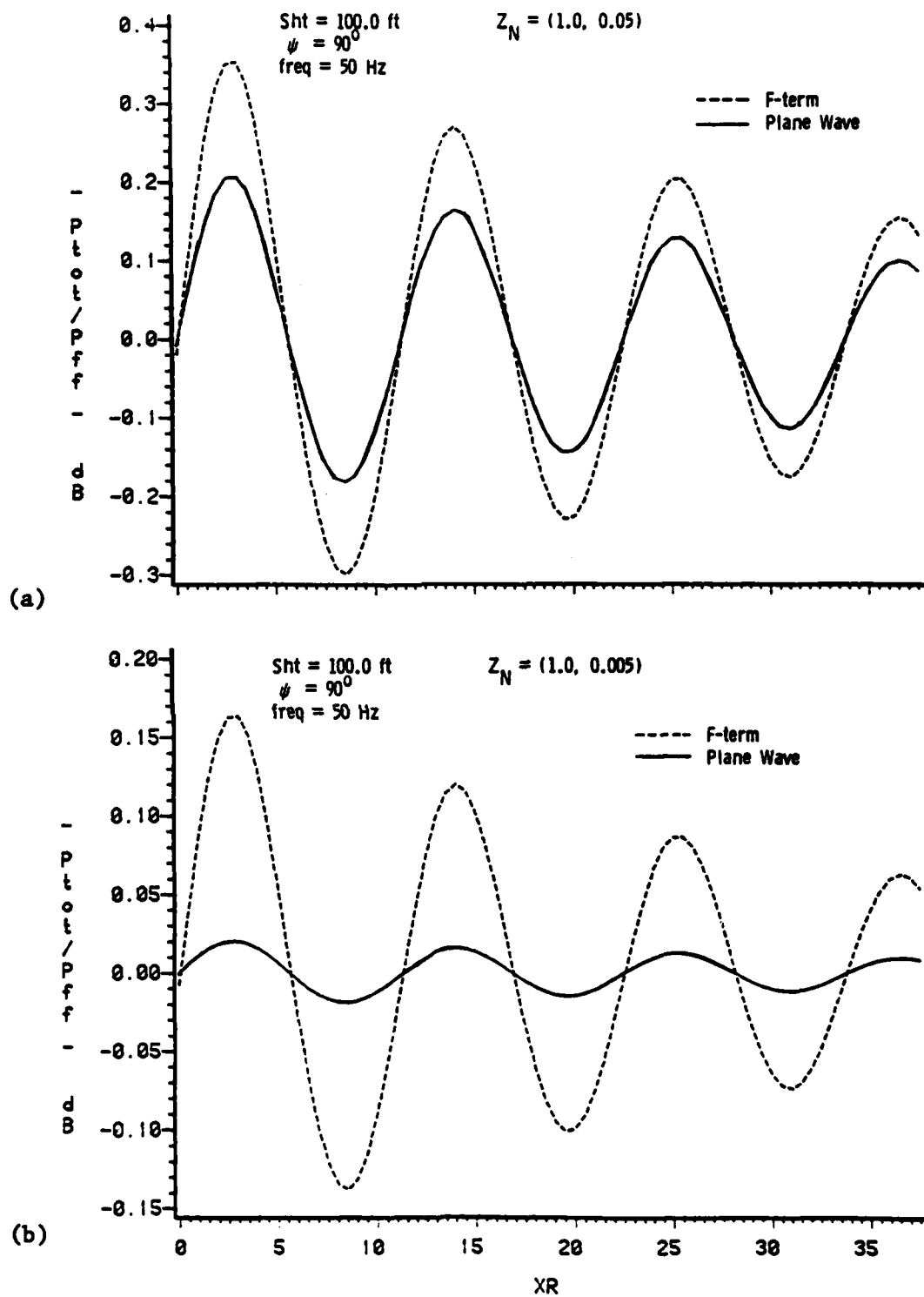


Figure 4.15 Calculated Data for Attenuation for Perpendicular Incidence. Exact, Two Terms in Asymptotic Series, Two Terms in Convergent Series, and Plane Wave Solutions. (a) $Z_N = (1.0, 0.05)$ (b) $Z_N = (1.0, 0.005)$

Although the scales on the vertical axes are greatly expanded, the difference in the theoretical predictions could be important in practice.

4.2 Results for the Barrier Diffraction Problem

This section presents numerical results from the combined sound propagation-barrier diffraction model described in Chapter 3. The ground on either side of the barrier is again assumed to be locally-reacting, and an arbitrary impedance may be assigned to each side separately. The source and receiver can be located at any non-coincident points, although the GTD method may become inaccurate if either is closer than a few wavelengths from the edge. The barrier itself will be assumed rigid for the present calculations.²⁶ The relevant parameters to be investigated in this section are again kR and ground impedance Z_N , but in addition, the dependence of the predictions on the barrier height and the diffraction angle ϕ will be examined.

The attenuation as defined in the previous section will again be plotted, since it is a useful quantity for comparing one solution to another or for comparing one geometry to another. In noise control

²⁶ Although the theoretical solution for an impedance-covered half-plane was presented in Chapter 3, prior sensitivity studies (Hayek, Lawther, Kendig, & Simowitz, 1978) have shown that the differences in the sound field for the impedance barrier relative to the rigid barrier were not significant for most practical cases. Computations using the diffraction coefficient given by Equation (3.6), then, were deemed unnecessary for the purposes of the present study.

practice, however, a more informative quantity is the "insertion loss" of the barrier, which relates the actual field at the receiver to the field that would have existed there in the absence of the barrier (but in the presence of the ground). Thus, graphs of the data will also be given here in terms of the insertion loss, defined formally as

$$\text{Insertion Loss} = -20 \log_{10} \left| \frac{\phi_{\text{barrier tot}}}{\phi_{\text{ground tot}}} \right| \text{ dB ,} \quad (4.8)$$

where $\phi_{\text{barrier tot}}$ is the total field at the receiver point when the barrier is present and $\phi_{\text{ground tot}}$ is the received field over the impedance plane alone. Note that the latter field must be calculated separately, using the ground propagation theory of Chapter 2. Because the Edge-Plus-Images model uses only the first term in the asymptotic series solution to compute the ground reflections, the calculation of $\phi_{\text{ground tot}}$ for the insertion loss data has also been performed with only the first term (the solution given in Section 2.3.5.5).

Some interesting features of the Edge-Plus-Images model should perhaps be pointed out before discussing the numerical results. First, because the critical angles defining the acoustic diffraction are measured from the top of the barrier edge (refer to Figure 3.2), the actual (absolute) location of the ground is of secondary importance. That is, from the standpoint of the model, the ground need not be horizontal. The configuration depicted in Figure 4.16 (a), which might represent a barrier on a hillside, is mathematically identical to that shown in Figure 4.16 (b), which could

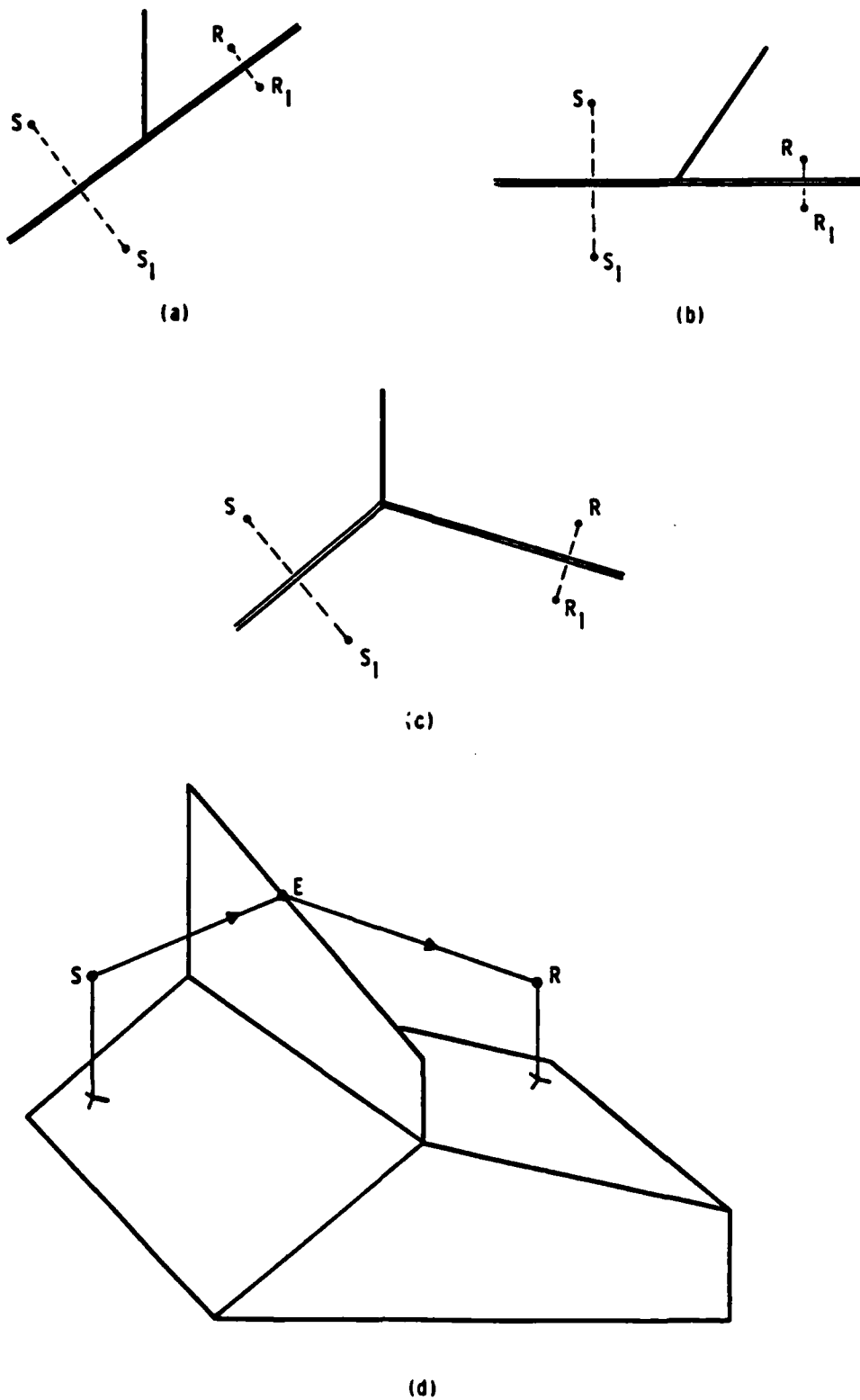


Figure 4.16 Several Configurations that can be treated by the Edge-Plus-Images Model. The geometries in (a) and (b) are mathematically equivalent. In (c) the ground need not be horizontal, and in (d) the barrier height need not be constant.

represent a "tilted" barrier on a horizontal ground. Furthermore, since the ground may have different "slopes" on either side of the barrier, geometries such as that in Figure 4.16 (c) can be addressed by the model (provided the source and receiver "images" in the ground remain on the same side of the extended half-plane as the source and receiver themselves). Finally, since the location of the edge point E (Figure 3.1) determines the diffraction angles, the "height" of the barrier need not be constant relative to the ground. Therefore, a very general configuration such as that illustrated in Figure 4.16 (d) can be solved by the Edge-Plus-Images model.²⁷

4.2.1 Dependence on the Parameter kR

Figure 4.17 (a), (b), and (c) shows the geometry of the barrier problem and defines the parameters which will appear on many of the graphs in this section. Rather than investigate the dependence on kR_1 and kR_2 separately, the following data will be plotted in terms of kR , where R is defined as $R = R_1 + R_2$. Furthermore, in all of the following cases, the distances R_1 and R_2 have been kept approximately equal in value. The data plotted in Figure 4.18 (a) and (b) is for a source located 0.2 feet above the ground (Sht) and "offset" from the barrier by 12.0 feet (Soff), while the receiver is located 0.1 feet

²⁷ Of course, some basic solid and analytic geometry is necessary for computing the locations in space of the various image points and propagation paths. Included in the computer program implementation of the present model are several geometrical subroutines for performing these tasks.

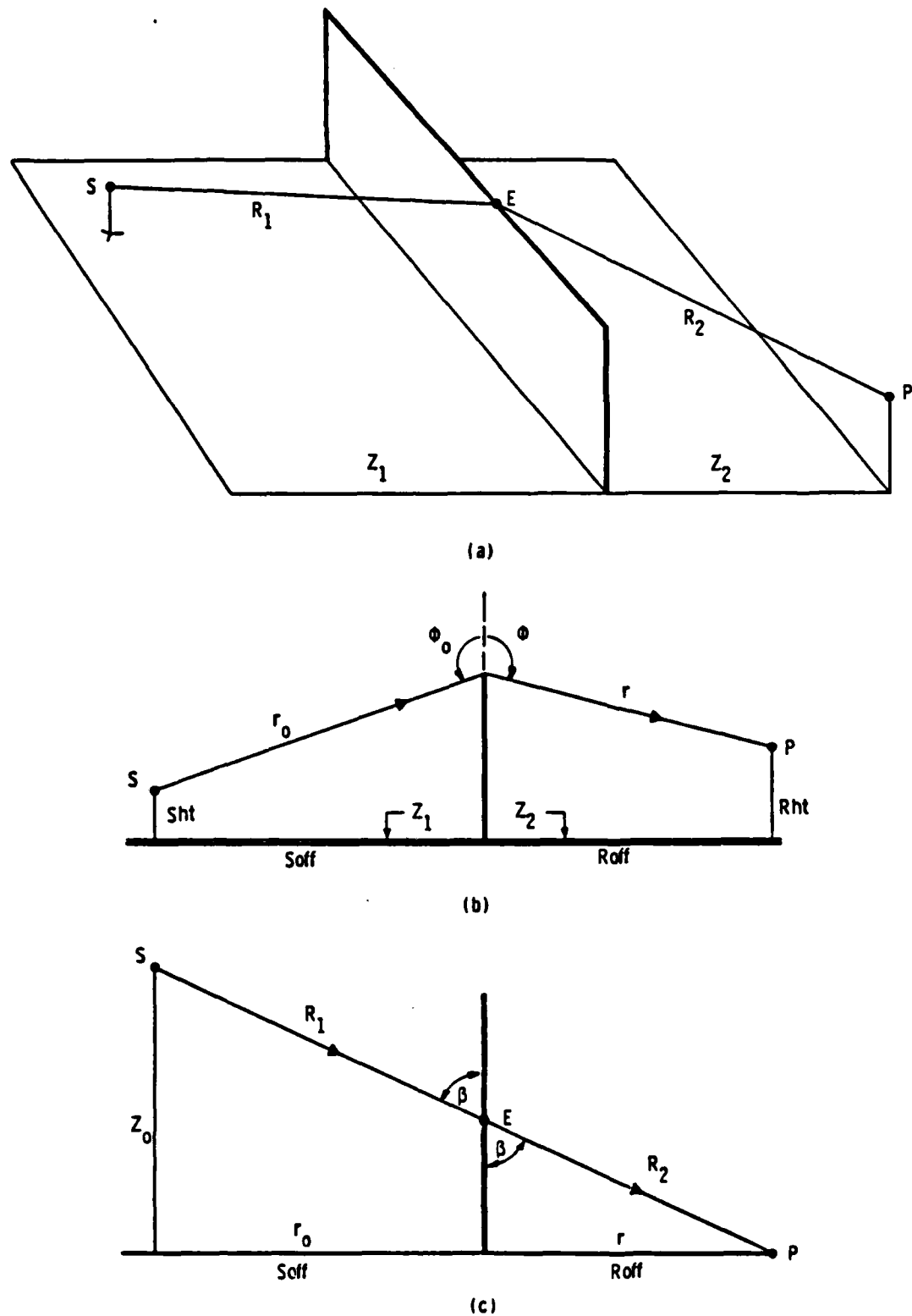


Figure 4.17 The Geometry of the Barrier-on-the-Ground Problem, showing Parameter Definitions for Graphical Data.
 (a) perspective view. (b) side view. (c) top view.

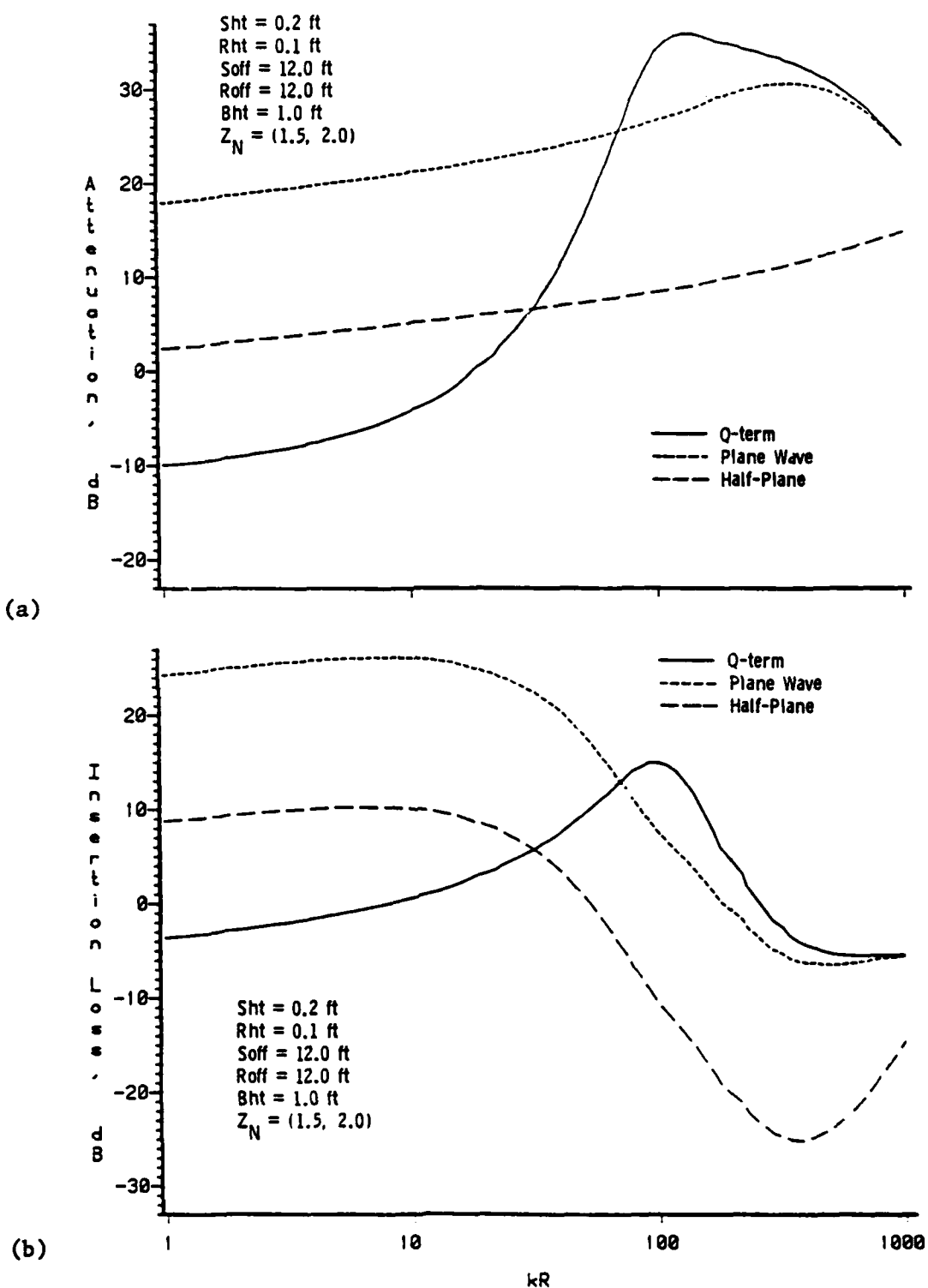


Figure 4.18 Calculated Data for (a) Attenuation and (b) Insertion Loss as a Function of kR . Q-term, Plane Wave, and Half-Plane Solutions. Small Source and Receiver Ht., Small Bht ., Low Z_N .

above the ground (R_{ht}) and offset by 12.0 feet (R_{off}). The barrier height (B_{ht}) is 1.0 feet and the ground impedance is $Z_N = (1.5, 2.0)$ on each side. As shall be true for most of the plots in this section, the source-receiver ray is perpendicular to the barrier ($z_0 = 0$ and $\beta = 90^\circ$).

Three curves are drawn corresponding to calculated data using (i) the "half-plane" theory (long-dashed line), (ii) the "plane wave" theory (short-dashed line), and the (iii) "Q-term" theory (solid line). For the half-plane computations, only the "direct" diffraction path (Path 1 in Figure 3.4 [a]) is used, as though the ground were absent and a semi-infinite barrier existed. The plane wave solution accounts for all the diffraction paths, but the plane wave reflection coefficient given by Equation (2.4) is used in place of the spherical wave reflection coefficient Q . The data computed with the Q-term solution is the most accurate of the three and employs the first term in the spherical wave reflection coefficient given by Equation (2.40) (that is, where " F " is simply replaced by " F_1 " from Equation [2.150]). In all cases, the diffraction coefficient D_e is that given by Equation (3.4).

The curves show some interesting features. The Q-term shows a broad peak in the attenuation (and insertion loss) similar to that found in the previous ground propagation graphs. This is again due to an "impedance effect," as path length interference can not occur in this kR region. For very large kR , the plane wave solution agrees with the Q-term solution, as expected, since in this region the

spherical wave reflection coefficient reduces to the plane wave reflection coefficient. However, the two predictions are very different for smaller values of kR . This can be explained as follows. Due to the short barrier height, the ground reflection angles on either the source or receiver sides are small (approximately 5°), and, consequently, the plane wave reflection coefficients approach -1.0. Therefore, instead of showing a gain over free field as predicted by the Q-term solution, use of the plane wave reflection coefficient shows an attenuation of about 20 dB.

The curve generated from the half-plane theory is inaccurate over the full range of kR considered here. The only discernible trend is the gradual increase in attenuation, reflecting the fact that the diffraction coefficient in Equation 3.4 decreases with increasing kR .

The insertion loss data in Figure 4.18 (b) reveals an interesting fact. Namely, for large kR the predicted insertion loss is negative, indicating that the field at the receiver behind the barrier is actually greater than it would be without the barrier.²⁸ The explanation for this phenomenon is simple: in the absence of the barrier, the reflection angle from source to receiver is of the order of 0.7° , and the "propagation loss" over the relatively "soft" impedance plane would be large. The barrier essentially forces the reflection angles higher (about 5°), causing the ground to appear

²⁸ This is also true for low values of kR , but the attenuation is likewise predicted to be negative there. Moreover, both the ground propagation theory and the GTD are extremely accurate for "large kR ," and hence the assertion of negative insertion loss can be made confidently.

"harder," and thereby reducing the propagation loss.

The numerical data in Figure 4.19 (a) and (b) is for the same geometry as in the previous case, only here the ground impedance has increased by a factor of 10. Immediately apparent is the fact that the overall attenuation is lower for the harder ground. Actually, as was the trend in the ground propagation studies in the previous section, the attenuation peak has shifted to higher values of kR . Also apparent is that the plane wave predictions are closer to the Q-term predictions (maximum deviation 5 dB, as opposed to 28 dB in Figure 4.18). This is not surprising since the influence of ground absorption diminishes as the ground impedance increases. Again, if the ground impedance were increased continuously, the two solutions would eventually give identical results.

Unlike the case for the soft ground, the insertion loss in Figure 4.19 (b) is appreciable at high frequencies. This is because the loss due to simple propagation would not be significant over this ground, so the "shadowing" effects of the barrier appear stronger by comparison.

The attenuation and insertion loss curves presented next in Figures 4.20 and 4.21 show some preliminary effects of increasing the barrier height (this dependence will be discussed in detail in the next section). All parameters are the same as those in Figures 4.18 and 4.19, respectively, only the barrier height is now 8.0 feet instead of 1.0 feet. For either impedance considered, the range of kR for which the plane wave solution is in accord with the Q-term

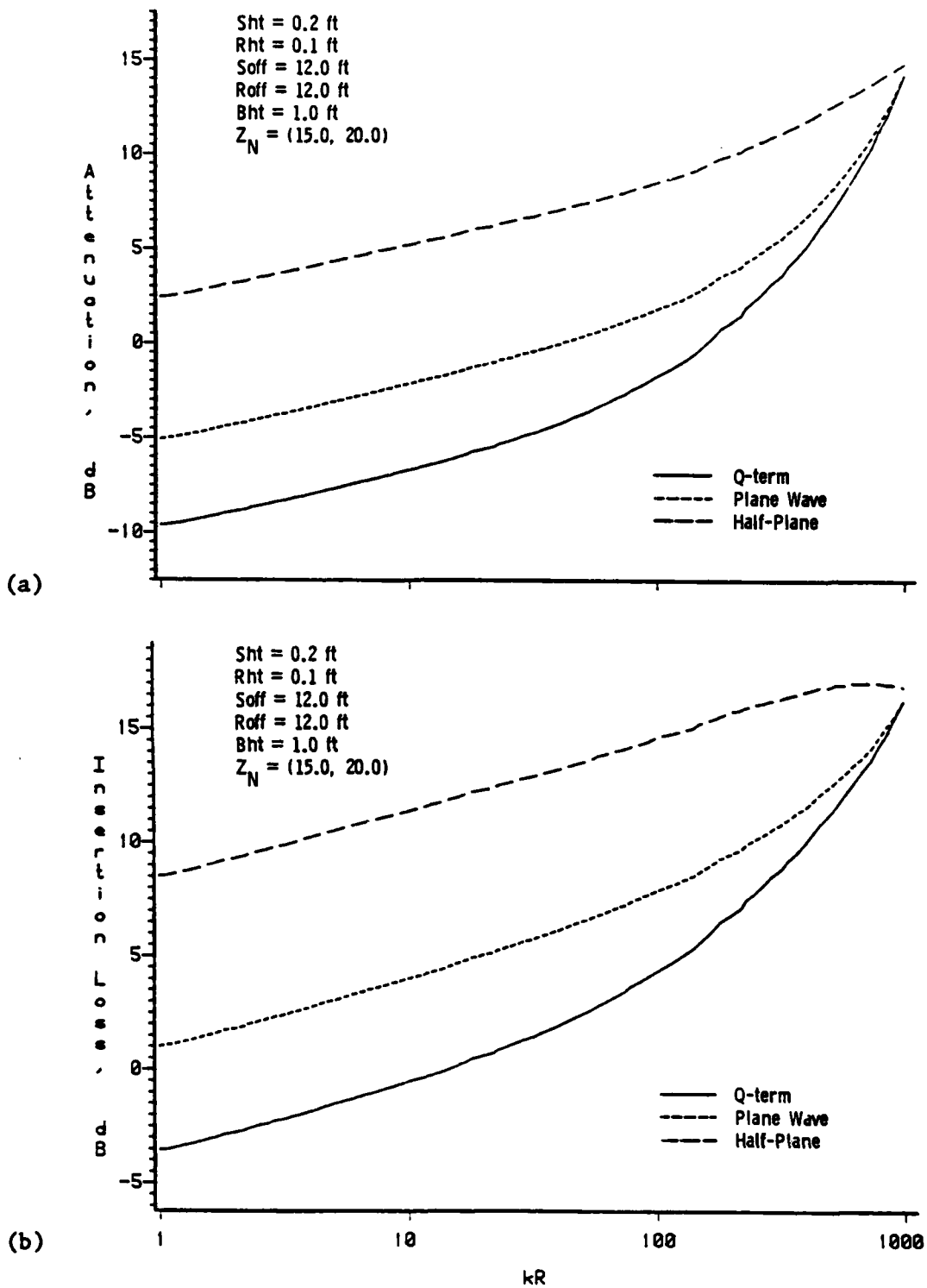


Figure 4.19 Calculated Data for (a) Attenuation and (b) Insertion Loss as a Function of kR . Q-term, Plane Wave, and Half-Plane Solutions. Small Source and Receiver Heights, Small Barrier Height, High Impedance.

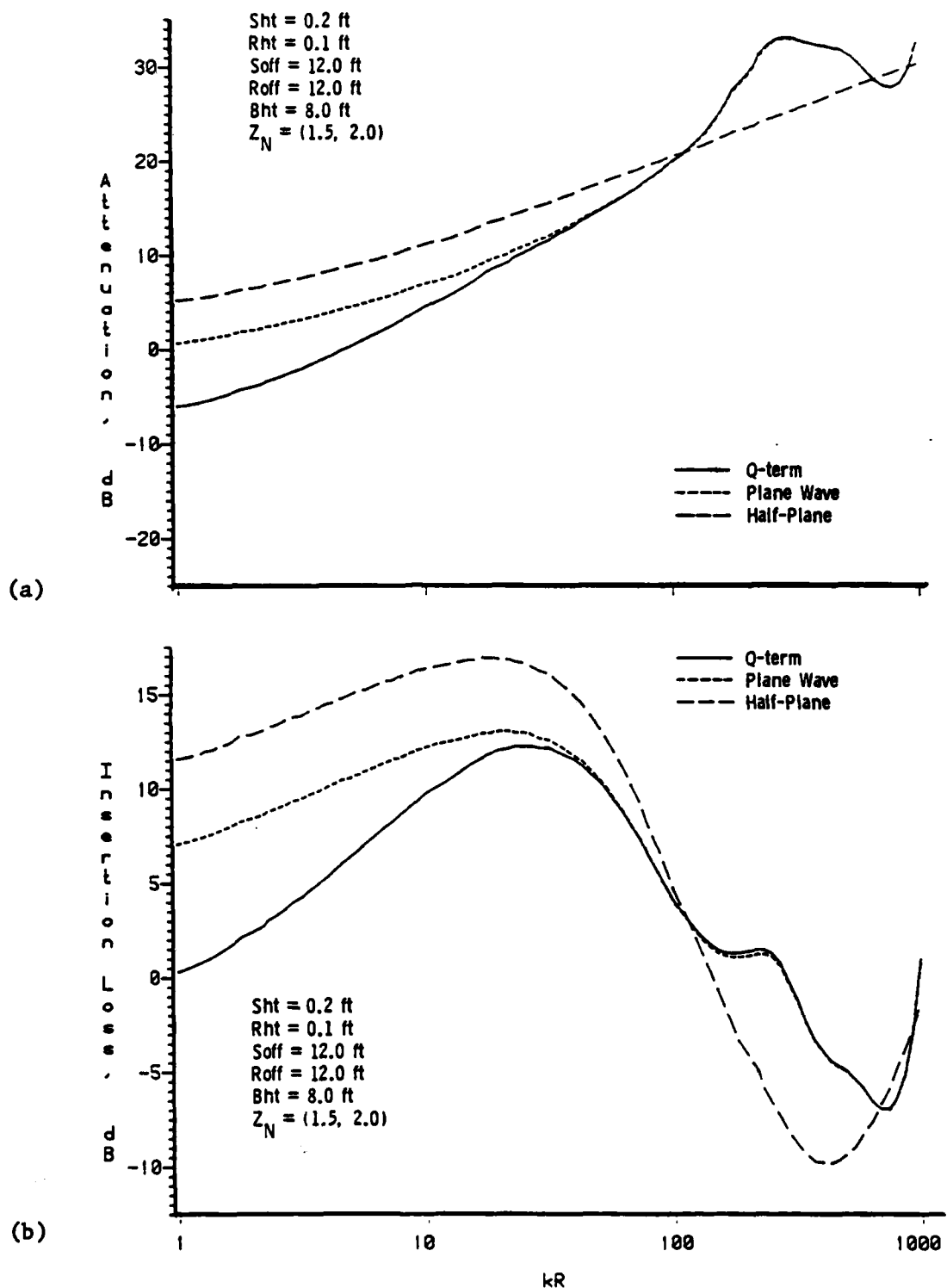


Figure 4.20 Calculated Data for (a) Attenuation and (b) Insertion Loss as a Function of kR . Q-term, Plane Wave, and Half-Plane Solutions. Small Source and Receiver Heights, Large Barrier Height, Low Impedance.

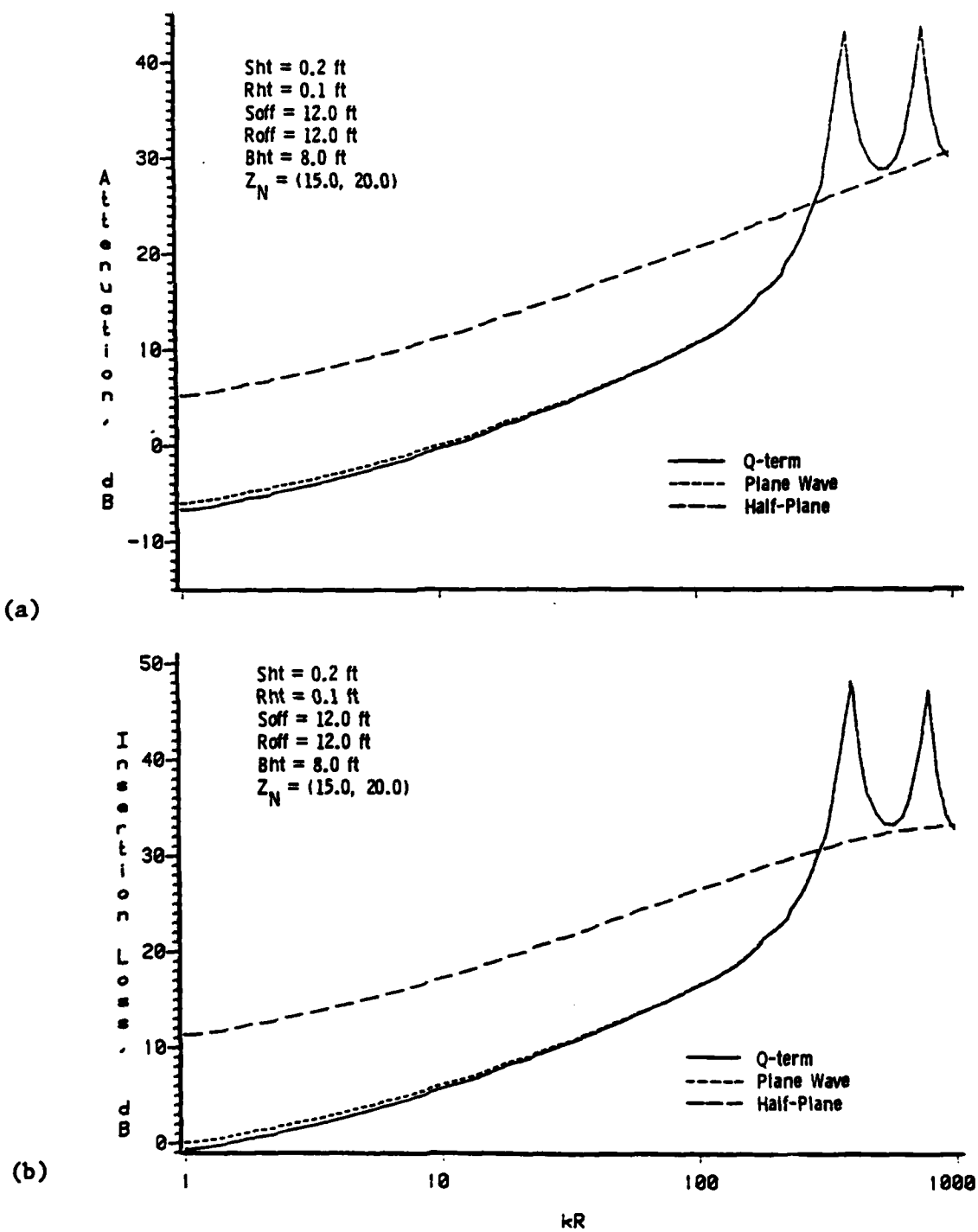


Figure 4.21 Calculated Data for (a) Attenuation and (b) Insertion Loss as a Function of kR . Q-term, Plane Wave, and Half-Plane Solutions. Small Source and Receiver Heights, Large Barrier Height, High Impedance.

solution begins at a lower value for the higher barrier. That is, for $Z_N = (1.5, 2.0)$, the 1-foot barrier dictates $kR \geq 700$ for agreement, whereas the 8-foot barrier requires $kR \geq 50$. For $Z_N = (15.0, 20.0)$, a large kR is still necessary for the 1-foot barrier, but the solutions for the 8-foot case are very close down to $kR = 10$.

Comparing Figure 4.21 with Figure 4.19 shows the expected result that the higher barrier provides the greater attenuation.

Mathematically, this is a result of the diffraction coefficient taking smaller values as the receiver moves deeper into the shadow zone. For soft grounds, however, a counteracting effect takes place as the barrier height increases. The reflection angles of the source-ground-barrier path and the barrier-ground-receiver path increase, and hence the "strength" of the ground-reflected rays gets larger. The net result can be seen most clearly when Figure 4.18 is compared to Figure 4.20 (attenuation or insertion loss). The attenuation is higher for the 8-foot barrier for kR less than about 50, but the attenuation is generally lower for kR above that. Apparently, then, the "diffraction effect" is the primary factor at the lower values of kR , while the "impedance effect" dominates at the higher values.

When both the source and receiver are raised above the ground to heights of 7.2 feet and 7.1 feet, respectively, the data plotted in Figure 4.22 result. Since the geometry chosen here defines diffraction angles ϕ_0 and ϕ equal to those for the case in Figure 4.18, the differences between the two sets of data are due entirely to the presence of the ground (the half-plane curve is identical for the

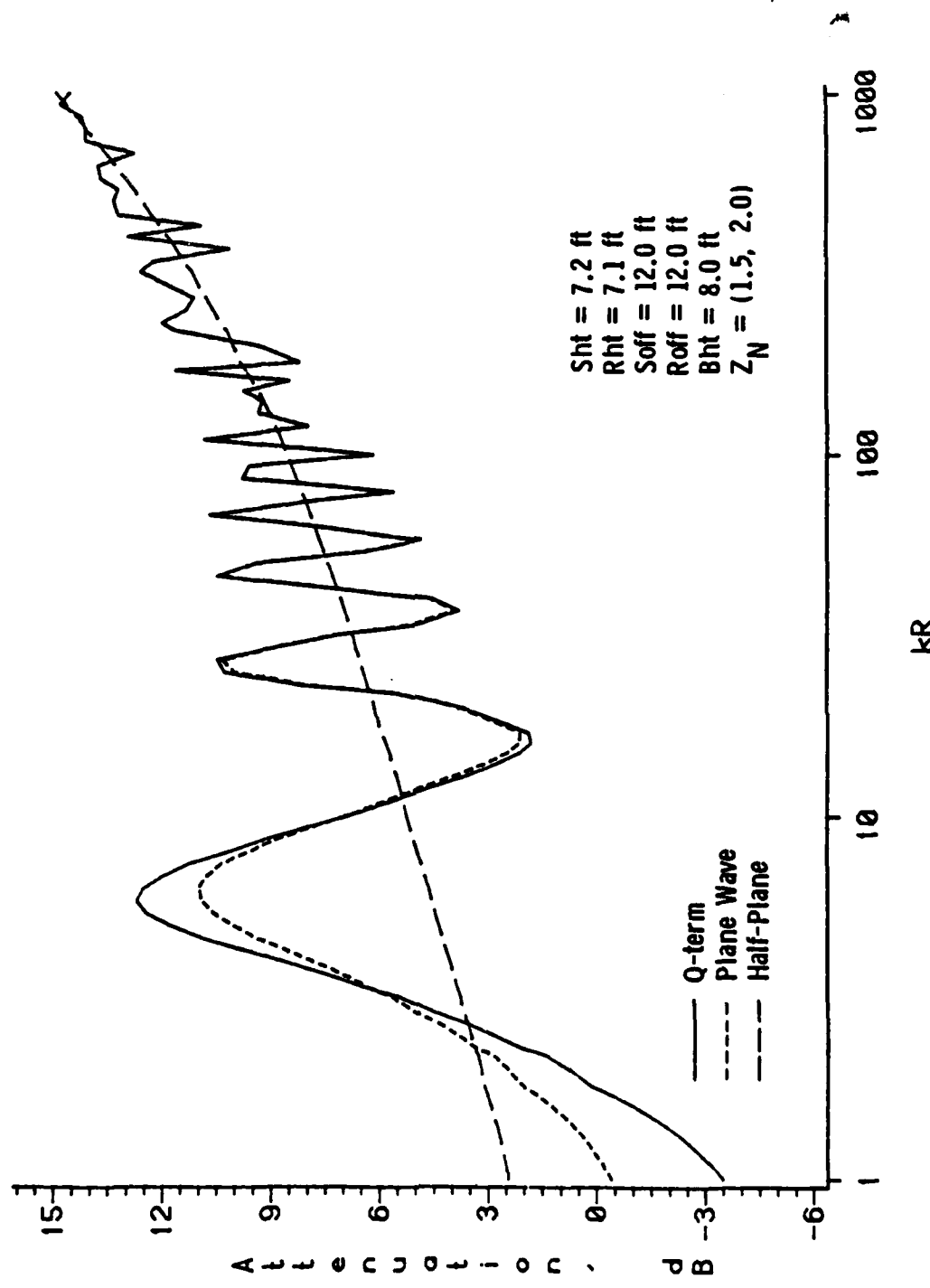


Figure 4.22 Calculated Data for Attenuation as a Function of kR . Q-term, Plane Wave, and Half-Plane Solutions. Large Source and Receiver Heights, Large Barrier Height, Low Impedance.

two geometries). The barrier is at 8.0 feet and the ground impedance is $Z_N = (1.5, 2.0)$. The first peak in the attenuation is due to the ground impedance; it occurs at a low value of kR because the reflection angles are now large (recall the trend noted in Section 4.1.1 that as ψ increased, the peak shifted to lower kR). The series of peaks and troughs for $kR \geq 10$ are due to path length interferences among the four ray paths considered in the Edge-Plus-Images model. Besides the fact that the plane wave solution is valid here for kR larger than 10, the interesting feature of the graph is that the half-plane solution seems to predict the "average" attenuation.

The next series of graphs, Figures 4.23 - 4.24 show the effects of having different impedances on each side of the barrier. For all four cases, the source height is 0.25 feet; the receiver height is 8.0 feet; the source and receiver are 60.0 feet from the barrier; and the barrier is 15.0 feet high. The geometry is realistic for a practical highway noise barrier problem. First, the data for a hard ($Z_N = [100.0, 150.0]$) ground beneath both source and receiver is plotted in Figure 4.23 (a) (plane wave and Q-term solutions only). For such a high impedance, both solutions are accurate. When the ground on the receiver side is assigned a constant impedance $Z_2 = (2.0, 2.5)$, the data in Figure 4.23 (b) result. The overall attenuation is increased at lower frequencies as the first peak in Figure 4.23 (a) shifts to the left; also, the solutions begin to show differences. The effect of the impedance at high frequencies is simply to "smooth" the peaks and troughs, as the average attenuation changes little.

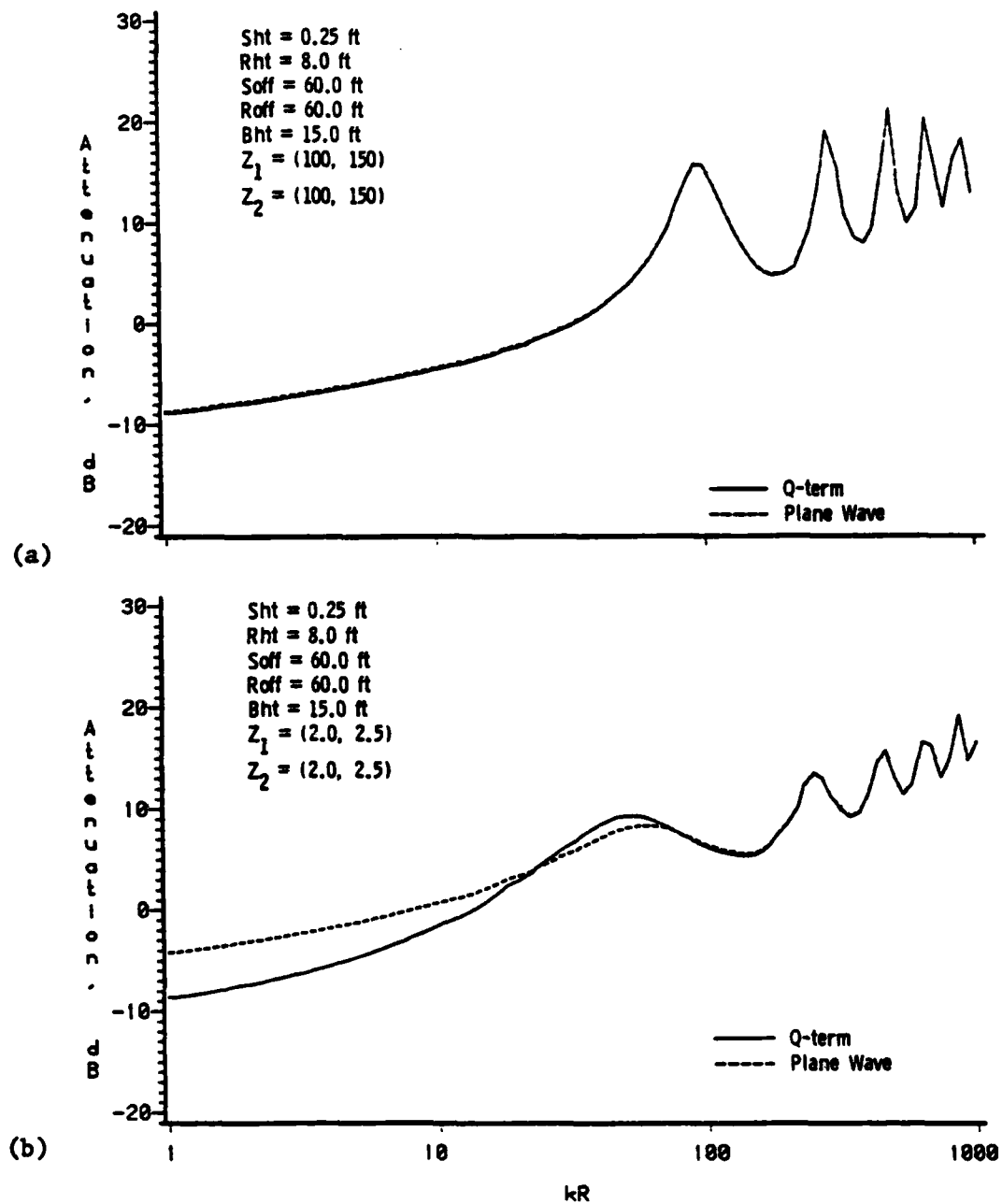


Figure 4.23 Calculated Data for Attenuation as a Function of kR .
Q-term and Plane Wave Solutions. $Sht=0.25$, $Rht=8.0$,
 $Bht=15.0$. In (a) $Z_1 = (100, 150)$, $Z_2 = (100, 150)$
and in (b) $Z_1 = (2.0, 2.5)$, $Z_2 = (2.0, 2.5)$.

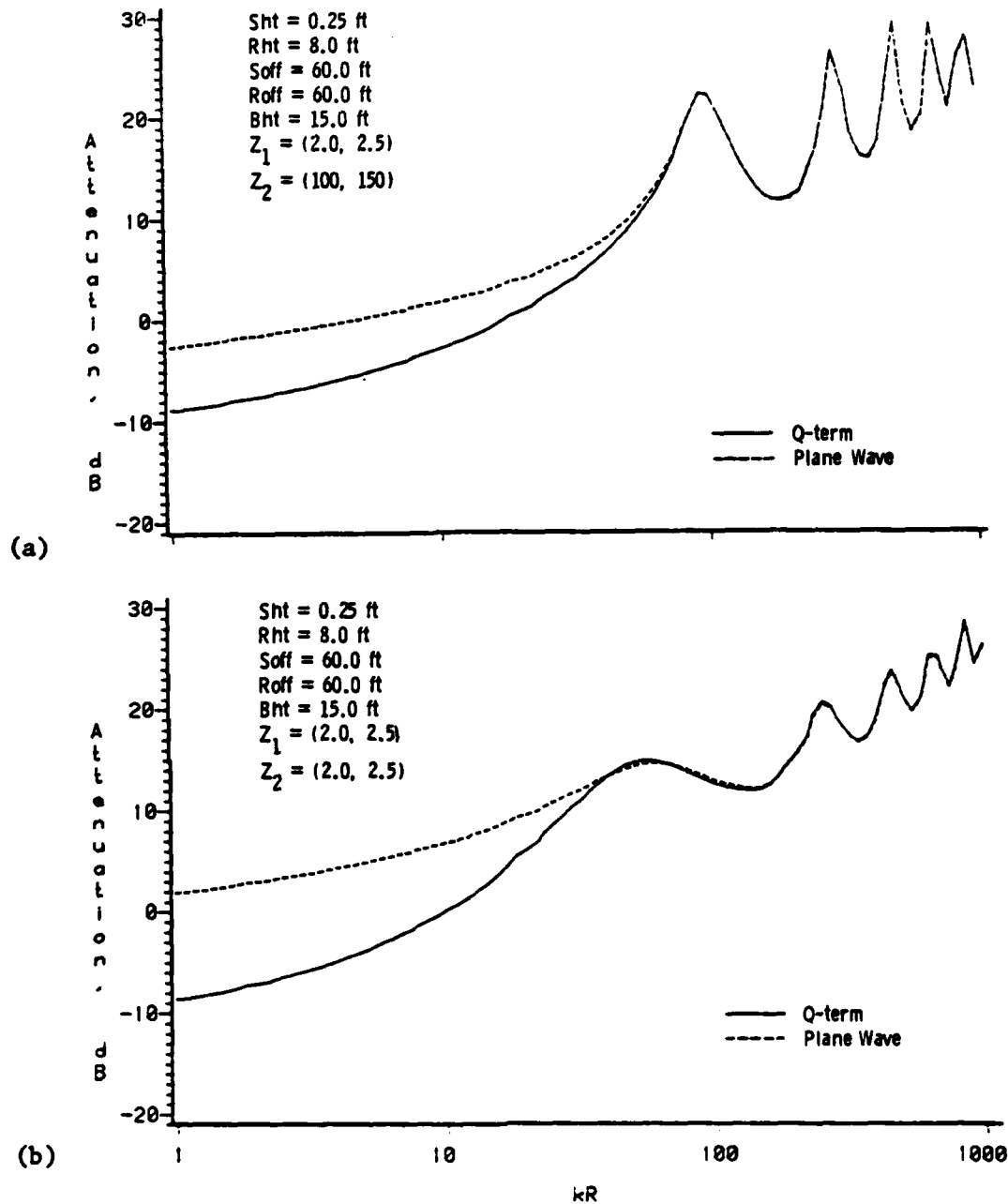


Figure 4.24 Calculated Data for Attenuation as a Function of kR .
 Q-term and Plane Wave Solutions. $Sht=0.25$, $Rht=8.0$,
 $Bht=15.0$. In (a) $Z_1 = (2.0, 2.5)$, $Z_2 = (100, 150)$
 and in (b) $Z_1 = (2.0, 2.5)$, $Z_2 = (2.0, 2.5)$.

If the soft ground were located under the source instead of the receiver, Figure 4.24 (a) would describe the resulting attenuation. This shows several noteworthy features. First, the entire curve is shifted up relative to the hard-ground case in Figure 4.23 (a). Second, the first peak of attenuation centered at about $kR=100$ does not shift; and third, there is no smoothing of the high-frequency peaks (although the average is now higher). All of these results are due to the fact that, unlike the receiver, the source is very close to the ground and the propagation is at near-grazing angles, resulting in higher losses. Since the "incident" field at the barrier edge is reduced by the source ground impedance layer, the entire pattern of receiver-side interference is shifted upward but not changed in character. Finally, when the ground on both sides is soft, as in Figure 4.24(b), the effects are cumulative: an overall increase in attenuation, a shifting of the first peak, and a smoothing of the interference peaks.

To conclude this section, a case for which the incident ray strikes the barrier edge obliquely will be investigated. The geometry is the same as in the previous case except that $z_0 = 100$ (Figure 4.17 [b]), giving an angle $\beta = 50^\circ$. The ground impedance is $Z_N = (100.0, 150.0)$. Figure 4.25 shows the resulting attenuation, with the results of Figure 4.23 (a) superimposed for comparison. Since a factor of $\sin\beta$ appears in the denominator of the diffraction coefficient given in Equation (3.4), the coefficient itself increases as the angle β decreases. The numerical predictions thus indicate a lower

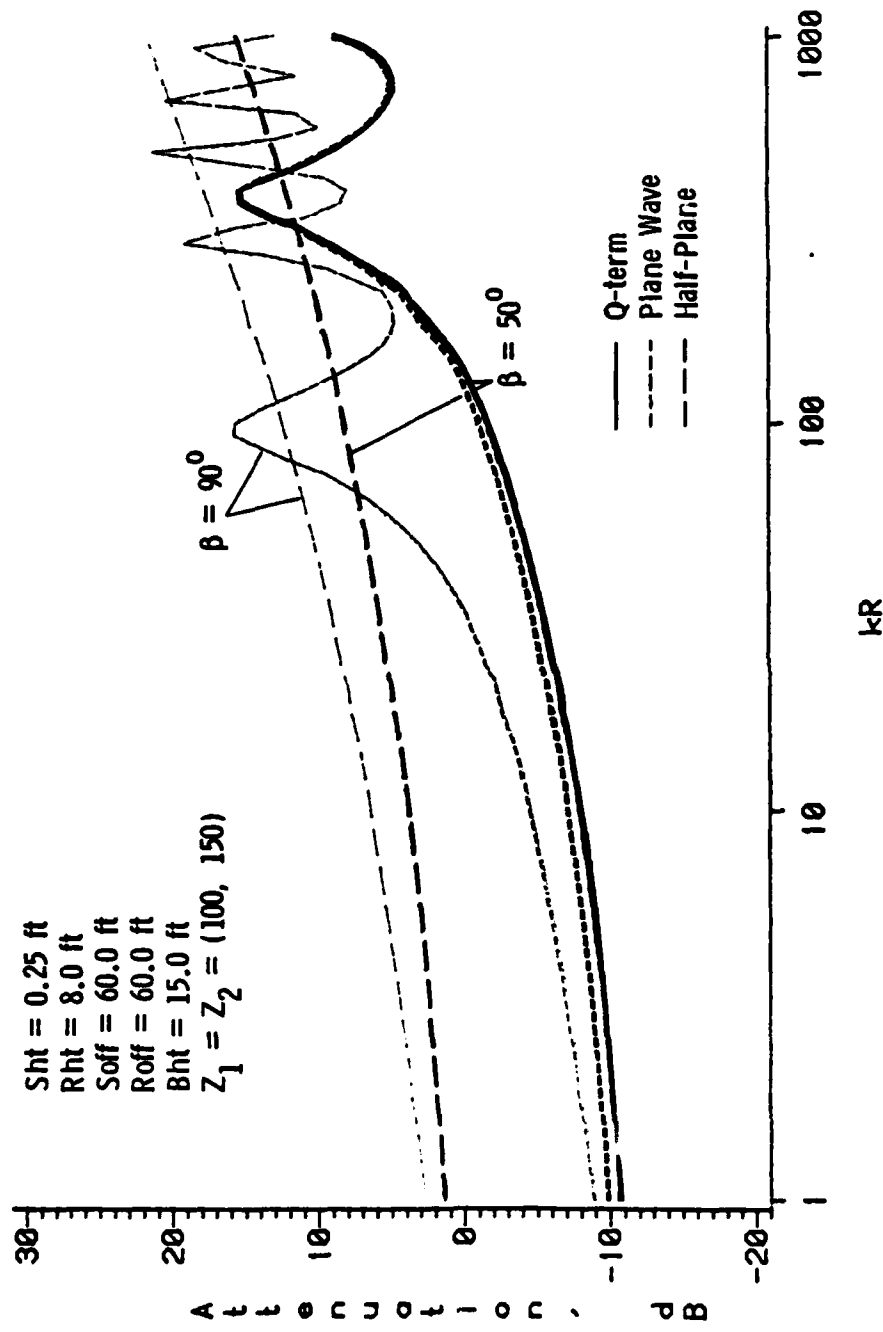


Figure 4.25 Comparison of Results for Perpendicular and Oblique Incidence on the Edge as a Function of kR . Q-term, Plane Wave, and Half-Plane Solutions. Hard Ground, $\beta = 90^\circ$ or $\beta = 50^\circ$.

attenuation for the oblique incidence case. As this is not a ground-related effect, the half-plane solution (long-dashed line) predicts the same trend.

The geometry and impedance conditions for the plots presented in this section are summarized in Table 4.6.

4.2.2 The Dependence on Barrier Height

Half-plane diffraction theory predicts the simple formula for fixed source and receiver positions: the greater the barrier height, the greater the attenuation. While this is generally true in practice, consideration of the ground reflections and impedance conditions greatly affects the predicted attenuation, and sometimes leads to unexpected results.

The data plotted in Figures 4.26 and 4.27 compare the predicted attenuation and insertion loss for a soft ($Z_N=[1.5, 2.0]$) ground with that for a relatively hard ($Z_N=[15.0, 20.0]$) ground. The source and receiver are close to the surface (0.5 feet) and relatively far from the barrier (60 feet), and kR is assigned a small value (5.0). The barrier height ranges from 0.1 to 25 feet. Several observations can be made. First, the low value of kR is responsible for the large differences between the plane wave solution and the Q-term solution. Even when the barrier is at maximum height (the ground reflection angles are near 25°), there remains a 7 dB difference for the low-impedance case and a 1 dB difference for the higher-impedance case. Second, the overall effects of diffraction are minimal on the Q-term

Table 4.6

Summary of the Geometry and Impedance Conditions
for the Numerical Data Plotted in Section 4.2.1

<u>Source Height (ft)</u>	<u>Receiver Height (ft)</u>	<u>Source Offset (ft)</u>	<u>Receiver Offset (ft)</u>	<u>Barrier Height (ft)</u>	<u>Z_N</u>	<u>Figure</u>
0.2	0.1	12.0	12.0	1.0	(1.5, 2.0)	4.18(a), 4.18(b)
0.2	0.1	12.0	12.0	1.0	(15.0, 20.0)	4.19(a), 4.19(b)
0.2	0.1	12.0	12.0	8.0	(1.5, 2.0)	4.20(a), 4.20(b)
0.2	0.1	12.0	12.0	8.0	(15.0, 20.0)	4.21(a), 4.21(b)
7.2	7.1	12.0	12.0	8.0	(1.5, 2.0)	4.22
0.25	8.0	60.0	60.0	15.0	$Z_1=(100, 150)$ $Z_2=(100, 150)$	4.23(a)
0.25	8.0	60.0	60.0	15.0	$Z_1=(100, 150)$ $Z_2=(2.0, 2.5)$	4.23(b)
0.25	8.0	60.0	60.0	15.0	$Z_1=(2.0, 2.5)$ $Z_2=(100, 150)$	4.24(a)
0.25	8.0	60.0	60.0	15.0	$Z_1=(2.0, 2.5)$ $Z_2=(2.0, 2.5)$	4.24(b)

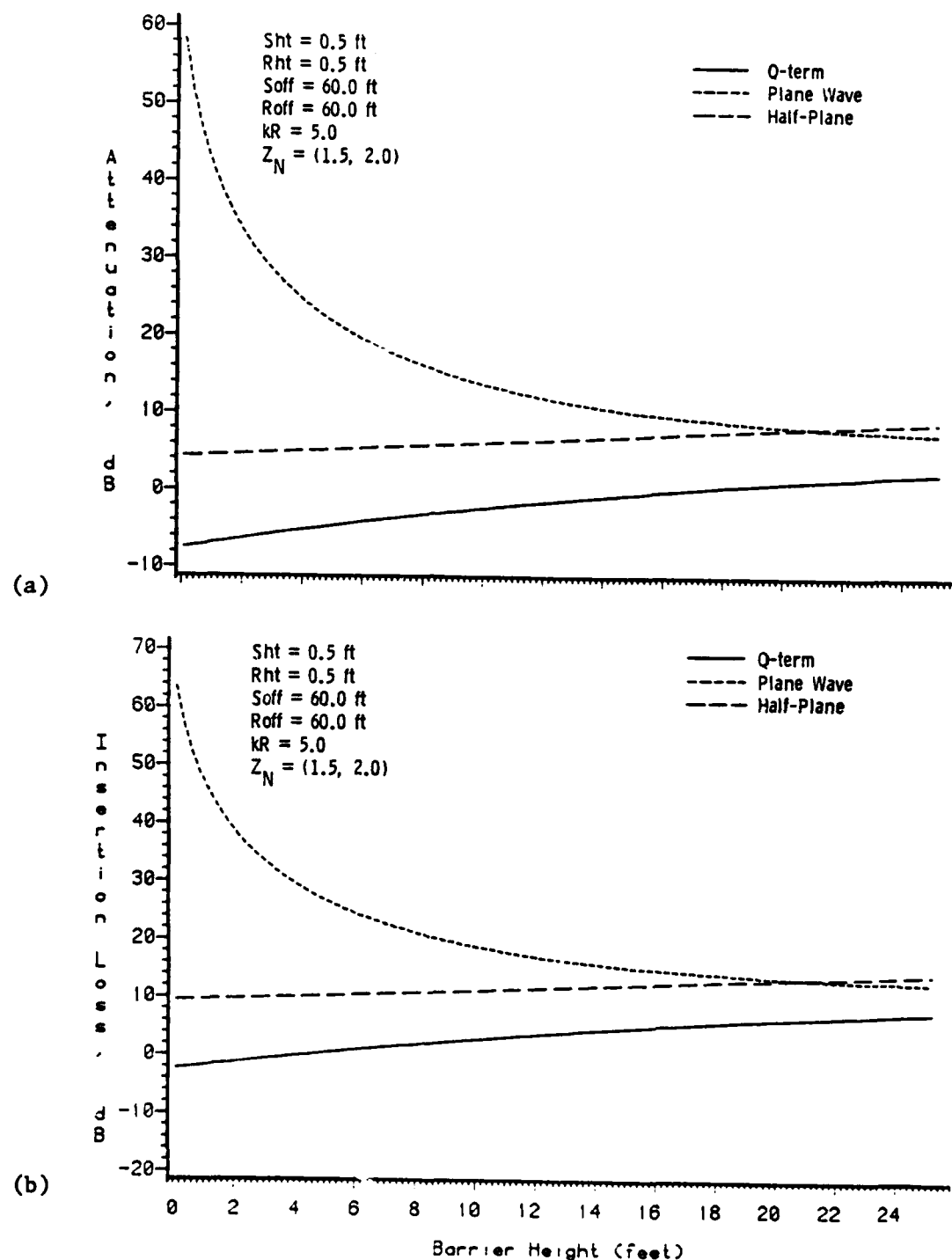


Figure 4.26 Calculated Data for (a) Attenuation and (b) Insertion Loss as a Function of Barrier Height. Q-term, Plane Wave, and Half-Plane Solutions. Small Source and Receiver Heights, Small kR, Low Impedance.

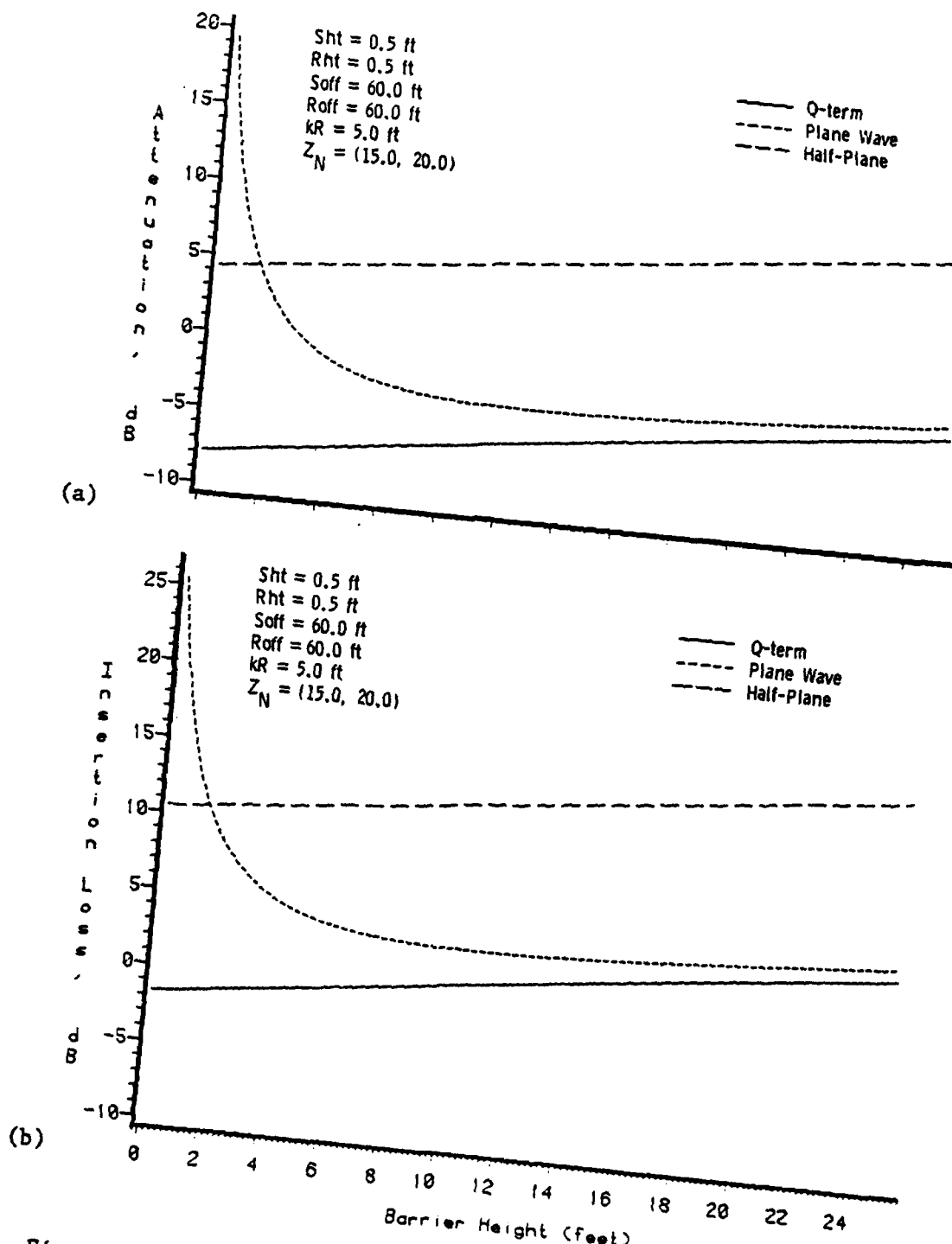


Figure 4.27 Calculated Data for (a) Attenuation and (b) Insertion Loss as a Function of Barrier Height. Q-term, Plane Wave, and Half-Plane Solutions. Small Source and Receiver Heights, Small kR, High Impedance.

predictions as the insertion loss is close to zero over most of the range of barrier height. This is simply a consequence of the very low frequencies being considered here.

Figures 4.28 and 4.29 show data for the same geometry as above, but here the value of kR has been increased by a factor of ten to $kR=50$. The plane wave and Q-term solutions are more in accord here. In fact, for barrier heights above 12 feet the predictions are within 1 dB for either impedance condition. The fact that a broad peak in attenuation appears for the soft ground and not for harder ground indicates that this is an "impedance effect" similar to that noticed in previous ground propagation curves.

The two insertion loss curves in Figures 4.28 (b) and 4.29 (b) reveal an interesting trend that was noted in the previous section. That is, the insertion loss is near zero for high barriers on the soft ground, while it steadily increases with height for barriers on the harder ground. In fact, for the soft ground, the insertion loss shows a steady decline (Figure 4.28 [b]) for heights above 4 feet; therefore, increasing the barrier height beyond this value would be counterproductive (in the noise control sense).

The counteracting impedance and diffraction effects mentioned in the previous section, are apparent in the next pair of graphs. In Figure 4.30 (a) and (b), the source and receiver have been raised above the ground to heights of 4 feet, but all other conditions are the same as in the previous curves. For the case where $Z_N = (1.5, 2.0)$, the attenuation stays relatively constant as the barrier height

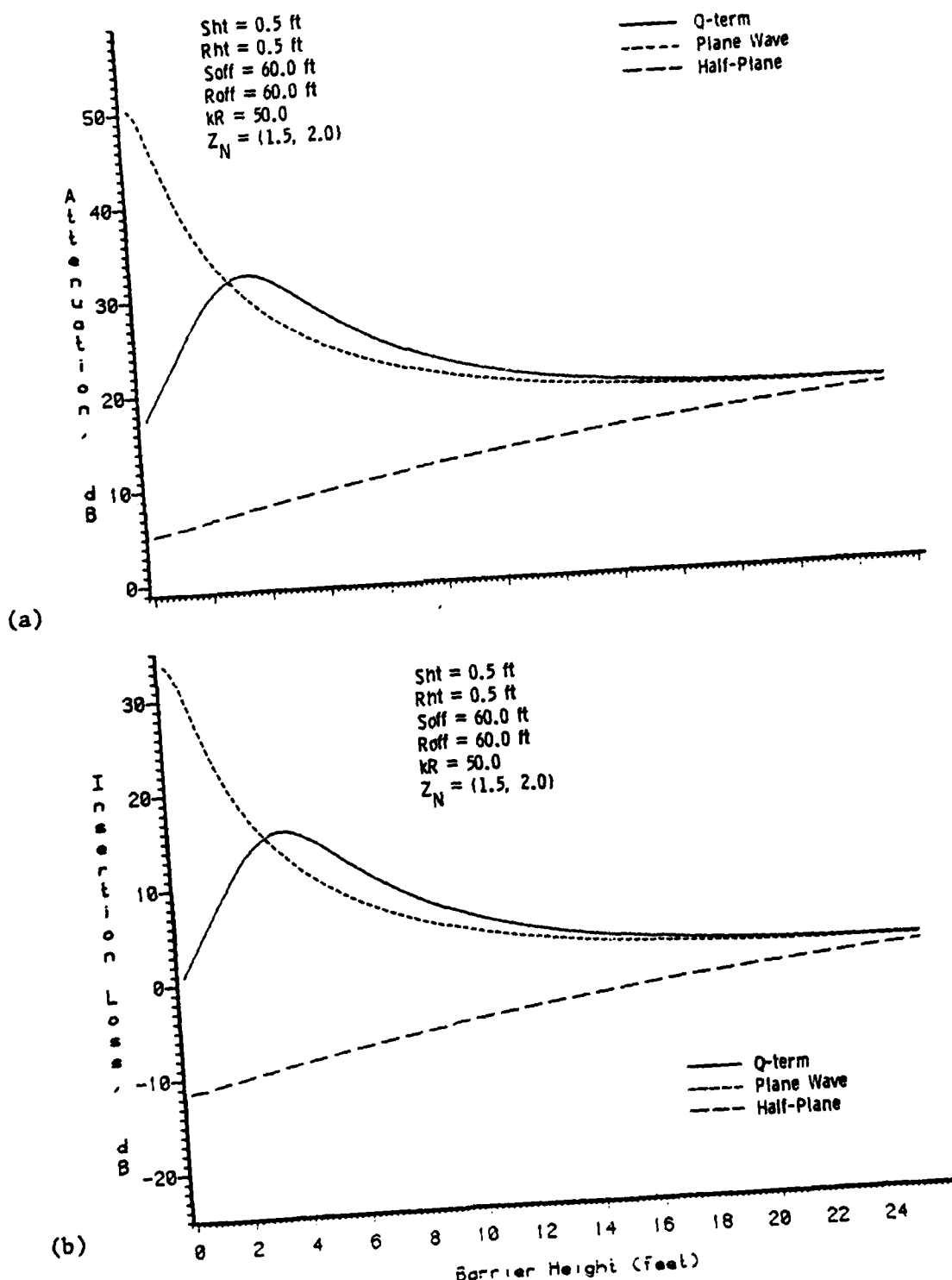


Figure 4.28 Calculated Data for (a) Attenuation and (b) Insertion Loss as a Function of Barrier Height. Q-term, Plane Wave, and Half-Plane Solutions. Small Sht and Rht, Large kR, Low Impedance

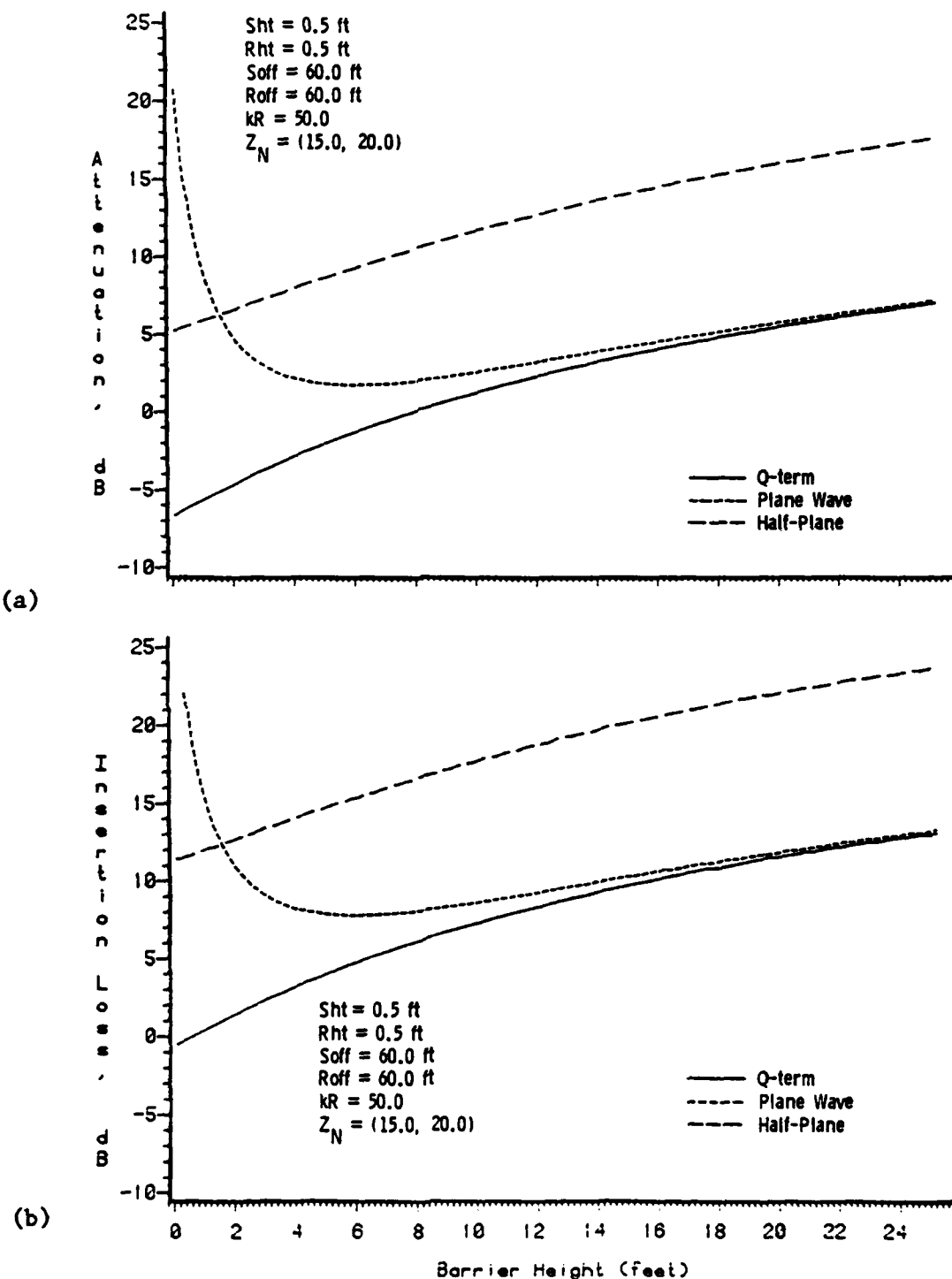


Figure 4.29 Calculated Data for (a) Attenuation and (b) Insertion Loss as a Function of Barrier Height. Q-term, Plane Wave, and Half-Plane Solutions. Small Source and Receiver Heights, Large kR , High Impedance.

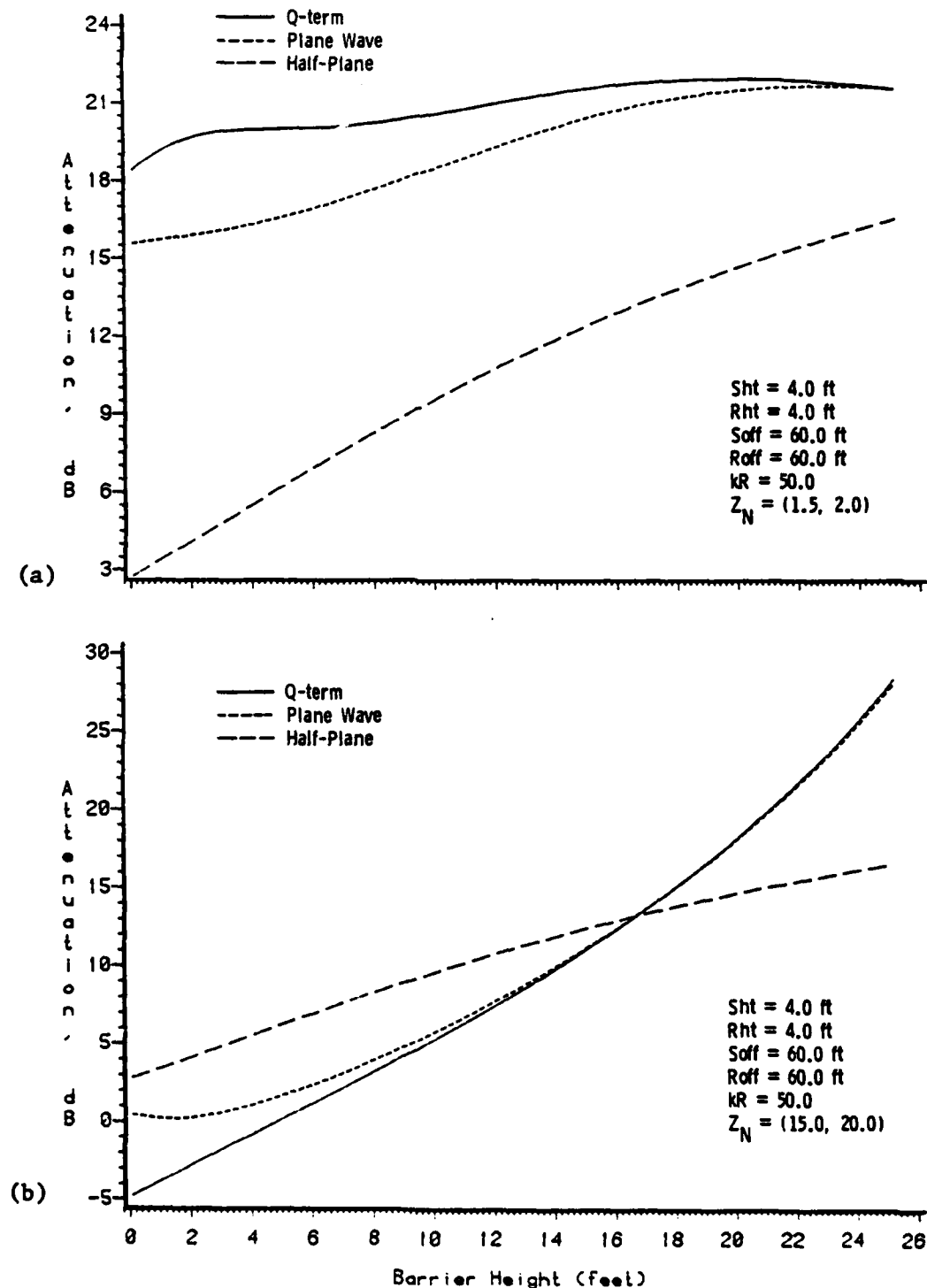


Figure 4.30 Calculated Data for Attenuation as a Function of Barrier Height. Q-term, Plane Wave, and Half-Plane Solutions. $S_{ht}=4.0$, $R_{ht}=4.0$, $kR=50.0$. In (a) $Z_N = (1.5, 2.0)$ and in (b) $Z_N = (15.0, 20.0)$.

increases. On the other hand, each ray path in the Edge-Plus-Images model (Figure 3.4) should experience a trend similar to that shown by the single-ray half-plane diffraction solution plotted on the same graph. That is, each of the four paths is attenuated more heavily as the barrier height increases. However, the strength of each ground-reflected path gets larger as the reflection angle increases (approximately, from 4° to 25° over the range of barrier heights). This effect offsets the increase in attenuation due to diffraction. Finally, it can be seen that this phenomenon does not occur for the harder ($Z_N=[100.0, 150.0]$) ground shown in Figure 4.30 (b); the impedance effect is not pronounced since the ground appears hard throughout the range of reflection angles. Thus, the attenuation steadily increases with barrier height.

To conclude this section, two additional sets of curves are presented in Figures 4.31 and 4.32 for large values of kR . The parameter values are indicated on the graphs. Essentially, both plots are for soft ground but the former has the receiver well above the ground while the latter has it very close to the ground. The plane wave solution is accurate in either case over the full range of barrier heights. Other important observations are that path length interference effects are present for the elevated receiver, and that the insertion loss is negative when the source and receiver are near the ground.

Table 4.7 presents a summary of the geometrical and impedance conditions for the numerical results plotted in this section.

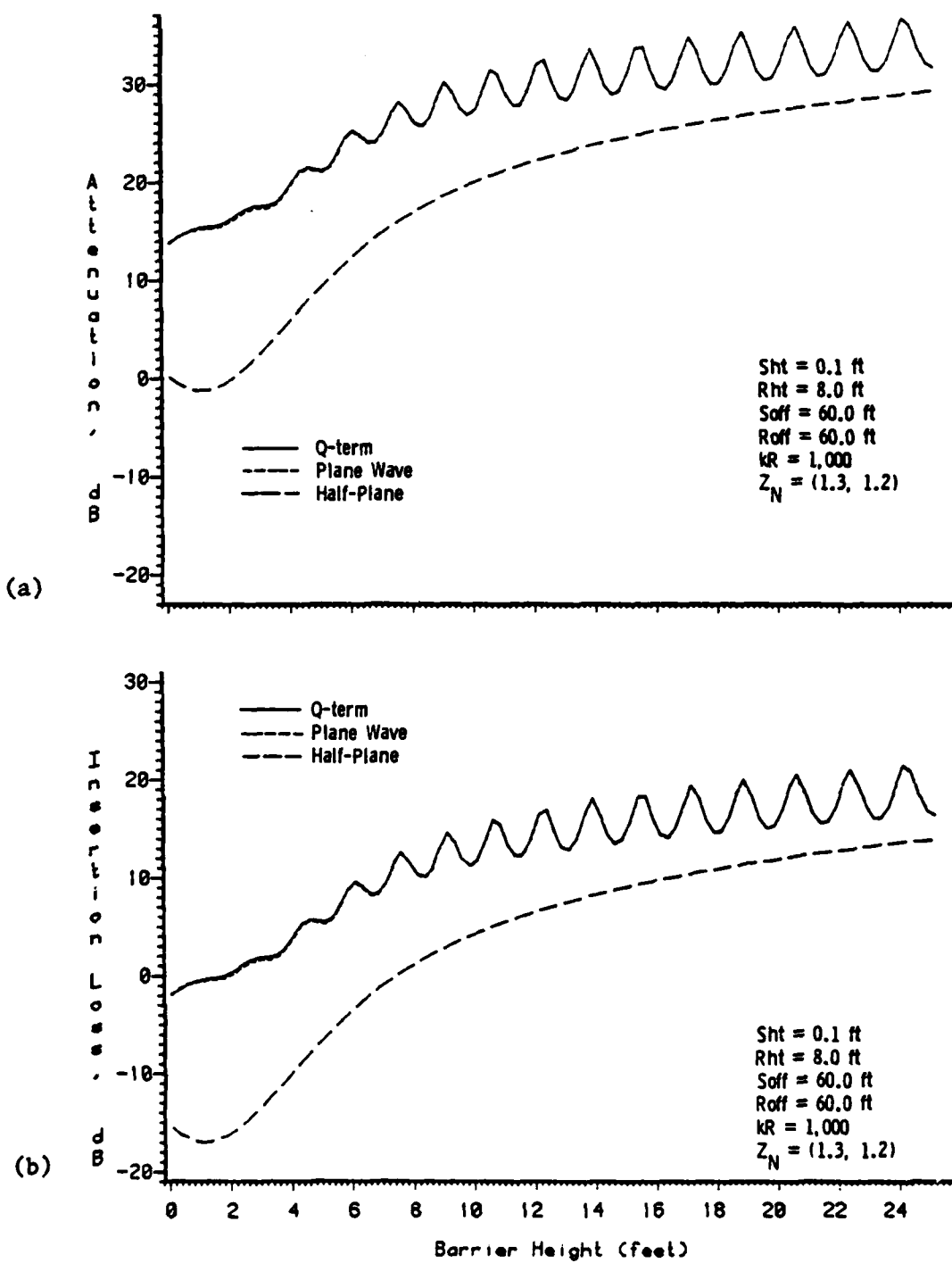


Figure 4.31 Calculated Data for (a) Attenuation and (b) Insertion Loss as a Function of Barrier Height. Q-term, Plane Wave, and Half-Plane Solutions. $S_{ht}=0.1$, $R_{ht}=8.0$, $kR=1000$, and $Z_N = (1.3, 1.2)$.

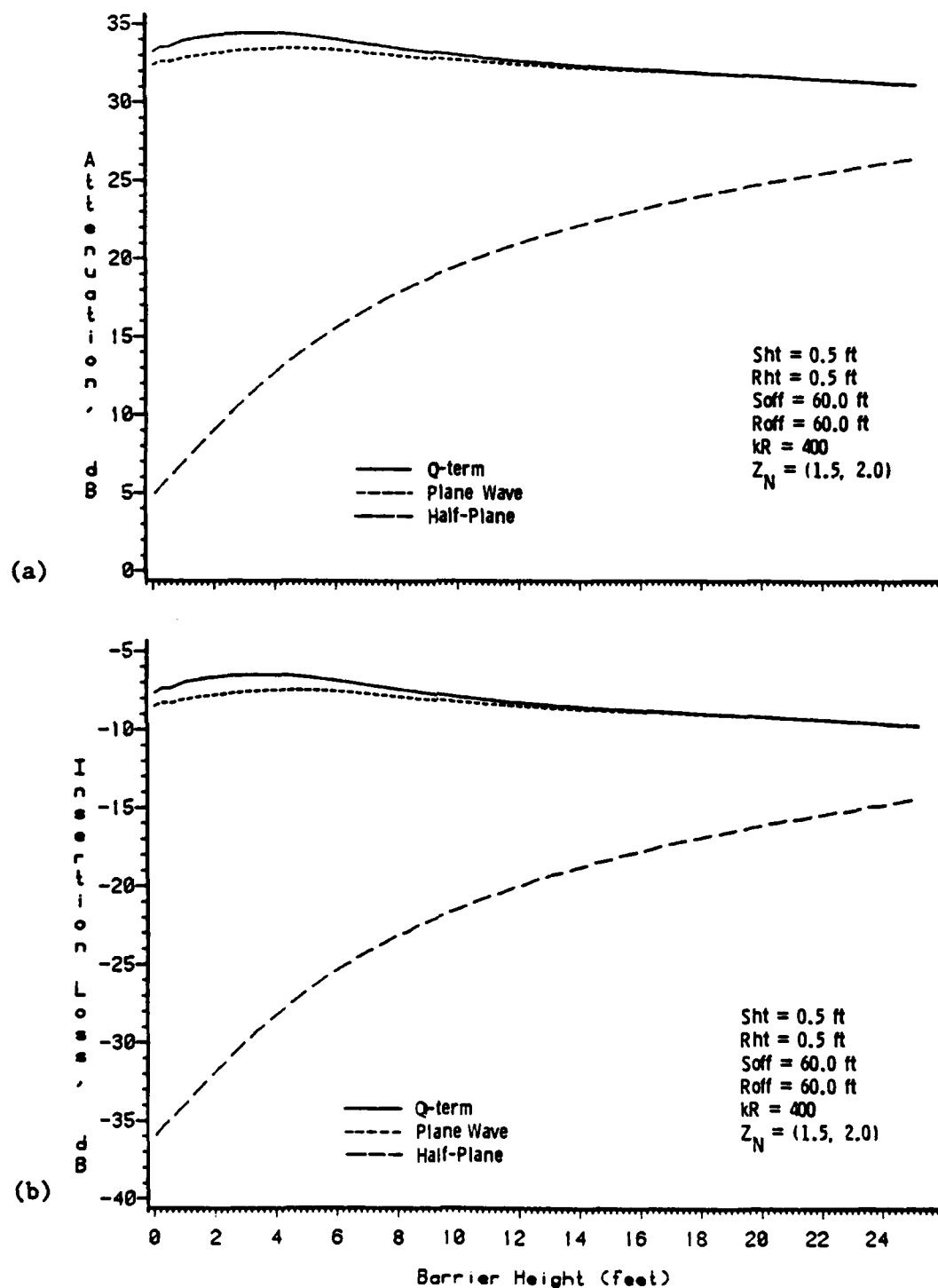


Figure 4.32 Calculated Data for (a) Attenuation and (b) Insertion Loss as a Function of Barrier Height. Q-term, Plane Wave, and Half-Plane Solutions. $S_{ht}=0.5$, $R_{ht}=0.5$, $kR=400$, and $Z_N = (1.5, 2.0)$.

Table 4.7

Summary of the Geometry and Impedance Conditions
for the Numerical Data Plotted in Section 4.2.2.

<u>Source Height (ft.)</u>	<u>Receiver Height (ft.)</u>	<u>Source Offset (ft.)</u>	<u>Receiver Offset (ft.)</u>	<u>kR</u>	<u>z_N</u>	<u>Figure</u>
0.5	0.5	60.0	60.0	5.0	(1.5, 2.0)	4.26(a), 4.26(b)
0.5	0.5	60.0	60.0	5.0	(15.0, 20.0)	4.27(a), 4.27(b)
0.5	0.5	60.0	60.0	50.0	(1.5, 2.0)	4.28(a), 4.28(b)
0.5	0.5	60.0	60.0	50.0	(15.0, 20.0)	4.29(a), 4.29(b)
4.0	4.0	60.0	60.0	50.0	(1.5, 2.0)	4.30(a)
4.0	4.0	60.0	60.0	50.0	(15.0, 20.0)	4.30(b)
0.1	8.0	60.0	60.0	1000.0	(1.3, 1.2)	4.31(a), 4.31(b)
0.5	0.5	60.0	60.0	400.0	(1.5, 2.0)	4.32(a), 4.32(b)

4.2.3 Dependence on Diffraction Angle ϕ

The diffraction angle ϕ defined in Figure 4.17 naturally depends on the barrier height and the receiver position. Consequently, many observations regarding the dependence of the field on ϕ have already been, or can be, made from the numerical data presented thus far. However, for completeness, several cases will be presented here showing this dependence explicitly.

The numerical data predicted from the plane wave, Q-term, and half-plane theories for a source 0.2 feet above the ground and a barrier of height 5.0 feet are plotted in Figures 4.33 - 4.36. Sequentially, the graphs show a small kR coupled with a low or a high ground impedance, and a large kR with a low or a high ground impedance. In these plots, the receiver distance from the edge, R_2 , is held constant as the angle ϕ is varied. Consequently, the receiver revolves about the the edge point E, moving from its starting point on the ground behind the barrier (ϕ maximum) to its final position directly above the edge ($\phi = 0^\circ$). At some point in this angular range, the receiver will cross the incident shadow boundary and pass into the illuminated region of the source. For the geometry considered here, the shadow boundary from the source occurs at 69.2° , and this value (Φ_{sb}) is marked by a vertical line on the graphs.²⁹

²⁹ The values marked on the axis for the angle ϕ are actually absolute values; the cylindrical coordinate system used in the development of the model define the angle ϕ to be negative on the receiver side of the barrier.

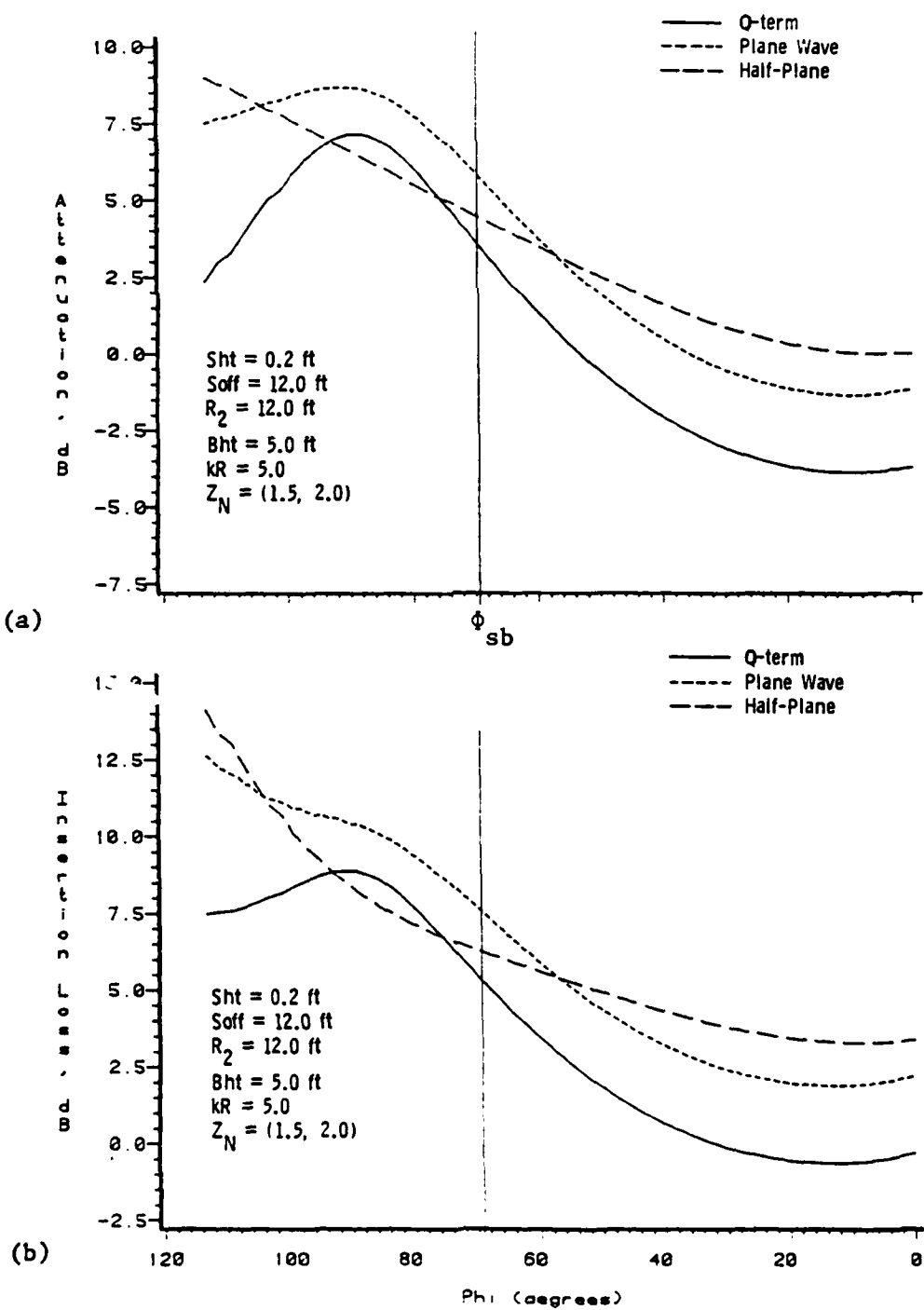


Figure 4.33 Calculated Data for (a) Attenuation and (b) Insertion Loss as a Function of Diffraction Angle. Q-term, Plane Wave, and Half-Plane Solutions $S_{ht}=0.2$, $R_2=12.0$, $kR=5.0$, $B_{ht}=5.0$, and $Z_N=(1.5, 2.0)$.

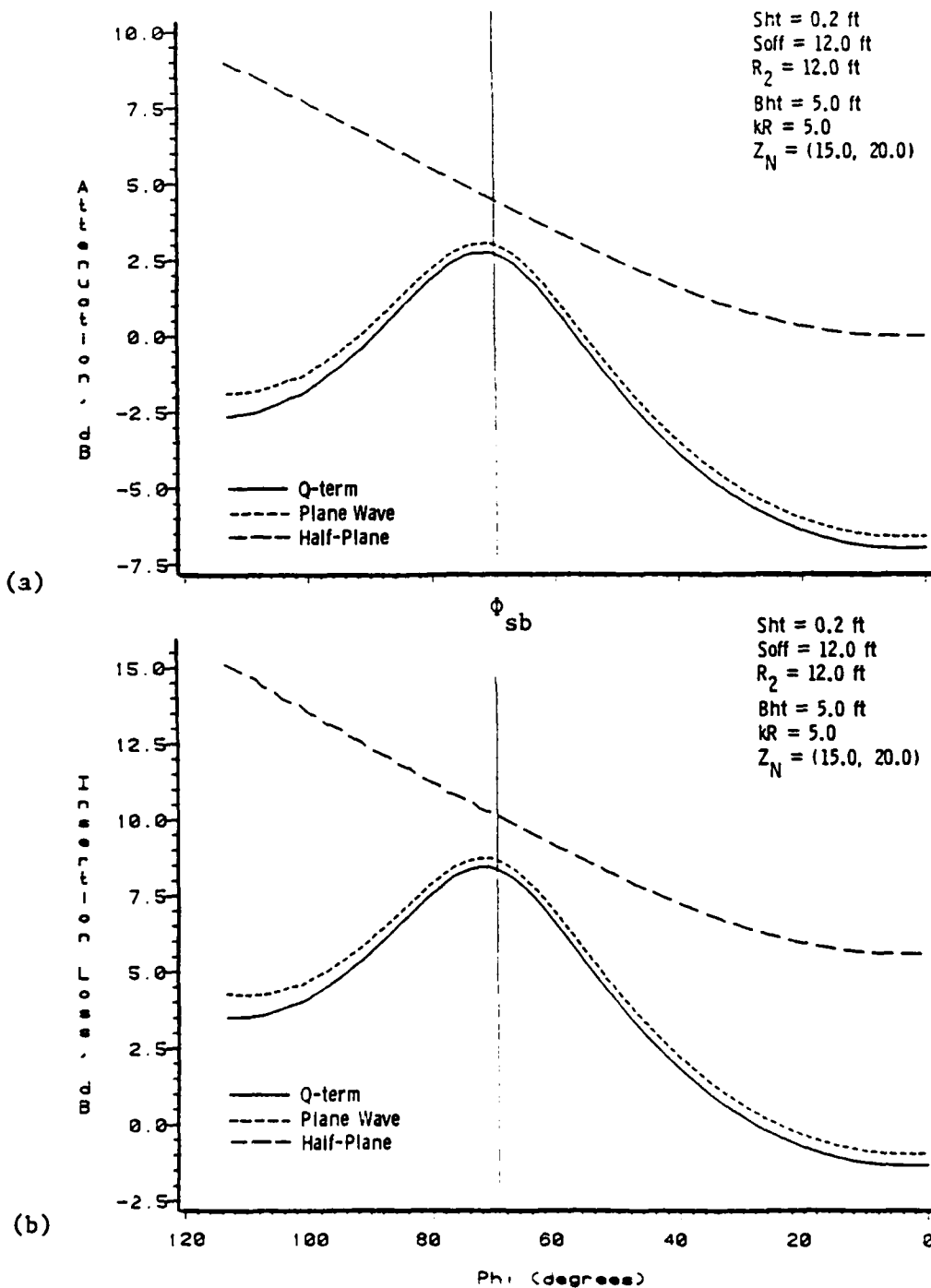


Figure 4.34 Calculated Data for (a) Attenuation and (b) Insertion Loss as a Function of Diffraction Angle. Q-term, Plane Wave, and Half-Plane Solutions. $Sht=0.2$, $R_2=12.0$, $kR=5.0$, $Bht=5.0$, and $Z_N=(15.0, 20.0)$.

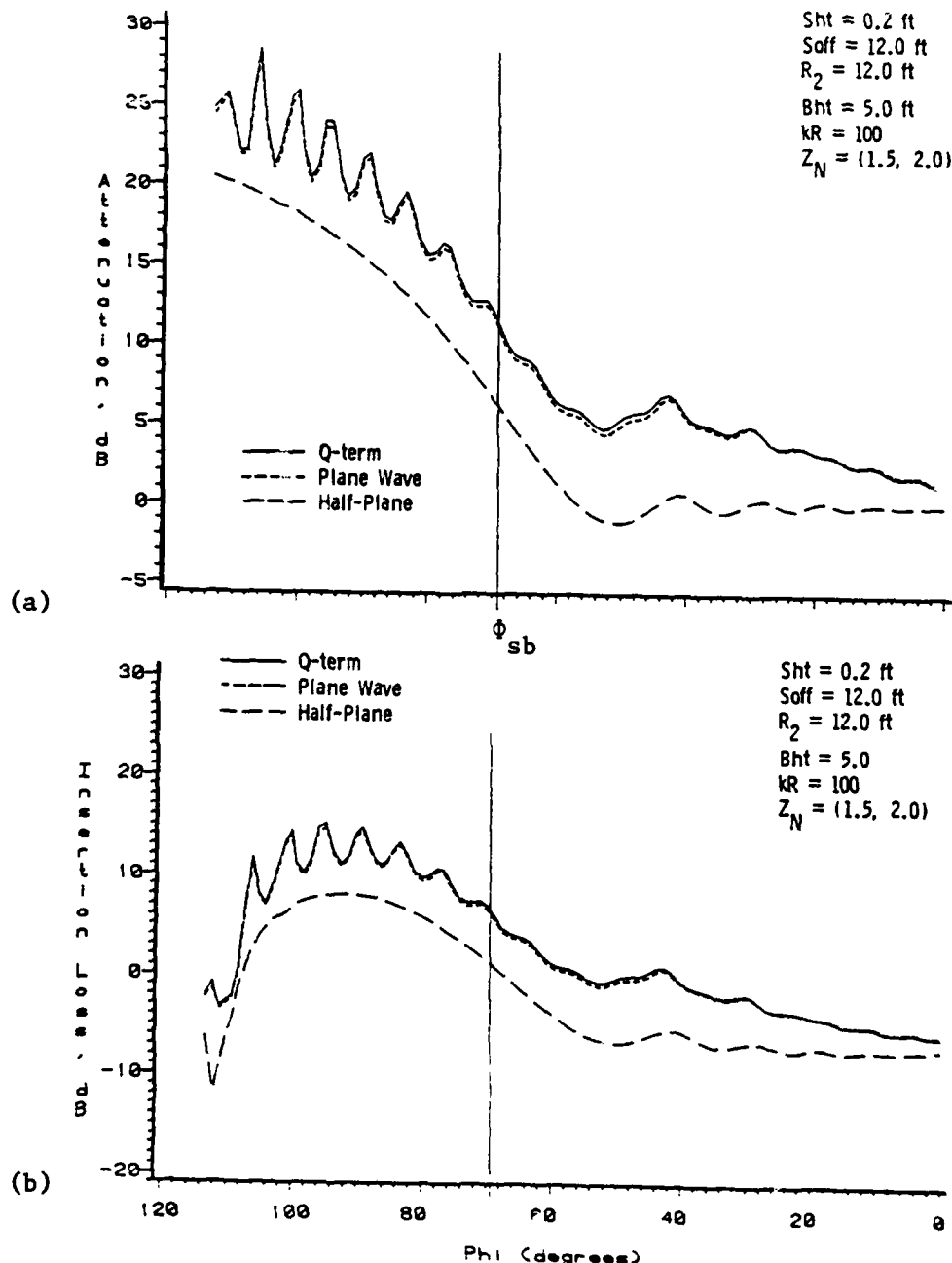
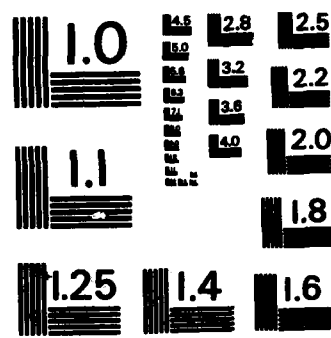


Figure 4.35 Calculated Data for (a) Attenuation and (b) Insertion Loss as a Function of Diffraction Angle. Q-term, Plane Wave, and Half-Plane Solutions. $S_{ht}=0.2$, $R_2=12.0$, $B_{ht}=5.0$, and $Z_N=(1.5, 2.0)$.

AD-A122 023 ACOUSTIC PROPAGATION AND BARRIER DIFFRACTION OVER AN 3/3
IMPEDANCE PLANE(U) PENNSYLVANIA STATE UNIV UNIVERSITY
PARK APPLIED RESEARCH LAB. M A NOBILE 13 OCT 82
UNCLASSIFIED ARL/PSU/TM-82-218 N00024-79-C-6043 F/G 12/1 NL

END

FILMED
SI
OTIC



MICROCOPY RESOLUTION TEST CHART
NATIONAL BUREAU OF STANDARDS - 1963 - A

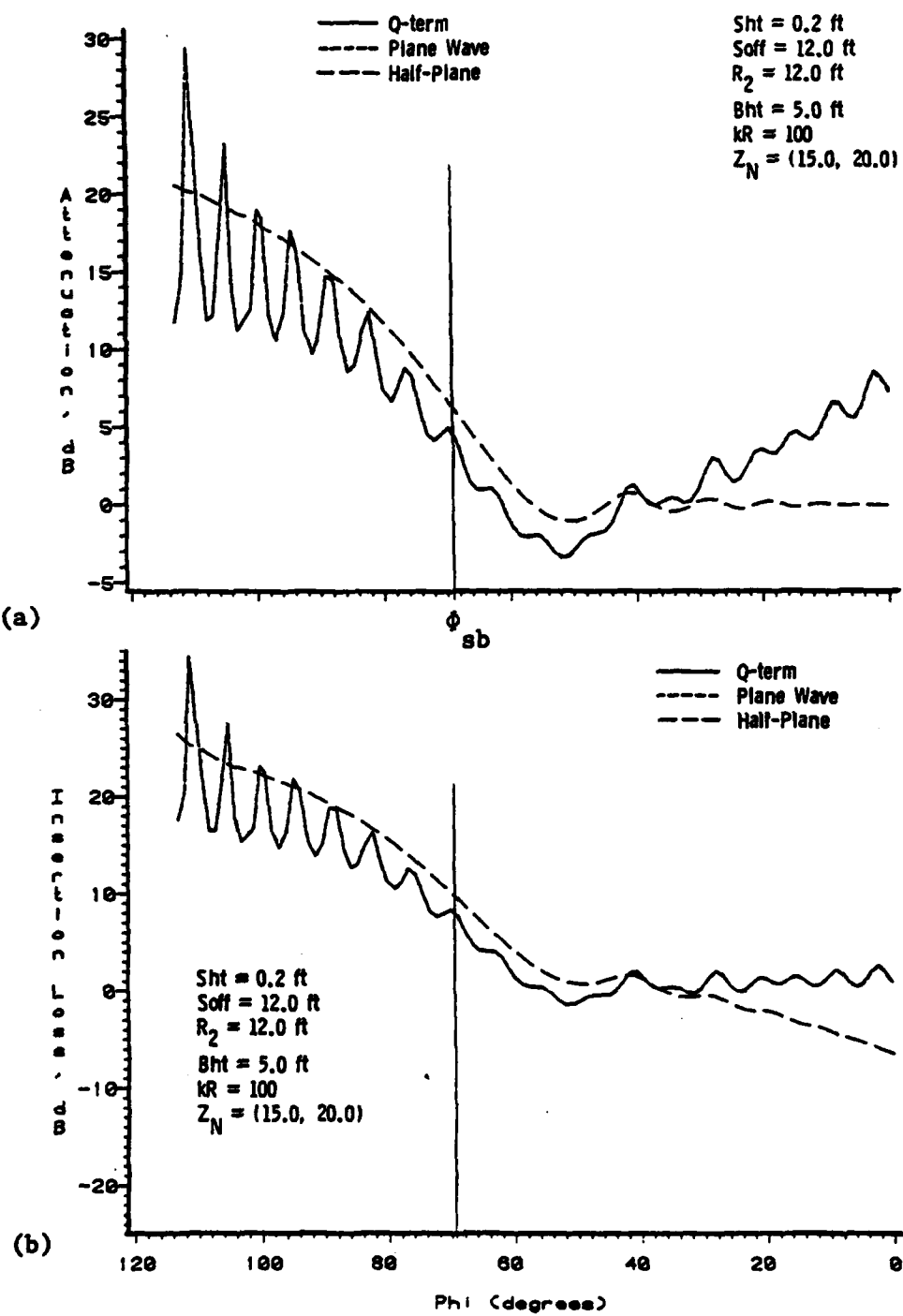


Figure 4.36 Calculated Data for (a) Attenuation and (b) Insertion Loss as a Function of Diffraction Angle. Q-term, Plane Wave, and Half-Plane Solutions. $Sht=0.2$, $R_2=12.0$, $kR=100$, $Bht=5.0$, and $Z_N=(15.0, 20.0)$.

The only significant differences between the plane wave and the Q-term predictions (for this particular barrier height) are for the low-impedance ($Z_N=[1.5,2.0]$), small kR ($kR=5.0$) case shown in Figure 4.33. For the distances considered here ($R=24.0$), this value of kR corresponds to a frequency of 37 Hz., and it is very unlikely that any practical material (in air) would possess such a low impedance at this low frequency. The cases with a low value of kR show a broad peak in the attenuation or insertion loss response, whereas the cases with the higher value of kR show the expected steady decline as the receiver approaches the incident shadow boundary. It is interesting to note that for the large kR case, the simple half-plane diffraction model overpredicts the attenuation for the hard ground and underpredicts it for the soft ground.

Some further comments about the shadow boundary may be appropriate here. It is well known that the presence of the Fresnel integrals in the diffraction coefficient (Equation [3.4]), ensures that the diffracted field is continuous across the shadow boundary. The numerical data plotted here confirm this fact; no abrupt changes occur in either the attenuation or insertion loss data in the vicinity of the shadow boundary. It is also well known that the diffracted field at the shadow boundary itself (for large kR) assumes a value one-half that of the incident field there. This, of course, applies to the diffraction of a single ray only. Therefore, the data in Figures 4.35 (a) and 4.36 (a) show a 6 dB attenuation for the half-plane predictions but a different value when the ground is taken into account (the plane-wave or Q-term data).

As mentioned in the description of the Edge-Plus-Images model in Chapter 3, the source image in the ground also defines its own shadow boundary. That is, there is a "shadow" and an "illuminated" region for the reflected acoustic energy as well as for the direct energy from the source. As the angle ϕ decreases, the receiver may also cross this "image shadow boundary," but, again, there should be no discontinuity in the predicted levels. This is again confirmed by the data, since the shadow boundary for the image source occurs within a few degrees of the incident shadow boundary shown on the graphs.

The relevant parameters for the plots in this section are summarized in Table 4.8.

4.2.4 Received Spectra for a Practical Ground Cover

As noted in Section 4.1.3, the ground impedance is rarely constant over a wide range of frequency values. Therefore, as a practical example, the Edge-Plus-Images prediction model has been applied to a barrier on a ground plane characterized by the third-octave values of impedance given in Table 4.3. The source and receiver are very close to the ground (0.25 feet), and the barrier height is 15.0 feet.

The data plotted in Figure 4.37 are for a perfectly rigid ground. Of course, the plane wave and Q-term solutions are identical, both indicating an attenuation that gradually increases with frequency (diffraction coefficient decreasing with increasing kR) until a sharp peak due to ground reflection interference (path length difference) is

Table 4.8

**Summary of the Geometry and Impedance Conditions
for the Numerical Data Plotted in Section 4.2.3.**

<u>Source Height (ft.)</u>	<u>Source Offset (ft.)</u>	<u>R₂</u>	<u>Barrier Height (ft.)</u>	<u>kR</u>	<u>z_N</u>	<u>Figure</u>
0.2	12.0	12.0	5.0	5.0	(1.5, 2.0)	4.33(a), 4.33(b)
0.2	12.0	12.0	5.0	5.0	(15.0, 20.0)	4.34(a), 4.34(b)
0.2	12.0	12.0	5.0	100.0	(1.5, 2.0)	4.35(a), 4.35(b)
0.2	12.0	12.0	5.0	100.0	(15.0, 20.0)	4.36(a), 4.36(b)

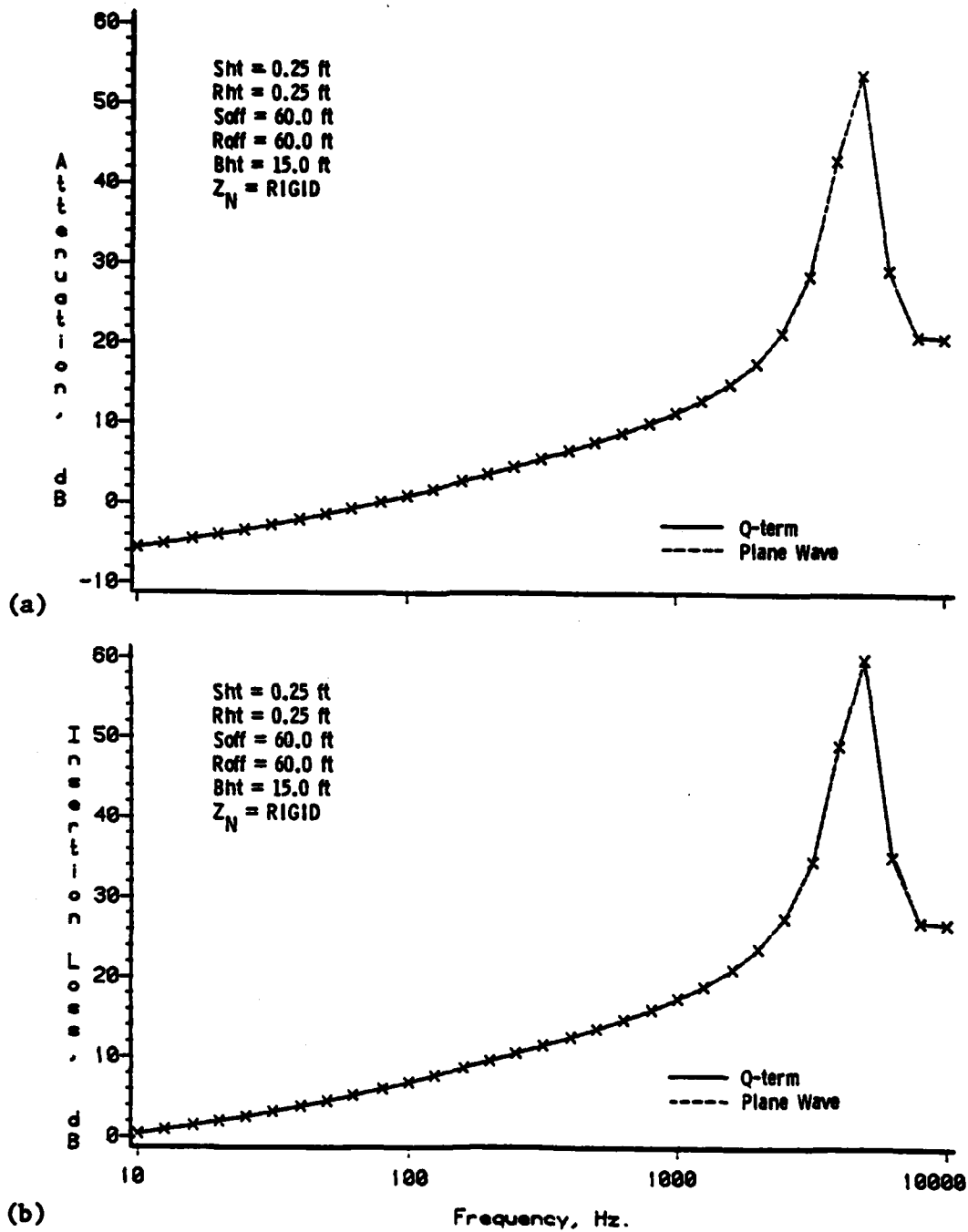


Figure 4.37 Calculated Data for (a) Attenuation and (b) Insertion Loss as a Function of Frequency. Q-term and Plane Wave Solutions. $S_{ht}=0.25$, $R_{ht}=0.25$, $B_{ht}=15.0$, and $Z_N=RIGID$.

reached. The insertion loss follows this trend exactly. When the ground is grass-covered, the data in Figure 4.38 is generated. An important feature here is that the plane wave solution remains valid even for very low kR . This can be explained with reference to Table 4.3, where it can be seen that for low frequencies, the impedance is rather high. This tends to counteract any "low kR " differences between the plane wave and Q-term solutions.

As has been observed in previous cases, the attenuation shows a broad peak in the response for the impedance-covered ground. However, Figure 4.38 (b) shows that the corresponding insertion loss drops rapidly in this region. Again, the barrier is "preventing" the large grazing-incidence propagation loss to take place over the soft ground.

As a final exercise, a case has been analyzed in which significant differences do exist between the plane wave and Q-term predictions, in spite of the high impedances at low kR values. That is, the barrier height has been reduced ($Bht=0.5$ feet) to force near-grazing incidence for the ground reflected rays. The numerical data are plotted in Figure 4.39 (a) and (b), where the plane wave solution is seen to be up to 30 dB inaccurate. This configuration of source, receiver, and barrier is certainly not representative of noise control applications, but it is interesting to note the single sharp peak in the insertion loss spectra.

Data for a variety of cases have been presented in this chapter, mainly to illustrate some key differences between the classical plane

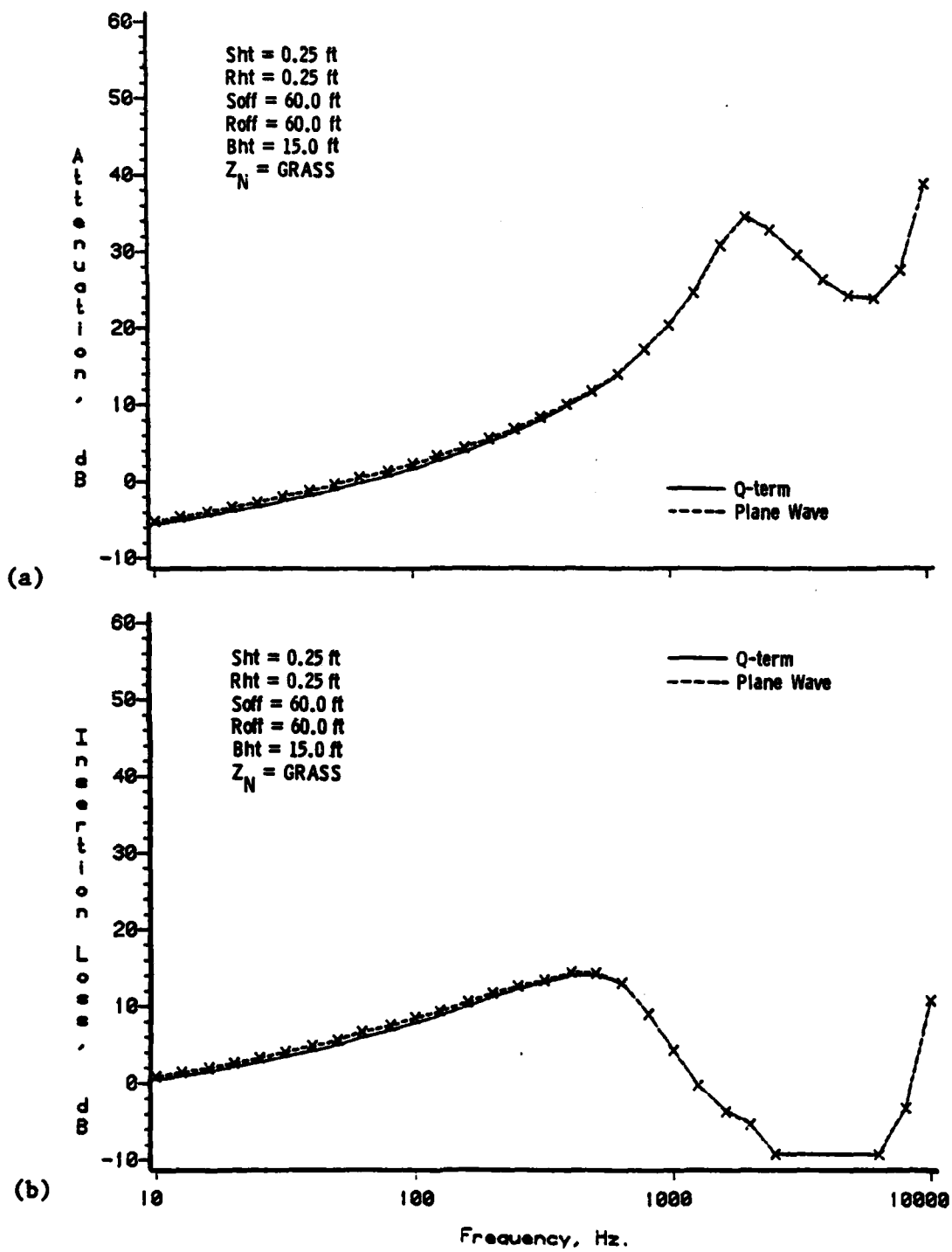


Figure 4.38 Calculated Data for (a) Attenuation and (b) Insertion Loss as a Function of Frequency. Q-term and Plane Wave Solutions. $Sht=0.25$, $Rht=0.25$, $Bht=15.0$, and $Z_N=GRASS$.

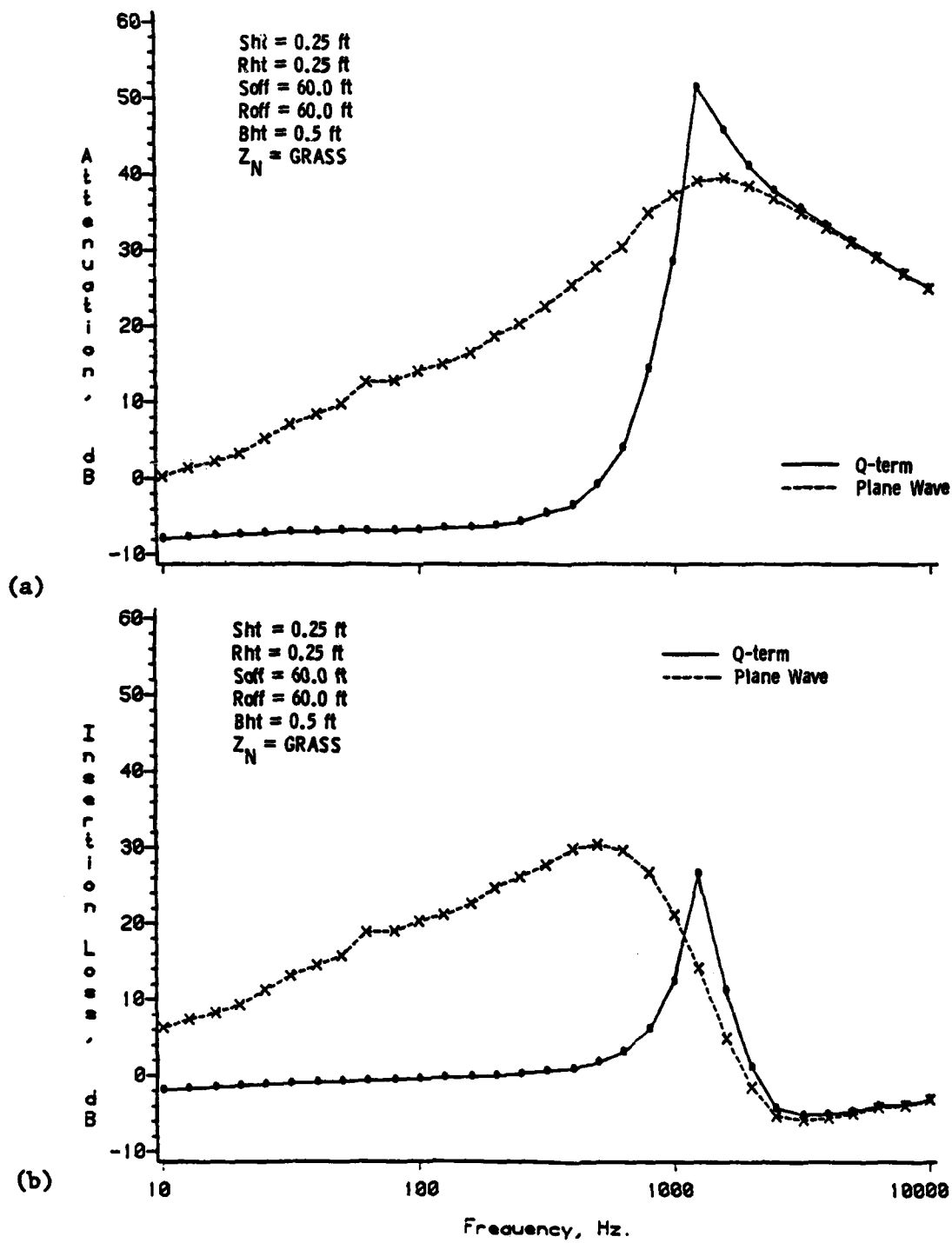


Figure 4.39 Calculated Data for (a) Attenuation and (b) Insertion Loss as a Function of Frequency. Q-term and Plane Wave Solutions. $Sht=0.25$, $Rht=0.25$, $Bht=0.5$, and $Z_N=GRASS$.

wave solution to the propagation problem and the more exact spherical wave solution. A secondary motivation was to collect a large sample of data for future reference. In view of the many parameters involved, this same data could provide much more information than has been presented here. Furthermore, numerical results for either the ground propagation solution or the Edge-Plus-Images model are relatively easy to generate with a digital computer, and so a particular feature or trend in any one plot could be investigated in detail, if desired.

CHAPTER V

SUMMARY AND CONCLUSIONS

The primary objective of the research behind this study was to derive a more exact analytical solution to the problem of point source propagation over an impedance plane. This goal has been met in obtaining the asymptotic solution described in Chapter 2. A second objective was to incorporate the new solution into a barrier model that would account for ground reflections in addition to diffraction. This was also accomplished, and the so-called Edge-Plus-Images model discussed in Chapter 3 was developed.

5.1 Summary

The mathematical problem was formulated as a boundary value problem, in terms of the acoustic Helmholtz equation in cylindrical coordinates (Equation [2.18]) and the local reaction boundary conditions (Equation [2.40]). Using Hankel Transforms, an integral solution was obtained (Equation [2.48]) which contained a pole and a branch point. The pole was replaced by an equivalent integral (Equation [2.51]), and the resulting double integral was found to contain a term resembling the Sommerfeld representation for a point source. The double integral thus reduced to the single integral given by Equation (2.57).

The major part of the research effort was directed toward evaluating the integral in Equation (2.57). Other researchers have

arrived at similar integrals when studying this problem and have invoked such asymptotic techniques as the method of steepest descents for its evaluation. The approach used in this study was to apply the variable transformation given by Equation (2.60) to the integrand. In this manner, the complicated exponential was reduced to a relatively simple polynomial expression. The remainder of the integrand was transformed using standard techniques, and the final real-axis integral given in Equation (2.93) was obtained.

Since the transformed integral is still intractable due to the square root function in the denominator, a Taylor series expansion of the latter was sought and obtained (Equation [2.95]). The important result here is that a general expression for the n^{th} Taylor coefficient was derived, making available (computationally) as many terms in the series as might be desired or necessary. This expansion of the denominator allowed the original integral in Equation (2.93) to be written as an infinite sum of integrals as in Equation (2.105).

The sum is an asymptotic series in the parameter " kR_2 ".

The final step in the formal derivation was to perform the term-by-term integration, that is, to evaluate the component integrals in the asymptotic series. Each integral was resolved in terms of parabolic cylinder functions (Equation [2.106]), which in turn were expressed in terms of the complex complementary error function. From the perspective of this study, the most important feature of the parabolic cylinder functions was found to be their recursive nature. Specifically, the recursion relations for the parabolic cylinder

functions led directly to recursion relations for the integral terms in the asymptotic series (Equations [2.117] - [2.119]). Thus, the final result of the mathematical derivation, the closed-form asymptotic series given by Equation (2.123) or (2.128), was obtained.

The formal solution was then re-phrased in several useful forms. The "Q-term" form in Equation (2.129), with Q defined by Equation (2.135), lends a physical interpretation. Namely, the quantity Q could be thought of as a "spherical wave reflection coefficient," since the equation in this form is analogous to that employing the classical plane wave reflection coefficient (Equation [2.5]). The Q-term form of solution is preferred here; for reference, it is restated in Figure 5.1. The "F-term" form given by Equation (2.137), with F defined by Equation (2.141), presents the solution as one containing a "correction" term for the classical plane wave solution. The form of the solution given in Section 2.3.5.4 shows that the Hankel function can be extracted from the asymptotic series (other researchers have generated approximate solutions containing the Hankel function). Finally, a form of solution using only the first term in the asymptotic series was presented in Section 2.3.5.5.

For the case of perpendicular incidence ($\sin\psi = 1.0$), an exact solution was derived in terms of the exponential integral (Equation [2.158]). Small- and large-argument expansions for the exponential integral were available and are given by Equations (2.156) and (2.157), respectively. It was found that the solution using the first term in the latter expansion is identical to the plane wave solution for this case.

$$\Phi_{\text{tot}}(P) = \frac{e^{ikR_1}}{R_1} + Q \frac{e^{ikR_2}}{R_2}$$

$$Q = 1 + \frac{2\beta}{(\beta + \sin\psi)} \sum_{n=0}^{\infty} T_n^* [e_1 E_n^* + K_n^*]$$

$$e_1 = i\sqrt{\pi} \lambda e^{-\lambda^2} \operatorname{erfc}(-i\lambda) \quad \lambda = \sqrt{i k R_2} \sqrt{1 + \beta \sin\psi - (1 - \beta^2)^{1/2} \cos\psi}$$

$$T_n^* = \sum_{k=0}^{n-2k>0} \binom{n-k}{k} a_{n-k} \left(\frac{4G}{H}\right)^{n-k}$$

$$G = 1 + \beta \sin\psi - (1 - \beta^2)^{1/2} \cos\psi$$

$$H = 1 + \beta \sin\psi + (1 - \beta^2)^{1/2} \cos\psi$$

$$a_0 = 1$$

$$a_m = \frac{1/2-m}{m} a_{m-1}$$

$$E_0^* = 1 \quad E_1^* = -1/2$$

$$E_m^* = -1/2 E_{m-1}^* - \frac{(m-1)}{8ikR_2 G} E_{m-2}^*$$

$$K_0^* = 0 \quad K_1^* = -1/2$$

$$K_m^* = -1/2 K_{m-1}^* - \frac{(m-1)}{8ikR_2 G} K_{m-2}^*$$

Figure 5.1 The Preferred Q-term Form of the Asymptotic Series Solution. Q is the Spherical Wave Reflection Coefficient.

The next phase of the research was directed toward incorporating the ground propagation solution into a barrier diffraction model. Following a brief review of the underlying diffraction concepts in Section 3.1, the principal result of this phase--the so-called Edge-Plus-Images model--is described in Section 3.2. The model is constructed using four separate half-plane diffracted ray paths. That is, a direct-diffracted ray, a reflected-diffracted ray, a diffracted-reflected ray, and a reflected-diffracted-reflected ray (Figure 3.4) are combined coherently, and the ground-reflected rays are appropriately modified by the spherical wave reflection coefficient.

A large quantity of numerical data generated from the ground propagation solution and from the Edge-Plus-Images diffraction model was analyzed next. The dependence of the predictions on several important parameters was investigated in Chapter 4 in a comprehensive series of graphs. For the ground propagation section, the dependence on the parameter kR , the reflection angle ψ , and the ground impedance Z_N was studied, and for the barrier section, the influence of barrier height and diffraction angle ϕ was studied in addition.

5.2 Conclusions

In the discussion of the numerical results from both the propagation solution and the barrier diffraction model, many specific observations of trends and features in the data were pointed out. Here, several general conclusions will be drawn and discussed.

The asymptotic series solution is very accurate. The only noticeable difference between the data predicted from the asymptotic series solution and the data from the numerical integration of the exact solution occurred at very low values of kR . Deviations in this region are expected, but the surprising fact is that these deviations cease to exist for values of kR that are still relatively small. For example, Figure 4.1 shows no difference between the exact and asymptotic solutions for kR down to a value $kR=3$. And Figure 4.2 shows only 0.25 difference for $kR=0.1$. Re-examining the integrand trends presented in Figure 2.7 (a), (b), and (c) might provide some insight into why this is possible. For the low kR values cited here, the integrand will show significant amplitudes outside the radius of curvature of the Taylor series (t_a). Presumably, then, the oscillatory nature of the integrand prevents any net contribution to the integral for all but the smallest values of t (for which the Taylor series is convergent).

The first term in the asymptotic series usually provides sufficient accuracy. For the geometries and impedance conditions considered in this study, the maximum deviation between the F-term (that is, F_1 from Equation [2.150]) solution and the full series solution can be seen in Figure 4.3. Here, a 3 dB deviation exists over a wide range of kR . However, this is an extreme case (grazing incidence, very soft ground), and a more typical behavior (Figures 4.5 and 4.6, for example) shows agreement with the exact solution for larger kR and only one or two dB deviation for small kR . It is

interesting to note that for extremely small kR , the solution using only the first term in the asymptotic series may give more accuracy than the solution using more terms--these terms are probably diverging here--as can be seen in Figures 4.1 (b) or 4.3, for example.

The magnitude of the difference between the solution using the first term only and that using the full series is highly dependent on the values of the parameters kR , Z_N , and ψ . The effects of these parameters are inter-related, and it is difficult to determine which is the "controlling" factor. The ground impedance seems to have a very strong influence. That is, even for relatively large kR and large ψ , a small value for Z_N will still produce deviations (for instance, in Figure 4.8 [b]).

The simple plane wave solution may be accurate over a wide range of parameter values. It is definitely inaccurate for small values of all three parameters and definitely accurate for large values of all three. No general rule can be stated for intermediate values, yet the numerical data in Chapter 4 may serve as a guide.

The ground reflections must be taken into account when considering diffraction by a barrier. For all the cases considered here, the half-plane prediction curve (diffraction alone) was significantly inaccurate, even for very practical geometries and impedance conditions. The only possible exception to this conclusion is the case where the source and receiver are well above the ground, for which the half-plane theory seems to predict the "average" attenuation through the interference maxima and minima (Figure 4.25).

The range of validity of the plane wave solution is great when a barrier is present. This is because of the larger ground reflection angles. The Edge-Plus-Images model may only require the use of the more-exact spherical wave reflection coefficient for very short barrier heights, source and receiver near the ground, and a relatively low ground impedance. Practical cases (in outdoor noise control, at least) show very little difference between the solutions (Figures 4.43 and 4.44).

5.3 Suggestions for Further Research

From the mathematical standpoint, more rigor could be applied to several points in the derivation of the ground propagation solution. An investigation of the convergence of the asymptotic series, and a more thorough treatment of the branch cuts and their dependence on the angle and the admittance could be made. For the Edge-Plus-Images model, the diffraction coefficient could be adapted to other types of barriers, such as wedges, trapezoids, or parallel edges.

An expanded series of sensitivity tests could also be undertaken to determine more precise relationships among the parameters. In addition, numerical data for the absorptive barrier might be generated and compared to the rigid barrier.

Finally, it may be interesting to apply the theoretical results of the present study to other fields such as underwater acoustics, seismology, or electromagnetics, for which certain values of the parameters kR and Z_N considered "unrealistic" in air acoustics might be more natural.

REFERENCES

Abramowitz, M., & Stegun, I. A. Handbook of mathematical functions (National Bureau of Standards Applied Mathematics Series, 55). Washington, D. C.: U. S. Government Printing Office, 1964.

Attenborough, K. Predicted ground effect for highway noise. Journal of Sound and Vibration, 1982, 81, 413-424.

Attenborough, K., Hayek, S. I., & Lawther, J. M. Propagation of sound above a porous half-space. Journal of the Acoustical Society of America, 1980, 68, 1493-1501.

Bafios, A., Jr. Dipole radiation in the presence of a conducting half-space. New York: Pergamon Press, 1966.

Bafios, A., Jr., & Wesley, J. P. The horizontal electric dipole in a conducting half-space (Report SIO Reference 53-3;). University of California Marine Physical Laboratory, 1953.

Bowman, J. J., Senior, T. B. A., & Uslenghi, P. L. E. Electromagnetic and acoustic scattering by simple shapes. Amsterdam, The Netherlands: North-Holland Publishers, 1969.

Bouwkamp, C. J. Diffraction theory. In Reports on Progress in Physics, (Vol. 17), London: The Physical Society, 1954.

Briquet, M., & Filippi, P. Diffraction of a spherical wave by an absorbing plane. Journal of the Acoustical Society of America, 1977, 3, 640-646.

Butov, P. A. Reflection of a spherical wave from an impedance boundary. Soviet Physics Acoustics, 1981, 27, 191-193.

Carslaw, H. S. Some multiform solutions of the partial differential equations of physics and mathematics and their applications. Proceedings of the London Mathematical Society, 1899, 30, 121-163.

Cheddell, C. I. Propagation of noise along a finite impedance boundary. Journal of the Acoustical Society of America, 1977, 62, 825-834.

Chien, C. F., & Soroka, W. W. Sound propagation along an impedance plane. Journal of Sound and Vibration, 1975, 43, 9-20.

Chien, C. F., & Soroka, W. W. A note on the calculation of sound propagation long an impedance surface. Journal of Sound and Vibration, 1980, 69, 340-343.

Clemmow, P. C. The plane wave spectrum representation of electromagnetic waves. London: Pergamon Press, 1966.

Copson, E. T. An introduction to the theory of functions of a complex variable. Oxford: The Clarendon Press, 1935.

Delany, M. E., & Bazley, E. M. Monopole radiation in the presence of an absorbing plane. Journal of Sound and Vibration, 1970, 13, 269-279.

Donato, R. J. Propagation of a spherical wave near a plane boundary with a complex impedance. Journal of the Acoustical Society of America, 1976a, 60, 34-39.

Donato, R. J. Spherical-wave reflection from a boundary of reactive impedance using a modification of Cagniard's method. Journal of the Acoustical Society of America, 1976b, 60, 999-1002.

Embleton, T. F. W., Piercy, J. E., & Olson, N. Outdoor sound propagation over ground of finite impedance. Journal of the Acoustical Society of America, 1976, 59, 267-277.

Fehr, R. O. The reduction of industrial machine noise. Proceedings of the Second Annual National Noise Abatement Symposium, Chicago, 1951, 93-103.

Filippi, P. J. T., & Habault, D. Reflexion of a spherical wave by the plane interface between a perfect fluid and a porous medium. Journal of Sound and Vibration, 1978, 56, 97-103.

Fujiwara, K. Comments on "Absorptive noise barrier on finite impedance ground" by Isei. Journal of the Acoustical Society of Japan, 1980, 1, 211-212.

Gradshteyn, I. S., & Ryzhik, I. M. Table of integrals, series, and products. New York and London: Academic Press, 1965.

Habault, D. Diffraction of a spherical wave by different models of ground: approximate formulas. Journal of Sound and Vibration, 1980, 68, 413-425.

Habault, D., & Filippi, P. J. T. Ground effect analysis: surface wave and layer potential representations. Journal of Sound and Vibration, 1981, 79, 529-550.

Hayek, S. I. Acoustic diffraction for highway noise barriers. In V. K. Varadan & V. V. Varadan (Eds.), Elastic wave scattering and propagation. Ann Arbor: Ann Arbor Science Publishers, 1982.

Hayek, S. I., Attenborough, K., & Lawther, J. M. Models for acoustic propagation over absorbent ground (DOT-FH-11-9515). Interim Report, The Federal Highway Administration, 1980.

Hayek, S. I., Lawther, J. M., Kendig, R. P., & Simowitz, K. T. Investigation of selected noise barrier acoustical parameters. Final Report, National Cooperative Highway Research Program 3-26, Transportation Research Board, National Research Council, 1978.

Hayek, S. I., Lawther, J. M., & Tate, D. C. Model for acoustic propagation over ground—theory and experiment. Technical report for the National Cooperative Highway Research Program 3-26, Transportation Research Board, National Research Council, 1980.

Hayek, S. I., & Nobile, M. A. Diffraction by barriers over absorbent ground. Proceedings of the 1981 international conference on noise control engineering, 1981, 1, 243-248.

Heins, A. E. The excitation of a perfectly conducting half-plane by a dipole field. IRE Transactions on Antennas and Propagation, 1956, AP-4, 343-365.

Ingard, U. On the reflection of a spherical sound wave from an infinite plane. Journal of the Acoustical Society of America, 1951, 23, 329-335.

Isei, T. Absorptive noise barrier on finite impedance ground. Journal

Isei, T., Embleton, T. F. W., & Piercy, J. E. Noise reduction by barriers on finite impedance ground. Journal of the Acoustical Society of America, 1980, 67, 46-58.

Jones, D. S. A simplifying technique in the solution of a class of diffraction problems. Quarterly Journal of Mathematics, 1952, 3, 189-196.

Jonasson, H. G. Sound attenuation by barriers on the ground. Journal of Sound and Vibration, 1972, 22, 113-126.

Keller, J. B. A geometrical theory of diffraction. In L. M. Graves (Ed.), Calculus of variations and its applications, Proceedings of Symposia in Applied Mathematics (Vol. 8), New York: McGraw-Hill, 1958.

Keller, J. B. Geometrical theory of diffraction. Journal of the Optical Society of America, 1962, 52, 116-130.

Kendig, R. P. Acoustic diffraction by an impedance covered half-plane (Doctoral dissertation, The Pennsylvania State University, 1977). Dissertation Abstracts International, 1977, 38, 2264. (University Microfilms No. 77-23246).

Kendig, R. P., & Hayek, S. I. Diffraction by a hard-soft barrier. Journal of the Acoustical Society of America, 1981, 70, 1156-1165.

Kouyoumjian, R. G., & Pathak, P. H. A uniform geometrical theory of diffraction for an edge in a perfectly conducting surface. Proceedings of the Institute of Electronic and Electrical Engineers, 1974, 62(11), 1448-1461.

Kurze, U. J., & Anderson, G. S. Sound attenuation by barriers. Applied Acoustics, 1971, 4, 35-53.

Lawhead, R. B., & Rudnick, I. Measurements on an acoustic wave propagated along a boundary. Journal of the Acoustical Society of America, 1951a, 23, 541-545.

Lawhead, R. B., & Rudnick, I. Acoustic wave propagation along a constant normal impedance boundary. Journal of the Acoustical Society of America, 1951b, 23, 546-549.

Lawther, J. M., & Hayek, S. I. A noise barrier parameter study. Proceedings of the Conference on Highway Traffic Noise Mitigation, Los Angeles, California, 1978, 11-15.

Lawther, J. M., Hayek, S. I., Tate, D. C., & Nobile, M. A. Theoretical and experimental investigations of selected noise barrier acoustical parameters. Final Report, National Cooperative Highway Research Program 3-26, 1980.

Levine, H., & Schwinger, J. On the theory of diffraction by an aperture in an infinite screen, I. Physical Review, 1948, 74, 958-974.

Levine, H. & Schwinger, J. On the theory of diffraction by an aperture in an infinite plane screen, II. Physical Review, 1949, 75, 1423-1431.

Lindblad, S. G. Reduction of sound by sound barriers near road traffic (Report L-739, in Swedish) Göteborg, Sweden: Akustikplanering AB, March, 1970.

Lindsay, R. B. (Ed.). Acoustics: historical and philosophical development. Stroudsburg, Pennsylvania: Dowden, Hutchison, and Ross, 1972.

MacDonald, H. M. Electric waves. Cambridge, England: Cambridge University Press, 1902.

MacDonald, H. M. A class of diffraction problems. Proceedings of the London Mathematical Society, 1915, 14, 410-427.

Maekawa, Z. Noise reduction by screens. Paper presented at the Fifth International Congress on Acoustics, Liège, September, 1965.

Maekawa, Z. Noise reduction by screens. Applied Acoustics. 1968, 1, 157-173.

Malyuzhinets, G. D. The radiation of sound by the vibrating boundaries of an arbitrary wedge, parts I and II. Soviet Physics Acoustics, 1955, 1, 152-174
240-248.

Malyuzhinets, G. D. Das Sommerfelddeche integral und die losung von beugungsaufgaben in winkelgebieten. Annalen der Physik, 1962, 6, 107-112.

Malyuzhinets, G. D., & Tuzhilin, A. A. Plane acoustic wave diffraction at a semi-infinite thin elastic plate. USSR Computational Mathematics and Mathematical Physics, 1970, 10, 179-199.

Morse, P. M., & Ingard, K. U. Theoretical acoustics. New York: McGraw-Hill Book Company, 1968.

Naghieh, M., & Hayek, S. I. Diffraction of a point source by two impedance-covered half-planes. Journal of the Acoustical Society of America, 1981, 69, 629-637.

Nobile, M. A., & Hayek, S. I. A new model for a noise barrier on a rigid ground plane. Journal of the Acoustical Society of America, 1981, 69(Supplement 1):S102.

Norton, K. A. The propagation of radio waves over the surface of the earth and in the upper atmosphere, Part I. Proceedings of the Institute of Radio Engineers, 1936, 24, 1367-1387.

Norton, K. A. The propagation of radio waves over the surface of the earth and in the upper atmosphere, Part II. Proceedings of the Institute of Radio Engineers, 1937, 25, 1203-1236.

Pao, S. P., & Evans, L. B. Sound attenuation over simulated ground cover. Journal of the Acoustical Society of America, 1971, 61, 1069-1075.

Oberhettinger, F. On asymptotic series for functions occurring in the theory of diffraction of waves by wedges. Journal of Mathematical Physics, 1956, 34, 245-255.

Paul, D. I. Acoustical radiation from a point source in the presence of two media. Journal of the Acoustical Society of America, 1957, 29, 1102-1109.

Pauli, W. On asymptotic series for functions in the theory of diffraction of light. Physical Review, 1938, 54, 924-931.

Pierce, A. D. Diffraction of sound around corners and over wide barriers. Journal of the Acoustical Society of America, 1974, 55, 941-955.

Rasmussen, K. B. Propagation of road traffic noise over level terrain. Journal of Sound and Vibration, 1982, 82, 51-61

Rathe, E. J. Note on two common problems of sound propagation. Journal of Sound and Vibration, 1969, 10, 472-479.

Rawlins, A. D. The solution of a mixed boundary value problem in the theory of diffraction by a semi-infinite plane. Proceedings of the Royal Society of London, 1975, A346, 469-484.

Redfearn, S. W. Some acoustical source-observer problems. Philosophical Magazine, 1940, 30, 223-236.

Rudnick, I. The propagation of an acoustic wave along a boundary. Journal of the Acoustical Society of America, 1947, 19, 348-356.

Senior, T. B. A. Diffraction by a semi-infinite metallic sheet. Proceedings of the Royal Society of London, 1952, A213, 436-458.

Skudrzyk, E. J. The foundations of acoustics. Vienna: Springer-Verlag, 1971.

Sommerfeld, A. Mathematische theorie der diffraction. Mathematische Annalen, 1896, 47, 317-374.

Sommerfeld, A. Über die ausbreitung der wellen in der drahtlosen telegraphie. [The propagation of waves in wireless telegraphy.] Annalen der Physik, 1909, 28, 665-736.

Sommerfeld, A. Über die ausbreitung der wellen in der drahtlosen telegraphie. [The propagation of waves in wireless telegraphy.] Annalen der Physik, 1926, 81, 1135-1153.

Stratton, J. A. Electromagnetic theory. New York: McGraw-Hill, 1941.

Thomasson, S. I. Reflection of waves from a point source by an impedance boundary. Journal of the Acoustical Society of America, 1976, 59, 780-785.

Thomasson, S. I. Sound propagation above a layer with a large refraction index. Journal of the Acoustical Society of America, 1977, 61, 659-674.

Thomasson, S. I. Diffraction by a screen above an impedance boundary. Journal of the Acoustical Society of America, 1978, 63, 1768-1781.

Thomasson, S. I. A powerful asymptotic solution for sound propagation above an impedance boundary. Acustica, 1980, 45, 122-125.

Van der Pol, B. Theory of the reflection of the light from a point source by a finitely conducting flat mirror, with an application to radiotelegraphy. Physica, 1935, 2, 843-853.

Van der Pol, B., & Niessen, K. F. The propagation of electromagnetic waves over a plane earth. Annalen der Physik, 1930, 6, 273-294.

Van Moorhem, W. K. Reflection of a spherical wave from a plane surface. Journal of Sound and Vibration, 1975, 42, 201-208.

Wenzel, A. R. Propagation of waves along an impedance boundary. Journal of the Acoustical Society of America, 1974, 55, 956-963.

Weyl, H. Ausbreitung elektromagnetischer wellen über einem ebenen leiter. [The propagation of electromagnetic waves over a plane conductor.] Annalen der Physik, 1919, 60, 481-500.

Wise, W. H. The grounded condenser antenna radiation formula. Proceedings of the Institute of Radio Engineers, 1931, 19, 1684-1689.

DISTRIBUTION LIST FOR TM 82-210

Commander (NSEA 0342)
Naval Sea Systems Command
Department of the Navy
Washington, DC 20362

Copies 1 and 2

Commander (NSEA 9961)
Naval Sea Systems Command
Department of the Navy
Washington, DC 20362

Copies 3 and 4

Defense Technical Information Center
5010 Duke Street
Cameron Station
Alexandria, VA 22314

Copies 5 through 10